Imaging and tailoring electric and antiferromagnetic textures in multiferroic thin films of BiFeO

Johanna Fischer

Thèse de doctorat

NNT : 2020UPASP013

université PARIS-SACLAY

Imaging and tailoring electric and antiferromagnetic textures in multiferroic thin films of $BiFeO_3$

Thèse de doctorat de l'université Paris-Saclay

École doctorale n° 564, Physique en Ile-de-France (PIF)
Spécialité de doctorat : physique
Unité de recherche : Université Paris-Saclay, CNRS, Thales, Unité mixte de physique CNRS/Thales, 91767, Palaiseau, France
Référent : Faculté des sciences d'Orsay

Thèse présentée et soutenue à Palaiseau, le 27.11.2020, par

Johanna FISCHER

Composition du Jury

Philippe LECOEUR Professeur, Université Paris-Saclay – C2N	Président
Brice GAUTIER Professeur, INSA Lyon - INL	Rapporteur & Examinateur
Morgan TRASSIN Professeur, ETH Zürich	Rapporteur & Examinateur
Béatrice GRENIER Maître de Conférences, ILL, Université Grenoble Alpes	Examinatrice
Michel VIRET Directeur de Recherche, SPEC-CEA	Examinateur
Vincent GARCIA Chargé de Recherche, Unité Mixte de Physique CNRS-Thales	Directeur de thèse
Stéphane FUSIL Maître de Conférences, Unité Mixte de Physique CNRS-Thales	Invité
Vincent JACQUES Chargé de Recherche, L2C, Université de Montpellier	Invité

Für meinen Papa, der das leider nicht mehr erleben durfte.

À mon père, qui n'a pas pu voir cette thèse.

To my father, who didn't live to see this.

Acknowledgments

The past three years took me on a journey not only through the electric and antiferromagnetic textures of $BiFeO_3$ thin films but also through the discovery of my strengths and weaknesses. Fortunately, I was not alone on my way and I want to thank all the great people that accompanied me, taught me various things and supported me from the beginning until the end. Thanks to the patience a lot of these people showed to me, did I not only learn a lot of physics, but French also became my second language. So here I want to thank everyone in the language I would speak with them.

Naturellement, mes premiers remerciements vont à mes deux encadrants de thèse Vincent Garcia et Stéphane Fusil. J'ai beaucoup appris et avancé scientifiquement et personnellement sous votre encadrement et j'admire votre connaissance scientifique. Je sais que je n'en ai parfois fait qu'à ma tête et je vous remercie de m'avoir laissé beaucoup de liberté pour mes manipes, ce qui m'a tout de même permis d'obtenir certains résultats alors qu'on ne les attendait plus. Vincent, je te remercie particulièrement pour ta patience lors de l'explication de l'analyse des cartes en espace réciproque et de m'avoir montré que quand on le comprend enfin, ça peut même devenir marrant. Steef merci pour ta pédagogie. Je connais peu de personnes qui arrivent à expliquer les sujets de recherche de façon aussi fascinantes et bien adaptée aux thésards. Je garde entre autres de très bons souvenirs de la semaine passée à Montpellier pour les manipes à une époque où les restos étaient encore ouverts... Finalement, je veux vous remercier tous les deux pour tout le temps que vous avez consacré cette dernière année à la relecture de mon manuscrit et aux répétitions de ma soutenance.

Je veux remercier tous les membres du jury, Philippe Lecoeur comme président du jury, Brice Gautier et Morgan Trassin comme rapporteurs et Béatrice Grenier et Michel Viret comme examinateurs, d'avoir fait tout leur possible pour permettre la soutenance à la date prévue malgré la situation sanitaire. Merci également pour vos commentaires et questions sur le manuscrit et la présentation.

Je suis très heureuse d'avoir pu faire cette thèse en collaboration avec Vincent Jacques et son équipe. Vincent, tu m'as accueillie au début de ma thèse deux mois à Montpellier, suivi par plusieurs séjours un peu plus courts et je te remercie beaucoup pour ce temps de collaboration. Merci à Angela Haykal et Waseem Akhtar pour le temps passé ensemble devant la manipe. Waseem you were a great teacher for me as a sometimes very motivated PHD in the lab and I will not forget the time you took for my repetition the night before the first presentation of my thesis' work. Angela, شكراً جزيلاً !! C'était génial de travailler avec toi pendant ces trois ans : au début vous m'avez accueillie avec Rana et introduite à la culture Libanaise, puis tout le temps passé ensemble devant la manipe (et le temps que tu as passé seule à retrouver les zones entre les marqueurs…) et finalement tout s'est terminé différemment que prévu et nous n'avons pas pu assister à la soutenance l'une de l'autre, mais vive la télécommunication et j'espère qu'on pourra le fêter un jour ensemble… (A3tazer 3an wade3 barghach fi daftar moula7azatiki :-P).

Je souhaite aussi remercier Manuel Bibes. Manu, tu m'as encadrée lors de mon stage de six mois et ensuite proposé de faire ma thèse au labo où tu m'as laissé le choix entre différents sujets. Tout au long de cette thèse tu as été impliqué dans les projets et aussi toujours trouvé

du temps pour moi et mes questions et soucis. Enfin pour la recherche du postdoc que je n'aurais pas pu espérer trouver mieux pour moi et le hasard faisant bien les choses, me voilà entre les mains d'une de tes anciennes thésardes qui a travaillé sur le $BiFeO_3$ quelques années avant moi.

Également présente depuis mon premier jour au labo, je remercie Cécile Carrétéro. Tu m'as appris à utiliser la PLD, le diffractomètre, l'AFM, le four, les logiciels pour analyser les données, et sans toi ma thèse n'aurait pas été la même… Merci également pour ta patience et ta bonne humeur. Tu as été là pour moi dans toutes les situations indépendamment de mon état émotionnel.

Je suis très reconnaissante à tous les collaborateurs avec lesquels j'ai pu travailler et publier pendant cette thèse en plus de la collaboration avec Montpellier. À Michel Viret, Jean-Yves Chauleau et Nicolas Jaouen, je dis merci pour les nuits au synchrotron, les discussions sur les résultats, la bonne ambiance et vos réponses à mes nombreuses questions. To Laurent Bellaiche and Yousra Nahas: it was an honour for me to work with you and I am very happy that I was given the possibility to do experiments supporting your theoretical calculations. To Daniel Sando: thank you for the time we spent together in the lab. I admire your endless motivation and experience with BFO growth and keep a lot of very nice souvenirs in mind from the conference in Lausanne, up to the point where the chairman introduced me as „a last speaker from Sydney…". It was a great time with all of you guys, Dan, Stuart and Oliver and even though I finally didn't make it to Australia, I hope to meet you again soon. À Brahim Dkhil, même si finalement les résultats des neutrons de notre semaine à Oxford n'ont pas été clairement interprétable c'était une bonne expérience pour moi de passer ce beamtime avec toi et j'espère que tu n'arrêteras jamais de raconter tes blagues, ça aide à faire passer une journée dans la météo anglaise en attendant des résultats.

I also want to thank Patrick Maletinsky with his group and Hai Zhong from Qnami. It was a pleasure to participate in the meetings in Montpellier and Basel and listen to all the talks about NV magnetometry, as well as in the discussions at the restaurants afterwards. Even though I just missed the arrival of the NV setup in Palaiseau, I hope at some point I will get in touch with this technique and all of you guys again.

Tout au long de ma thèse j'ai rencontré beaucoup de collègues super sympas et je garde plein de bons souvenirs de bonnes conversations et de manipes faites ensemble. La liste va être longue et je veux commencer par les permanents qui ont été là, déjà pendant le stage et ensuite aussi la thèse. Je veux dire merci à Frédéric Petroff et Frédéric Nguyen Van Dau, suivis par Vincent Cross et Paolo Bortolotti comme chefs de l'UMR pour la possibilité d'avoir fait ma thèse au labo et le temps que vous avez consacré pour les entretiens annuels et toutes les formalités de thèse. Dans ce contexte merci beaucoup également à Anne Dussart et Nathalie Lesauvage pour votre patience avec moi et les procédures administratives, ça a toujours été un plaisir de passer vous voir. Éric Jacquet, comme Cécile nous avons partagé le bureau et au-delà ton aide au labo PLD tu as toujours compris ma fascination pour le sport, tu as su me remonter le moral quand des fois j'étais un peu triste et on a bien rigolé ensemble. Karim Bouzehouane et Aymeric Vecchiola, merci pour la bonne ambiance dans la salle de manipe PFM/MFM et tous les petits

coups de mains, c'était bien sympa pendant ces trois ans et je suis un peu triste de ne pas vivre l'ère microscope NV à l'UMR. Javier Briatico, même si tu n'as certainement pas toujours été heureux de me voir apparaitre devant ta porte pour te demander du temps à la PLD, tu as toujours été très gentil avec moi et j'en ai finalement fait un bon tas d'échantillons REALXXXX. Sophie Colin, tu m'as fait la formation en salle blanche, mais pas que. Tu as toujours été là pour aider avec tous les petits trucs qu'on cherche au labo dans la vie quotidienne et j'ai beaucoup apprécié ton oreille ouverte à toutes les occasions. Anke Sander, auch dir möchte ich für die vielen guten Unterhaltungen und Ratschläge in den letzten Jahren danken. Es war immer schön und hat mich sehr aufgebaut mit dir über alltägliche Ereignisse zu ratschen und ich hoffe, dass du deinen guten Humor beibehältst und wir uns auch in den nächsten Jahren nicht aus den Augen verlieren. Bruno Dlubak, tu as été mon parrain de thèse et je n'aurais pas pu tomber mieux. Tu as toujours réussi à calmer mes émotions des fois bien fortes quand je suis partie avec tout mon cœur dans ce que je voulais obtenir au travail. En me donnant le sentiment de compréhension pour mes petits soucis, tu m'as bien montré qu'on peut voir un problème de différents côtés et j'ai beaucoup appris au niveau des perspectives psychologiques de ces différents points de vues. Je me rappelle toujours de nos conversations comme si c'était hier et je pense que ça sera des leçons pour la vie pour moi. Nicolas Reyren, merci pour ton temps et ta patience pour répondre à tous mes questions, il n'y a aucune meilleure motivation pour les manipes que de les comprendre ! Agnès Barthélémy, tu m'as toujours aidée que ce soit avec les répétitions pour mon talk à Lausanne où plein d'autres choses. Florian Godel, je n'aurais pas pu imaginer le labo sans toi et je suis bien contente que tu aies eu le poste finalement ! Nos petites conversations le matin et le soir dans la voiture vont me manquer. Ce qui va me manquer seront tous les gens rencontrés à midi en salle café où dans les couloirs, même si je ne peux pas nommer tout le monde individuellement.

Quand je suis arrivée en début de thèse c'était génial de revoir les potes du stage et de reprendre le sport du midi, notamment avec Lucile Soumah et William Legrand. Lulu, je t'ai convertie au meilleur sport du monde et ça m'a fait trop plaisir de grimper avec toi à coté de la course à pied, de la natation, … !! T'étais trop longtemps trop loin, va falloir retourner en France avec de la montagne maintenant 😉. William, merci de m'avoir montré entre autres la boucle interdépartementale autour du labo et m'avoir motivée pour un petit footing de 17km à midi, dommage qu'il n'y ait finalement plus eu le temps pour faire les manipes SAFS/BFO à la fin. Danjela Marcovic, ça faisait déjà presque un an que j'étais en thèse quand on s'est rencontré, mais si tu me demandes maintenant je ne peux plus imaginer un labo sans toi. Heureusement que je t'ai toi aussi transformée en une grimpeuse passionnée et maintenant la question pour les vacances ce n'est plus si, mais où on veut grimper et je ne m'inquiète pas de pouvoir t'amener faire plein de grandes voies autour de Grenoble dans l'avenir. Mais plus important que toutes les activités – merci d'être comme tu es pour moi, une copine avec qui on peut bien se marrer, s'aider pour passer des moments difficiles et savoir que l'autre va toujours être là. Hvala Dzoni, un jour il faut que tu me montres la Serbie aussi !! Alice Mizrahi, tu nous as rejoints rapidement aux boucles de courses à pied et c'était toujours un grand plaisir de passer devant ton bureau pour tchatcher. Je vous souhaite à Dani et toi beaucoup de projets passionnants dans les années à venir avec le super groupe neuromorphique ! Ralph El Hage, merci ktir pas que pour ton aide avec mes phrases arabes, mais surtout pour tous les joyeux moments qu'on

a passés ensemble pendant ces trois ans de thèse, au badminton, pendant les soirées où dehors dans des parcs. Je croise les doigts pour ta nationalisation et j'espère que tu ne partiras pas trop loin quand même ! Pauline Dufour et Diane Gouere, je suis trop contente que vous soyez restées après le stage en thèse, ça va être triste une vie sans Paupau et Dianou au quotidien ! Pauline, ça ma beaucoup changé la vie d'avoir eu une « sœur thésarde » et quelqu'un avec qui on peut discuter des rsms et de l'espace réciproque aussi bien que de tout autre chose. Tu vas voir, quand t'auras troué tous les chaussons d'escalade que je t'ai donnés, tu grimperas les mêmes voies et blocs qu'ils ont déjà grimpé sans toi ;-P. I also want to thank all the PHds and post-docs from the Oxitronics group, Sara Varotto, Jin Hong Lee, Srijani Mallik, Lucia Iglesias, Felix Trier, Raphael Aeschlimann, Julien Brehin, Luis Moreno Vicente-Arche for being great teammates in the lab and I keep nice souvenirs of the parties in Palaiseau. Jin, thank you for all the discussions and advice on BFO, PLD growth and at the end on the transport measurements. Sorry for having you made ride my bike at night and bringing you to our apartment the night of a fire in our building… Sara, I am sad you only arrived towards the end of my thesis, it was great fun to work together. I wish you good luck and a loooot of results with all the stripy and non-stripy samples. I admire your mindset, "if someone else can grow these samples I will find the parameters too", take care of yourself and enjoy your post-doc, including the well-earned vacation. Maybe you could come to Grenoble 😉? Je veux remercier également tous les autres doctorants, post-docs des autres groupes qui ont été au labo en même temps que moi. Il y avait toujours une super bonne ambiance en salle de manipe et dans le labo en général ou au sport, vous m'avez même fait jouer au foot pour la première fois dans ma vie… Je croise les doigts pour un retour à la vie normale un jour et j'espère pouvoir revenir pour un petit pot de thèse tardif.

En dehors de l'UMR, merci aussi aux sportifs du bâtiment, notamment pour la course à pied, l'aviron et la piscine. Merci notamment à Colin Mismer d'être devenu mon partenaire et pote d'escalade à l'ESM, d'avoir été en grande voie Munich avec moi, d'avoir grimpé à Bleau sous toutes conditions météo, au Viaduc où même la nuit à la frontale à la Troche avec Seb… Il faudra absolument que vous veniez à Grenoble pour des aventures en falaise !!

Und natürlich wäre diese Doktorarbeit weder zustande gekommen noch hätte ich sie so gut hingekriegt, wenn ich nicht meinen festen Rückhalt in der Heimat gehabt hätte. Ich denke an alle meine Freunde die ich regelmäßig besuchen durfte und mit denen ich so manchen Abend oder Klettertag erleben durfte um ein bisschen durchzuschnaufen… Von alles möchte ich einer Person im Zusammenhang mit dieser Doktorarbeit besonders danken: Matthias Opel, du hast mich dazu gebracht quer durch München zu radeln um an Manus Seminar teilzunehmen, mir mit einer Engelsgeduld viele Male alles Mögliche erklärt und vor allem immer an mich geglaubt. Die Liste wäre lang, wenn ich hier alle Momente aufzähle, bei denen ich schon beim Aufschreiben lachen muss, ich denke zurück an deine Besuche hier in Paris, gemeinsame Abenteuer in den Bergen zu Fuß, auf Ski, ja sogar am Seil, … „Sockenkontrolle" 😉, Konferenz im Wohnzimmer (nächstes Mal mache ich mein Mikro aus, versprochen…) und vieles mehr. Zuletzt sogar eine offizielle Kollaboration letzten Dezember in München, schade dass es nicht ganz so geklappt hat wie wir gehofft hatten… Vielen vielen Dank für alles und ich bin sicher du kommst auch bald nach Grenoble, stimmts?

Und wenn ich nach München komme empfängt mich natürlich immer meine liebe Mama mit offenen Armen. Auch wenn du von meiner Physik nicht viel verstehst so hast du doch immer gespürt, wenn ich ein paar aufbauende Worte gebrauchen konnte. Du hast mich in jeglicher Hinsicht bei meinem Vorhaben in Frankreich zu promovieren unterstützt. Ich bin stolz auf dich, dass auch dein Französisch mit Kurs an der Uni und allem noch besser geworden ist und freue mich schon auf deine Besuche in Zukunft. Auch wenn er das alles nicht mehr erleben durfte, so hast du mir trotzdem oft schöne Erinnerungen an die gemeinsame Zeit mit Papa in Erinnerung gerufen und in Gedanken war auch er oft bei mir.

En dernier je veux dire merci à la personne qui m'a soutenue le plus pendant toute cette thèse, Colin Dessornes. De partager ma vie pendant toute cette thèse avec toi a inclus de partager plein de moments joyeux, mais aussi un peu difficiles pour moi. Tu as toujours su comprendre pourquoi j'étais la plus heureuse du monde un soir à cause d'un petit échantillon de 5x5mm^2, m'attendre plein de vendredi soir, parce que le réglage aux rayons X ne voulait que rarement se terminer tôt, tu as même dans ce contexte eu la motivation d'écouter mes réflexions sur la maille pseudo-hexagonale et programmer totofaitduvélo avec moi en plein milieu de la nuit. Tu as eu beaucoup de patience avec moi quand j'ai récemment essayé d'apprendre à programmer en Python et tu as passé toute la rédaction de ce manuscrit avec moi à l'appart, des fois confinés et beaucoup trop rarement ensemble à Bleau. Finalement tu vas même quitter la forêt pour qu'on continue notre aventure ensemble à Grenoble. Je ne peux pas te remercier assez, toi et ta famille vous êtes devenus la mienne et je suis contente de voir venir notre avenir ensembles.

Table des matières

Introduction

Materials with a complex long-range magnetic order are emerging as a new paradigm for spintronics applications. More than 80% of known magnetic substances have dominant antiferromagnetic interactions and have moved into the focus of current research. On the one hand, appealing assets like insensitivity to spurious magnetic fields, suppression of the cross-talk between neighbouring device cells, fast magnetization dynamics in the THz range and long-distance spin transport make them favourable candidates for low-power spintronics. Hence, understanding the fundamental basis of antiferromagnetic manipulation to harness their unique features is highly desirable. On the other hand, a major bottleneck is the electrical control and readout of their antiferromagnetic magnetization state. In multiferroics, the magnetoelectric coupling between ferroelectric and antiferromagnetic orders may represent an efficient way to control antiferromagnetism with an electric field.

In this thesis, we investigate the archetypical room-temperature multiferroic oxide bismuth ferrite, $BiFeO_3$. We exploit the unique performances of scanning NV magnetometry to image a wide variety of complex antiferromagnetic textures at the nanoscale, textures that we control by strain engineering and electric field. Epitaxial $BiFeO_3$ thin films grown on various substrates give access to a fine tuning of the strain level. Various pristine ferroelectric domain landscapes, imaged by piezoresponse force microscopy, are elaborated. We furthermore resort on an inverse ferroelectric phase transition triggered by an a posteriori annealing, theoretically predicted and experimentally validated. This transition enhances the global electrical order from a maze to a perfect array of striped ferroelectric domains. We correlate the ferroelectric landscapes to the antiferromagnetic ones, as imaged with a scanning NV magnetometer. We demonstrate that strain stabilizes bulk or exotic spin cycloids, as well as collinear antiferromagnetic order. A complementary resonant elastic X-ray scattering investigation allows corroborating the nanoscale real-space images of the magnetic arrangements by the macroscopic spin textures in reciprocal space. Using this synchrotron-based technique, we reveal the periodic chiral antiferromagnetic order and confirm the existence of two types of cycloids. Beyond the observations of ferroelectric domains pristine configurations, in which the spin cycloid propagation is locked to the electric polarization, we manipulate the ferroelectric order aiming at designing antiferromagnetic landscapes on demand. Taking advantage of the magnetoelectric coupling in $BiFeO_3$, we deterministically change one type of cycloid to another or turn collinear states into non-collinear ones. Finally, resorting on anisotropic strain, we stabilize a single domain ferroelectric state, in which a single spin cycloid propagates. We unravel the physics of spin cycloids with data from NV scanning magnetometry as well as resonant elastic X-ray scattering. This opens a fantastic avenue to investigate the coupling between electrically-reprogrammable non-collinear antiferromagnetism and spin transport.

This thesis is structured as follows: **Chapter 1** presents the context of this study starting with an introduction to the state of the art in antiferromagnetic spintronics and the material properties of $BiFeO_3$. These last are first discussed in bulk and then in thin films. Preceding the results, **chapter 2** describes the technical requirements to understand the measurements and introduces the data analysis. Besides the growth technique (pulsed laser deposition) and meth-

ods for investigating ferroic orders (piezoresponse force microscopy, scanning NV magnetometry and resonant elastic X-ray scattering), this includes information about the crystallographic lattices in $BiFeO_3$ and their characterizations with X-ray diffraction. **Chapter 3** focuses on the actual structural and ferroelectric properties obtained in as-grown thin films. Results of the growth optimization towards ordered ferroelectric domain patterns are presented, followed by the astonishing influence of an a posteriori ex-situ annealing step. The latter is described in an ab-initio theory developed by our collaborators from the University of Arkansas, predicting the "inverse phase transition" that is experimentally observed here. Finally, in **chapter 4**, real-space images in combination with resonant elastic X-ray scattering data result in a phase diagram of the antiferromagnetic textures, including two types of spin cycloids. The dependence with epitaxial strain is highlighted here, and the antiferromagnetic electrical manipulation is demonstrated. In the last paragraph, we investigate a single multiferroic domain thin film grown on a peculiar crystal, which will serve as a reference system to detect electrically the non-collinear antiferromagnetic order.

1. Context of the study

The modern evolution of data processing and storage demands highly stable devices with fast switching dynamics in smaller spatial volumes. At some point, the enhancement of already existing device types will be limited by the intrinsic material properties. Hence, novel effects and material classes with advantageous properties need to be explored. In this regard, antiferromagnets come into the focus of research. In this chapter, I will present the assets of antiferromagnets for spintronic devices. More specifically, I will introduce the promising properties of the room-temperature multiferroic antiferromagnet $BiFeO_3$.

1.1 Introduction to antiferromagnetic spintronics

A problem in current electronic devices is the production of waste heat, limiting amongst other things the downscaling of the devices. A possible solution proposed in spintronics is the use of the electron spin instead of its charge to store and transmit information with less dissipation. Non-volatile spintronic devices, integrating ferromagnetic materials, are already well established basic elements in the field of data storage. For future spintronic applications, however, antiferromagnetic materials are under consideration, beyond their traditional use for exchange biasing.

1.1.1 Assets of antiferromagnets

The first advantage of antiferromagnets is their robustness against external field perturbations. In contrast to ferromagnetic memory devices where the magnetisation state can be erased by an external magnetic field, the antiferromagnetic order persists due to the large antiferromagnetic exchange energy (Figure 1**a**).[1] Secondly, ultrafast magnetization dynamics are observed and promise switching speeds in the terahertz regime.[2,3] This is illustrated in Figure 1**b**, where the magnetic component of a terahertz pulse generates ultrafast Faraday rotation in a 45 µm thick antiferromagnetic NiO sample. The harmonic oscillations with a period of 1 ps are due to the antiferromagnetic spin precession of NiO.[4] Figure 1**c** illustrates a third advantage of antiferromagnetic materials in data storage devices: a higher-density packing of storage elements becomes possible, because in contrast to ferromagnetic devices, no magnetic stray field causes an interbit crosstalk. In addition, one may envision to use insulating antiferromagnets to propagate spins over long distances as it was previously demonstrated in the prototypical iron garnet insulating ferromagnet. A recent observation demonstrates the long-distance magnon propagation in antiferromagnetic α-Fe_2O_3 single crystals (Figure 1**d**).[5] Spin accumulation is generated at the interface to a Pt injector wire via the spin Hall effect (SHE). The resulting transfer of angular momentum to the antiferromagnet creates a symmetry breaking, responsible for the generation of magnons that travel across α-Fe_2O_3. They are then detected via the inverse SHE in a second Pt wire. It is demonstrated that this effect persists for promising distances as large as 80 µm.

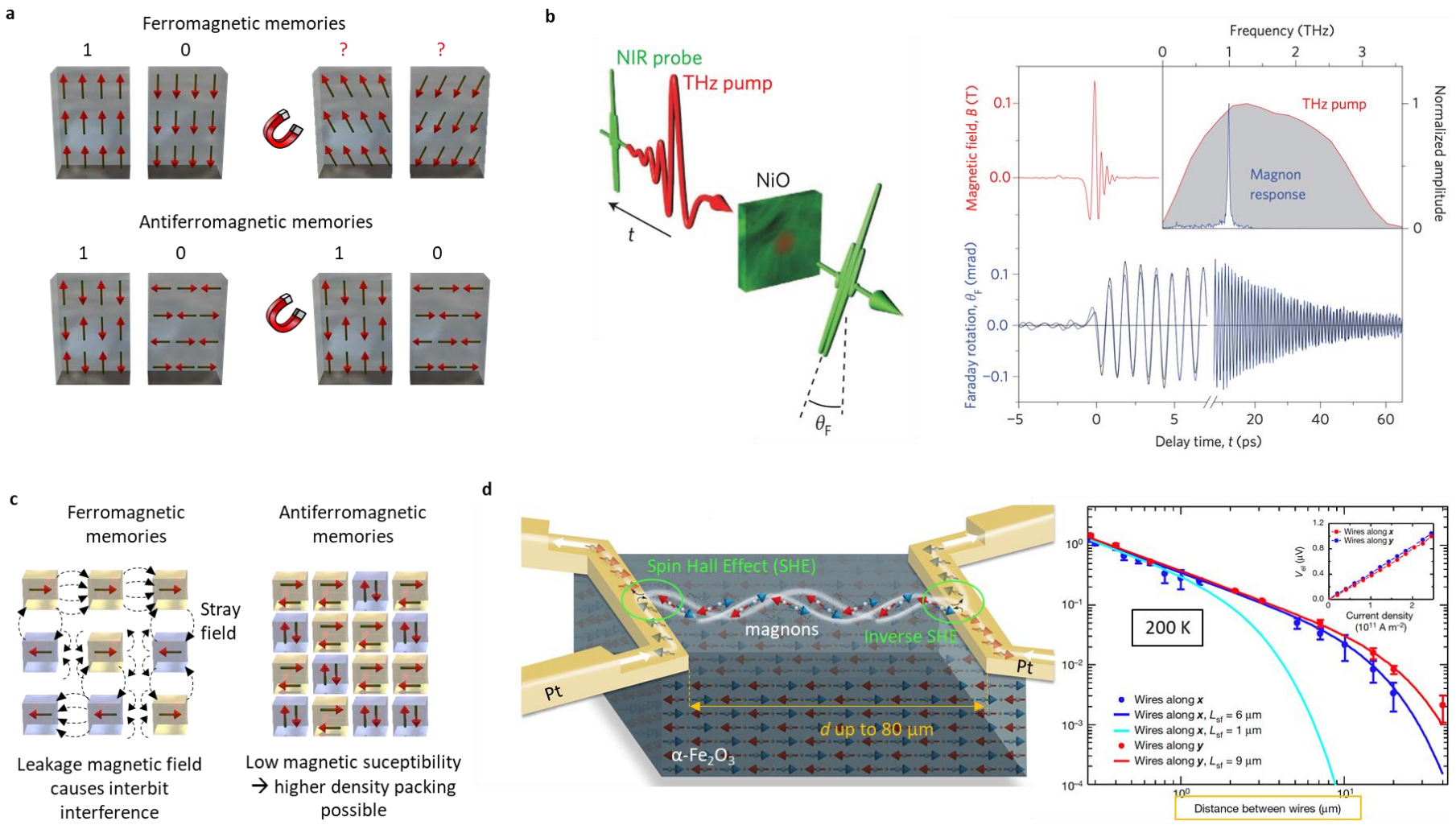

*Figure 1 : Advantages of antiferromagnets for spintronics: **a** Insensitivity to spurious magnetic fields. Figure adapted from reference [1]. **b** Fast magnetization dynamics in the THz range as illustrated in NiO (adapted from reference [4]). **c** Possibility for higher density packing due to the absence of magnetic stray fields. **d** Long distance spin transport, shown in an example adapted from reference [5] in α-Fe_2O_3 single crystals.*

1.1.2 Electrical writing and reading of antiferromagnets

The insensitivity to external magnetic fields, on the other hand, represents a big challenge for reading and writing information and hence for the practical operation of devices. Several promising approaches have been proposed over the last few years to circumvent these issues.

Since in ferromagnets the giant magnetoresistance and the tunnelling magnetoresistance effects are utilized in spin valves and magnetic tunnel junctions for readout, respectively,[6] a possibility would be to adapt these devices for antiferromagnets. Even though in theory, concepts of spin transfer torque and giant magnetoresistance are possible in antiferromagnets as well,[7] scattering processes reduce the effect significantly in experimental realizations.[8] Similarly in antiferromagnetic tunnel junctions, where the torque is supposed to be more robust against scattering processes,[9] a magnetoresistance exists, even if its value stays relatively low.[10]

At first neglected because of its much smaller amplitude, the anisotropic magnetoresistance effect has come into the focus of attention for antiferromagnetic memory resistors. Since it is a bulk phenomenon, no complex multilayer structures are required. Whereas the read-out via anisotropic magnetoresistance could be realized in a promising way in FeRh as a proof of principle for an antiferromagnetic memory resistor (Figure 2**a**), the writing process requires a field-cooling step from the ferromagnetic to the antiferromagnetic phase, this latter being hardly compatible with realistic device applications.[11] To avoid a cooling element, an antiferromagnetic/ferromagnetic phase transition in FeRh induced by Joule heating via a current flow opens the possibility to operate the device only by magnetic field and electric current.[12] In the context of devices based on anisotropic magnetoresistance as readout scheme, a memory with multistable antiferromagnetic states becomes possible, as demonstrated in MnTe.[13] There, the multitude of stable states is ascribed to different antiferromagnetic domain configurations.

Increasing the amplitude of the anisotropic magnetoresistance is possible using a tunnelling mechanism. From the theoretical point of view, the so-called tunnelling anisotropic magnetoresistance effect can be found in antiferromagnets utilizing bi-metallic *3d-5d* antiferromagnetic alloys.[14] This is for instance realized in a stack composed of IrMn, an MgO barrier and a non-magnetic Pt electrode.[15] In this device, the antiferromagnetic moments in IrMn are rotated via the exchange spring effect[16] by an adjacent magnetically soft NiFe ferromagnet (Figure 2**b**).

However, the majority of antiferromagnets are insulators and on the path towards low-power spintronic devices, the use of pure spin currents (no charge flow) would be highly desirable to reduce the dissipation associated with the Joule effect. Up to now, only a few antiferromagnetic insulators have been considered in the framework of spintronics, because alternative ways are needed to probe their antiferromagnetic spin state. One example is the readout using the spin Hall magnetoresistance in a simple electrical transport measurement. This effect is observed in antiferromagnetic NiO and α-Fe_2O_3. It is based on an interfacial exchange of angular momentum (via spin transfer torque) from the sublattice magnetizations to the conduction electrons of an adjacent heavy metal layer. As shown in Figure 2**c**, the size of the effect is found to be even larger in the antiferromagnetic α-Fe_2O_3 (blue curve) compared to the reference ferrimagnetic insulator, $Y_3Fe_5O_{12}$ (black curve). [17–19]

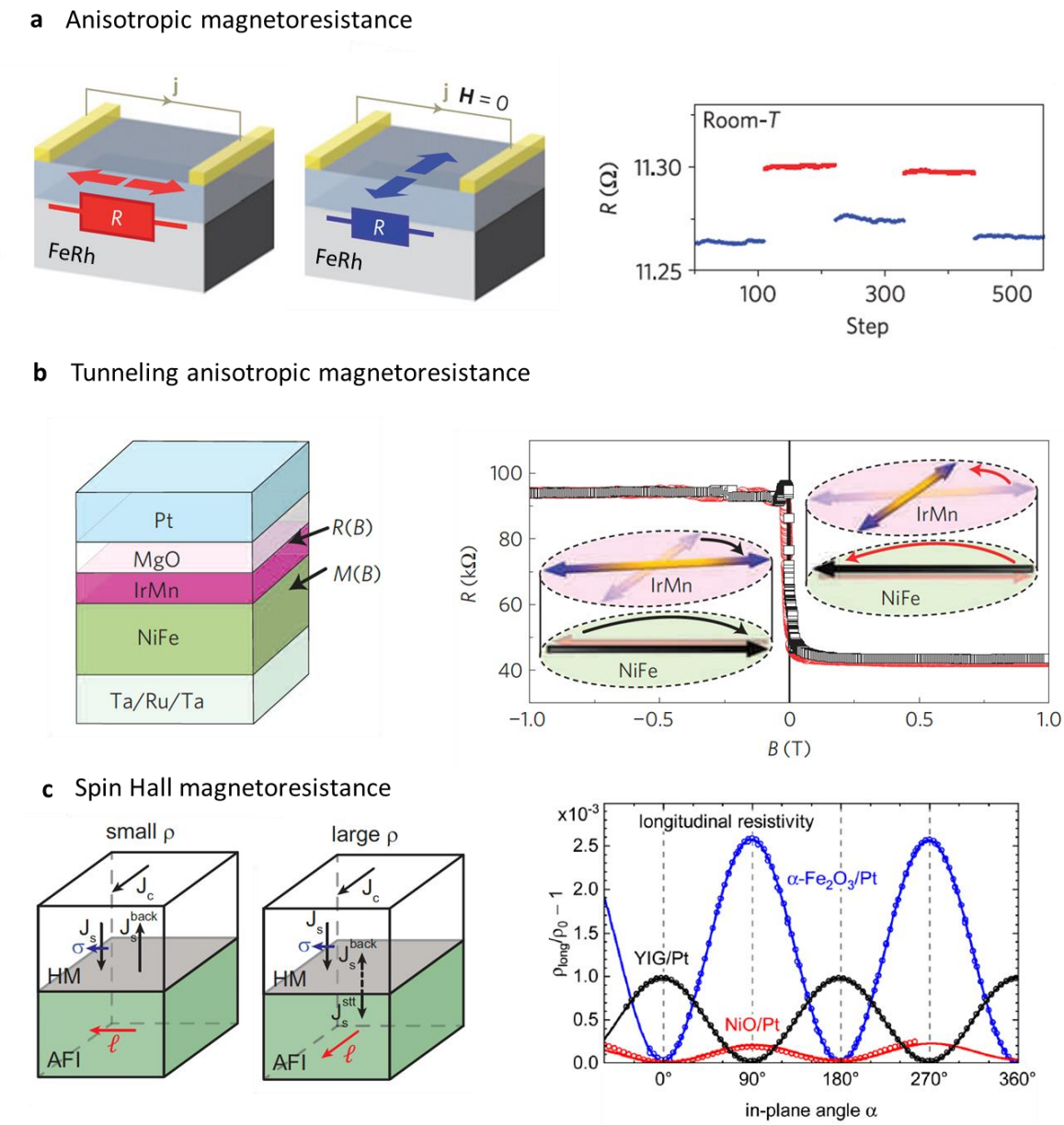

Figure 2 : Antiferromagnetic spintronics: electrical reading of the antiferromagnetic order. ***a*** *Anisotropic magnetoresistance in FeRh. Figure adapted from reference [11].* ***b*** *Tunneling anisotropic magnetoresistance in a IrMn/MgO/Pt stack, controlling the antiferromagnetic order of IrMn via the exchange spin effect by the adjacent NiFe layer. Figure adapted from reference [15].* ***c*** *Spin Hall magnetoresistance in NiO and α-Fe_2O_3 antiferromagnetic insulators at the interface to a Pt top electrode. Figure adapted from references [17–19].*

After having discussed various read-out principles in antiferromagnetic devices, we now focus on different approaches to manipulate the antiferromagnetic spins and hence to write information. First proposed in theory[20] and then realized in experiments[21], is the approach to combine ferromagnets with antiferromagnets in multilayer heterostructures. Here, via the non-relativistic spin transfer torque, the electron spin is transferred to the antiferromagnetic layer and switching of the latter is possible for high current densities. Whereas a uniform magnetic field is useless to manipulate antiferromagnetic sublattices, the field generated by this torque must be staggered, such that it alternates sign from one sublattice to the next one.[22] The exchange

coupling between the ferromagnetic and the antiferromagnetic layers leads to a so-called exchange bias[23], associated with a shift of the ferromagnetic hysteresis loop. On the experimental side, observations made in antiferromagnetic spin valves[24–28] demonstrated that the exchange bias can be influenced by an electrical current. This strategy is a possible path towards the electrical manipulation of the antiferromagnetic order.

More promising in terms of writing of the memory state is the relativistic spin orbit torque. Being a locally generated bulk effect, it is relatively insensitive to disorder and no thin film heterostructure is necessarily required. However, combining the spin and orbital degree of freedom induces a coupling to the properties of the crystallographic lattice. Hence, the occurrence of a spin orbit torque demands a broken inversion symmetry. A current-induced spin polarization is exchange-coupled to the equilibrium magnetic moment of a magnetic material via the inverse spin galvanic effect (Edelstein effect), creating a spin-orbit torque. This is consistent with experimental investigations in the ferromagnetic semiconductor (Ga,Mn)As[29,30] or the room-temperature ferromagnetic metal NiMnSb[31]. In the context of antiferromagnetic spintronics, this effect is proposed as a way to efficiently manipulate the antiferromagnetic order via a spin-polarized current.[32] It could be experimentally realized in CuMnAs thin films (Figure 3**a**), combined with anisotropic magnetoresistance used for read-out.[33] In the same device type, by varying the writing pulse duration and the application of multiple pulses along the same writing path, a multilevel resistive device is realized.[34] These neuron-like switching characteristics reveal that antiferromagnetic spintronics has a huge potential to satisfy the modern needs in data storage and computing purposes. However, when the antiferromagnetic domain structure is imaged (Figure 3**b**), it turns out that only a small percentage of the domains changes its orientation.[35,36] This is depicted in the last coloured image, representing the difference between the domain configurations taken before and after the electrical switching. Hence, the imaging and control of antiferromagnetic domains is mandatory to understand and optimize the switching effects.

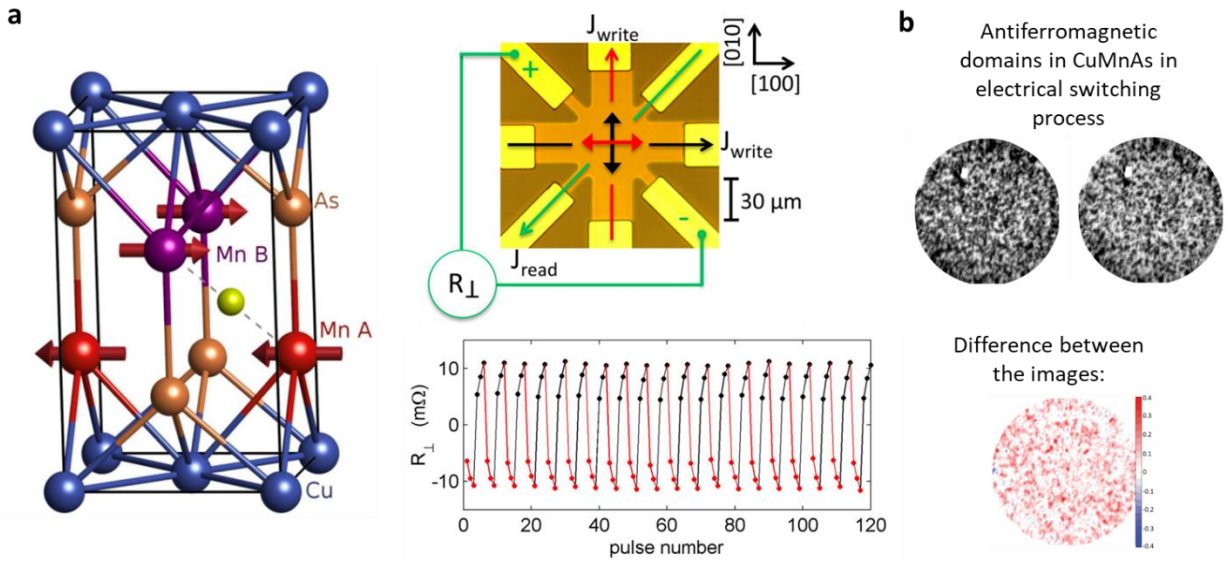

*Figure 3 : **a** First experimental realization of electrical writing in the non-centrosymmetric antiferromagnet CuMnAs via a relativistic current-induced spin torque mechanism. Figure adapted from reference [33]. **b** Incomplete antifer-*

romagnetic domain switching demonstrated in a CuMnAs antiferromagnetic domain pattern. Images captured before and after the switching process by photoemission electron microscopy (PEEM), with antiferromagnetic contrast enabled by x-ray magnetic linear dichroism (XMLD), calculated difference between the two images shown in colour. Figure adapted from reference [35].

Several examples of antiferromagnetic devices can be found in the literature, such as car parking and counting systems, geodynamic sensing devices to measure distances over a long timescale off the grid. [37–40] Another example is a memory device based on a piezoelectric substrate $0.72PbMg_{1/3}Nb_{2/3}O_3$-$0.28PbTiO_3$ to strain-control an antiferromagnetic MnPt layer.[41] A last example resorting on antiferromagnetic FeRh layers coated with a textured rock-salt MgO layer, shows that the effect of the anisotropic magnetoresistance is still functional in flexible devices.[42]

1.1.3 Microscopic insights on antiferromagnetic domains

Even though the first lights of antiferromagnetic spintronics have been attested in the aforementioned devices, the microscopic understanding of the switching mechanisms is still lacking. Due to the absence of a magnetic stray field, only a few techniques are suitable to image antiferromagnetic textures. One option is to use canted antiferromagnets and to measure the small ferromagnetic moment with techniques such as magneto-optical Kerr effect microscopy. Lebrun *et al.* investigate a R-cut α-Fe_2O_3 single crystal at room temperature (Figure 4**a**)[5] and observe domain sizes of hundredths of micrometres. However, at temperatures below the Morin transition, a reorientation of the spins takes place: the canted moment vanishes and can no longer be observed. An alternative technique not relying on measurable finite stray fields relies on synchrotron-based linearly polarized light to measure the direction of the antiferromagnetic vector. Ross *et al.* imaged the collinear antiferromagnetic structure along the (0001) direction in α-Fe_2O_3 thin films at 100K (Figure 4**b**) and obtained smaller domain sizes in the order of 500 nm for the R-cut and a few 100 nm for the C-cut.[43] In another antiferromagnetic insulator, NiO, the domain sizes are determined in the order of hundreds of nanometres as well (Figure 4**c**).[46] Interestingly, spin transport experiments in these different types of antiferromagnetic thin films show that the spin diffusion length scales with the size of antiferromagnetic domains, suggesting that antiferromagnetic domain walls play a significant role for spintronic applications with antiferromagnets. Microscopic insight into the antiferromagnetic landscape is then mandatory to understand and optimize electrical device operation.

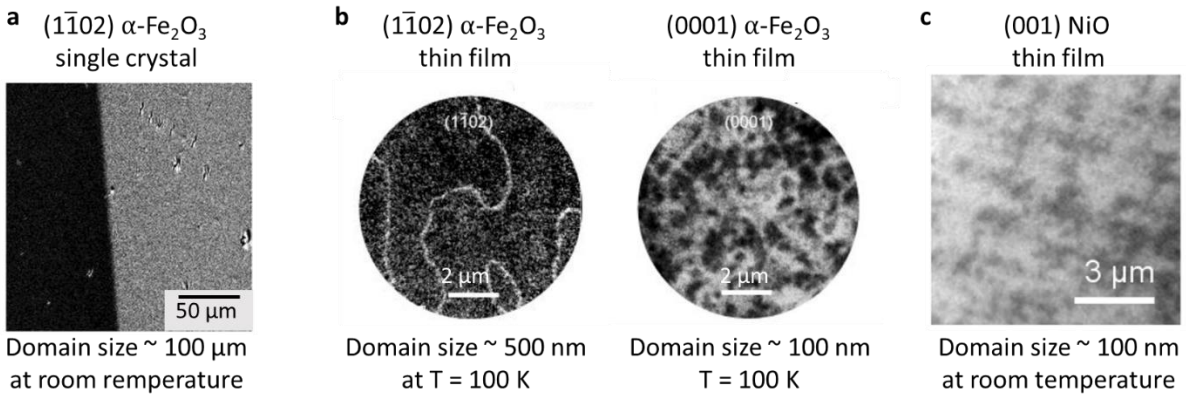

Figure 4 : Antiferromagnetic domain sizes. ***a*** *Magneto optical Kerr effect image of an antiferromagnetic domain in the canted α-Fe_2O_3 single crystal, figure adapted from reference [5]. b X-ray magnetic linear dichroism photoelectron emission imaging at the Fe L_2 edge in α-Fe_2O_3 thin films, figure adapted from reference [43].* ***c*** *Results in NiO thin films show similar results, obtained with X-ray magnetic linear dichroism. Figure adapted from reference [44].*

1.1.4 Multiferroics for reconfigurable antiferromagnetic domains

The main challenges in antiferromagnetic spintronics remain the reading and writing of information at room temperature without a cooling/heating step or the use of external magnetic fields such as in most of the recent reports from the previous section. For antiferromagnetic insulators one would naturally desire a material that additionally possesses an electric setscrew to manipulate the magnetic sublattices. Antiferromagnetic multiferroics like $YMnO_3$ are promising candidates for such an approach. Using second harmonic generation, Fiebig *et al.* were able to discriminate ferroelectric and antiferromagnetic domains in $YMnO_3$.[45] The coincidence of ferroelectric domain walls with antiferromagnetic ones is observed, but within one ferroelectric domain, multiple antiferromagnetic domains can coexist (Figure 5**a**). However, the prerequisite for a functional device is the coupling between the electric and the antiferromagnetic domain microstructures. In the most investigated room-temperature multiferroic, i.e. $BiFeO_3$, Zhao *et al.* observe a clear correlation between ferroelectric and antiferromagnetic stripe domains. Additionally, they show that some of the antiferromagnetic domains can be switched by an electric field (Figure 5**b**),[46] as deduced from the contrast change in the photoemission electron microscopy image. This result might be controversial as X-ray linear dichroism is sensitive to both ferroelectric and antiferromagnetic orders.

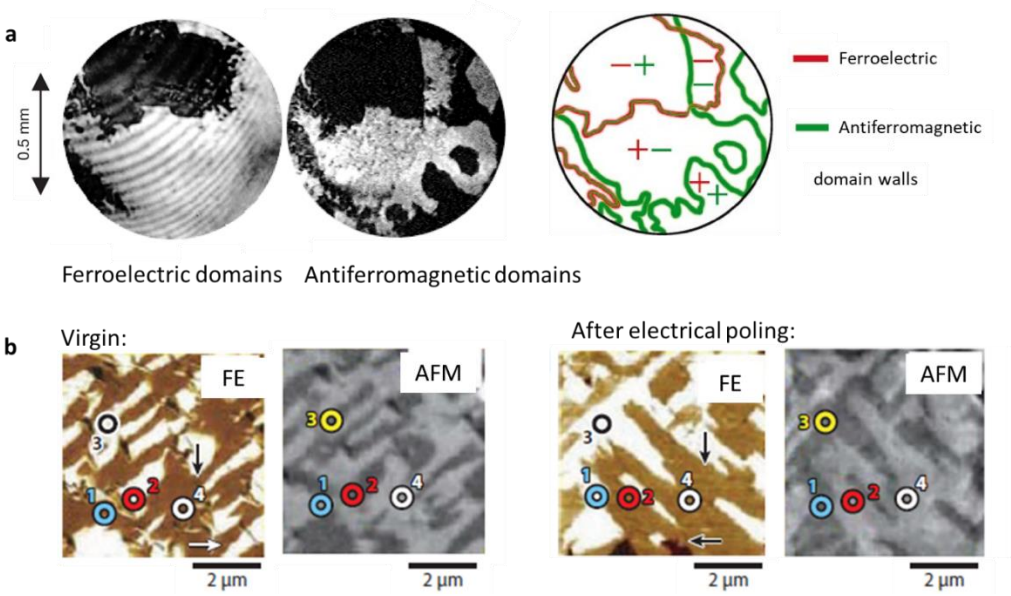

Figure 5 : Coexistence of ferroelectric and antiferromagnetic domains. ***a*** *In hexagonal $YMnO_3$, domains are visualized by second harmonic generation. Bright and dark areas correspond to regions with different orientations of the order parameter (polarization in the ferroelectric domain image, antiferromagnetic staggered vector in the magnetic domain image). The sketch on the right shows the correlation between ferroelectric and antiferromagnetic domain walls. Figure adapted from reference [45].* ***b*** *In-plane piezoresponse force microscopy images of the ferroelectric and photoemission electron microscopy images of the antiferromagnetic domains, before and after electric switching showing the correlation between antiferromagnetic and ferroelectric domains, as well as the control of antiferromagnetic domains by an electric field (figure adapted from reference [46]).*

1.2 Introduction to multiferroic $BiFeO_3$

A material is called ferroic when a spontaneous electric polarization $\mathbf{P}$, magnetization $\boldsymbol{m}$ or strain $\boldsymbol{\varepsilon}$ are formed. These ferroic orders can be controlled by an external electric field $\boldsymbol{E}$, magnetic field $\boldsymbol{H}$ or stress $\boldsymbol{\sigma}$, respectively (Figure 6**a**).[47] In a multiferroic, at least two of those ferroic orders coexist. A very attractive property for spintronics is that, in case of magnetoelectric coupling, the magnetic field may control the polarization or the electric field may control the magnetic sublattices (orange arrows in Figure 6**a**). In the case of $BiFeO_3$, these ferroic orders are ferroelectricity and antiferromagnetism with transition temperatures at $T_c \approx 1100\ \mathrm{K}$ and $T_N = 650\ \mathrm{K}$,[48,49] related to spatial inversion and time reversal symmetry breaking, respectively (Figure 6**b**). In other words, a non-centrosymmetric crystal structure with a charge asymmetry and an antisymmetric magnetic exchange interaction are present.

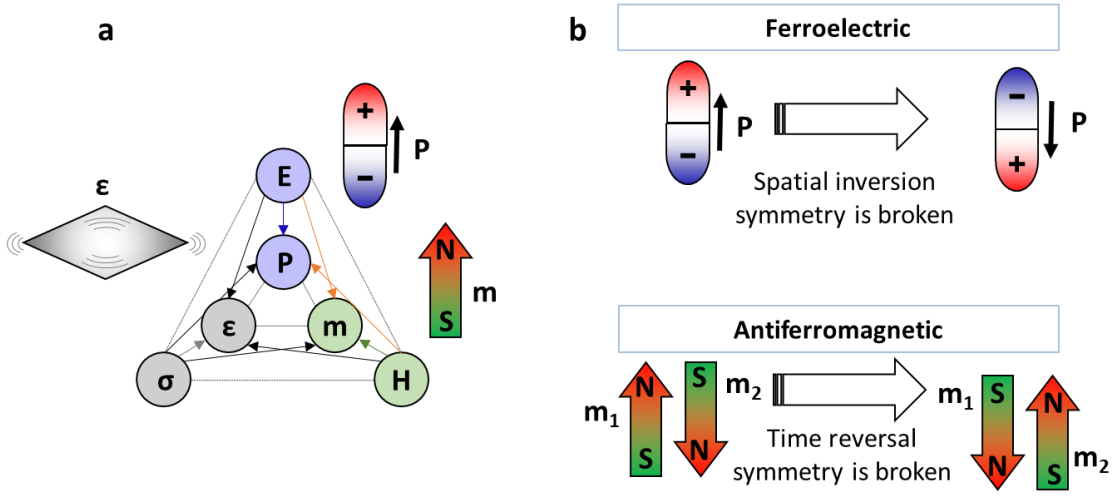

*Figure 6 : **a** Interplay between ferroic orders in multiferroics, adapted from [47]. **b** Relation to symmetry breakings in $BiFeO_3$.*

In this chapter, I focus on the room-temperature material properties of $BiFeO_3$, without considering external stimuli like temperature, pressure or electric and magnetic fields. Ferroelectricity and antiferromagnetism in $BiFeO_3$ are strongly related to the crystal structure. The ferroic orders are first presented for bulk $BiFeO_3$. Then, the role of epitaxial strain in thin films is tackled in the second paragraph. To the end, a $BiFeO_3$-based magnetoelectric device is presented, showing the feasibility to integrate this prototypical multiferroic as a functional material.

1.2.1 Ferroelectric and antiferromagnetic properties in single crystals

Due to its large spontaneous ferroelectric polarization $P = 100\ \mu\mathrm{C\ cm^{-2}}$,[50] and multiferroicity at room-temperature, $BiFeO_3$ has been extensively investigated over the past two decades.[51]

Crystal structure and the origin of the strong ferroelectric polarization

The simple $BiFeO_3$ perovskite crystalizes in the $R3c$ rhombohedral space group at room temperature. The rhombohedral unit cell contains two cubic unit cells as shown in Figure 7**a**. The polarization vector P is parallel to the three-fold rotational symmetry axis along the cubic $[111]$ axis, since the origin of the ferroelectricity in $BiFeO_3$ relies in the stereochemical activity of the Bi $6s$ lone-pair (Figure 7**b**).[52] This pair of valence electrons, that are not shared with another atom in a covalent bond, is chemically inactive but influences the spatial arrangement of the

atoms (i.e. sterically active). Via hybridization, the atomic orbitals mix to form a new atomic orbital and the spherical symmetry of the lone pair is lost. The charge asymmetry induces an off-centre displacement of the Bi^{3+} ion. Theoretical analysis show that it is not enough to consider solely the hybridization of the $6s$ and $6p$ orbitals, but a more complex mixing takes place. This treatment of the electrons in their whole orbital configuration is needed to study the spontaneous polarization as shown by Neanton *et al.*[53] and Ravindran *et al.*[54]

The Fe^{3+} ions are moved in the same direction as the Bi^{3+} ions with respect to the O^{2-} octahedron as a consequence of electrostatic repulsion, while their relative displacement is smaller. The induced collective displacement of the Bi^{3+} and the Fe^{3+} cations with respect to the O^{2-} anions along the $[111]$ direction directly relates the ferroelectricity to the elastic deformation of the crystallographic lattice with a major contribution of the Bi atoms ($> 89\%$) to the absolute value of the polarization. The polarization can point in one of the eight structurally equivalent cubic $\langle 111 \rangle$ directions.

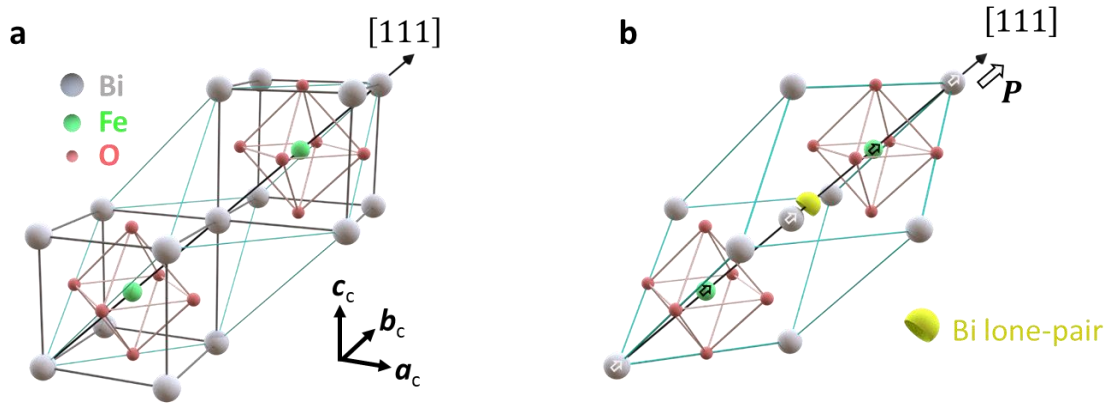

*Figure 7: **a** Relation between the rhombohedral unit cell (turquoise lines) and two cubic perovskite unit cells (black lines) without polar distortion. **b** Due to the* Bi *lone-pair (yellow) a collective displacement of the* Bi^{3+} *and* Fe^{3+} *cations is induced (small arrows on the atoms).*

If there were only the polar displacements, the symmetry of the structure would be reduced from the cubic symmetry $Pm\bar{3}m$ to rhombohedral $R3m$. In perovskite-like ABO_3 oxides, the stabitilty of the ideal structure can be described using the ratio between the cation radii r_A and r_B and the anion radius r_O in the Goldschmidt tolerance factor

$$t = \frac{r_A + r_O}{\sqrt{2}(r_B + r_O)}.$$ [55]

In contrast to $t = 1$ for the ideal cubic perovskite, a value of $t = 0.96$ is calculated[54] for $BiFeO_3$, using the ionic radii from Shannon *et al.*[56]. As a consequence, the FeO_6 octahedra are tilted out of phase with respect to the cubic $[111]$ axis (Figure 8). The two-dimensional view on the (111) plane (Figure 8**b**) clarifies this and suggests the use of a hexagonal lattice setting with the hexagonal c axis parallel to the cubic $[111]$ axis. This will be described in detail in the second chapter of this thesis. The anti-phase FeO_6 tilting angle is about 11°.[57] The counter rotations of the neighbouring oxygen octahedra alone would reduce the symmetry to a paraelectric phase with the $R\bar{3}c$ space group. Together with the aforementioned ferroelectric distortion, this results in the $R3c$ space group for $BiFeO_3$.

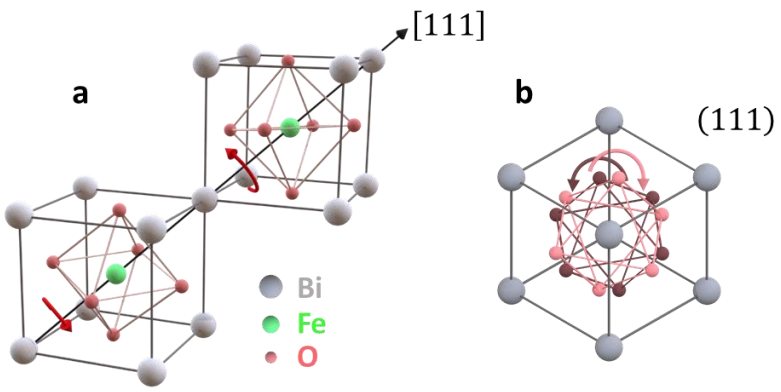

Figure 8: Anti-phase tilting (red arrows) of the FeO_6 octahedra around the [111] *axis due to the ion radii.* ***a*** *Three-dimensional representation,* ***b*** *two-dimensional view on the* (111) *plane.*

Magneto-electric coupling mechanisms

The dominant magnetic interaction in $BiFeO_3$ is the 180° superexchange between the Fe^{3+} via the O^{2-} ions.[58] Fe^{3+} has the electronic configuration [Ar]$3d^5$. Three of the five 3d electrons are in the t_{2g} orbitals and two are located in the e_g orbitals, one in the $3d_{x^2-y^2}$ and one in the $3d_{z^2}$ (Figure 9**a**). A virtual hopping process between the electron from the oxygen $2p$ orbitals and each of the e_g orbitals takes place and forms the G-type antiferromagnetic order shown in Figure 9**b**. The magnetic moments in all nearest neighbouring Fe^{3+} ions are antiparallel, resulting in a ferromagnetic arrangement within the (111)-planes and an antiferromagnetic one between adjacent planes, i.e. in the [111] direction.

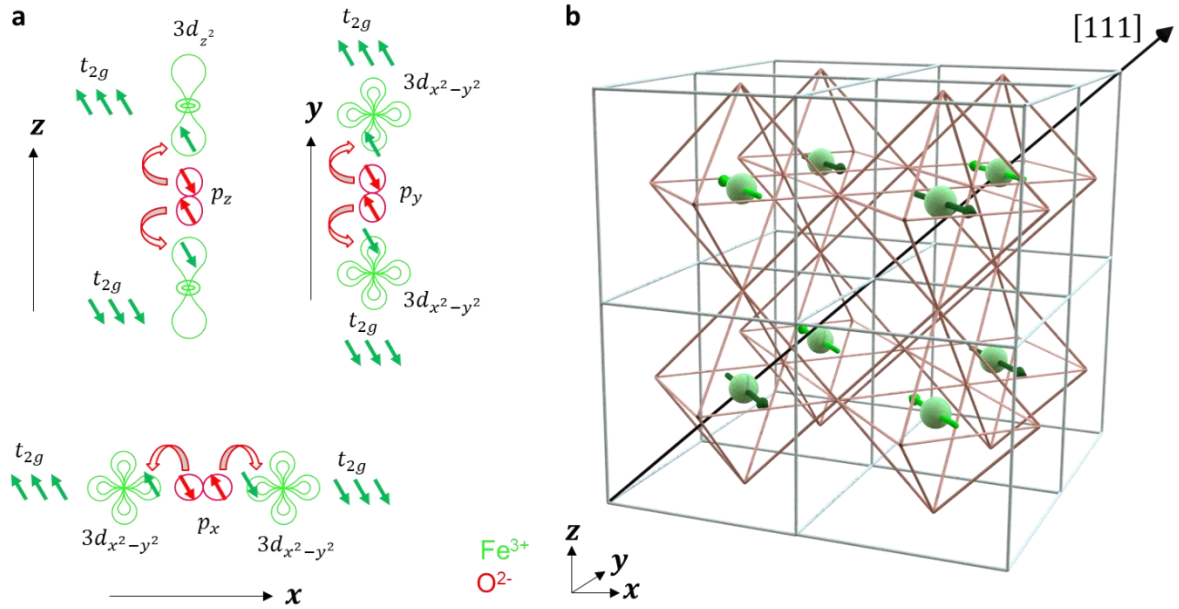

Figure 9 : ***a*** *Superexchange interaction between neighbouring* Fe^{3+} *(green) via the* O^{2-} *ions (red).* ***b*** *G-type antiferromagnetic order.*

Using neutron scattering, Sosnovska *et al.* observed in 1982 a modulation of the G-type order perpendicular to the [111] direction, inducing an incommensurate cycloid with a long wavelength period of 620 Å.[59] In a detailed neutron diffraction experiment on single crystals by

Lebeugle *et al.* in 2008 (Figure 10**a**), the cycloid magnetic structure is confirmed and a propagation vector **k** along one of the three $\{1\bar{1}0\}$ directions is determined. Furthermore, these authors demonstrate the coupling of the magnetic order to the electric polarization in a polarization switching experiment.[60]

The magnetic domains at the surface of a millimetre-size $BiFeO_3$ single crystal were studied by Johnson *et al.* (Figure 10**b**) using circularly polarized X-ray diffraction.[61] Magnetic domains up to several hundred microns in size inside a single ferroelectric domain are investigated. Three domain variants, characterized by their cycloidal modulation direction along the wave vectors $\mathbf{k_1}$, $\mathbf{k_2}$ and $\mathbf{k_3}$, respectively, are observed. Furthermore, the absolute rotation direction of the Néel vector in each individual magnetic domain is found to have the same magnetic polarity. In other words, the cycloid is rotating clockwise in the reference frame spanned by **k** and **P** as shown in Figure 10**b**.

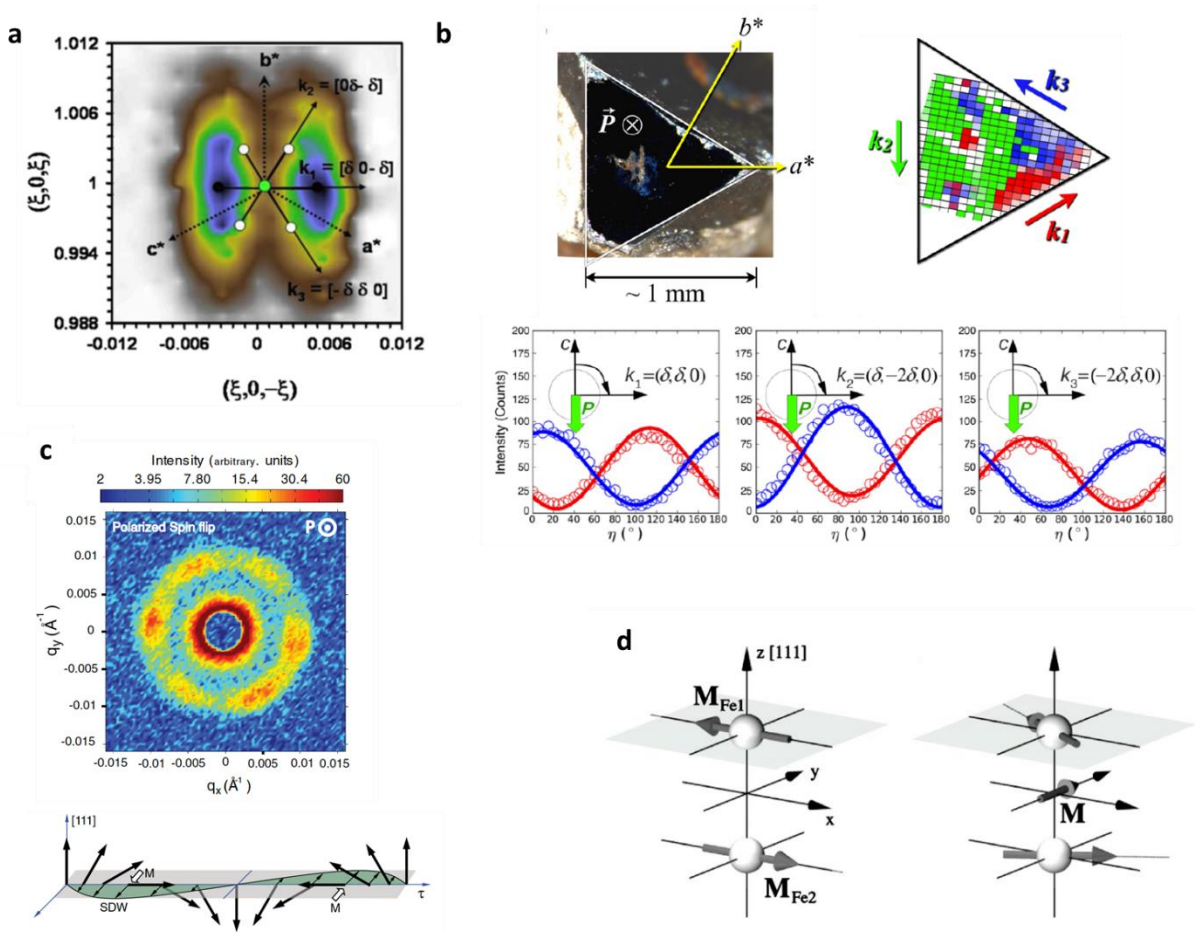

*Figure 10 : Experimental and theoretical results on the magnetic structure in $BiFeO_3$ single crystals. **a** Satellite peaks in a neutron diffraction experiment indicate a spin cycloid with a period of 64 nm in a single ferroelectric domain. Figure adapted from reference [60]. **b** Multiple cycloidal variants in a single ferroelectric domain found in a hard-x-ray magnetic scattering study, using circular polarized light. Photograph of the polished single crystal surface and sketch of the distribution of the antiferromagnetic wave vectors along the indicated k-directions. Angular dependence of the beam intensity, attesting for the same magnetic polarity in each antiferromagnetic domain variant. Figure adapted from reference [61]. **c** Polarized small-angle neutron scattering study attesting for a long wavelength spin density wave generated by spin canting of the spins out of the rotation plane of the antiferromagnetic cycloid, signifying weak ferromagnetism within mesoscopic regions of the sample. The average local magnetization is de-*

*termined to 0.06 μ_B / Fe. Figure adapted from reference [62]. **d** Theoretical study, starting from the magnetic moments, M_{Fe1} and M_{Fe2}, of the two iron atoms in a $BiFeO_3$ crystal where the cycloid is suppressed by doping. The calculated magnetic structure includes the spin-orbit interaction and induces the magnetic moments to rotate in the (111) plane so that there is a resulting spontaneous magnetization **M**. Figure adapted from reference [63].*

In the literature, the origin of this spin cycloid is assigned to the Dzyaloshinskii-Moriya interaction.[64,65] The Hamiltonian of this anisotropic exchange interaction has the form

$$H_{DM} = \boldsymbol{D} \cdot \boldsymbol{S}_i \times \boldsymbol{S}_j,$$

with $\boldsymbol{D}$ the Dzyaloshinskii-Moriya vector and $\boldsymbol{S}_{i,j}$ the spins at the sites i and j. In $BiFeO_3$, two magnetic interactions of this mathematical form govern the long-range spin structure. However, for none of them, the microscopic origin is the Dzyaloshinskii-Moriya interaction in the standard sense. The first one can be explained using an inverse spin current model.[66–68] It was initially proposed by Katsura *et al.* and describes a family of multiferroics where, via a spin current mechanism (Figure 11**a**), a small electric polarization can arise from a non-collinear spin configuration. In a cluster of two transition metal ions (M_i and M_j) carrying two canted magnetic moments $\boldsymbol{m}_i$ and $\boldsymbol{m}_j$ and an oxygen atom O in between, a hopping process via the empty p-orbitals of the oxygen ion leads to a spin current with spin direction $\boldsymbol{j}_s \propto \boldsymbol{m}_i \times \boldsymbol{m}_j$ (yellow arrow), perpendicular to the magnetic moments $\boldsymbol{m}_i$ and $\boldsymbol{m}_j$. This spin current in the system induces a small polarization $\boldsymbol{P} \propto \hat{\boldsymbol{e}}_{\boldsymbol{ij}} \times \boldsymbol{j}_s$, with $\hat{\boldsymbol{e}}_{\boldsymbol{ij}}$ the unit vector parallel to the direction of the bond. So, no polarization is induced if the canting is in a plane perpendicular to $\hat{\boldsymbol{e}}_{\boldsymbol{ij}}$. Rahmedov *et al.* present how in $BiFeO_3$ the inverse spin current effect (Figure 11**b**) is at the origin of the spin cycloid. In this model, the intrinsic ferroelectric polarization induces a canting between the 2nd nearest neighbouring Fe atoms (Figure 11**c**). The spin canting can only be generated in a plane spanned by the polarization $\boldsymbol{P}$ and $\hat{\boldsymbol{e}}_{\boldsymbol{ij}}$. This defines hence the propagation direction of the spin cycloid and the grey shaded rotation plane of the cycloid.[67] Proving the spin current model in multiferroics from a theoretical point of view, Raeliarijaona *et al.* propose that, in the same way spin orbit effects couple to the angular momentum of a particle, an angular momentum density associated with the electromagnetic field directly couples to the magnetic moments.[68] To summarize, the spin cycloid in $BiFeO_3$ can hence be described by a mathematical term similar to the Dzyaloshinskii-Moriya interaction, but the ferroelectric polarization and the inverse spin-current effect are needed to explain its origin.

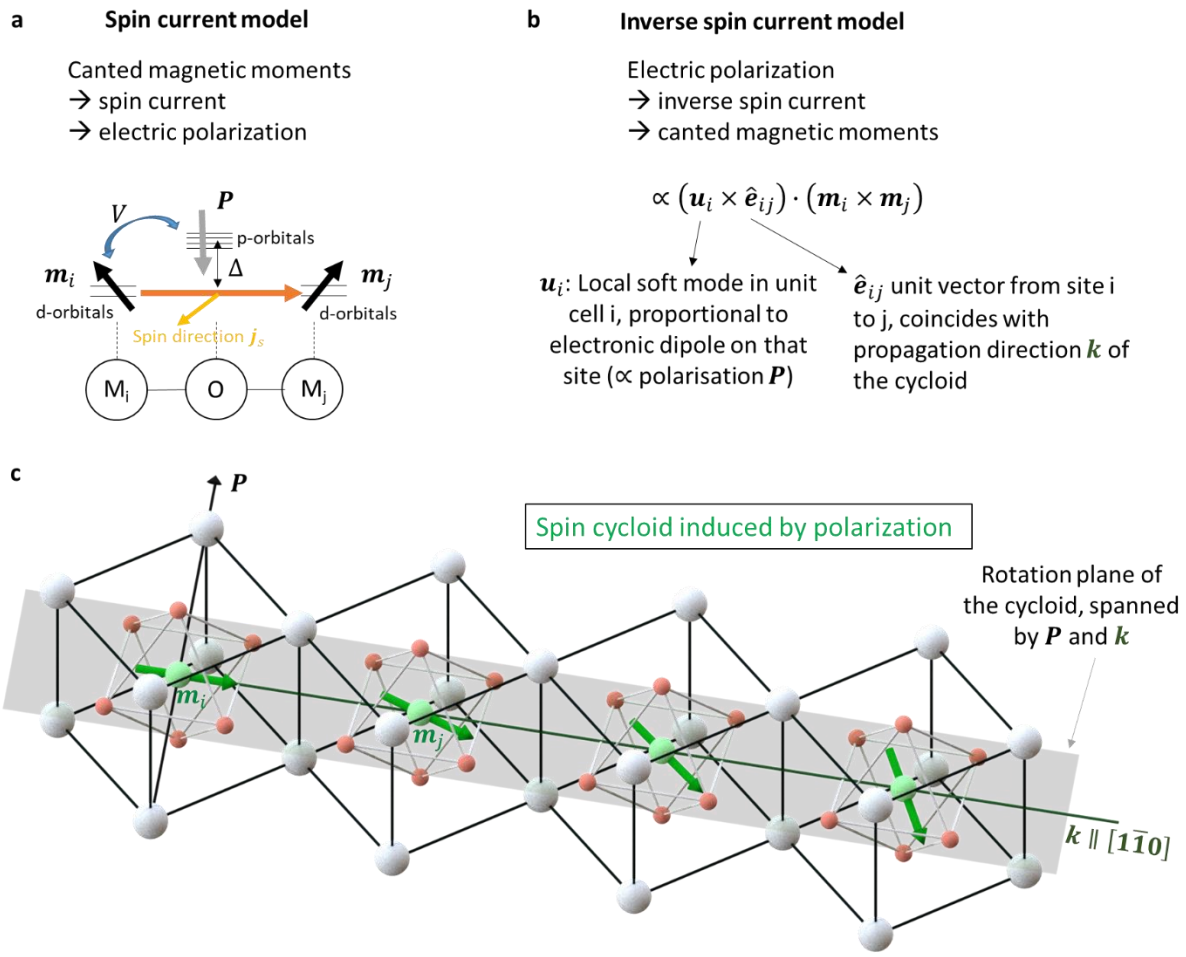

Figure 11 : ***a*** *Spin current model in multiferroic models. Figure adapted from reference [66].* ***b*** *Inverse spin current model that can be used to explain the spin cycloid in BiFeO3.[67]* ***c*** *Visualization of this spin cycloid in the $BiFeO_3$ lattice.*

It takes until 2011 that Ramazanoglu *et al.* observe the second modulation in the spin cycloid where a slight canting out of the cycloidal rotation plane is observed in a neutron scattering study (Figure 10**c**).[62] This so-called spin density wave may be interpreted with a second Dzyaloshinskii-Moriya interaction. In a $BiFeO_3$ crystal where the cycloid is supressed by doping for example, the same mechanism results in a canted antiferromagnetic structure with a weak ferromagnetic moment. This is described by Ederer & Spaldin, investigating weak ferromagnetism due to a Dzyaloshinskii-Moriya like interaction because of symmetry reductions in the crystal structure (Figure 10**d**).[63]

In a microscopic model, this second Dzyaloshinskii-Moriya like interaction term is at the origin of the spin canting between neighbouring Fe spins along the [111] direction (note here, that these are third nearest neighbours) and can be derived from the antiphase tilting of the FeO_6 octahedra. Using first principle calculations, Albrecht *et al.* explain how a weak canted ferromagnetic moment arises when the initial alignment of the magnetic moments in the cycloid is perpendicular to the polarization $\boldsymbol{P}$.[69] Here the intrinsic polarization is not at the origin of the mechanism, this rather originates from the tilting of the octahedra by an angle of ω around the same axis, namely the [111] direction (Figure 12**a**). When the magnetic moments $\boldsymbol{M}_{Fe_1}$ and

$\boldsymbol{M}_{Fe_2}$ are parallel to the [111] axis, no canting is possible. As a result of the canting, a spin density wave (Figure 12**b**) with the same incommensurate long period as the cycloid propagates along the same propagation direction $\boldsymbol{k} \parallel \{1\bar{1}0\}$ through the crystal. The difference is in the strength of this canting which is weaker than the cycloidal motion itself, namely $0.027\mu_B$ / Fe in the direction generated by the cross product of the magnetic moment vectors and the octahedral tilting axis. The plane of the spin density wave, defined by one of the $\{11\bar{2}\}$ directions for each $\boldsymbol{k}$ and the $\boldsymbol{k}$ itself, is perpendicular to the cycloid rotation plane (Figure 12**b**).

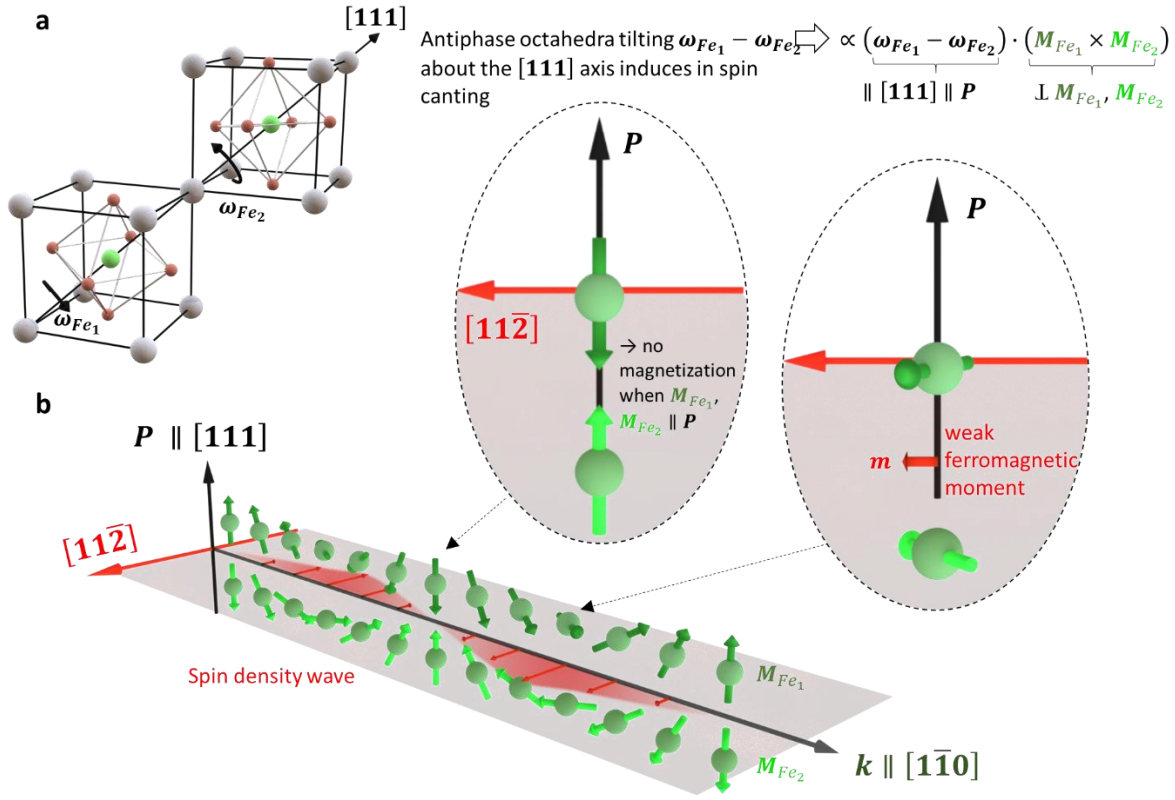

*Figure 12 : Visualisation of the octahedral tilting (**a**) as microscopic origin for the spin density wave (**b**).*[62,69]

Finally, the total energy of the system can be reduced to

$$E_{tot} = E_{FE-AFD} + E_{Mag}$$

The first term concerns the ferroelectric energy (details hereon can be found in Kornev *et* al.[70]). All the previously cited theory papers, mainly from the group of Bellaiche *et al.*, successively expand the second term, i.e. the magnetic energy. This energy depends on the magnetisation vector $\boldsymbol{m}_i$ at each Fe site, which is assumed to be $4\,\mu_B$ from first principle calculations.[53] But local soft modes, proportional to the electronic dipole at each Fe site and hence the polarization there, are taken into account as well as the strain tensor and the octahedral tilts. Lisenkov *et al.* perform their initial calculations only at the basis of the first five summands in Figure 13.[71] Classical dipolar interactions as well as the superexchange interaction are modified by three terms treating the couplings of the soft modes, octahedral tilts and strain with m. Then to explain the spin density wave and the spin cycloid, the 6th and 7th term are introduced, respectively.[67,69] However, more than one type of cycloid may exist: another propagation direction, namely along the $[11\bar{2}]$ direction, is indeed observed by Ratcliff *et al.*[72] using neutron diffraction

in a 1 µm thick $BiFeO_3$ film. Bhattcharjee *et al.* distinguish between pure G-type AFM state and type 1 and 2 cycloid depending on the value of the parameter C in the last term.[73] Xu *et al.* even expand this to five possible types of cycloids by introducing a sum over the first and second nearest neighbours for the inverse spin current model. Hence there appear two coefficients C_1 and C_2. The solutions of the first and second nearest neighbour terms coexist with different magnitude or even sign and therefrom for each cycloid type, three propagation directions can be calculated. These authors report for example that the experimental accessibility of a type 2 cycloid may involve effects beyond epitaxial strain with surface effects as possible suggested hints.[74]

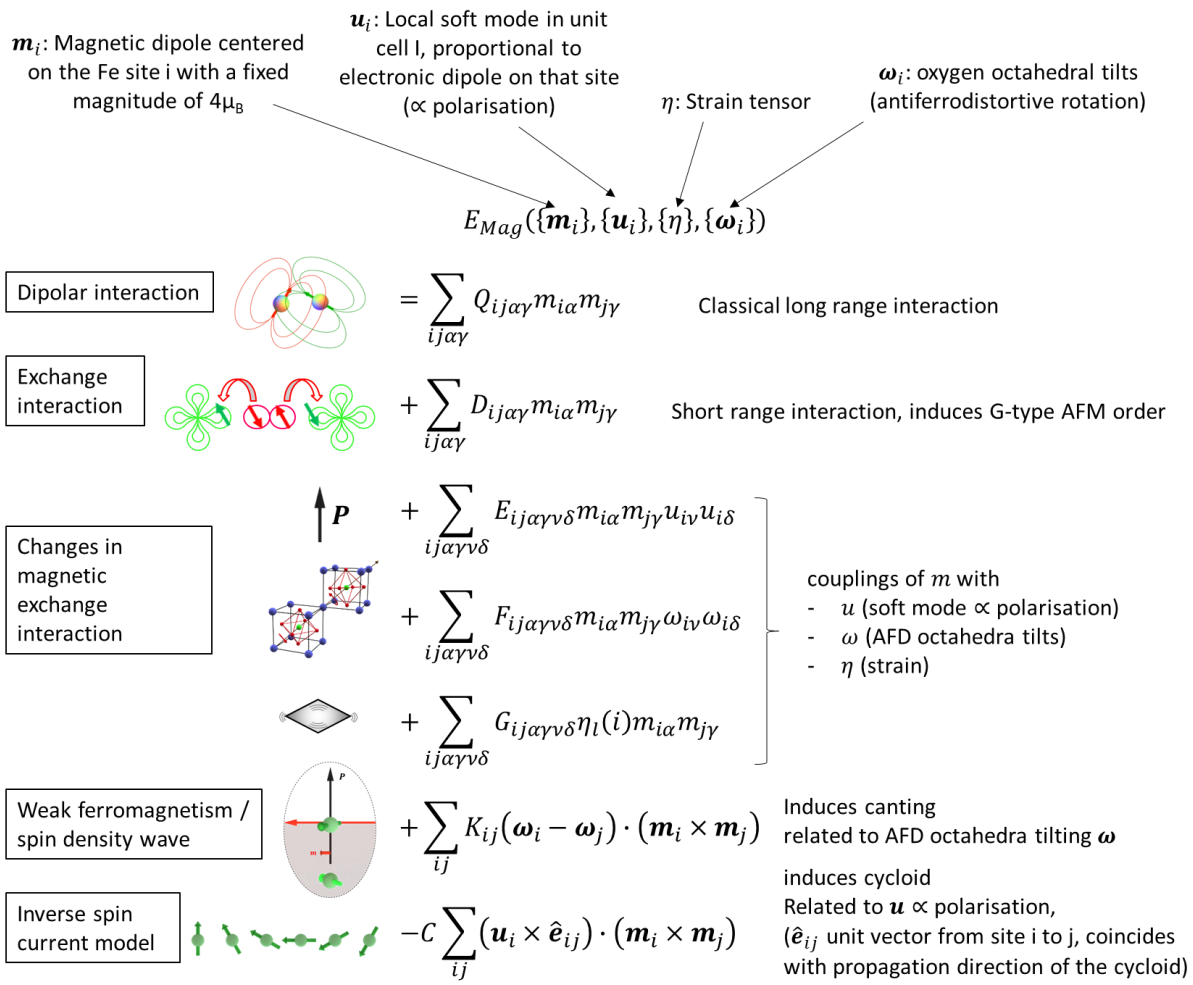

Figure 13 : State-of-the-art theoretical expression for the magnetic energy terms in $BiFeO_3$. Equation from reference [74].

Beyond this analysis of the experimental and theoretical background of the cycloid, other important issues like the single ion anisotropy and anharmonicity of the spin cycloid are neglected as they are not in the focus of this thesis. A comprehensive summary on them can be found in Park *et al.*[75]

1.2.2 Tunability of the ferroelectric and antiferromagnetic order in thin films

Beyond single crystals, $BiFeO_3$ thin films offer a pathway to access and influence the ferroelectric and antiferromagnetic properties using epitaxial strain, different substrate orientations or

electric field. In addition, high quality thin films with a flat surface can be produced in larger lateral sizes than single crystal samples up to strain levels where the latter would fracture. Due to this capability to tailor the multiferroic properties in thin films, $BiFeO_3$ appears as a fantastic platform for spintronic applications as well as for fundamental research on the interplay between structure, ferroelectricity and non-collinear antiferromagnetic properties.

Ferroelectric domain formation and thin film growth

Each one of the eight possible ferroelectric variants may harbour three different magnetic domains. An ordered ferroelectric domain pattern, harbouring 4, 2, or even 1 of these variants can be obtained by combining several strategies in the growth optimization process. This greatly simplifies all further analysis of the samples. The symmetry of the substrate, and an additional bottom electrode, can favour some of the ferroelectric polarization variants. In the case of two ferroelectric polarization variants, typically three different arrangements of stripe patterns can be formed, as shown in Figure 14. The polarization direction (red arrows) in the neighbouring domains is rotating either by 71° (**a, d**), 109° (**b, e**) or 180° (**c, f**).[76] Three different types of domain walls (blue) are formed (**d-f**) and produce different stripe domain patterns in the thin films (**a-c**). In contrast to atomic steps on the flat surface for the 71° and 180° domain walls (**a, c**), the 109° domain walls imprint as a "puckering" of the surface (**b**).[77,78]

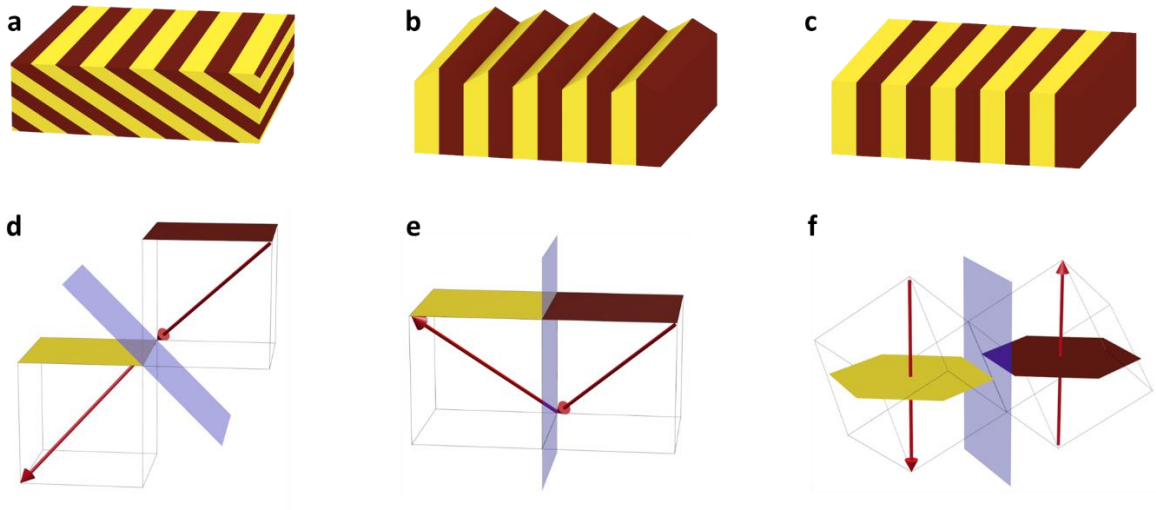

*Figure 14: Three different types of striped domains in $BiFeO_3$ thin films with **a** 71°, **b** 109°, and **c** 180° domain walls. We note that the surface of the 109° domain wall-sample (**b**) is different. Polarization direction (red arrows) in neighbouring domains and the domain wall between them (blue) are shown for 71°, 109° and 180° polarization rotation in **d**, **e** and **f**, respectively.*

However, ferroelectric domains may form more irregular patterns (maze, mosaic) and the optimization of the growth parameters is necessary to obtain higher order. The influence of the growth deposition parameters of $BiFeO_3$ thin films has been thoroughly investigated in the literature and I will give a short insight on the variety of possibilities by citing some examples. Thin films are grown in various growth chambers using different types of lasers. First studies to eliminate parasitic phases of Bi_2O_3 and Fe_2O_3 defined the growth windows for pressure and temperature around $P = 1 \cdot 10^{-2}$ mbar and $T = 580$ °C, using a frequency-tripled Nd:YAG laser.[79] Those films tend to deliver highly mosaic ferroelectric patterns.[80] Jang *et al.* reported the growth of ferroelectric stripes when using $SrTiO_3$ substrates with a high miscut angle of -0.15°.

All the ferroelectric patterns relax towards a more mosaic structure within two days after growth.[81] However, we can trace back in the literature that using an excimer laser seems to be more suited for the formation of highly-ordered ferroelectric stripes.[82] The deposition temperature (700°C) and pressure ($1.3 \cdot 10^{-3}$ mbar) are differing from those initially found for the Nd:YAG laser growth chamber.

The order of the ferroelectric domains tends to go hand in hand with the surface roughness and hence the growth mechanism. For example, decreasing the laser repetition rate may change the growth mode of the bottom electrode from step bunching to step flow, leading to a reduction from four to two ferroelectric variants with associated atomic steps on the surface.[82] Another way to favour striped domains is presented in a study on the influence of the target composition in combination with the laser repetition rate. It showed that this is a way to play with the bismuth and the oxygen content in the films which dramatically affects the interface between $BiFeO_3$ and $SrRuO_3$, creating a diffuse mixed interface and favouring striped domains and atomic steps on the surface.[83] Samples with 71° domain walls are most common in the literature. 109° domain walls are scarcer with pure $BiFeO_3$ targets. La-substituted (La,Bi)FeO_3 targets seem to promote 109° domain walls when grown without a bottom electrode.[78] This configuration influences the electric boundary conditions: while a bottom electrode may promote efficient screening for downward polarization, an insulating substrate favours domains with alternated polarization to reduce the depolarization field. Striped 180° domain walls with a "smooth" surface are grown by Chen *et al.*,[84] but because of the substrate orientation the polarization directions and hence the domain walls are not perpendicular to the surface in contrast to the illustration in Figure 14**c, f**.

Spin cycloid in $BiFeO_3$ thin films under the influence of epitaxial strain

As it is intimately connected to their functional properties, the crystallographic structure of $BiFeO_3$ thin films has been extensively investigated. A rhombohedral bulk-like $BiFeO_3$ crystallographic structure can be grown along the $[111]_{pc}$ direction, on cubic $SrTiO_3$ $(111)_c$ for example[85–89]. The same relaxed crystallographic structure is obtained on cubic $(LaAlO_3)_{0.3}(SrAlTaO_6)_{0.7}$ $(001)_c$[90] or $SrTiO_3$ $(001)_c$[91] substrates by increasing the film thickness until film relaxation takes place. At low compressive strain $BiFeO_3$ adopts a monoclinic M_A phase in ~200 nm thin films on $SrTiO_3$ $(001)_c$.[92–94] For tensile strain, the monoclinic M_B structure is found on $SrTiO_3$ $(110)_c$ or on orthorhombic $PrScO_3(110)_o$.[95,96] For high compressive strain, a polymorph of $BiFeO_3$ stabilizes with monoclinic M_C, or tetragonal symmetries. However those are not in the focus of this work and the reader is referred to the literature in references [[97]] and [[98]] for more information.

At first it was suspected by theory and experiments that the magnetic cycloid is generally supressed in $BiFeO_3$ thin films due to epitaxial strain.[87,99,100] Using neutron scattering, Ke *et al.* first observed a unique spin cycloid in single domain relaxed thin films (800 nm) of $BiFeO_3$ grown by rf sputtering on a $SrTiO_3$ $(001)_c$ substrate with 4°-miscut along $[110]_c$ (Figure 15**a**).[101] Following this first report, Sando *et al.* investigated the influence of epitaxial strain (-2.6% to +1.3%) on the magnetic order in a series of thinner (50-70 nm) $BiFeO_3$ $(001)_{pc}$ thin films using low-energy Raman and Mössbauer spectroscopy.[102] Figure 15**b** displays the dependence of the

antiferromagnetic order with epitaxial strain. The authors find two types of cycloids: one at low compressive strain (type I) and the other at low tensile strain (type II), distinguishable by their propagation direction **k** relative to the polarization direction **P** and the rotation plane of the cycloid (grey shaded area) spanned by those vectors. At higher compressive and tensile strain, the cycloidal modulation is suppressed leading to a pure G-type antiferromagnetic order, likely because of an additional anisotropy term of elastic origin as destabilizing factor for the spin cycloid.[87] The G-type order is described by the antiferromagnetic staggered vector which is lying in the film surface plane on the compressive side and almost perpendicular to it on the tensile side.

Another route to stabilize single ferroelectric domain thin films of $BiFeO_3$, and hence facilitate the investigation of its antiferromagnetic order, is to use $(110)_c$ $SrTiO_3$ substrates.[103,104] On such $(110)_c$ $SrTiO_3$ substrates, $BiFeO_3$ crystallizes in a M_B monoclinic structure with $(100)_m$ orientation, corresponding an average tensile strain in the $(001)_m$ plane.[105] However, the strain is anisotropic between the out-of-plane a_m and in-plane b_m axis, with a distortion of 0.5-1.5% .[105] The magnetic structure of these specific $BiFeO_3$ thin films on $(110)_c$ $SrTiO_3$ were investigated in several neutron diffraction studies, revealing a type II cycloid with $[11\bar{2}]_{pc}$ propagation direction (Figure 15**c**) for thicknesses ranging from 25 to 200 nm.[72,103,105,106] Combining previous studies[72,103,107] of $BiFeO_3$ films on $SrTiO_3$ $(110)_c$ and $(LaAlO_3)_{0.3}(SrAlTaO_6)_{0.7}$ $(110)_c$, Sando *et al.* present a new magnetic phase diagram as a function of tensile strain and distortion (Figure 15**d**).[105] To summarize, combining tensile strain and large distortion favours a transition from the type II cycloid to a pure G-type antiferromagnetic order. Recent theoretical works suggest that the magnetic phase diagram contains even more exotic types of cycloids, distinguishable by their propagation directions (Figure 15**e**).[74]

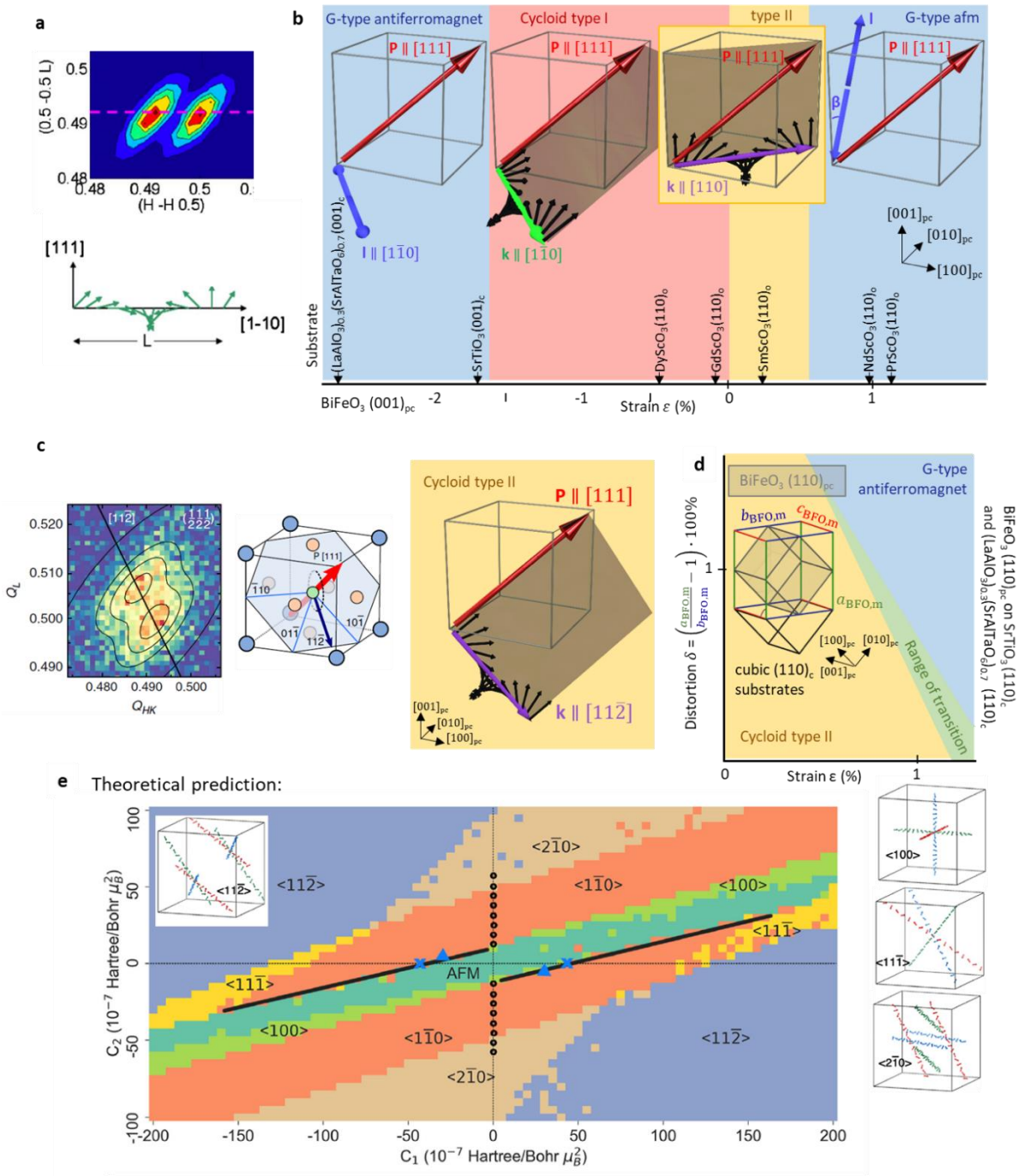

Figure 15 : Experimental and theoretical results on the magnetic structure in $BiFeO_3$ thin films. ***a*** *Neutron scattering data in an 800 nm thick film grown on a $SrTiO_3$ $(001)_c$ substrate, revealing an antiferromagnetic G-type order, modulated by the spin cycloid. Figure adapted from reference [101].* ***b*** *Strain tuning of the antiferromagnetic state in $BiFeO_3$ $(001)_{pc}$ samples grown on the indicated substrates. Pure G-type antiferromagnetic order, observed in the blue zones with staggered antiferromagnetic vector* ***l*** *along $[1\bar{1}0]_{pc}$ at higher compressive strain and deviating at an angle β from the $[001]_{pc}$ direction on the tensile side. Type 1 cycloid with propagation direction* ***k*** *along the $[1\bar{1}0]_{pc}$ direction in the red zone and type 2 cycloid with* ***k*** *along the $[110]_{pc}$ in the yellow zone, rotation plane of the cycloid in the grey areas. Figure adapted from reference [102].* ***c*** *Neutron diffraction reciprocal space map of the 100 nm $BiFeO_3$ $(110)_{pc}$ film grown on $SrTiO_3$ $(110)_c$ reveals the type 2 cycloid propagation direction along $[11\bar{2}]_{pc}$. Figure adapted from reference [106].* ***d*** *Magnetic phase diagram for $BiFeO_3$ $(110)_{pc}$ films from experimental results on $(110)_c$ substrates. By a variation of the distortion, indicating the ratio between the monoclinic in-plane lattice parameter b_m and the out-of-plane lattice parameter a_m, pure G-type antiferromagnetic order is accessible. Figure adapted from reference [105].* ***e*** *Theoretical calculations predict an even more complicated cycloidal phase diagram containing five types of cycloids. Figure adapted from reference [74].*

1.2.3 State of the art of magnetoelectric devices

In the 2000s, multiferroics attracted a lot of interest in the spintronic community due to the possible control of magnetization by a potentially low-energy electric field through the magnetoelectric coupling between ferroelectric and ferromagnetic ferroic orders. As $BiFeO_3$ is a room-temperature ferroelectric antiferromagnet, concepts of magnetoelectric memory consisted in combining these films with metallic ferromagnets, using the interfacial exchange bias between the antiferromagnet and the ferromagnet.[108] In this context, Heron *et al.* demonstrated in 2014 the non-volatile electric control of magnetization of a $Co_{0.9}Fe_{0.1}$ ferromagnetic layer deposited on top of a 100 nm thick $BiFeO_3$ film grown on $DyScO_3$ $(110)_o$ substrates. Using time-dependent piezoresponse force microscopy, they showed that the 180° reversal of polarization in a two-step switching process (71° and 109° switching) leads to the reversal of the canted magnetic moment (Figure 16**a**).[76] The magnetization reversal of the adjacent $Co_{0.9}Fe_{0.1}$ layer is confirmed from x-ray magnetic circular dichroism - photoelectron emission microscopy, and detected electrically with giant magnetoresistance in a spin-valve spintronic element. In the explanation of their measurements, however, the authors assume a canted G-type antiferromagnetic order in $BiFeO_3$, in contradiction with the results presented in the previous paragraph, where a cycloidal modulation is observed for the same type of sample.[102]

In the last few years, key experimental developments enabled the investigation of the local antiferromagnetic textures in $BiFeO_3$ and their coupling to the ferroelectric polarization. Using scanning NV magnetometry, Gross *et al.* showed the undisputable existence of a spin cycloid in $BiFeO_3$ thin films on $DyScO_3$ substrates.[109] In addition, the authors demonstrated that the propagation direction of the spin cycloid is intimately linked to the ferroelectric polarization via the magnetoelectric coupling (Figure 16**b**). Using second harmonic generation, Chauleau *et al.* were able to reconstruct the distribution of submicron antiferromagnetic domains in single ferroelectric domains (Figure 16**c**) designed in pure G-type antiferromagnetic thin films of $BiFeO_3$ on $SrTiO_3$.[110] In addition, they showed indications that electric fields, temperature, and sub-picosecond light pulses enable to manipulate these antiferromagnetic domains.

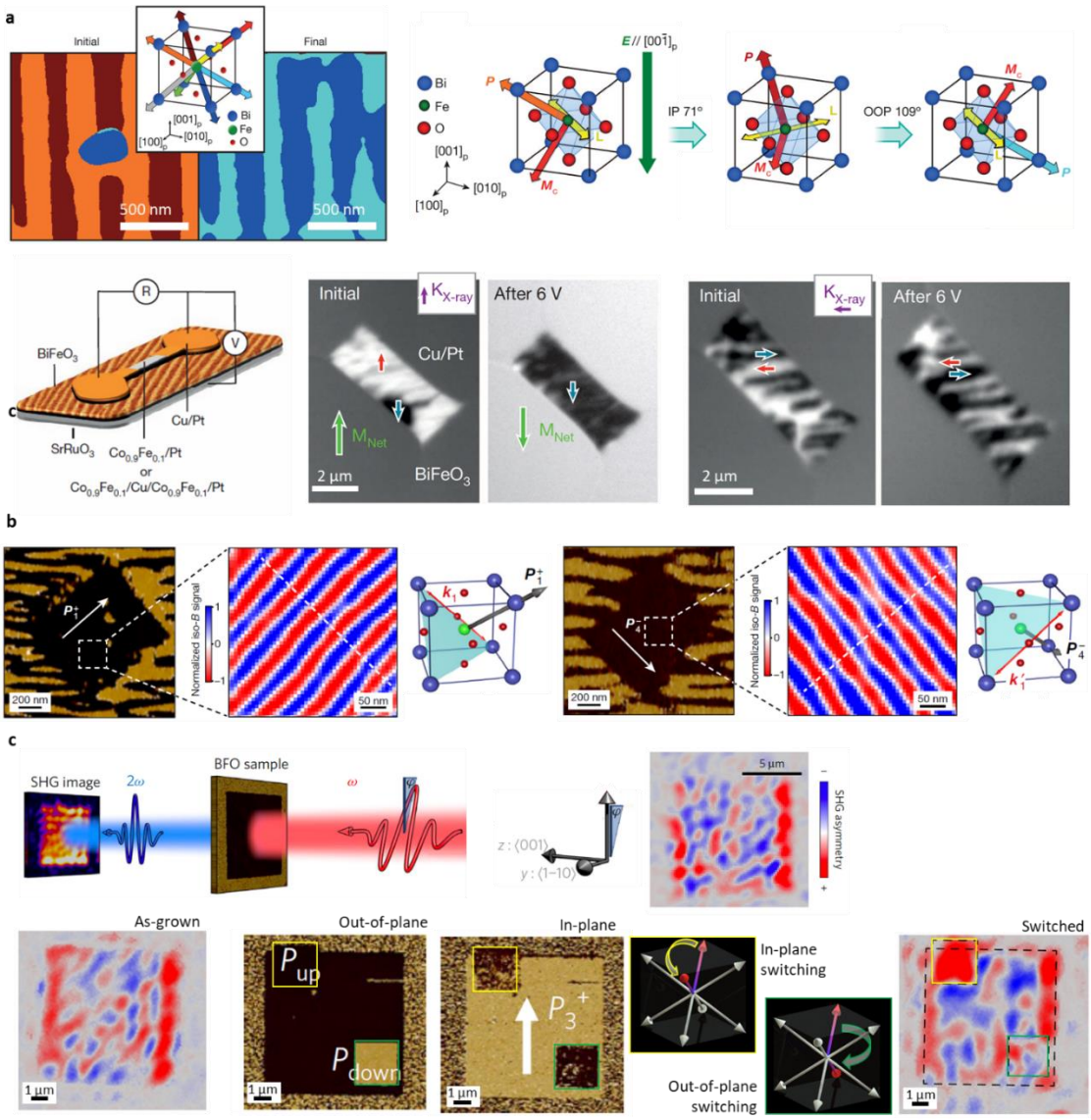

Figure 16 : Electric field control of magnetism in multiferroic $BiFeO_3$ thin films. ***a*** *Polarization vector images determined from PFM measurements before (initial) and after applying an out-of-plane field (final) to a 100 nm thick $(001)_{pc}$ $BiFeO_3$ film grown on $SrRuO_3/DyScO_3$ $(110)_o$. On the right, schematic of the two-step 180° switching of polarization (**P**) with a 71° and a subsequent 109° switching. The antiferromagnetic vector (**L**) and canted moment (**M_C**) are also represented. Consequently, the two-step switching is accompanied by a 180° rotation of the canted moment of $BiFeO_3$. Second line, spin valve structure used for electric poling measurement with x-ray magnetic circular dichroism - photoelectron emission microscopy images of the in-plane moment of a $Co_{0.9}Fe_{0.1}$ layer deposited on $BiFeO_3$ with components viewed perpendicular (vertical $K_{X\text{-}ray}$, where $K_{X\text{-}ray}$ defines the in-plane component of the incident X-ray beam) and parallel to the stripe domains (horizontal $K_{X\text{-}ray}$). The directions of the magnetizations in each domain are highlighted with blue and red arrows, which correspond to the local moment direction being perpendicular or parallel to $K_{X\text{-}ray}$. The net $Co_{0.9}Fe_{0.1}$ magnetization (green arrows) reverses after the voltage is applied. Figure adapted from reference [76].* ***b*** *Electrical control of the spin cycloid in a 32 nm thin $BiFeO_3$ $(001)_{pc}$ film grown on $SrRuO_3$ /$DyScO_3$ $(110)_o$. In-plane piezoresponse force microscopy images of micron-sized ferroelectric domains with $\mathbf{P}_1^+$ and $\mathbf{P}_4^-$ polarizations, respectively. The white arrows indicate the in-plane projection of the ferroelectric polarization vector. Corresponding magnetic field distributions recorded from the respective boxed areas with the scanning-NV magnetometer, operating in dual-iso-B imaging mode. Schematic sketch for the corresponding direction of the polarization **P** and the propagation vector **k** of the spin cycloid. Figure adapted from reference [109].* ***c*** *Principle of the experiment of second harmonic generation on a 110 nm thick $BiFeO_3$ $(001)_{pc}$ film grown on $SrRuO_3$ /$SrTiO_3$ $(001)_c$. Reconstructed image of the antiferromagnetic textures in a single ferroelectric domain, where the colour scale represents the asymmetry of the second harmonic generation polar plots. Figure adapted from reference [110].*

In summary, it is possible to access a large variety of antiferromagnetic textures in $BiFeO_3$, i.e. different cycloidal states or pure G-type order, via strain engineered thin films. Using neutron diffraction,[72,106,111] Raman and Mössbauer spectroscopy,[102,103,105] and X-ray scattering techniques[106], the spin structure is studied and magnetic phase diagrams, indicating the magnetic texture depending on the epitaxial strain, are more and more accurately defined.[102,105,111] Furthermore, several works demonstrated that electrical switching of the magnetic order is possible.[76,109,110] However, local information on the antiferromagnetic textures of $BiFeO_3$ thin films and their coupling to ferroelectricity are very limited due to the scarcity of the imaging techniques. Recently, Gross *et al.*[109] showed images of spin cycloidal domains in "low strained" $BiFeO_3$ thin films, and Chauleau *et al.*[110] visualized G-type antiferromagnetic domains in "highly-strained" $BiFeO_3$. A more systematic investigation of the magnetic textures in $BiFeO_3$, providing unambiguous images in real space, was one of the motivations when this thesis started in 2017.

2. Experimental techniques / Methods

This chapter describes the main experimental techniques I utilized for the elaboration of $BiFeO_3$ thin films and their structural and ferroelectric characterizations. After a brief introduction of the possible crystal structures of $BiFeO_3$ in relation with scandate substrates in different crystalline orientations, I will describe the experimental growth technique and the X-ray diffraction setup and methods used for the structural characterization of the films. Next, I will present the scanning probe microscopy techniques I used to investigate the topography and ferroelectric properties of the films, as well as scanning NV magnetometry that is employed to image the corresponding magnetic textures. In the last section, X-ray resonant magnetic scattering is presented as a complementary method to study the spin cycloid in reciprocal space.

2.1 Crystal structures

As already discussed in the previous chapter, the strong ferroelectric polarization of $BiFeO_3$ is directly related to an elastic deformation of its crystallographic lattice. In $BiFeO_3$ thin films, the polarization can therefore be tuned via elastic strain imposed by the lattice mismatch with the substrate. Here, the basic crystallographic aspects of films and substrates will be discussed. After describing the relevant $BiFeO_3$ unit cells for the structural X-ray diffraction analysis, I will introduce the substrates used for thin film growth. A theoretical calculation of the strain induced in such a fully strained $BiFeO_3$ thin film is also presented in the first section.

2.1.1 Crystal structure of $BiFeO_3$ thin films

In bulk $BiFeO_3$, the polar deformation results in a rhombohedral distortion along one of the <111> pseudo-cubic directions (turquoise lines, Figure 17**a**). The four possible elastic deformations, projected along the (001) plane, are shown in Figure 17**b.**

When growing $(001)_{pc}$-oriented thin films under coherent biaxial strain, the in-plane axes are clamped to the substrate surface. This reduces the rhombohedral symmetry to a monoclinic one (blue lines, Figure 17**a**), also known as "R-like" phase (blue lines)[91]. The monoclinic unit cell is rotated by 45° around the z-axis of the pseudo-cubic one (black lines). While the antisymmetric oxygen octahedra rotations of $BiFeO_3$ require a doubling of the monoclinic cell along the c axis, we will use a reduced out-of-plane lattice parameter $c_m = c_{pc}$ as commonly reported by experimentalists. The resulting monoclinic phase can be either monoclinic M_A or M_B for low compressive or tensile strain, respectively[92,96,97].

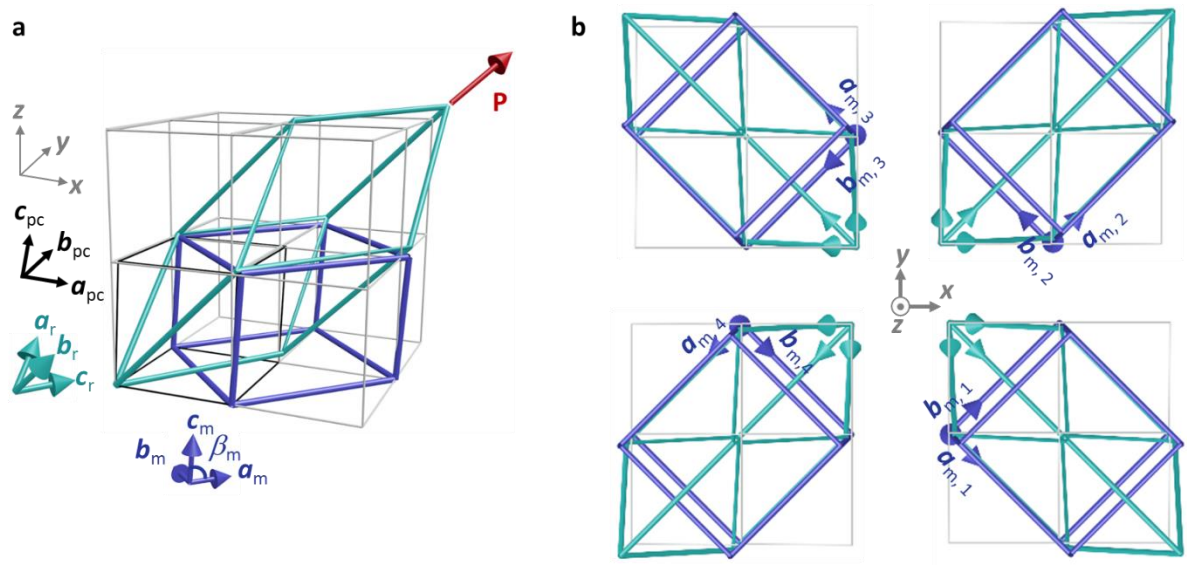

Figure 17 : ***a*** *Rhombohedral polar-distorted (turquoise), monoclinic (blue) and pseudo-cubic (black) unit cells. The corresponding polarization is indicated by the red arrow.* ***b*** *Top view of the four ferroelastic variants represented in the rhombohedral and monoclinic unit cells.*

In Table 1, the lattice parameters for different $BiFeO_3$ unit cells are listed from the literature. The rhombohedral and the pseudo-cubic ones are taken from an X-ray diffraction study on bulk $BiFeO_3$ by Kubel *et al.*[112], the monoclinic unit cell is reported by Xu *et al.*[92] on $BiFeO_3$ thin films grown on $SrTiO_3$ $(001)_c$.

Table 1 : Lattice parameters for $BiFeO_3$ from the indicated literature.

rhombohedral, bulk[112]		**pseudo-cubic**[112]		**hexagonal**[112]			
$a_r = b_r = c_r$ (nm)	α_r (°)	$a_{pc} = b_{pc} = c_{pc}$ (nm)	α_r (°)	$a_h = b_h$ (nm)	c_h (nm)	$\alpha_h = \beta_h$ (°)	γ_h (°)
0.56343	59.348	0.3965(1)	89.45	0.558	1.38	90	120

Monoclinic M_A $BiFeO_3$ thin film on $SrTiO_3$[92]					
a_m (nm)	b_m (nm)	c_m (nm)	α_m (°)	β_m (°)	γ_m (°)
0.5525	0.5619	0.3997	90	89.2	90

For the growth of $(111)_{pc}$-oriented films of $BiFeO_3$, the rhombohedral symmetry is preserved and can be described with a hexagonal unit cell. It contains six $BiFeO_3$ perovskite cells, explaining the larger hexagonal lattice parameters in Table 1 (pink). Figure 18 shows the relation between this hexagonal cell (pink) and the rhombohedral cell (turquoise) and two pseudo-cubic unit cells (black). The hexagonal c_h axis points upwards, fulfilling the relation $[001]_h = 2[111]_{pc} = [111]_r$ (Figure 18**a**) while in the hexagonal plane $[110]_h = [1\bar{1}0]_{pc} = [\bar{1}10]_r$ (Figure 18**b**).[75]

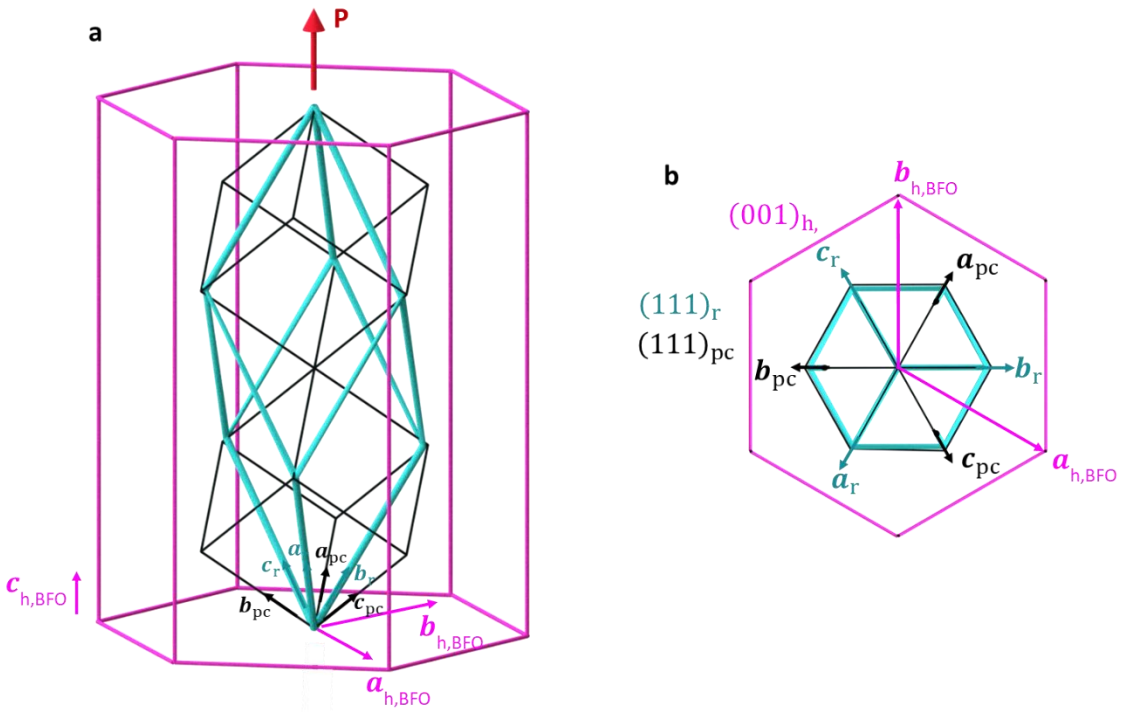

*Figure 18 : Hexagonal (pink), rhombohedral (turquoise) and pseudo-cubic (black) unit cell of $BiFeO_3$ in **a** the side 3D-view and **b** the top view on the (001) hexagonal plane.*

2.1.2 Crystal structure of the substrates for $(001)_m$ monoclinic $BiFeO_3$ thin films

To obtain $(001)_m$ monoclinic thin films of $BiFeO_3$ at different strain levels, we either use $(110)_o$-oriented orthorhombic $XScO_3$ (X = Dy, Tb, Gd, Sm and Nd), or $(001)_c$-oriented cubic $SrTiO_3$ substrates. The growth of the monoclinic (blue) and pseudo-cubic (grey) $BiFeO_3$ unit cells on the lattice of the substrates (monoclinic and cubic in red, orthorhombic in black) are shown in Figure 19. This representation demonstrates, that the monoclinic lattice, in case of the orthorhombic $XScO_3$ substrates, (Figure 19**b**) can be treated similarly to the pseudo cubic $SrTiO_3$ lattice (Figure 19**c**).

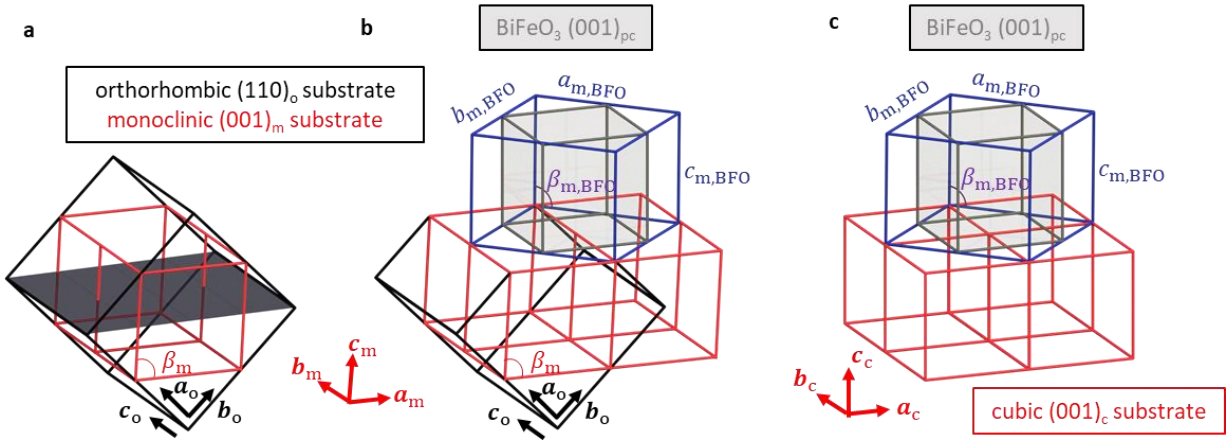

*Figure 19 : **a** Relation between the orthorhombic $(110)_o$ unit cell (black lines) and the monoclinic $(001)_m$ one (red lines). **b** Growth of the $BiFeO_3$ film on this substrate. The monoclinic $BiFeO_3$ $(001)_m$ unit cell is shown in blue, the pseudo-cubic $BiFeO_3$ unit cell in grey. **c** Very similar scenario for $BiFeO_3$ growth on cubic $(001)_c$ substrates (red).*

From Figure 19**a** the relation between the orthorhombic (black) and the monoclinic (red) unit cell can be derived.[113] The values of the monoclinic cell calculated using the following equations

$$a_{\mathrm{m}} = c_{\mathrm{m}} = 0.5 \cdot \sqrt{a_{\mathrm{o}}^2 + b_{\mathrm{o}}^2},$$

$$b_{\mathrm{m}} = 0.5 \cdot c_{\mathrm{o}}$$

and

$$\beta_{\mathrm{m}} = 2 \cdot \tan\left(\frac{a_{\mathrm{o}}}{b_{\mathrm{o}}}\right),$$

are listed in red in Table 2.

In reciprocal space, the relations $[hk0]_o^* \parallel [00l]_m^*$ and $[00l]_o^* \parallel [0k0]_m^*$ are valid.

Table 2: Symmetry and corresponding lattice parameters for the $SrTiO_3$, $DyScO_3$, $TbScO_3$, $GdScO_3$, $SmScO_3$ and $NdScO_3$ substrates. The scandates can be described in an orthorhombic or a monoclinic unit cell (Figure 19). Last column: calculated strain induced in a fully-strained epitaxial thin film of $BiFeO_3$ on each substrate.

Substrate	Symmetry and lattice parameters										strain $BiFeO_3$ (%)
	Cubic										
	$a_c = b_c = c_c$ (nm)			$\alpha=\beta=\gamma$ (°)							
$SrTiO_3$	**0.3905**			**90**							**-1.51**
	Orthorhombic				**Monoclinic**						
	a_o (nm)	b_o (nm)	c_o (nm)	$\alpha=\beta=\gamma$ (°)	a_m (nm)	b_m (nm)	c_m (nm)	α (°)	β (°)	γ (°)	
$DyScO_3$	**0.5440**	**0.5717**	**0.7903**	**90°**	**0.3946**	**0.3952**	**0.3946**	**90**	**87.16**	**90**	**-0.41**
$TbScO_3$	**0.5466**	**0.5731**	**0.7917**	**90°**	**0.3960**	**0.3959**	**0.3960**	**90**	**87.29**	**90**	**-0.15**
$GdScO_3$	**0.5480**	**0.5746**	**0.7932**	**90°**	**0.3970**	**0.3966**	**0.3970**	**90**	**87.29**	**90**	**0.08**
$SmScO_3$	**0.5527**	**0.5758**	**0.7965**	**90°**	**0.3991**	**0.3983**	**0.3991**	**90**	**87.65**	**90**	**0.54**
$NdScO_3$	**0.5575**	**0.5776**	**0.8003**	**90°**	**0.4014**	**0.4002**	**0.4014**	**90**	**87.97**	**90**	**1.08**

A value for the strain ε of a thin film, perfectly adapting the monoclinic in-plane lattice of the substrate, can be estimated by comparing its in-plane lattice parameters *a* and *b* to the volume *V* of the unit cell.

$$\varepsilon = \frac{\sqrt{a \cdot b} - \sqrt[3]{V}}{\sqrt[3]{V}}$$

In a fully strained $BiFeO_3$ thin film grown on such substrates, we assume a perfect match of the pseudo-cubic BFO in-plane parameters on the monoclinic substrate unit cell and set

$$a = b \approx \sqrt{a_{\mathrm{m,substrate}} \cdot b_{\mathrm{m,substrate}}}$$

(with the monoclinic values of each substrate in Table 2). For $SrTiO_3$, we simply consider the cubic $a_c = b_c$ substrate lattice parameters. $V = a_{pc,BFO}^3$ is the volume of the pseudo-cubic unit cell of $BiFeO_3$ with $a_{pc,BFO}$ = 0.3965 nm from Table 1. The results of the calculated strain values are listed in the last column of Table 2.

2.1.3 Crystal structure of the substrates for $(111)_{pc}$ pseudo-cubic $BiFeO_3$ thin films

The common approach for the growth of $BiFeO_3$ $(111)_{pc}$ thin films is to use $SrTiO_3$ $(111)_c$-oriented cubic substrates. While rarely mentioned in the literature, it is also possible to employ $(011)_o$ orthorhombic $XScO_3$ substrates (X = Dy, Tb). Figure 20**a** shows the $XScO_3$ $(011)_o$ substrate orientation (black). In the same way as we inserted the monoclinic cell in the previous section, we now construct an almost cubic cell (red) within the orthorhombic lattice (black). It becomes clear that its space diagonal is almost perpendicular to the orthorhombic $(011)_o$ plane. With this we can assume the $BiFeO_3$ $(111)_{pc}$ growth as a continuation of those slightly distorted $XScO_3$ cubes with the pseudo-cubic $BiFeO_3$ cubes (Figure 20**b**). The pseudo-cubic $BiFeO_3$ cell is shown in black, the rhombohedral one in turquoise and the hexagonal one in pink. As for the hexagonal cell $(001)_{h,BFO} \parallel (011)_{o,XSO}$, we will in the following describe $BiFeO_3$ and $XScO_3$ in the hexagonal and orthorhombic systems, respectively.

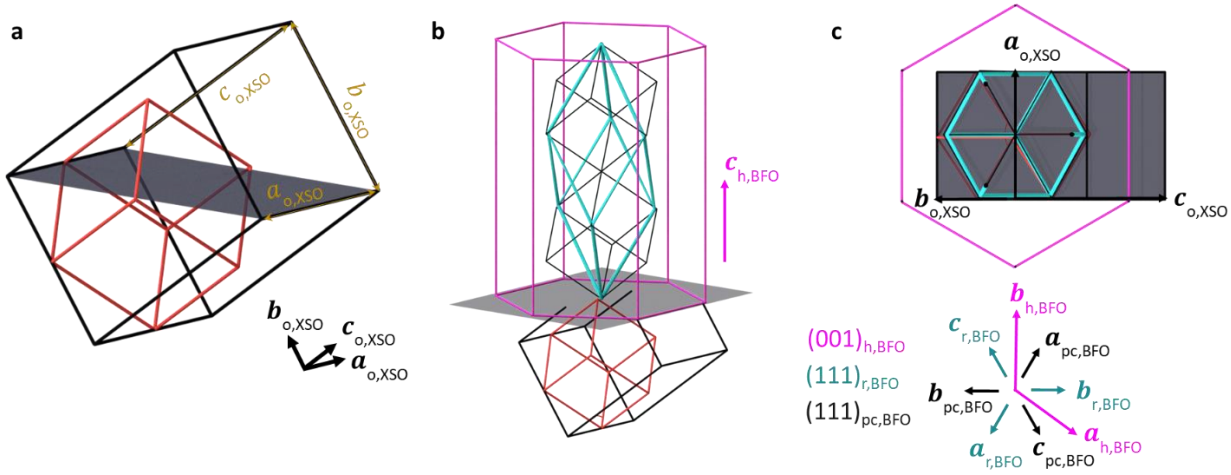

Figure 20 : ***a*** *$XScO_3$ (011) orthorhombic substrate (black lines) with the construction of a pseudo-cubic cell in red.* ***b*** *Sketch of a $BiFeO_3$ film growing along the pseudo-cubic (black) $(111)_{pc}$, rhombohedral (turquoise) $(111)_r$ direction and the hexagonal (pink) $(001)_h$ direction on top of it.* ***c*** *Top view on the $(011)_o$ orthorhombic plane.*

However, as illustrated in the top view (Figure 20**c**), the hexagonal $BiFeO_3$ unit cell does not match exactly with the $XScO_3$ cell. An anisotropic in-plane strain is imposed upon the film in the case of epitaxial growth. Therefore, for an accurate treatment of the X-ray diffraction data, we use a pseudo-hexagonal cell (Paragraph 2.3.2). Because of the anisotropic strain that is imposed on the $(111)_{pc}$ $BiFeO_3$ thin film, the comparison of the strain value with $(001)_{pc}$ films does not make much sense.

2.2 Pulsed laser deposition

All the $SrRuO_3$ and $BiFeO_3$ thin films presented in this thesis were grown on single crystalline $SrTiO_3$, $DyScO_3$, $TbScO_3$, $GdScO_3$, $SmScO_3$ and $NdScO_3$ substrates using a technique called pulsed laser deposition (PLD).

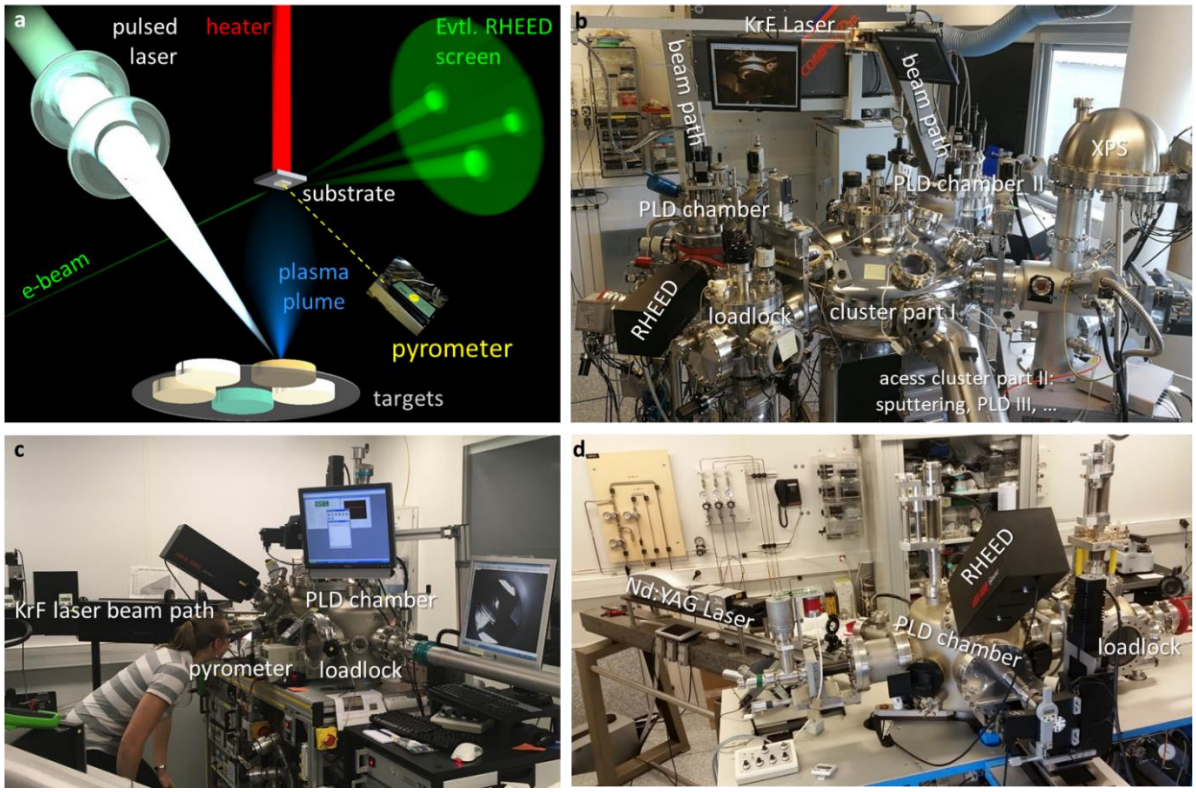

Figure 21 : ***a*** *Schematic representation of the PLD process.* ***b-d*** *Four different growth chambers in our lab.*

As shown in Figure 21**a**, pulses of a highly energetic UV excimer laser (KrF, 248 nm), or a frequency-tripled Nd:YAG laser (355 nm), are focussed on a polycrystalline target to generate a plasma plume[114]. The ionized material accumulates on the single crystal substrate that is heated from the backside. The actual substrate temperature is measured via a pyrometer from outside the chamber and the heating current can be adapted to reach the desired temperature between 550°C and 800°C. Since we grow oxide materials, the films are generally deposited in an oxygen atmosphere under pressures between 0.1 and 0.4 mbar. For the growth of $BiFeO_3$, we use a target with Bi excess ($Bi_{1.15}FeO_3$) because of the Bi-volatility. The growth can be monitored by reflection high-energy electron diffraction (RHEED) in our PLD systems, but most of the samples were prepared without using it. By varying the growth parameters, namely the growth temperature, pressure, energy per laser pulse, its repetition rate and the target-to-substrate distance, we aim at obtaining an epitaxial thin film of high crystalline quality for a desired thickness (Chapter 3.1.1). For the samples presented in this thesis, three different PLD chambers, shown in Figure 21**b-d**, have been used. As each chamber has its own geometry and slightly different operation system, adjustments in the growth parameters are required when moving from one chamber to the other. After the growth, selected samples were annealed ex situ under ambient pressure in an oven to investigate possible phase transitions in $BiFeO_3$ thin films (Chapter 3.3).

2.3 X-ray diffraction

We determine the structural properties of the films by X-ray diffraction (XRD), using a Panalytical Empyrean diffractometer with a hybrid monochromator for Cu $K_{\alpha 1}$ radiation and a PIXcel3D detector. The geometry of the experimental setup is shown in Figure 22**a**. The angle between the incident beam and the sample surface is denoted as ω. The diffracted beam encloses an angle of 2θ with the incident beam and θ with the scattering planes. To study different orientations of the lattice, the sample can be rotated by ϕ around its out-of-plane axis. To determine the growth direction, exclude the existence of parasitic phases and calculate the out-of-plane lattice parameter we perform symmetric 2θ-ω scans, also known as θ-2θ scans. Here, by simultaneously rotating the XRD source and the detector in opposite directions, we scan along the scattering vector (Figure 22**b**).

Furthermore, it is possible to obtain the out-of-plane gradual change of strain, by comparing the linewidth of the film peaks at different orders in the 2θ-ω scan. In a so-called Williamson-Hall plot[115], according to the equation[116]

$$\beta \cos(\theta) = \frac{K\lambda}{D} + 4\varepsilon_i \sin(\theta)$$

with $\beta = \beta_{\text{film}} - \beta_{\text{substrate}}$ (linewidth of the film and the nearby substrate peak, respectively), we plot $\beta \cos(\theta)$ versus $4 \sin(\theta)$. The x-ray wavelength λ, the the coherence length D along the scattering vector and a geometrical constant K add an offset on the y-axis, but are not needed to determine a numerical value for the inhomogeneous strain ε_i from the slope of a linear fit function. When all points are well aligned and the slope is close to zero, we can assume homogeneous out-of-plane strain in the sample.

An indicator for the crystalline sample quality is the linewidth of an ω-scan around the film peak. In this scan, also known as rocking curve, the angle between incident beam and detector is held constant. This corresponds to a scan following an arc centred on the origin of the scattering vector (Figure 22**c**). For samples with a large mosaic spread, the linewidth is large (> 0.1°), whereas a high crystalline quality is marked by a linewidth of a few hundredths of degree.

For the determination of the in-plane lattice parameters, asymmetric scans are necessary (Figure 22**c**). A reciprocal space map consists of ω-scans recorded at a certain range of 2θ angles, corresponding to a two-dimensional scanning area in reciprocal space (pink shaded area).

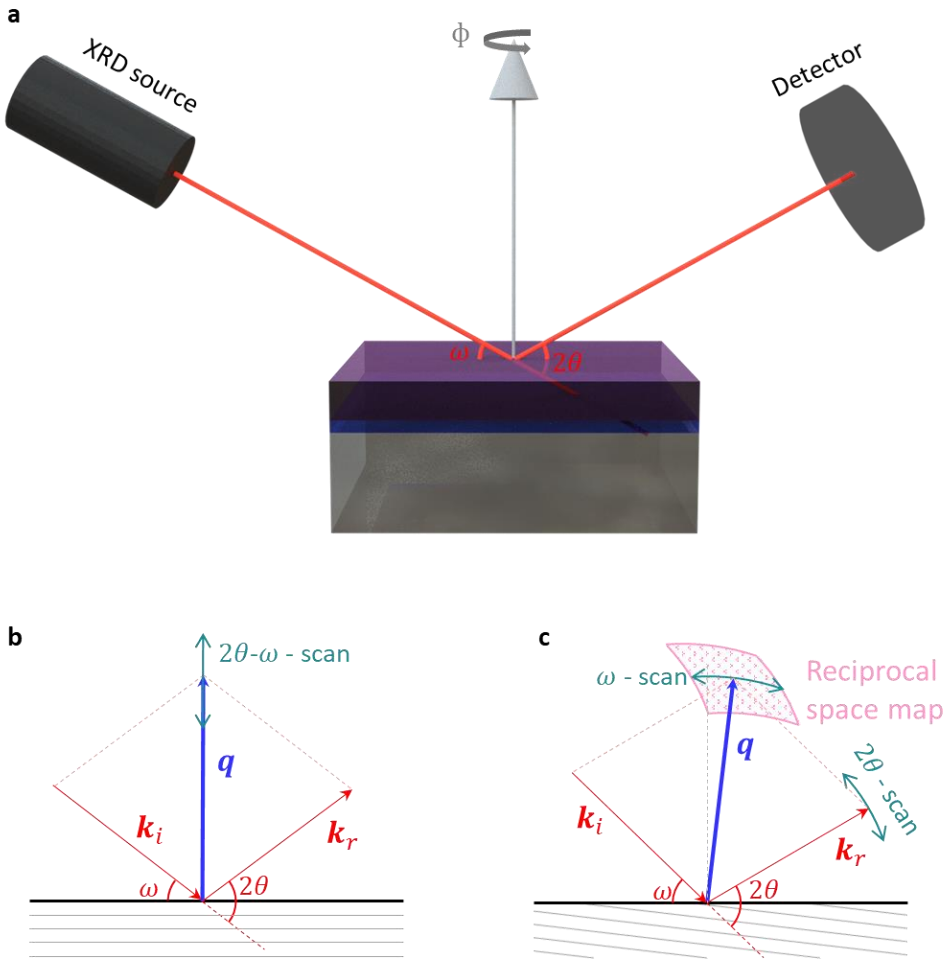

*Figure 22 : **a** Measurement geometry of the X-ray diffractometer. **b** Symmetric 2θ - ω scan. **c** Asymmetric reciprocal space map, spanned by the 2θ and ω scan direction.*

As we study elastic X-ray scattering processes, the scattering vector $\boldsymbol{q}$ can be written as the difference between the wave vectors of the incident beam $\boldsymbol{k}_i$ and the reflected beam $\boldsymbol{k}_r$.

$$\boldsymbol{q} = \boldsymbol{k}_i - \boldsymbol{k}_r$$

with

$$|\boldsymbol{k}_i| = |\boldsymbol{k}_r| = \frac{2\pi}{\lambda},$$

with $\lambda = 0.154056\ \mathrm{nm}$, the wavelength of the Cu $K\alpha_1$ radiation.

A lattice in reciprocal space can be constructed from the three lattice unit vectors $\boldsymbol{a}$, $\boldsymbol{b}$, $\boldsymbol{c}$ and the angles $\alpha \sphericalangle (\boldsymbol{b}, \boldsymbol{c})$, $\beta \sphericalangle (\boldsymbol{a}, \boldsymbol{c})$ and $\gamma \sphericalangle (\boldsymbol{a}, \boldsymbol{b})$ in real space as

$$\boldsymbol{a}^* = 2\pi \frac{(\boldsymbol{b} \times \boldsymbol{c})}{V},$$

$$\boldsymbol{b}^* = 2\pi \frac{(\boldsymbol{c} \times \boldsymbol{a})}{V},$$

$$\boldsymbol{c}^* = 2\pi \frac{(\boldsymbol{a} \times \boldsymbol{b})}{V},$$

and

$$\alpha^* = 180° - \alpha,$$

$$\beta^* = 180° - \beta,$$

$$\gamma^* = 180° - \gamma.$$

with

$$V = \boldsymbol{a} \cdot (\boldsymbol{b} \times \boldsymbol{c})$$

the volume of the unit cell. All vectors and angles in reciprocal space are marked with the asterisk *.

Hence, any reciprocal lattice vector $\boldsymbol{G}_{hkl}$ can be written as a combination of those reciprocal lattice vectors:

$$\boldsymbol{G}_{hkl} = h \cdot \boldsymbol{a}^* + k \cdot \boldsymbol{b}^* + l \cdot \boldsymbol{c}^*$$

with the Miller indices (hkl) and the distance d_{hkl} between two such adjacent planes

$$d_{hkl} = \frac{2\pi}{|\boldsymbol{G}_{hkl}|}.$$

X-ray diffraction is detected when the incident and the reflected beam interfere constructively. This so-called *Laue condition* is fulfilled when the scattering vector is equal to a reciprocal lattice vector:

$$\boldsymbol{q} = \boldsymbol{G}_{hkl}.$$

From this, the *Bragg equation*, relating every point under an angle of constructive interference to d_{hkl}, can be derived as

$$2 \cdot d_{hkl} \cdot \sin\Theta = n \cdot \lambda$$

with n the order of reflection.

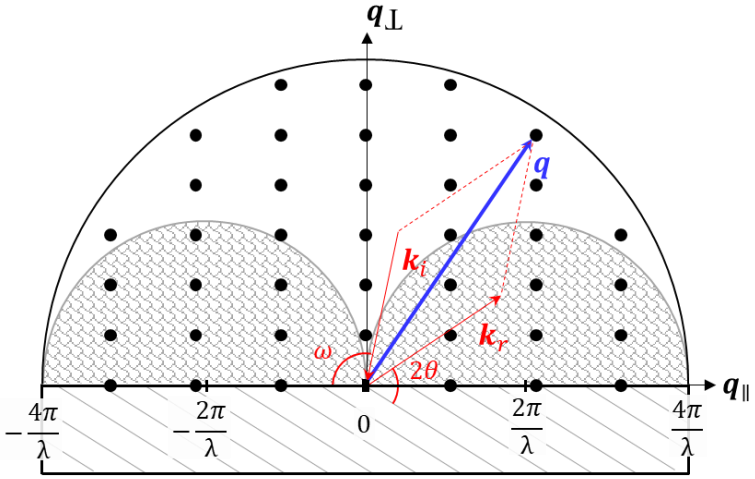

Figure 23 : Ewald sphere illustrating the scattering geometry. The scattered points within the grey semicircles are not accessible in a conventional scattering geometry.

To calculate the lattice vectors from the position of a scattering vector in reciprocal space we plot the data in reciprocal space. To visualize this situation, we look at the *Ewald sphere* (Figure 23). The length of the scattering vector $\boldsymbol{q}_{\max}$ is limited by the angle $\theta = 90°$ for the case of backscattering with

$$\boldsymbol{q}_{\max} = 2|\boldsymbol{k}| = \frac{4\pi}{\lambda},$$

corresponding to the outer sphere.

Due to the measurement geometry, reflections within the grey semicircles are only accessible in transmission and not in diffraction.

The reciprocal space is spanned in horizontal direction by $\overrightarrow{q_{\parallel}}$ and in vertical direction by $\overrightarrow{q_{\perp}}$. Geometrical analysis leads to

$$q_{\parallel} = \frac{4\pi}{\lambda}\left|\sin\left(\frac{2\Theta}{2}\right)\cdot\sin\left(\frac{2\Theta}{2}-\omega\right)\right|$$

and

$$q_{\perp} = \frac{4\pi}{\lambda}\left|\sin\left(\frac{2\Theta}{2}\right)\cdot\cos\left(\frac{2\Theta}{2}-\omega\right)\right|.$$

For the sake of simplicity, we plot our reciprocal space maps in reciprocal lattice units (rlu) without the pre-factor:

$$Q(\mathrm{rlu}) = \frac{\lambda}{4\pi}\,q$$

Consequently, each scattering vector in a reciprocal space map will be analysed as

$$\boldsymbol{Q}[hkl] = \frac{\lambda}{4\pi}\cdot\boldsymbol{G}_{hkl} = \frac{\lambda}{4\pi}(h\cdot\boldsymbol{a}^* + k\cdot\boldsymbol{b}^* + l\cdot\boldsymbol{c}^*)$$

with $Q_{x,y} = \sqrt{Q_x^2 + Q_y^2}$ on the horizontal axis and Q_z on the vertical axis.

(As in the transformation to reciprocal space there is a pre-factor 2π as well it is equivalent to: $\boldsymbol{Q}[hkl] = \frac{\lambda}{2}(h\cdot\boldsymbol{a}^* + k\cdot\boldsymbol{b}^* + l\cdot\boldsymbol{c}^*)$ with $\boldsymbol{a}^* = \frac{(\boldsymbol{b}\times\boldsymbol{c})}{V}$, $\boldsymbol{b}^* = \frac{(\boldsymbol{c}\times\boldsymbol{a})}{V}$, $\boldsymbol{c}^* = \frac{(\boldsymbol{a}\times\boldsymbol{b})}{V}$ and $V = \boldsymbol{a}\cdot(\boldsymbol{b}\times\boldsymbol{c})$.)

In the two following paragraphs, we present a systematic treatment of the XRD data. First, monoclinic $BiFeO_3$ $(001)_m$ thin films on orthorhombic $XScO_3$ $(110)_o$ scandate substrates are analysed in a monoclinic $(001)_m$ lattice (Paragraph 2.1.2). Second, pseudo-cubic $(111)_{pc}$ or rather hexagonal $(001)_h$ $BiFeO_3$ thin films on orthorhombic $(011)_o$ scandates (Paragraph 2.1.3) are presented.

2.3.1 Monoclinic lattice constants and strain value for BFO $(001)_m$ growth

When grown on $(110)_o$ orthorhombic $XScO_3$ substrates, with X = Dy, Tb, Gd, Sm, Nd, we obtain $(001)_m$ monoclinic $BiFeO_3$ thin films, that will be all treated in a monoclinic lattice setting.

The lattice vectors $\boldsymbol{a}_m$, $\boldsymbol{b}_m$, $\boldsymbol{c}_m$ for a monoclinic cell (Figure 24**a**) are converted into reciprocal space (Figure 24**b**).

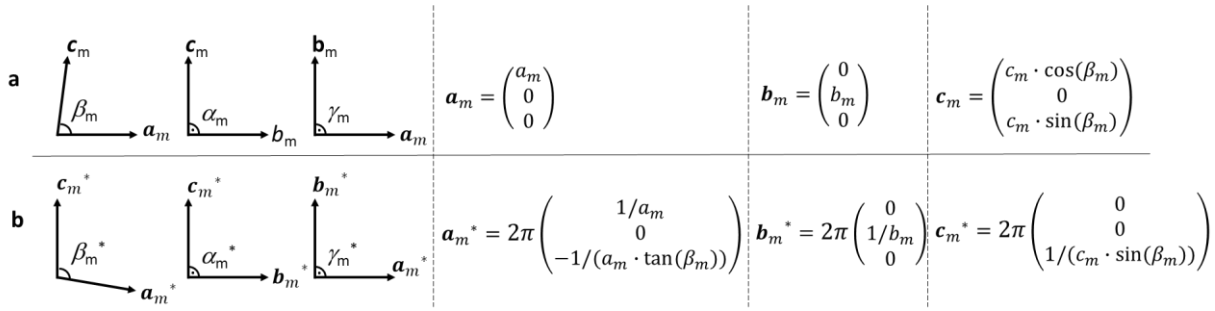

*Figure 24 : Lattice vectors of a monoclinic unit cell in **a** real space and **b** reciprocal space.*

We use these relations for $BiFeO_3$ films and $XScO_3$ substrates. For the cubic $SrTiO_3$ we simply set $\beta_m = \beta_c = 90°$.

Recalling paragraph 2.1.1, we expect four different elastic $BiFeO_3$ domains (Figure 25). To match the monoclinic $BiFeO_3$ lattice with the substrate, $\boldsymbol{a}^*_{m,BFO1}$, $\boldsymbol{a}^*_{m,BFO2}$, $\boldsymbol{a}^*_{m,BFO3}$ and $\boldsymbol{a}^*_{m,BFO4}$ grow respectively with an angle of 45°, 135°, 225° and 315° with regard to the reciprocal $\boldsymbol{a}^*_{m,XSO}$ on the substrate (Figure 26). However, the monoclinic crystal symmetry of the substrate is expected to favour only the two ferroelastic domains of $BiFeO_3$ with angles of 45° and 315°.

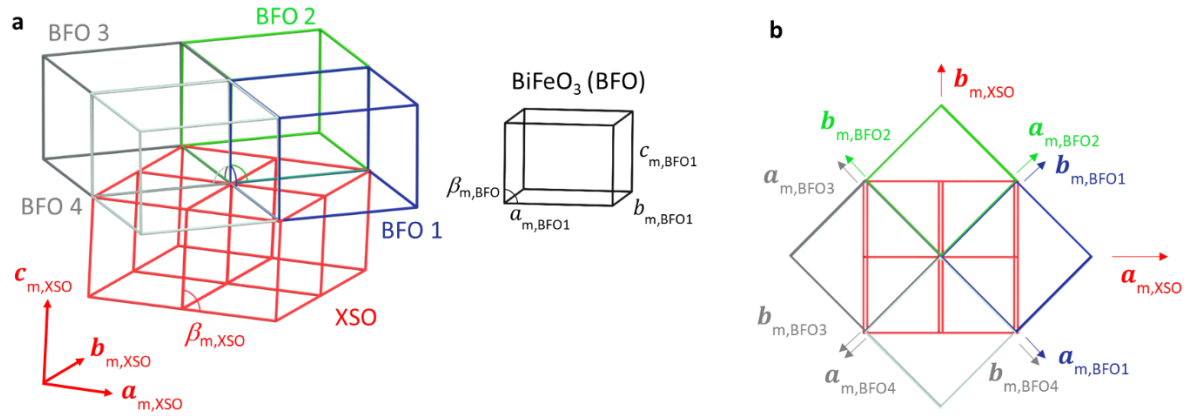

*Figure 25 : Four monoclinic $BiFeO_3$ domains (BFO1-4) in blue, green, dark and light grey, respectively, on top of the $XScO_3$ $(001)_m$ substrate in red. **a** Three dimensional view, **b** top view on the sample surface.*

The corresponding reciprocal lattice vectors for a monoclinic scandate $XScO_3$ (red) and the four possible $BiFeO_3$ variants (BFO1-4) are represented in the (001), (010) and (-100)-planes (Figure 26**a**, **b**, **c**, respectively). The colour-code for $BiFeO_3$ is blue and green for the two domains (BFO1, 2) found in the samples that will be analysed. I choose grey for the other two less favourable ones (BFO3, 4) due to the monoclinic substrate, and black for relations that are valid for all $BiFeO_3$ domains. Dashed lines mark the fact that the corresponding axes point in a direction slightly out of the plane, as shown in Figure 26**a**. In Figure 26**d** the reciprocal [hk0] - [00l] space is shown, corresponding to a vertical cut along the yellow line in Figure 26**a**. Again, those schematics can be easily adapted for STO with $\beta_m = \beta_c = 90°$. To calculate all the lattice parameters from one map, the space represented by the black box in Figure 26**d** was scanned in the experiments. The first information comes from the number of peaks. In Figure 26**d**, the BFO1-4 peaks are located differently from the (113) substrate peak. In Figure 26**d**, starting from the (003) BFO peak on the [00l] axis, we move horizontally to the right for the [0k0] and $[0\bar{k}0]$

direction, but slightly downwards for the [h00] and slightly upwards for the $[\bar{h}00]$ direction, due to the monoclinic angle β_{m}^{*}. Therefore, the BFO1 (023) peak and the BFO3 ($0\bar{2}3$) peak overlap with a vertical position in between the BFO2 (203) peak and the BFO4 ($\bar{2}03$) peak. For a small difference between a_{m}^{*} and b_{m}^{*} this also results in a slight shift for the BFO2 (203) peak and the BFO4 ($\bar{2}03$) peak to the left.

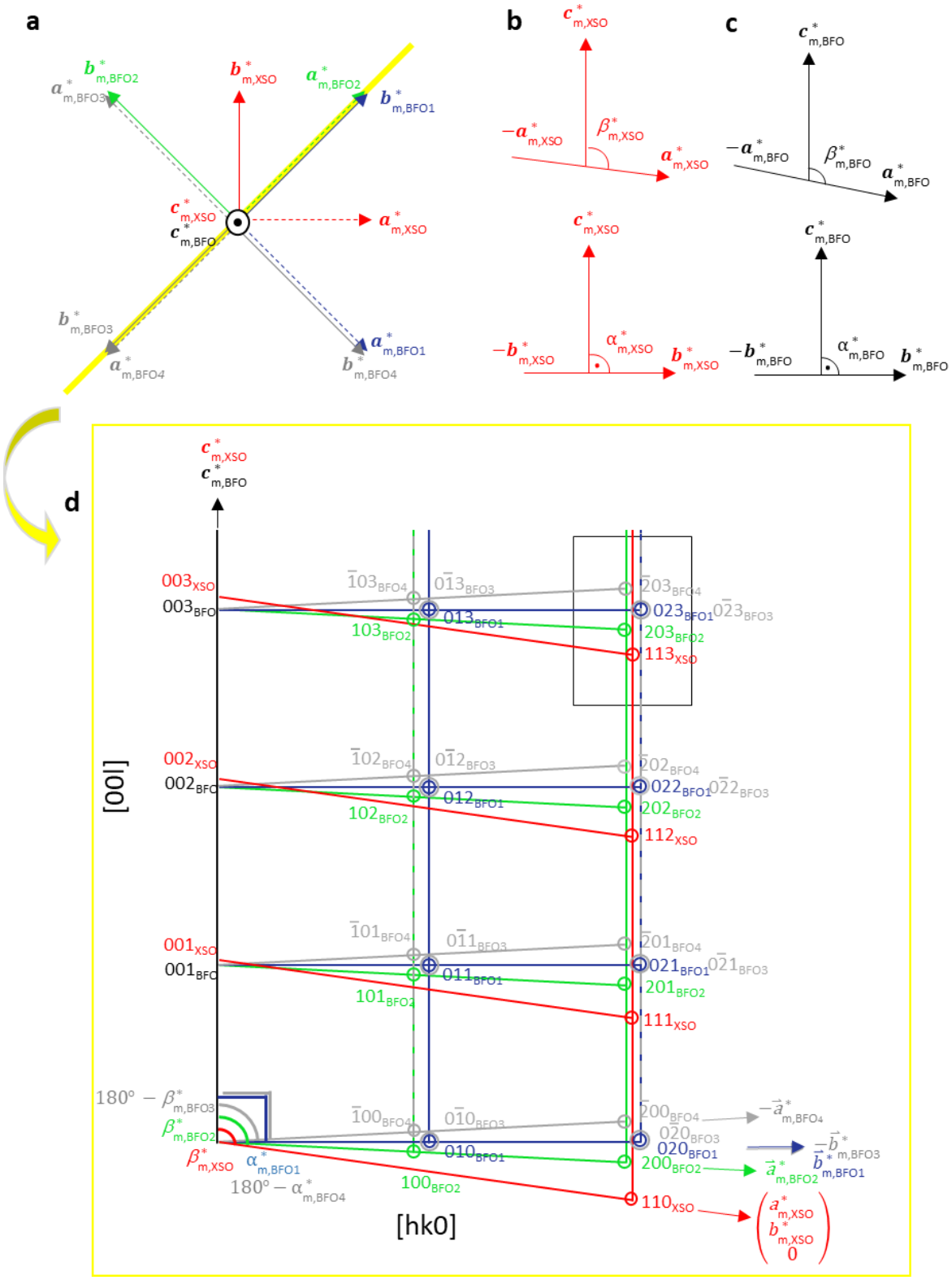

Figure 26 : Crystallographic axes of the four elastic BFO domains with respect to the scandate substrate. The two elastic variants present in our films are BFO1 (blue) and BFO2 (green). BFO3 and BFO4 (grey) are not present due to the monoclinic symmetry of the substrate XSO, $XScO_3$ with X = Dy, Tb, Gd, Sm, Nd, (red). Dotted lines represent axes that are slightly rotated out of the represented plane. ***a*** *(001) plane, $BiFeO_3$ grows at an angle of 45° on top of the substrate, the four possibilities are represented by BFO1-4.* ***b,c*** *(0-10) and (100) planes for the substrates (red) and all four variants of BFO1-4 (black), respectively.* ***d*** *[hk0]/[00l] plot, corresponding to a cut along the yellow line in* ***a****.*

The relations between the monoclinic lattice parameters and the $Q_{x,y}$ and Q_z values for different asymmetric x-ray peaks of $BiFeO_3$ are given by:

$$\boldsymbol{Q}[023] = \frac{\lambda}{2} \cdot \begin{pmatrix} 0 \\ 2/b_\mathrm{m} \\ 3/(c_\mathrm{m} \cdot \sin\beta_\mathrm{m}) \end{pmatrix},$$

$$\boldsymbol{Q}[203] = \frac{\lambda}{2} \cdot \begin{pmatrix} 2/a_\mathrm{m} \\ 0 \\ -2/(a_\mathrm{m} \cdot \tan\beta_\mathrm{m}) + 3/(c_\mathrm{m} \cdot \sin\beta_\mathrm{m}) \end{pmatrix}$$

and therefore

$$Q_y[023] = \frac{\lambda}{2} \cdot \frac{2}{b_\mathrm{m}},\ Q_z[023] = \frac{\lambda}{2} \cdot \frac{3}{c_\mathrm{m} \cdot \sin\beta_\mathrm{m}},$$

$$Q_x[203] = \frac{\lambda}{2} \cdot \frac{2}{a_\mathrm{m}},\ Q_z[203] = \frac{\lambda}{2} \cdot \left(\frac{-2}{a_\mathrm{m} \cdot \tan\beta_\mathrm{m}} + \frac{3}{c_\mathrm{m} \cdot \sin\beta_\mathrm{m}}\right).$$

Solving this system of equations gives

$$a_\mathrm{m} = \frac{\lambda}{2} \cdot \frac{2}{Q_{x,y}[203]},$$

$$b_\mathrm{m} = \frac{\lambda}{2} \cdot \frac{2}{Q_{x,y}[023]},$$

$$c_\mathrm{m} = \frac{\lambda}{2} \cdot \frac{3}{Q_z[023] \cdot \sin\beta_\mathrm{m}}$$

With

$$Q_z[203] = Q_z[023] - \frac{Q_x[203]}{\tan\beta_\mathrm{m}}$$

we obtain

$$\beta_\mathrm{m} = \tan^{-1}\left(\frac{Q_x[203]}{Q_z[023] - Q_z[203]}\right).$$

The strain

$$\varepsilon = \frac{\sqrt{\frac{a_\mathrm{m} \cdot b_\mathrm{m}}{2}} - \sqrt[3]{\frac{V_\mathrm{m}}{2}}}{\sqrt[3]{\frac{V_\mathrm{m}}{2}}}$$

in each film is then calculated with

$$V_\mathrm{m} = a_\mathrm{m} \cdot b_\mathrm{m} \cdot c_\mathrm{m} \cdot \sin\beta_\mathrm{m}.$$

Thus, it is necessary to perform reciprocal space maps around those film peaks including the neighbouring substrate peaks (Figure 26) to prove that a thin film grows fully strained with the in-plane lattice of the substrate. Instead of the (113) substrate peak, we can choose the (013) and the (103) substrate peaks to access the lattice parameters of the films. Figure 27**a** shows the (00l) film plane with an orange and a violet line highlighting the [0k0]* and the [h00]*, respectively, that we choose as Q_{xy} axes for the reciprocal space maps. The Q_z axis corresponds to the [00l]* out-of-plane direction.

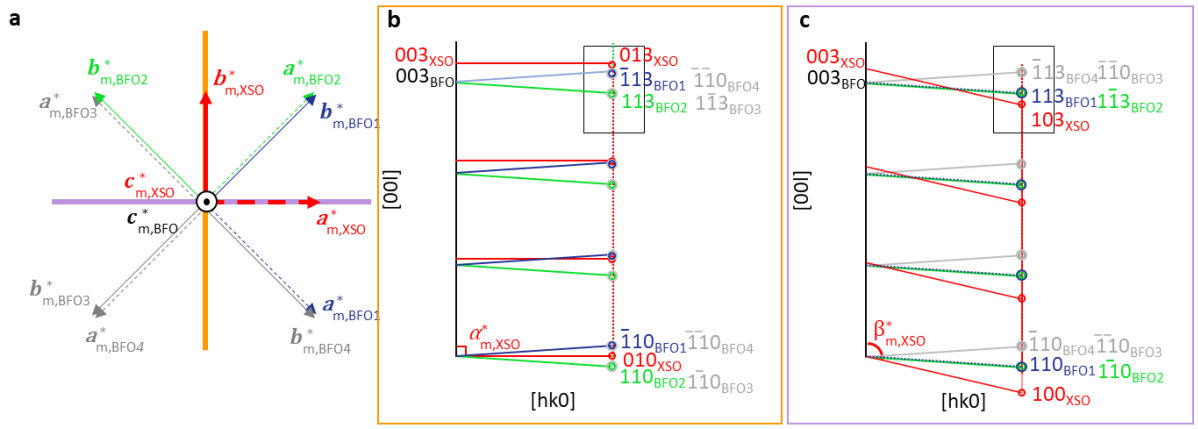

Figure 27 : Reciprocal space maps along around the (013) and (103) substrate peaks of STO, DSO, TSO, GSO, SSO and NSO. ***a*** *(00l) film plane with indication of the [0k0]* and the [h00]* substrate directions in orange and violet, respectively. The reciprocal space maps along these two substrate directions are sketched in* ***b***, ***c***.

Figure 27**b**-**c** show sketches to localize the experimental data around the (013) and the (103) substrate peaks for $SrTiO_3$, $DyScO_3$, $TbScO_3$, $GdScO_3$, $SmScO_3$ and $NdScO_3$ in reciprocal space. We will see that in our films only the blue domain BFO1 and the green domain BFO2 are present, and therefore BFO3 and BFO4 are only drawn for comprehension in grey. To answer the question whether or not our films grow fully strained, we can verify the perfect vertical alignment of the substrate and $BiFeO_3$ peaks in the reciprocal space maps around (013) and (103), without any calculation. Moreover, it is possible to compare the strain values calculated above with the Q_{xy} and Q_z values of $BiFeO_3$ measured from the (113) and $(1\bar{1}3)$ peaks:

$$Q_{xy}[113] = Q_{x,y}[1\bar{1}3] = \frac{\lambda}{2} \cdot \sqrt{\frac{1}{a_m^2} + \frac{1}{b_m^2}},$$

$$Q_z[113] = Q_z[1\bar{1}3] = \frac{\lambda}{2} \cdot \left(\frac{3}{c_m \cdot \sin \beta_m} - \frac{1}{a_m \cdot \tan \beta_m}\right).$$

When those equations are fulfilled with the lattice parameters calculated before, this confirms the equal amount of strain in both types of domains (BFO1 and BFO2), as we will see in the mixed in-plane direction [11l] compared to the data set before, where information for [02l] came from BFO1 and [20l] from BFO2.

2.3.2 The pseudo-hexagonal lattice in the case of $BiFeO_3$ $(111)_{pc}$ growth

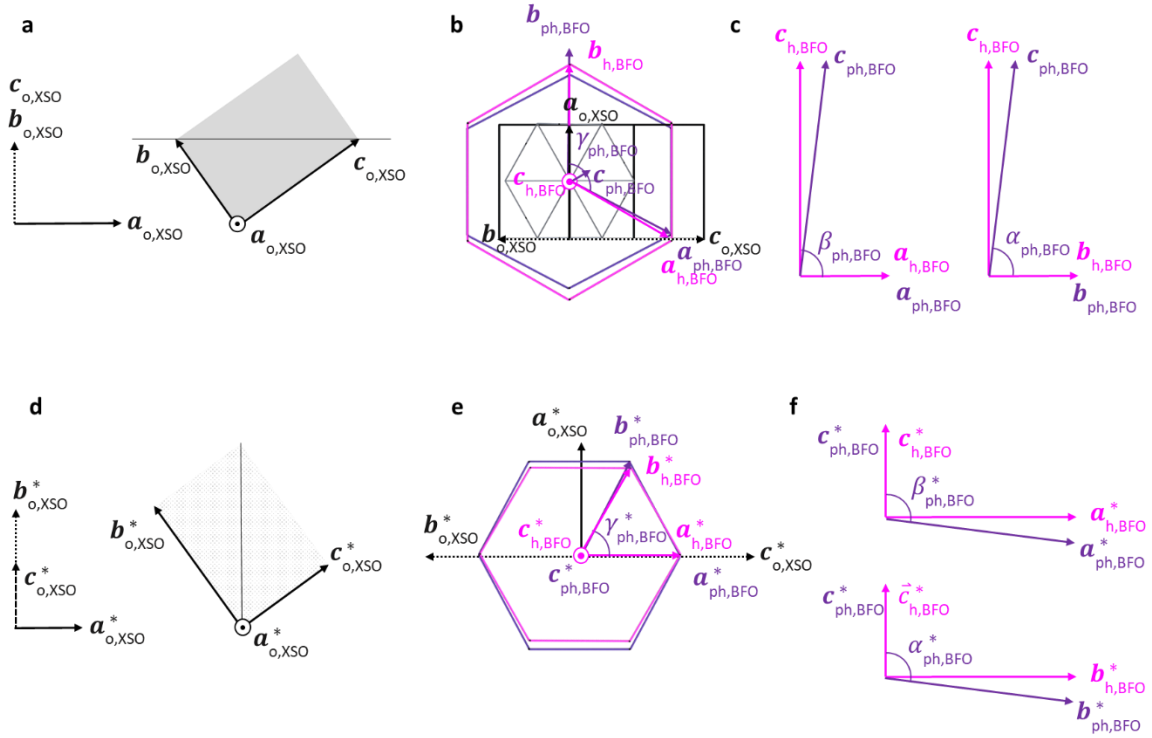

Figure 28 : ***a-c*** *Real space and* ***d-e*** *reciprocal space lattice vectors for $XScO_3$ (black) and $BiFeO_3$ hexagonal (pink) and pseudo-hexagonal (violet).*

To construct the reciprocal lattice, the real space lattice vectors of the orthorhombic (black) and the hexagonal (pink) unit cell are converted into reciprocal space (Figure 28). Moreover, the distortion of a pseudo-hexagonal lattice, where $a_{ph,BFO} \neq b_{ph,BFO}$ and the angles $\alpha_{ph,BFO}$, $\beta_{ph,BFO}$ and $\gamma_{ph,BFO}$ are unequal to 120° and 90°, respectively, is added in violet. From the symmetry group, this is a triclinic lattice, but we use the fact of only slight deviation from the hexagonal lattice to interpret the reciprocal space maps in an easier way.

The pseudo-hexagonal distortion of the $BiFeO_3$ lattice (Figure 28**c, f**) comes from the fact that in real space the vector $\vec{c}_{ph,BFO}$ is not easily describable in Cartesian coordinates. It contains projections depending on $\alpha_{ph,BFO}$, $\beta_{ph,BFO}$ and $\gamma_{ph,BFO}$. This problem does not exist in reciprocal space as $\vec{c}^{*}_{ph,BFO}$ is the reciprocal out-of-plane lattice parameter. We approach the pseudo-hexagonal lattice parameters by calculating first the reciprocal ones and then converting them into real space. We start with the angles:

$$\alpha = 180° - \alpha^{*},$$

$$\beta = 180° - \beta^{*},$$

$$\gamma = 180° - \gamma^{*}.$$

Then we use

$$\frac{V}{a \cdot b \cdot c} = \sqrt{1 - \cos(\alpha)^2 - \cos(\beta)^2 - \cos(\gamma)^2 + 2 \cdot \cos(\alpha) \cdot \cos(\beta) \cdot \cos(\gamma)} = W$$

with

$$a = \frac{2\pi}{a^* \cdot W} \cdot \sin\alpha,$$

$$b = \frac{2\pi}{b^* \cdot W} \cdot \sin\beta,$$

$$c = \frac{2\pi}{c^* \cdot W} \cdot \sin\gamma.$$

The reciprocal lattice parameters are deduced from Figure 28. **e, f** as

$$\boldsymbol{a}^* = \begin{pmatrix} 0 \\ -a^* \cdot \cos(\beta^* - 90°) \\ -a^* \cdot \sin(\beta^* - 90°) \end{pmatrix} = \begin{pmatrix} 0 \\ -a^* \cdot \sin(\beta^*) \\ a^* \cdot \cos(\beta^*) \end{pmatrix},$$

$$\boldsymbol{b}^* = \begin{pmatrix} b^* \cdot \sin(\gamma^*) \cdot \cos(\alpha^* - 90°) \\ -b^* \cdot \cos(\gamma^*) \cdot \cos(\alpha^* - 90°) \\ -b^* \cdot \sin(\alpha^* - 90°) \end{pmatrix} = \begin{pmatrix} b^* \cdot \sin(\gamma^*) \cdot \sin(\alpha^*) \\ -b^* \cdot \cos(\gamma^*) \cdot \sin(\alpha^*) \\ b^* \cdot \cos(\alpha^*) \end{pmatrix}$$

and

$$\boldsymbol{c}^* = \begin{pmatrix} 0 \\ 0 \\ c^* \end{pmatrix}.$$

In the next step, we determine reciprocal space map areas for the measurements. Figure 29**a** shows a projection of the reciprocal lattice of the orthorhombic $XScO_3$ substrate and the hexagonal $BiFeO_3$ film on the Q_x-Q_y plane. For the orthorhombic lattice in the Q_z direction, we have to combine the $\boldsymbol{b}^*_{o,XSO}$ and the $\boldsymbol{c}^*_{o,XSO}$ vectors as shown in Figure 29**b-d**. The $BiFeO_3$ Q_z value is explained with the pink $\boldsymbol{c}^*_{h,BFO}$ arrows.

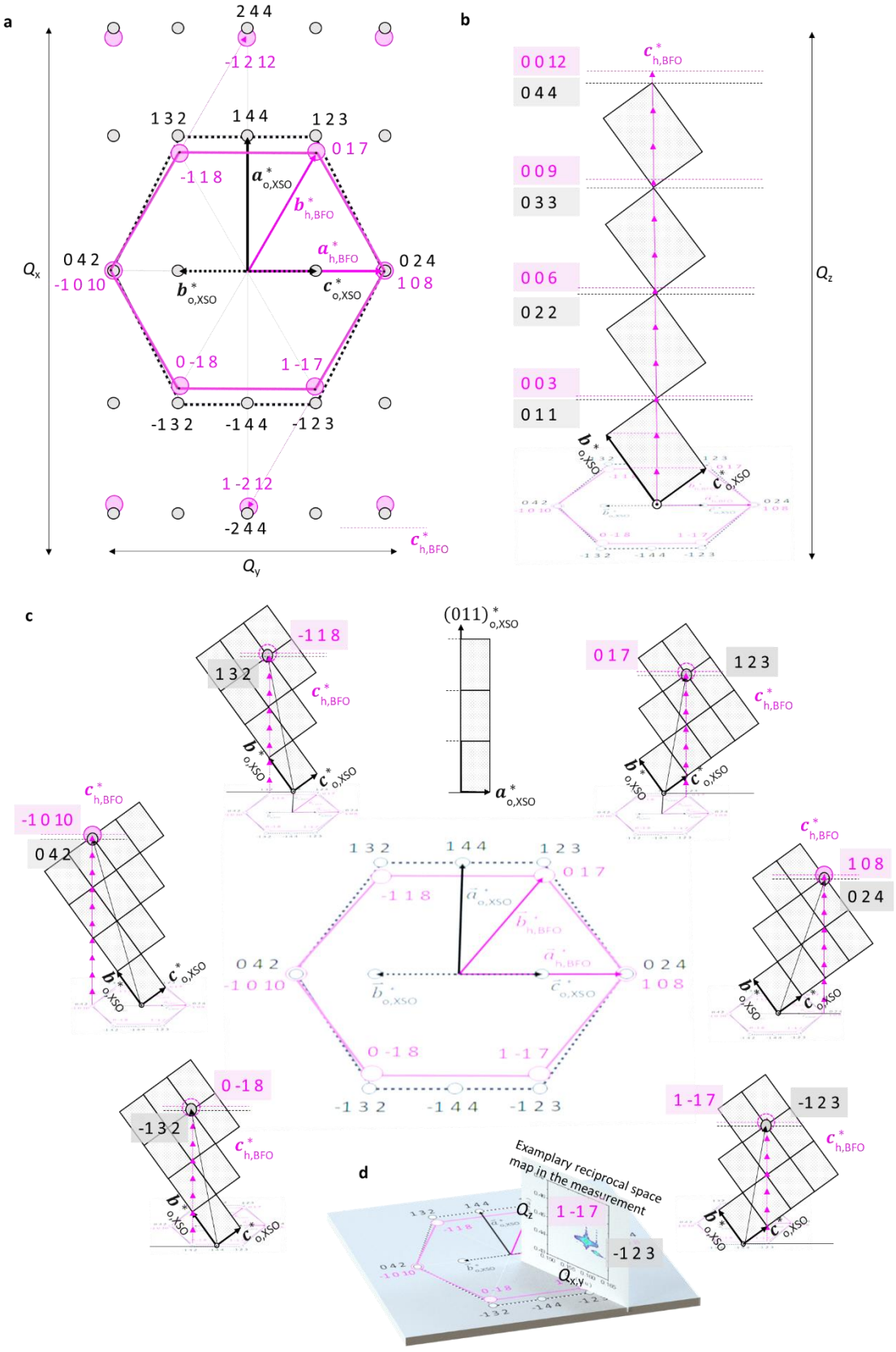

Figure 29 : Reciprocal lattice of the orthorhombic $XScO_3$ substrate and the hexagonal $BiFeO_3$ film. ***a*** *The Q_x-Q_y plane.* ***b*** *Corresponding representation along the Q_z direction.* ***c*** *$XScO_3$ in-plane lattice and the corresponding Q_z values.* ***d*** *Example in 3D for the measurement around the $(\bar{1}23)$ $DyScO_3$ substrate peak.*

One way to determine values for the reciprocal lattice parameters using the $BiFeO_3$ $\boldsymbol{Q}[1\ 0\ 8]$, $\boldsymbol{Q}[\bar{1}\ 0\ 10]$, $\boldsymbol{Q}[0\ \bar{1}\ 8]$ and $\boldsymbol{Q}[\ \bar{1}\ 2\ 12]$ vector is to calculate in the following order:

$$c^* = \frac{\frac{4\pi}{\lambda}(Q_z[108] - Q_z[\bar{1}010])}{18},$$

$$\beta^* = \tan^{-1}\left(\frac{\frac{4\pi}{\lambda}Q_z[108] - 8\cdot c^*}{\frac{4\pi}{\lambda}Q_{xy}[108]}\right),$$

$$a^* = \frac{\frac{4\pi}{\lambda}Q_{xy}[\bar{1}010]}{\sin(\beta^*)},$$

$$\alpha^* = \tan^{-1}\left(-\frac{\frac{4\pi}{\lambda}Q_{xy}[0\bar{1}8]}{\frac{4\pi}{\lambda}Q_z[0\bar{1}8] - 8\cdot c^*}\right),$$

$$b^* = -\frac{\frac{4\pi}{\lambda}Q_z[0\bar{1}8] - 8\cdot c^*}{\cos(\alpha^*)},$$

and

$$\gamma^* = \cos^{-1}\left(\frac{-\left(\frac{4\pi}{\lambda}Q_{xy}[\bar{1}212]\right)^2 + 4\cdot\beta^{*2}\cdot\sin^2(\alpha^*) + \alpha^{*2}\cdot\sin^2(\beta^*)}{4\cdot a^*\cdot b^*\cdot\sin(\alpha^*)\cdot\sin(\beta^*)}\right).$$

Because of the uniaxial strain imposed by the substrate on the hexagonal BFO lattice, two strain values along the two hexagonal lattice vectors will be calculated as

$$\varepsilon_a = \frac{a_{ph,RSM} - a_{h,Bulk}}{a_{h,Bulk}}$$

and

$$\varepsilon_b = \frac{b_{ph,RSM} - a_{h,Bulk}}{a_{h,Bulk}}.$$

We will employ this formalism later in Chapter 3 to calculate the lattice parameters from the X-ray diffraction data.

2.4 Scanning probe microscopy

The generic term 'scanning probe microscopy' encompasses a lot of techniques where the properties of a sample are investigated under the motion of a scanning tip at the atomic scale. There are three main sub-groups: scanning tunnelling microscopy where a tunnelling current flows between the tip and the sample, different types of scanning near-field optical microscopies and scanning force microscopy, also known as atomic force microscopy (AFM).[117] Here only the latter is explained in detail. After an introduction to its basic use to map the surface of a sample, I will focus on piezoresponse force microscopy, where a bias voltage between the tip and the surface enables to map and manipulate the ferroelectric domain structure. The last part of this section will be dedicated to scanning NV magnetometry in which a single nitrogen vacancy (NV) defect, used as an ultrasensitive magnetic sensor, is embedded in a diamond AFM tip to map magnetic textures.

2.4.1 Atomic force microscopy

Atomic force microscopy is commonly employed to map the topography of a thin film within the so-called 'tapping mode'. In this mode, the cantilever holding the AFM tip oscillates close to its resonance frequency. The motion of this cantilever, probed by a laser focused on its backside and reflected onto a four-quadrant photo-diode, is used to control the tip-sample distance (Figure 30**a**). The approach of the tip to the surface is monitored by a target oscillation amplitude that is typically 80% of the free resonance amplitude. The surface is scanned at constant oscillating amplitude and the feedback loop adapts the z-piezo motor, which enables to reconstruct the topography of the sample (Figure 30**b**). The intermittent contact at each cycle is the origin of the name of this operating mode, separating it from 'non-contact' and 'contact scanning' modes. As compared to the contact mode, the biggest advantage of the tapping mode consists in a great reduction of lateral forces on the tip, preserving its sharpness.

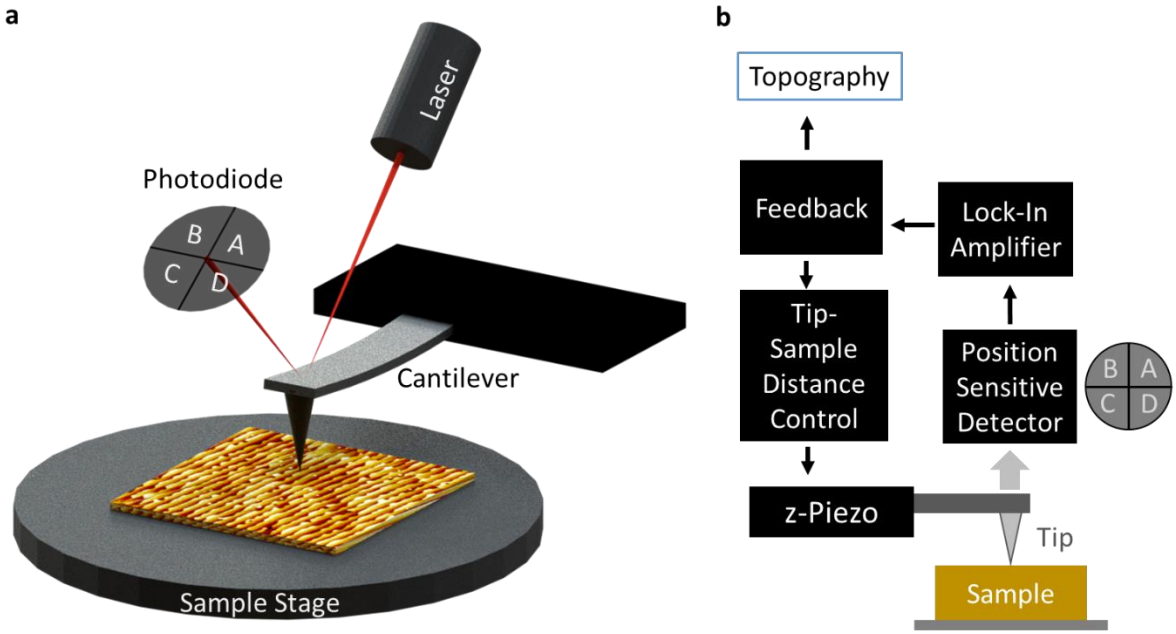

*Figure 30 - Sketch (**a**) and working principle (**b**) of an atomic force microscope.*

An example of a topography AFM image is shown in Figure 31 for a scan over a single crystalline substrate with atomic steps on its surface.

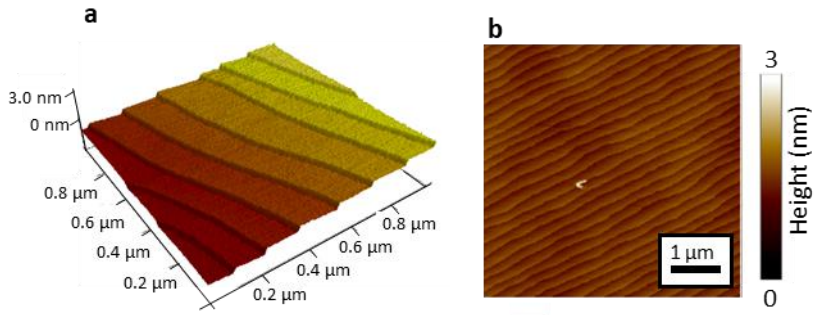

Figure 31 : AFM measurements of terraces and atomic steps on the surface of single crystalline $DyScO_3$ substrate. ***a*** *3D-view of a 1 x 1 µm² sample,* ***b*** *2D-view of a 5 x 5 µm² scan.*

2.4.2 Piezoresponse force microscopy

Ferroelectric materials are characterized by their switchable polarization states. Thanks to the inverse piezoelectric effect and because all ferroelectrics are piezoelectric, it is possible to measure the hysteresis loop and the polarization direction as an elastic deformation when a bias is applied across the material.

Figure 32 shows an example for a single ferroelectric domain with a polarization direction perpendicular to the surface. It expands when the polarization P is parallel to the external electric field E and contracts when P is antiparallel to it. While the polarization P shows a square ferroelectric hysteresis loop with the external electric field (Figure 32**a**), the strain η evolution with electric field follows a characteristic butterfly loop (Figure 32**b**). The piezoelectric deformation tensor d_{ij} in meters per volt describes this deformation determined by the crystal symmetry of the material via

$$\eta_{ij} = d_{ij}E.$$

In this example, where the ferroelectric polarization is perpendicular to the surface and the electric field applied (anti-)parallel, only the component d_{33} is non-zero. As the electric field can be determined by the applied voltage drop V along the sample, it can be expressed as

$$\Delta z = d_{33}V.$$

By measuring Δz it is possible to extract d_{33}. If one knows the sign of the piezoelectric coefficient, the sign of Δz indicates the orientation of the polarization.

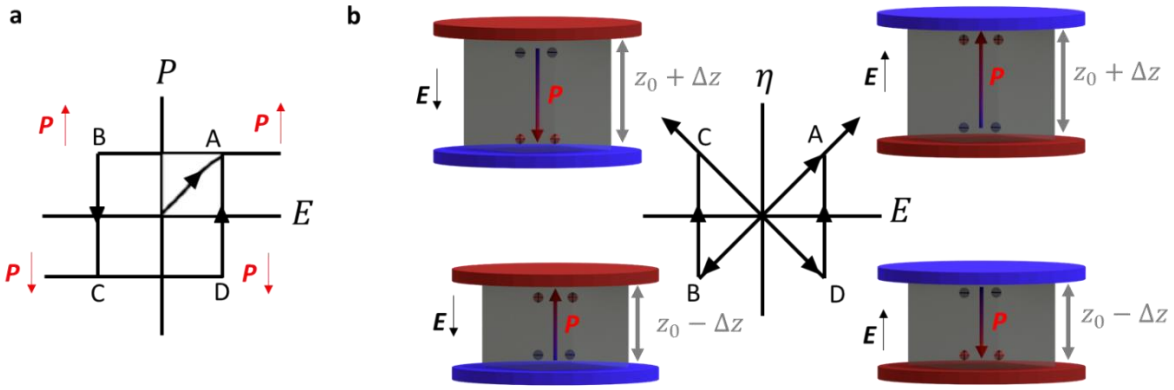

Figure 32 : ***a*** *Schematic ferroelectric hysteresis loop for a single domain ferroelectric.* ***b*** *Corresponding induced strain of the material.*

In piezoresponse force microscopy (PFM), an extended AFM set-up is used (Figure 33). An electric field is applied between a conducting tip scanning the sample surface in 'contact' mode and a bottom electrode underneath the ferroelectric thin film. The cantilever deflection and torsion due to the piezoelectric deformation is recorded in the four quadrants photodiode (Figure 33**a**). As the deformations Δz due to the inverse piezoelectric effect are very small (pm-range) compared to the topography (nm-range), an AC-voltage

$$V_{AC} = V_0 \cos(\omega t)$$

is applied and the resulting vibration

$$\Delta z = |d_{33}| V_0 \cos(\omega t + \phi(d_{33}))$$

is sensed as a deflection signal and processed via a lock-in amplifier (Figure 33**b**). The output values are the PFM phase and amplitude. The PFM phase provides information about the sign of the polarization direction, the amplitude contains information about the absolute value of d_{33} and vanishes at ferroelectric domain walls (Figure 33**c**). The out-of-plane polarization can be determined from the difference in intensity between the upper two quadrants B+A and C+D. We consider that the AFM tip is grounded and the voltage is applied to the sample stage connected to the bottom electrode. For domains pointing downwards, the phase will be shifted by 180° compared to the input AC-voltage, whereas there will be no phase shift for domains pointing upwards. We shift the phase of the lock-in by -90° so that domains pointing down-wards are bright (+90°) and domains pointing upwards are dark (-90°).

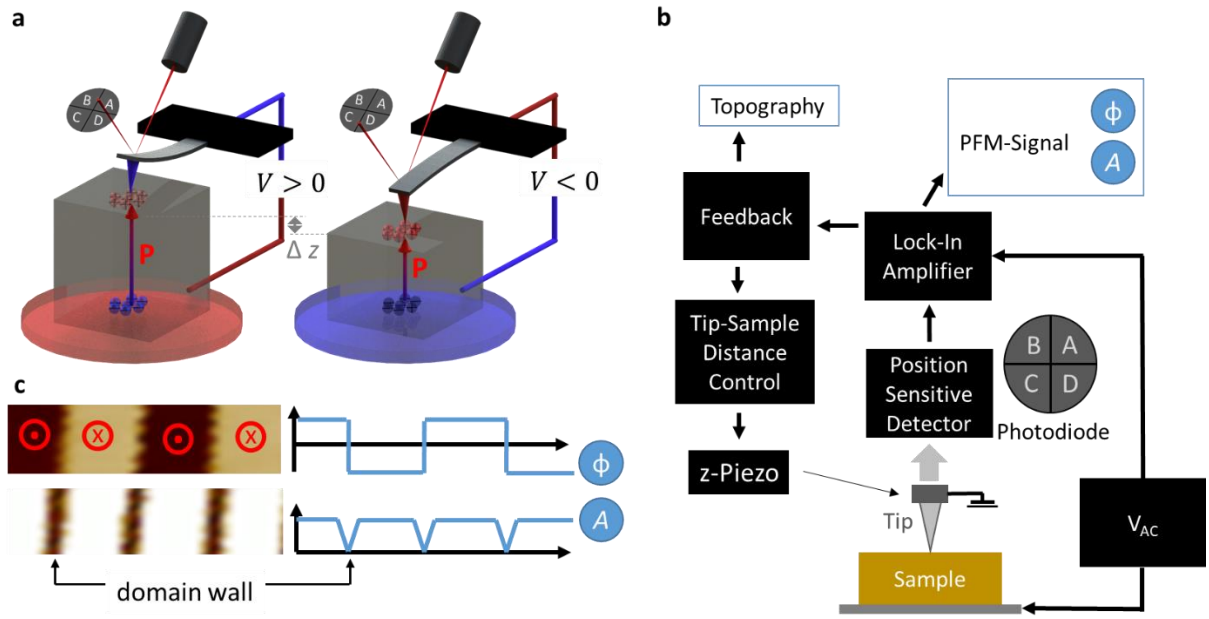

Figure 33: Schematic **a** *and working principle* ***b*** *of a piezoresponse force microscope.* ***c*** *Output phase and amplitude on four domains with alternated up and down polarization states.*

To measure the piezoelectric loop associated to polarization switching with a PFM, the polarization is manipulated locally without scanning, combining the AC voltage with a DC one

$$V = V_{\mathrm{DC}} + V_{\mathrm{AC}} \cdot \cos(\omega t).$$

In this local spectroscopic mode, the phase shows a square hysteretic behaviour as a function of the DC voltage (Figure 34**a**), while the amplitude shows a characteristic butterfly loop, decreasing at the coercive voltage and saturating at higher voltages (Figure 34**b**). The piezoelectric coefficient d_{33} for a material with a purely out-of-plane polarization (such as tetragonal $BaTiO_3$) corresponds to the product of the amplitude with the cosine of the phase as shown in Figure 34**c**.

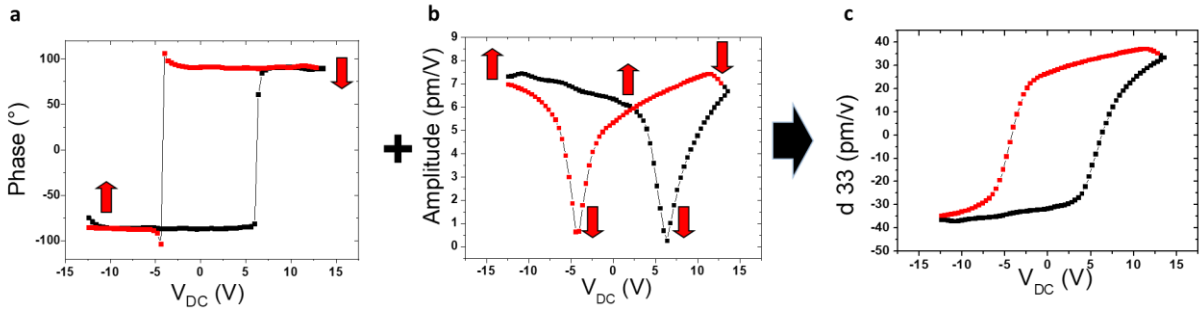

Figure 34 : Local piezoelectric hysteresis loop collected with PFM. ***a****, PFM phase and* ***b****, amplitude after applying rectangular voltage pulses of varying amplitude. The red arrows denote the polarization direction.* ***c****, Combined* d_{33} *vs. voltage.*

When the polarization has a component being non-perpendicular to the electric field, other entries of the dielectric tensor are non-zero and the material elongates and shrinks laterally, too. To determine a three-dimensional map of the polarization direction in the ferroelectric

domains in $BiFeO_3$ thin films, we mainly use PFM in scanning mode, applying an AC voltage below the coercive field without measuring a full ferroelectric hysteresis loop at each step. We record the topography image, the out-of-plane phase and amplitude (Figure 35**a, b**) as well as the in-plane phase and amplitude (Figure 35**c, d**). The principle of detection stays unchanged with the only difference that for the in-plane component we are interested in the torsion of the cantilever, instead of its deflection. The in-plane piezoresponse is the difference between domains pointing to the right and to the left of the cantilever. Here domains pointing to the right of the tip (seen from its point of view) are associated with bright contrast (180° phase shift) and domains pointing to the left with dark contrast (zero phase shift). The in-plane and out-of-plane phase signals are recorded simultaneously in the same scan. However, different stiffness values of the cantilever (typically between 2 N/m and 40 N/m) can be either more adapted to out-of-plane or in-plane PFM imaging.

To reconstruct the exact polarization direction in each domain of a $BiFeO_3$ thin film, it is necessary to combine advanced structural characterizations with vectorial PFM analysis. Here the sample is positioned at different angles with respect to the cantilever and scanned sequentially. More details about this are shown as a concrete example in section 3.1.

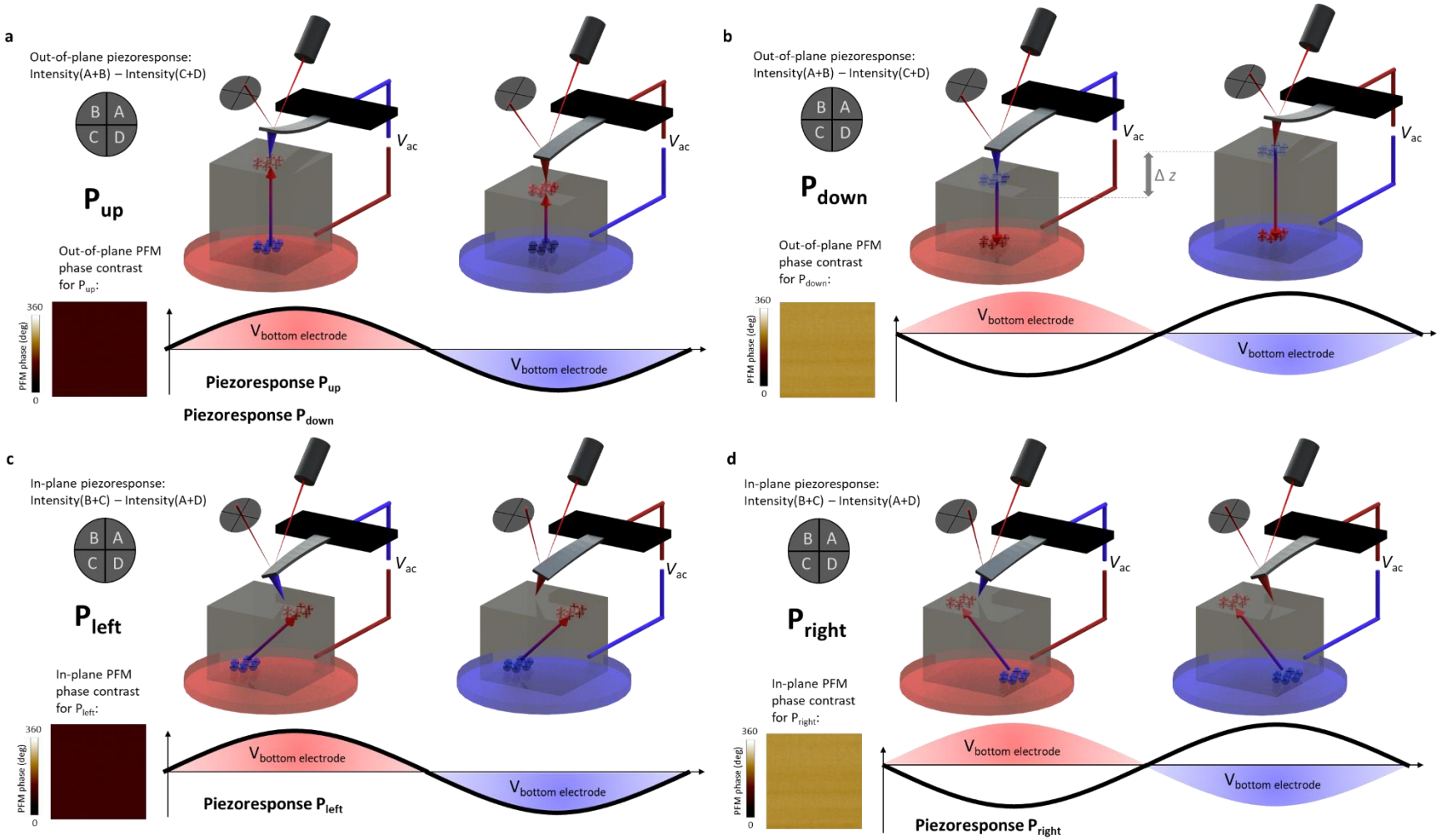

*Figure 35 : Out-of-plane piezoresponse for a ferroelectric domain pointing upwards P_{up} (**a**) and downwards P_{down} (**b**). The difference in the piezoresponse compared to the input AC-Voltage (V_{AC}) set to the bottom electrode is a phase shift by 180° or 0° for P_{down} and P_{up}, respectively. In-plane piezoresponse for a ferroelectric domain pointing to the left P_{left} (**c**) and to the right P_{right} (**d**). The difference in the piezoresponse compared to the input AC-voltage (V_{AC}) set to the bottom electrode is a phase shift by 180° or 0° for P_{right} and P_{left}, respectively.*

Designing artificial domains

Applying a constant DC bias between the tip and the bottom electrode while scanning enables to locally switch the polarization direction. Whereas for reading AC-voltages below the coercive field of the material are used, it is important to apply a DC bias larger than the coercive field in order to change the polarization direction. Figure 36 shows besides the unaffected topography, the out-of-plane PFM phase and amplitude images after writing a square domain with positive voltage at the tip in a zone that had been switched upwards before. Areas with P_{down} (P_{up}) appear with bright (dark) contrast in the PFM phase image and the PFM amplitude decreases significantly at the domain walls, visible as black lines.

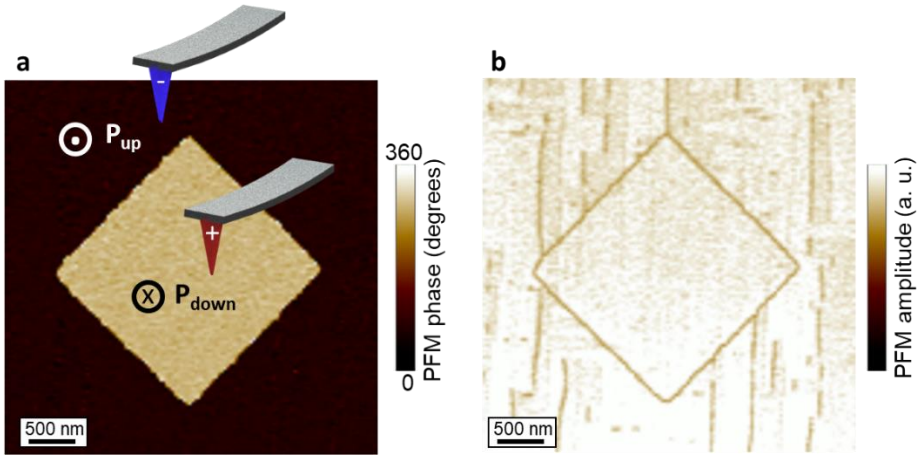

*Figure 36 : Switched ferroelectric domains detected by out-of-plane PFM: **a** Out-of-plane PFM phase and **b** amplitude images. We note that the amplitude of the initial upward polarization and the written downward polarization are similar.*

To change the in-plane polarization direction, we always switch the out-of-plane component, too. The in-plane component depends on the scanning direction and the direction of the out-of-plane switching. The electric field of a tip in motion sensed by the sample at the surface is not isotropic which gives rise to a so-called "trailing field"[118]. The motion of the tip consists of a fast scan axis to the right and to the left, moving globally in a direction perpendicular to it along the slow scan axis (Figure 37**a**). This slow motion "trails" the in-plane polarization direction either along it, for positive bias at the bottom electrode (negative tip), or antiparallel to it for negative bias at the bottom electrode (positive tip), as shown in Figure 37**b**.

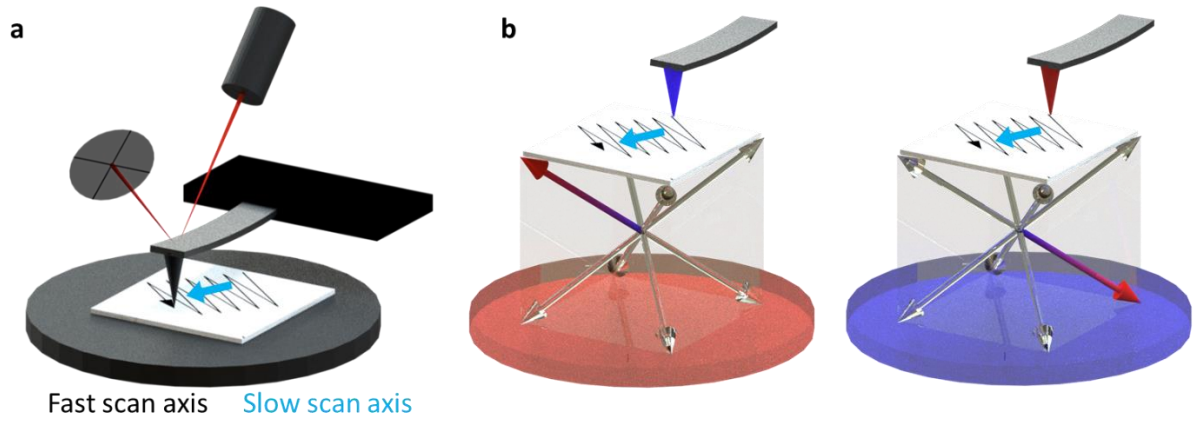

Figure 37 : ***a*** *Fast scan axis of a moving tip (black arrow) and slow scan axis (blue arrow).* ***b*** *Switching of the polarization with a trailing field. The in-plane polarization component becomes parallel to the slow scan axis for positive bias at the bottom electrode (negative voltage at the tip) and antiparallel to it for negative bias at the bottom electrode (positive voltage at the tip).*

An experimental example of such an in-plane switching experiment (Figure 38**a, b**) is shown, with the simultaneously recorded out-of-plane phase and amplitude (Figure 38**c, d)**. It is worth noting that all the PFM images of written areas are actually recorded after the actual switching scan and under application of only a V_{AC} bias.

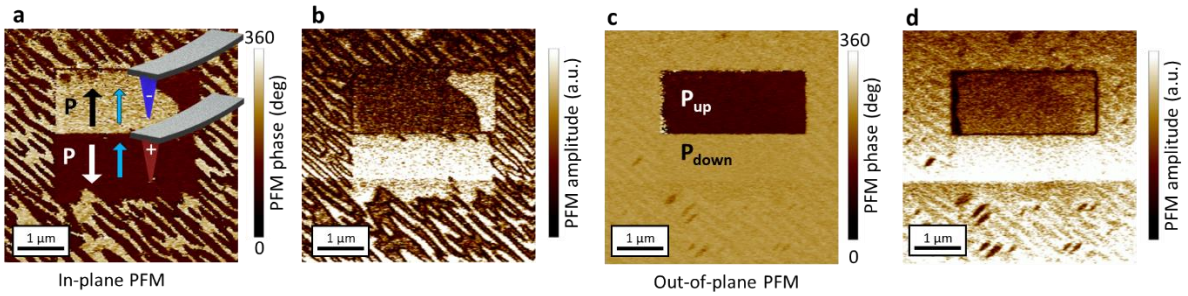

Figure 38 : Illustration of the in-plane control of polarization with the trailing field. ***a*** *In-plane phase and* ***b*** *amplitude,* ***c*** *out-of-plane phase and* ***d*** *amplitude images recorded after trailing the AFM tip first upward (blue arrow in* ***a****) with a positive bias voltage at the bottom electrode (negative voltage at the tip) and then upward on the bottom half of the square with negative voltage at the bottom electrode (positive voltage at the tip).*

2.4.3 Scanning NV magnetometry

The observation of the antiferromagnetic order in real space is a challenging task. High-resolution imaging techniques such as X-ray linear magnetic dichroism resort on large-scale synchrotron facilities, while spin-polarized scanning tip microscopy is operating in cryogenic and/or ultra-high vacuum conditions and only suitable for metallic systems. However, scanning NV magnetometry provides table-top, ambient atmosphere and temperature, high sensitivity magnetic imaging of the stray fields as a powerful avenue to addressing nanoscale spin textures even in antiferromagnets. Indeed, symmetry breaking on surfaces or domain-walls give rise to uncompensated magnetic moments, which can be mapped by magnetic field imaging.

Because of its sensitivity to small magnetic stray fields in the order of a few $\mu\mathrm{T}/\sqrt{\mathrm{Hz}}$, scanning nitrogen vacancy (NV) magnetometry is applied to image the stray fields from antiferromagnetic domains in $BiFeO_3$ thin films. The NV colour centre is a point defect in diamond, where one carbon atom is substituted by a nitrogen atom (Figure 39**a,** red) and one of the neighbouring carbon atoms is missing, creating a vacancy (Figure 39**a,** white). The symmetry of the diamond lattice defines the quantisation axis for the magnetic field $\boldsymbol{B}_{\mathrm{NV}}$ along one of the $\langle 111 \rangle$ directions (Figure 39**b**). For magnetic field sensing applications, a spin triplet state is necessary. This is only realised in the negatively charged NV^- centre. The nitrogen atom is covalently bound to three surrounding carbon atoms (Figure 39**c**). At the site of the vacancy, a spare electron from the nitrogen is naturally present and an additional electron is captured from a neighbouring defect for example. The occupation of the molecular orbital states with the six electrons surrounding the vacancy leads to a total spin $S = 1$ of the NV^- centre (Figure 39**d**).

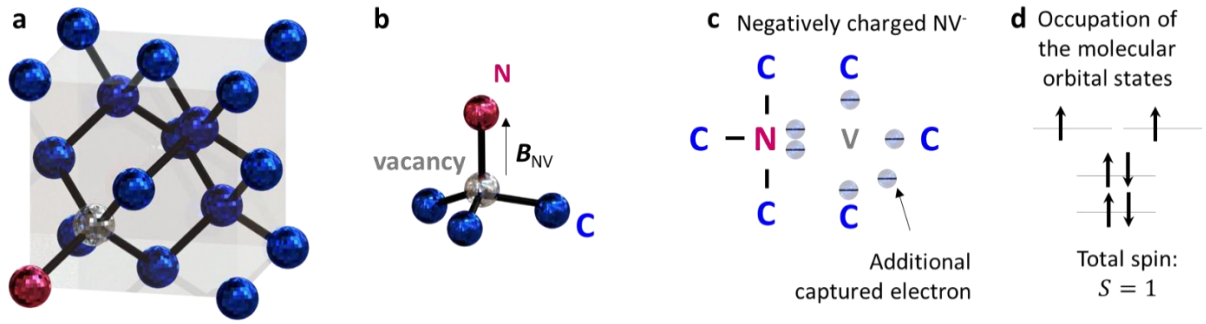

*Figure 39 : **a** Nitrogen-vacancy centre in a diamond lattice. **b** Direction of the magnetic field of the NV-centre. **c** Negatively charged colour centre NV-. **d** Occupation of the molecular orbital states.*

In the absence of a magnetic field, the ground state of this NV colour centre is thus a spin triplet (Figure 40**a**) with a splitting of 2.87 GHz (1.42 GHz) between the $m_s = 0$ and the $m_s = \pm 1$ ground (excited) state. Under off-resonance optical excitation with a green laser at 532 nm, the NV defect is first brought into higher vibronic states and relaxes phonon-mediated to the excited spin triplet state. From here, each of the $m_s = 0$ and $m_s = \pm 1$ excited state recombines radiatively at 637 nm to its respective ground state. However, for the $m_s = \pm 1$ excited state, there exists an alternative non-radiative decay channel over singlet states with a high probability. As a result, the NV defect exhibits a spin-dependent photoluminescence, with the $m_s = 0$ and $m_s = \pm 1$ states considered as the "bright" and "dark" states, respectively. In addition,

while optical transitions are mainly spin conserving, the NV decays preferentially from the metastable spin singlet states to the $m_s = 0$ ground state. Therefore, using optical pumping, the NV is efficiently polarized after a few excitation cycles into the $m_s = 0$ spin sublevel. These two properties enable the optical detection of the magnetic resonance (ODMR) via photoluminescence in an electron spin resonance (ESR) experiment. The system is driven from the $m_s = 0$ ground state to the $m_s = \pm 1$ ground state using a resonant microwave field. When the resonance frequency between the two states is reached the probability for the decay via the "dark" channel is increased and we observe a dip in the photoluminescence at the zero-field splitting frequency of 2.87 GHz (Figure 40**b**).

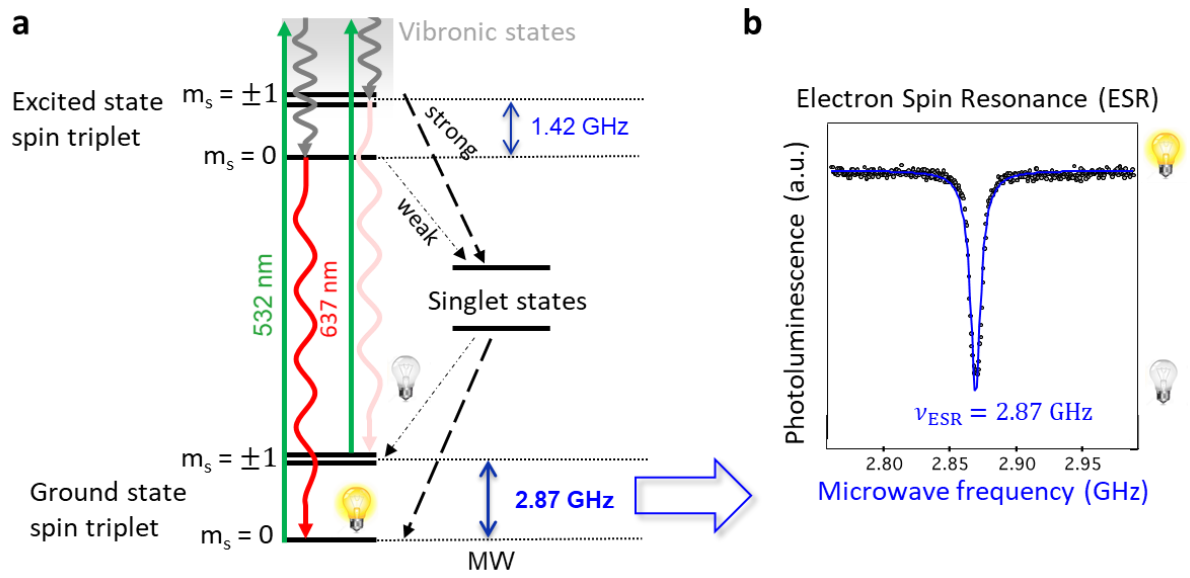

*Figure 40 : Optically detectable magnetic resonance (ODMR) explained with **a**, the electronic level structure of the NV centre and **b**, the optical detection of the electron spin resonance spectrum.*

If the NV centre is exposed to an external magnetic field, the Zeeman splitting of the $m_s = \pm 1$ state (Figure 41**a**) results in two dips observed in the photoluminescence (Figure 41**b**), that are separated by

$$\Delta\nu_{\mathrm{ESR}} = 2\gamma_{\mathrm{NV}} B_{\mathrm{NV}}$$

with $\gamma_{\mathrm{NV}} = 28\ \mathrm{MHz/mT}$, the gyromagnetic ratio of the NV, and B_{NV} the projection of the external magnetic field onto the NV-axis. Hence, by measuring this separation $\Delta\nu_{\mathrm{ESR}}$, we are able to detect external magnetic fields in the order of a few micro Tesla in the proximity of the NV centre.[119–122]

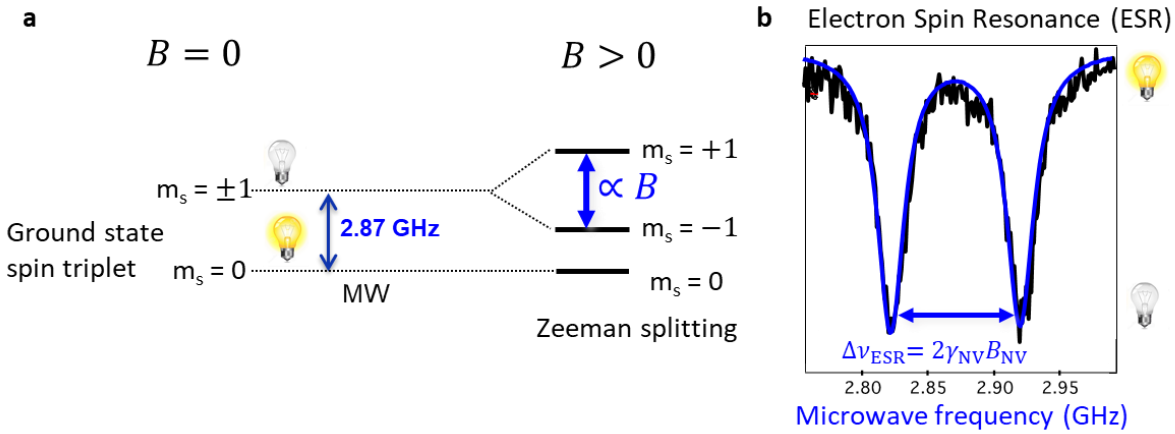

Figure 41 : Magnetic field sensing with a single NV centre. ***a*** *Zeeman splitting of the NV centre ground state in an external magnetic field.* ***b*** *The resulting splitting of the dip in the ESR spectrum is proportional to the external magnetic field.*

In the context of this thesis, we apply NV centre magnetometry to detect the magnetic stray fields above antiferromagnetic thin films. For this purpose, we use a modified AFM setup. In the experiment (Figure 42**b**), the green laser is focussed onto the single NV centre, implemented in an all-diamond single crystalline AFM tip, using a confocal microscope.[123] The photoluminescence from this single NV defect can be seen in Figure 42**a**. An antenna is patterned on the sample surface with lift-off lithography techniques and generates the GHz microwave field while we scan the surface of the sample in its proximity. Two imaging modes (Figure 42**c**) are available. In the so-called "Full B" mode, the whole broadband ESR spectrum is recorded for each point and we can quantitatively calculate the magnetic stray field projected onto the NV-centre axis. Prior to this experiment, the orientation of the NV-axis in the diamond tip is determined in a calibration measurement. In the second and faster acquisition "Iso-B" imaging mode, the intensity difference of the photoluminescence, recorded for two fixed microwave frequencies at the FWHM of the ESR, is monitored while we are scanning over the sample. The variation of the magnetic field sign is mapped in this mode. The experiments are performed with a NV-to-sample distance around 50-60 nm. Since we examine magnetic stray fields from antiferromagnetic samples in the weak-magnetic field regime for external fields smaller than 5 mT, these imaging modes can be used. Additionally, a bias magnetic field of 2 mT needs to be applied along the NV quantization axis to obtain a linear dependence of the microwave frequency on the external field (and to be able ascribing + or – sign to B, minor detail). More information about the behaviour of the NV centre in an external magnetic field can be found in reference [[122]].

All the scanning NV magnetometry experiments presented in this manuscript were carried out at the Laboratoire Charles Coulomb during the joint PhD thesis of Angela Haykal, supervised by Vincent Jacques.

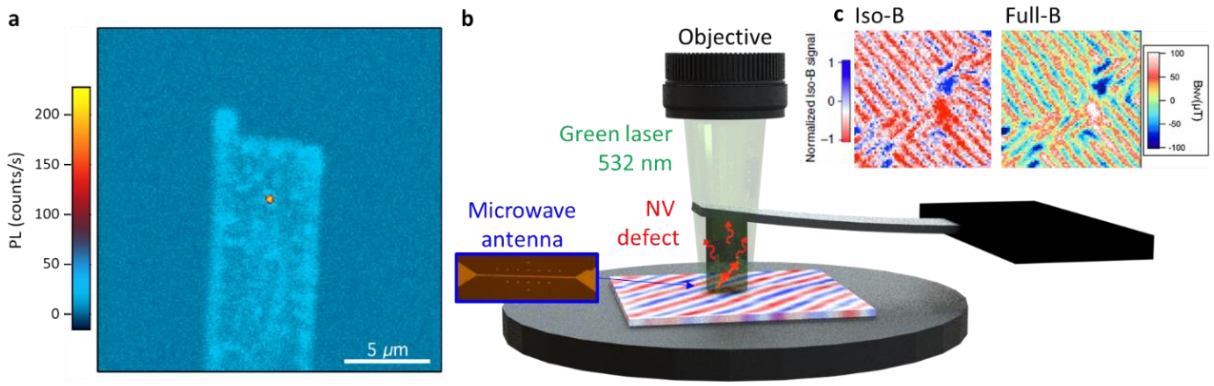

*Figure 42 : **a** Photoluminescence (PL) of a single NV centre embedded in the diamond AFM tip. **b** Scanning NV-centre magnetometer set-up. **c** Example of the two different imaging modes.*

2.5 Resonant elastic X-ray scattering

Polarized X-rays in the soft energy range can be employed to investigate magnetic structures in the samples. The measurements shown in this thesis are performed at the SEXTANTS beamline[124] of the SOLEIL synchrotron with nearly fully circular left and right polarised X-ray light, using the RESOXS diffractometer[125] in reflectivity geometry (Figure 43). The typical photon flux is 10^{13} s^{-1} with an energy resolution of 100 meV. The diffraction patterns in reciprocal space are recorded with a charge-coupled device (CCD) camera. Beam-stops in front of it are used to block the specular beam, the intensity of the unwanted strong Bragg reflections, or peaks arising from the atomic steps on the surface for example. By tuning the incoming photon energy in resonance with the absorption edge of a specific atom, one can select the response of a specific chemical element in the sample. Resonant elastic X-ray scattering (REXS) measurements are performed at the O K edge in order to study the striped domains arising from elastic crystalline deformations related to ferroelectric domains and the domain walls in between them (Figure 43**a**). The antiferromagnetic signal of $BiFeO_3$ is detected at the Fe L edge (Figure 43**b**). In the example, shown here, of a sample containing two spin cycloids propagating in perpendicular directions, two diagonal pairs of diffraction spots are observed at an angle of 90° one to the other. More precisely, at each step, two consecutive images with circular left (CL) and circular right (CR) polarized light are measured. To generate the dichroism image, the difference between the diffraction intensities for CL and CR is calculated and normalized by the polarization independent intensity, CL+CR, as shown in Figure 43**c**. Here for simplification an example from a sample containing one single cycloid is shown.

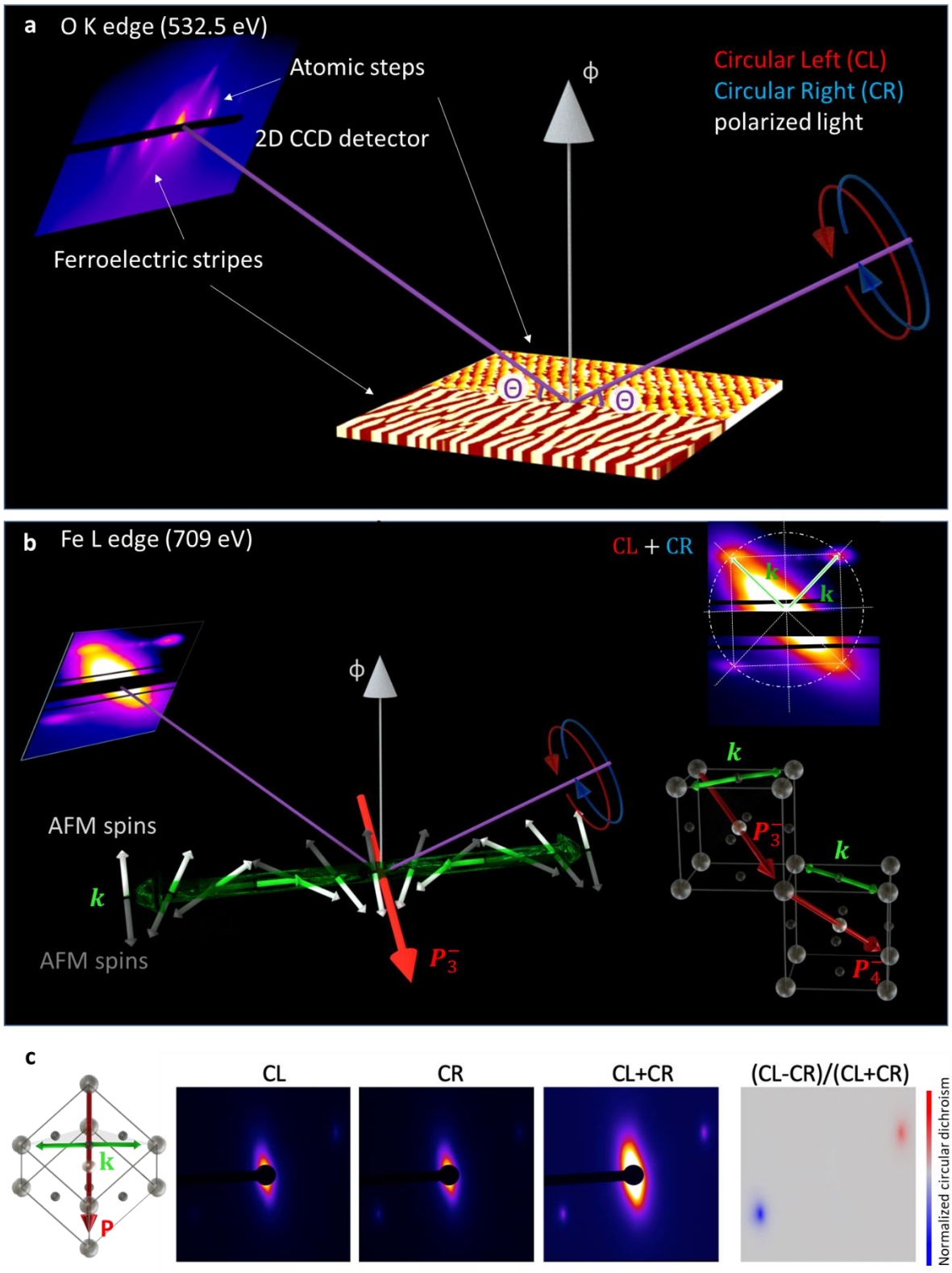

*Figure 43 : Resonant elastic X-ray scattering experiment at **a** the oxygen K edge to investigate the structural/ferro-electric domains and domain walls and **b** at the iron L edge to determine the magnetic properties of the sample, such as the spin cycloid in $BiFeO_3$. **c** Normalization of the dichroic pattern to determine the circular dichroism (blue and red contrast in the last picture) at the iron L edge. Example shown for a single cycloid propagation direction.*

REXS is used as a complementary method to scanning NV magnetometry to macroscopically identify the propagation vector $\boldsymbol{k}$ and the wavelength of the spin cycloids in our $BiFeO_3$ thin

films and determine their rotation planes. The intensity I of the scattered photons measured in the diffraction experiment for a scattering vector $\boldsymbol{Q}$ depends on the scattering amplitude f_n for each single atom at position $\boldsymbol{r}_n$

$$I(\boldsymbol{Q}) \propto \left|\sum_n f_n e^{i\boldsymbol{Q}\boldsymbol{r}_n}\right|^2.$$

In resonant electrical dipole scattering conditions, the scattering amplitude can be written as

$$f_n = f_0(\hat{\boldsymbol{e}} \cdot \hat{\boldsymbol{e}}') - i f_1(\hat{\boldsymbol{e}} \times \hat{\boldsymbol{e}}') \cdot \boldsymbol{m}_n + f_2(\hat{\boldsymbol{e}}' \cdot \boldsymbol{m}_n)(\hat{\boldsymbol{e}} \cdot \boldsymbol{m}_n),$$

where $\hat{\boldsymbol{e}}$ and $\hat{\boldsymbol{e}}'$are the polarization vectors of the incident and scattered X-rays, respectively, and $\boldsymbol{m}_n$ is the local magnetization unit vector. f_0, f_1 and f_2 are the photon energy dependent resonance factors, used to describe the atomic excitation and decay processes. The first term is independent of the magnetization and expresses the scattering from the O or Fe charge distribution, i.e. the crystal structure. The second term is analogous to the circular dichroism term in absorption, containing the resonance factor for a magnetic dipole and can be used to probe ferromagnetic structures. In antiferromagnets, however, those contributions cancel out due to the opposite sign of the magnetic moments and only the last term, quadratic in $\boldsymbol{m}$ and analogous to linear dichroism in absorption is probed here at the Fe L-edge. The magnetization profile can be reconstructed for regular domain patterns since the lateral domain periodicity leads to a purely magnetic superstructure around the specular reflected beam. In other words, in our case, the first term only contributes to the specular spot and from the splitting of the surrounding peaks we can directly analyse the properties of the cycloid. Each cycloid corresponds to a pair of diffraction spots at $\pm q$ in reciprocal space with opposite dichroic contrast, as they are chiral objects. The wavelength λ of the cycloid for an antiferromagnetic material can be calculated from the distance $2q$ between the two spots as

$$\lambda = \frac{2\pi}{q}.$$

Dichroism can be detected at the Fe L-edge, since the magnetization is a parity even and time-odd observable and CL and CR polarized light tackle the time reversal symmetry. In contrast, no circular dichroism is expected to arise from the electric polarization, as $\boldsymbol{P}$ is time even and parity odd and there should be no difference between CL and CR.[126] However, in recent experiments [[127]] dichroism, indicating chiral electric textures at the domain walls in $BiFeO_3$ thin films, was found at the O K edge and can only be explained by contributions from the orbital quadrupole moments f_2 of the scattering amplitude. Hence, it is worth noting that, in synchrotron experiments, the electric polarization, arising from orbital deformations due to spin-orbit coupling, can be probed at the oxygen K-edge and contains information about the polarization at the domain walls for example.

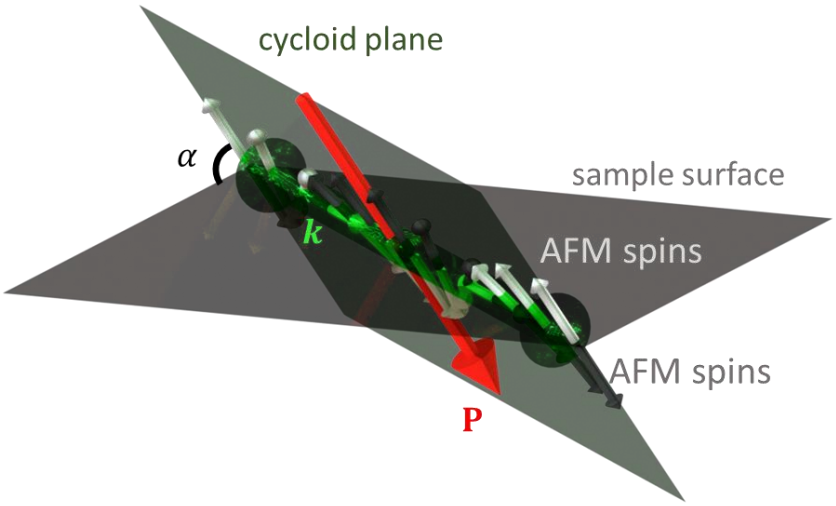

Figure 44 : Visualisation of the angle α between the sample surface and the rotation plane of a cycloid propagating along $\boldsymbol{k}$.

The propagation direction $\boldsymbol{k}$ of the cycloid does not provide information about the cycloid plane and its angle α to the sample surface (Figure 44). In an ideal picture as for bulk $BiFeO_3$, shown in Figure 44, it is spanned up by $\boldsymbol{k}$ (transparent green arrow, containing the AFM ordered black and white spins) and the polarization $\boldsymbol{P}$ (red arrow). Additional modifications induced by strain or electrical boundary conditions (depolarizing field) in the films can further influence the tilt of the cycloidal plane and an experimental observation is therefore highly desired. To access the cycloid rotation plane, we need to record a series of diffraction patterns at different azimuthal angles φ. In Figure 45, this experiment is sketched for a (111) $BiFeO_3$ sample where the polarization direction is vertical, $\boldsymbol{k}$ lies in the film plane and the cycloidal propagation plane is vertical. The intensity of the dichroic pattern is proportional to the projection of the helicity of the circular polarized light on the cycloidal plane. Therefore, the variation of the intensity vs. the φ rotation provides information about the cycloidal plane.

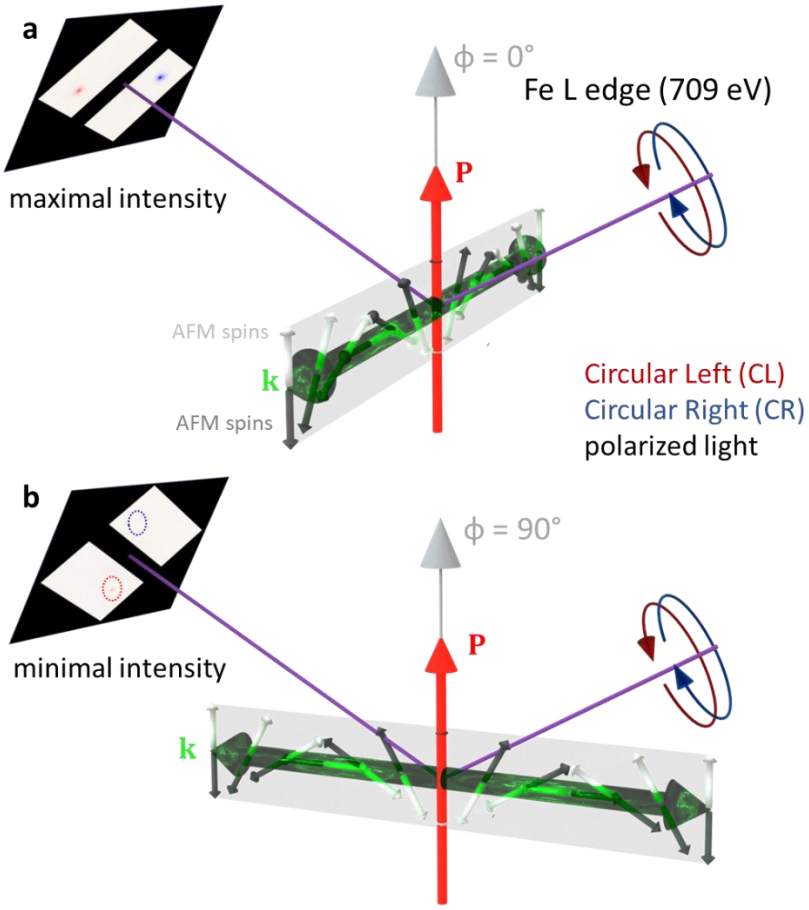

Figure 45 : Circular dichroism measured at the Fe L-edge for different azimuthal orientations Φ, illustrated for a (111) $BiFeO_3$ sample with polarization perpendicular to the sample surface and a cycloid propagating along k in the film plane. The image on the detector is the calculated normalized dichroism. ***a*** *Maximal intensity in the diffraction pattern and horizontal spots,* ***b*** *minimal intensity and vertical spots (dotted circles indicate the positions).*

3 Structural and ferroelectric properties of $BiFeO_3$ thin films

In $BiFeO_3$, the polarization can point in any of the diagonals of the pseudo-cubic unit cell, resulting in eight possible ferroelectric domain configurations. Consequently, depending on the growth conditions, the substrate crystal symmetry and its orientation, the ferroelectric domains in $BiFeO_3$ thin films can either form complex mosaic patterns, regular stripes or single domains. In this chapter, I will describe how by optimizing the growth conditions of these films, I successfully obtain two-polarization-variant striped-domain patterns for a wide range of epitaxial strain or single as-grown domains for another crystal orientation. Finally, in agreement with predictions by our theoretician colleagues, I will show that temperature can be used as a powerful tool to either control the ordering of these domains from a labyrinthine structure to a perfectly-ordered striped domain structure or to transform mosaic domains into striped-domains.

3.1 Mosaic vs. striped domains

The selection of two ferroelectric domain variants due to electric boundary conditions and substrate symmetry in $BiFeO_3$ $(001)_{pc}$ films does not directly result in a perfectly striped pattern. The growth dynamics related to the ensemble of the growth parameters during the PLD process has a very sensitive impact on the ordering of the actual domain pattern at the sample surface. Even though the perfectly striped domain arrangement is theoretically supposed to be the ground state, various labyrinthine patterns with different degrees of ordering or even mosaic domain patterns can be obtained.

The surface of each sample is imaged with PFM after the growth process. A vectorial PFM analysis is necessary to determine the three-dimensional polarization directions. Here we focus on two examples containing $\mathbf{P}_3^-$ and $\mathbf{P}_4^-$ ferroelectric domains. Figure 46 shows a striped sample grown with an excimer laser. In Figure 47, a sample from the Nd:YAG laser growth chamber with the same ferroelectric domains, but ordered in a mosaic pattern, is presented. An AFM topography image is recorded simultaneously in each PFM scan. In contrast to the imprint of the atomic steps of the substrate on the film surface in the first example (Figure 46**a**), the surface roughness is increased in the latter (Figure 47**a**), indicating a tilting of the $BiFeO_3$ unit cells and lower ordering of the domains. From the bright phase in the out-of-plane PFM scan (Figure 46**b** and Figure 47**b**), we conclude that out of the eight possible directions represented by the arrows in the cube, only the four ones pointing downwards ($\boldsymbol{P}_1^-$, $\boldsymbol{P}_2^-$, $\boldsymbol{P}_3^-$, $\boldsymbol{P}_4^-$) can be present (red colour in Figure 46**b** in the sketch). Whereas in the striped sample the amplitude is high everywhere (Figure 46**b**), the rough topography influences the amplitude of the mosaic one (Figure 47**b**) resulting in less defined spots. In a next step, we combine the out-of-plane PFM signal with at least two in-plane PFM images recorded at different azimuthal angles, as presented in the sketches in Figure 46**c**-**d**. From the dark phase and well defined amplitude in the in-plane signal (Figure 46**c** and Figure 47**c**), the two domains pointing to the right of the tip ($\boldsymbol{P}_1^-$, $\boldsymbol{P}_2^-$) can be eliminated. To complete the picture, a scan from another in-plane position (Figure 46**d** and Figure 47**d**) shows, that in all stripes/patches with dark contrast the polarization direction is $\boldsymbol{P}_3^-$ and in every bright zone it is $\boldsymbol{P}_4^-$. In the amplitude images of Figure 46**d** and Figure 47**d**, the dark lines correspond to domain walls. At the transition from a domain

pointing to one side of the cantilever to the other, no PFM response is detected, corresponding to 71° domain walls.

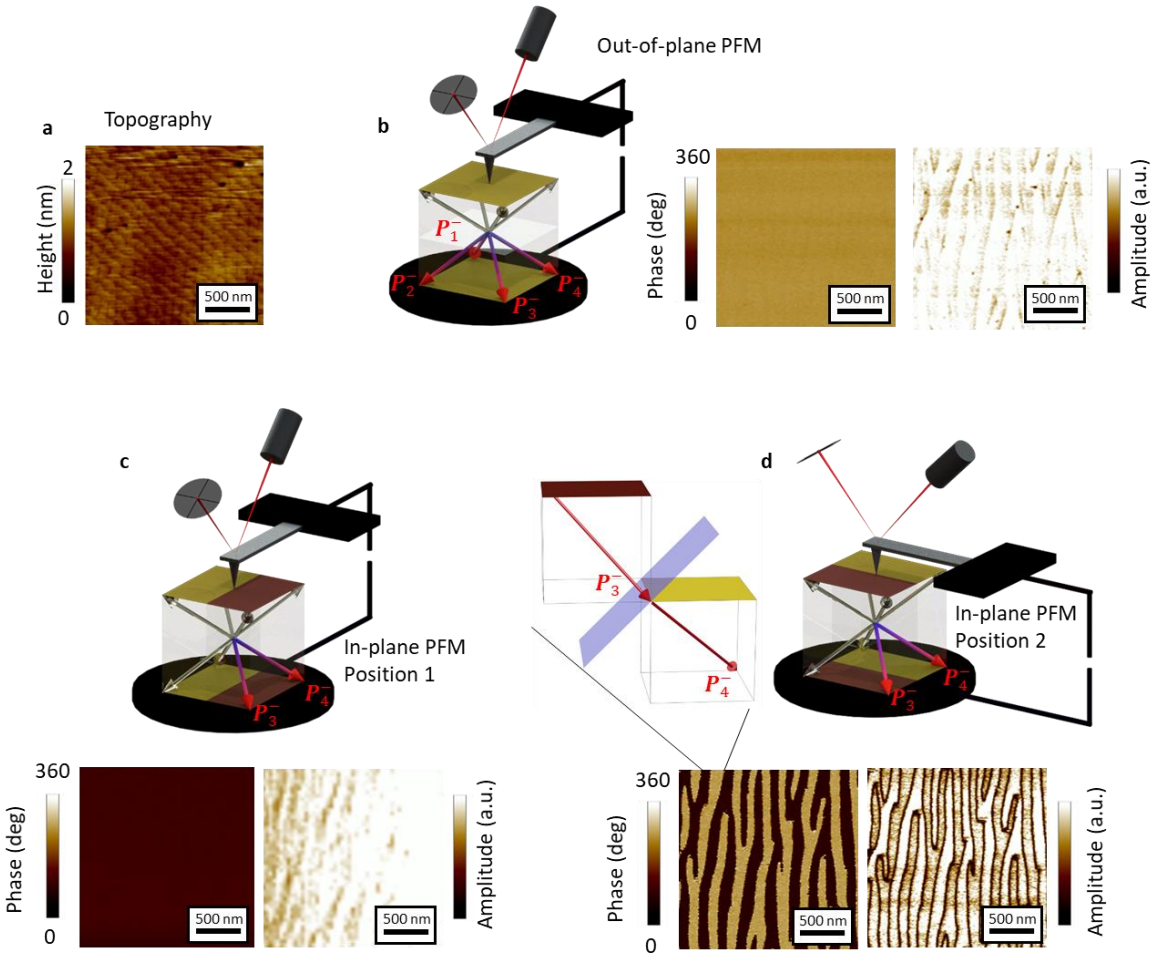

Figure 46 : Vectorial PFM analysis of a striped $BiFeO_3$ thin film grown on $DyScO_3(110)_o$ with an excimer laser. ***a*** *Surface topography,* ***b*** *out-of-plane PFM phase and amplitude,* ***c, d*** *in plane PFM phase and amplitude for two different probe-to-sample configurations, show* $\mathbf{P}_3^-$ *and* $\mathbf{P}_4^-$ *polarization directions.*

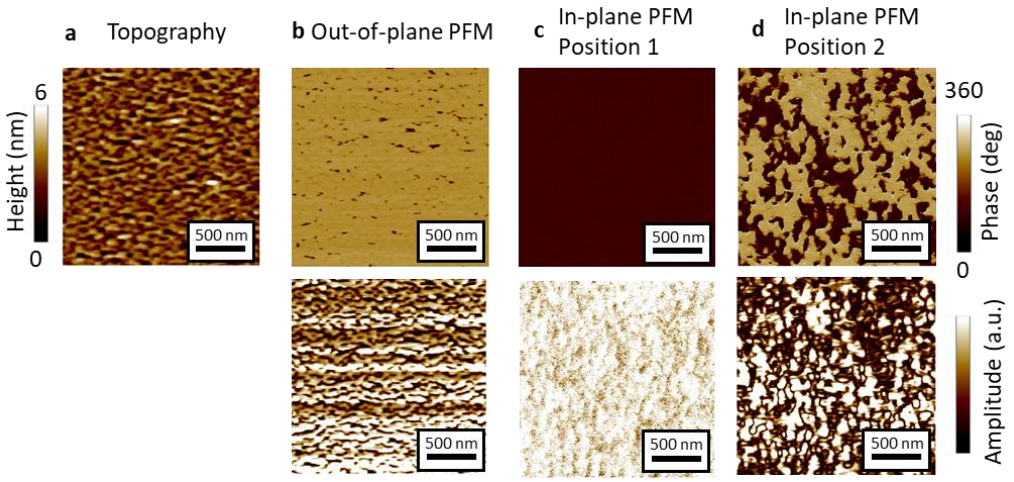

Figure 47: Vectorial PFM analysis of a $BiFeO_3$ thin film grown on $DyScO_3(110)_o$ with a Nd:YAG laser. ***a*** *Surface topography,* ***b*** *out-of-plane PFM phase and amplitude,* ***c, d*** *in plane PFM phase and amplitude for two different probe-to-sample configurations, show as well* $\mathbf{P}_3^-$ *and* $\mathbf{P}_4^-$ *polarization directions, but ordered in a mosaic pattern.*

This gives a first idea that $BiFeO_3$ thin films, fabricated via pulsed laser deposition in our lab, are crucially different depending on the laser that has been used for their growth. Whereas for samples fabricated with the KrF excimer laser, the crystalline quality of the film approaches that of the substrate in a layer by layer growth (Figure 46**a**), the mosaic spread in the samples grown with the Nd:YAG laser is much higher (Figure 47**a**).[109,80] The morphological difference is accompanied by striped ferroelectric domains vs. a mosaic ferroelectric pattern but with the same two polarization variants pointing downwards in both cases.

We conduct a comparative study of the strain and strain-gradients in KrF excimer and Nd:YAG grown samples in collaboration with Daniel Sando, combining X-ray diffraction with high-angle annular dark field images, taken with a scanning transmission microscope. A detailed analysis of the crystallographic structure using X-ray diffraction is presented first. See chapter 2.3 for details on the measurement technique and note that monoclinic notation is used in this paragraph to be in accordance with the following measurements in this chapter. However, for the moment the distortion about the angle β is not in the focus of the investigation. One can assume nearly pseudo-cubic cells in this paragraph, for example, when comparing to similar data shown in reference [[128]]. The results, presented here in Figure 48, are measured on very similar samples like the afore mentioned stripy (excimer laser) and the mosaic (Nd:YAG laser) sample in the PFM measurements. For both samples, the 2θ-ω scan (Figure 48**a**) demonstrates a single-phase growth. Note also that the $BiFeO_3$ film peaks in the excimer-grown sample remain narrow and maintain their intensity even at higher diffraction orders, compared to the Nd:YAG-grown sample, where the BFO film peaks become progressively broader and less intense upon increasing order. The rocking curves (Figure 48**b**) around the monoclinic $(002)_{\mathrm{m}}$ reflection of $BiFeO_3$ show a full width at half maximum (FWHM) of 0.02° and 0.16° for the stripy and the mosaic sample, respectively. They differ by almost one order of magnitude, revealing a level of crystalline perfection approaching that of the substrate for the first and a pronounced stronger crystalline mosaicity of the latter. The Williamson-Hall plots[115,116] (Figure 48**c**), giving an estimate of the average strain gradient in the out-of-plane direction, demonstrate an almost zero inhomogeneous strain ($\varepsilon_i = 0.03\ \%$) for the stripy sample. However, the value for the mosaic one yields a significantly larger value of inhomogeneous strain of $\varepsilon_i = 0.25\ \%$. Finally, the reciprocal space maps around the monoclinic $(003)_{\mathrm{m}}$ and $(013)_{\mathrm{m}}$ $DyScO_3$ substrate reflections (Figure 48**d**) are used to analyse the in-plane lattice. Whereas the $BiFeO_3$ $(003)_{\mathrm{m}}$ peak is one well defined spot for the excimer laser sample, a horizontal splitting is observed for the Nd:YAG laser sample, being the result of a tilting of the $(00l)$ lattice planes in two different directions.[113,129] Around the $(013)_{\mathrm{pc}}$ $DyScO_3$ substrate peak, two film peaks reveal in both cases two monoclinic domains, $(\bar{1}13)_{\mathrm{m}}$ and $(113)_{\mathrm{m}}$. However, their arrangement is different: the peaks observed in the excimer laser sample are split along the Q_z direction establishing evidence for a coherently strained film in the stripy sample, whereas the domains are separated horizontally, implying again the formation of tilted domains through the strain accommodation process when grown with the Nd:YAG laser.

In other words, both films are coherently strained to the substrate. However, in the case of growth with the Nd:YAG laser, the shift of the film peaks to smaller angles than the substrate peaks in the 2θ-ω scan (blue curve in Figure 48**a**) could potentially indicate a slight relaxation

along the out-of-plane direction. But a strain accommodation via tilting is observed from the reciprocal space maps (Figure 48**d**) and confirmed by the slope in the Williamson-Hall plot (blue curve in Figure 48**c**). The reason for the formation of mosaic domains is very likely related to the faster growth rate and an interfacial strain gradient, formed in the first grown unit cells, influencing the structure of the whole film. This leads to a decoupling of the film from the substrate, preventing long-range order and inducing mosaic domains.[128]

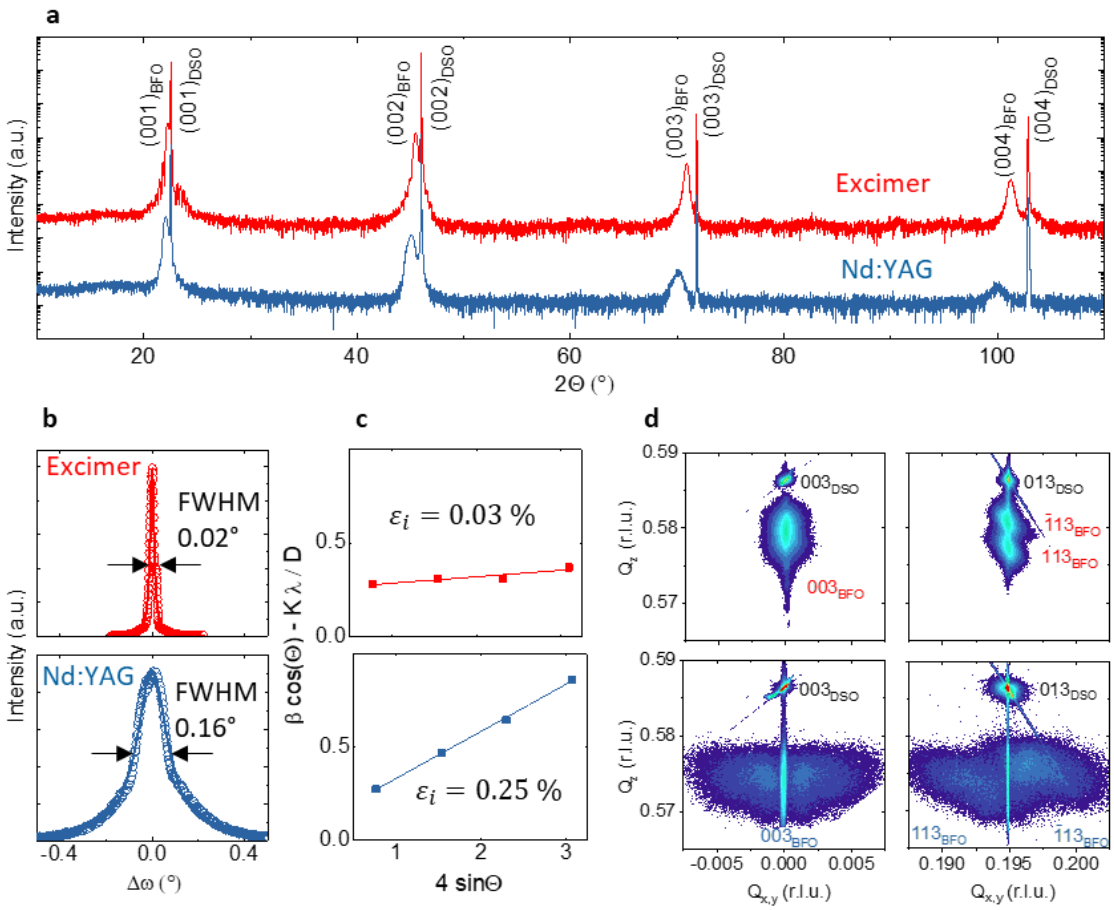

Figure 48 : Structural properties of $BiFeO_3$ films grown by the KrF excimer laser and the Nd:YAG laser. ***a*** *2Θ-ω scans,* ***b*** *rocking curves,* ***c*** *Williamson-Hall plots and* ***d*** *reciprocal space maps.*

In addition to the X-ray diffraction study, high-angle annular dark field images are taken with a scanning transmission electron microscope (Figure 49). While the out-of-plane and in-plane strain are homogeneous for the stripy sample (Figure 49**a**-**c**), the out-of-plane strain decreases in the first 2-3 nm to -1.5%, before increasing to ≈1.5% at about 6 nm away from the interface for the mosaic sample (Figure 49**d**-**f**). Electron energy loss spectroscopy results are consistent with this scenario and point out, that the strain change does not originate from stoichiometry, but from the different oxygen coordination at the interface, which change the distortion of the oxygen octahedra and hence the polarization displacement.[128]

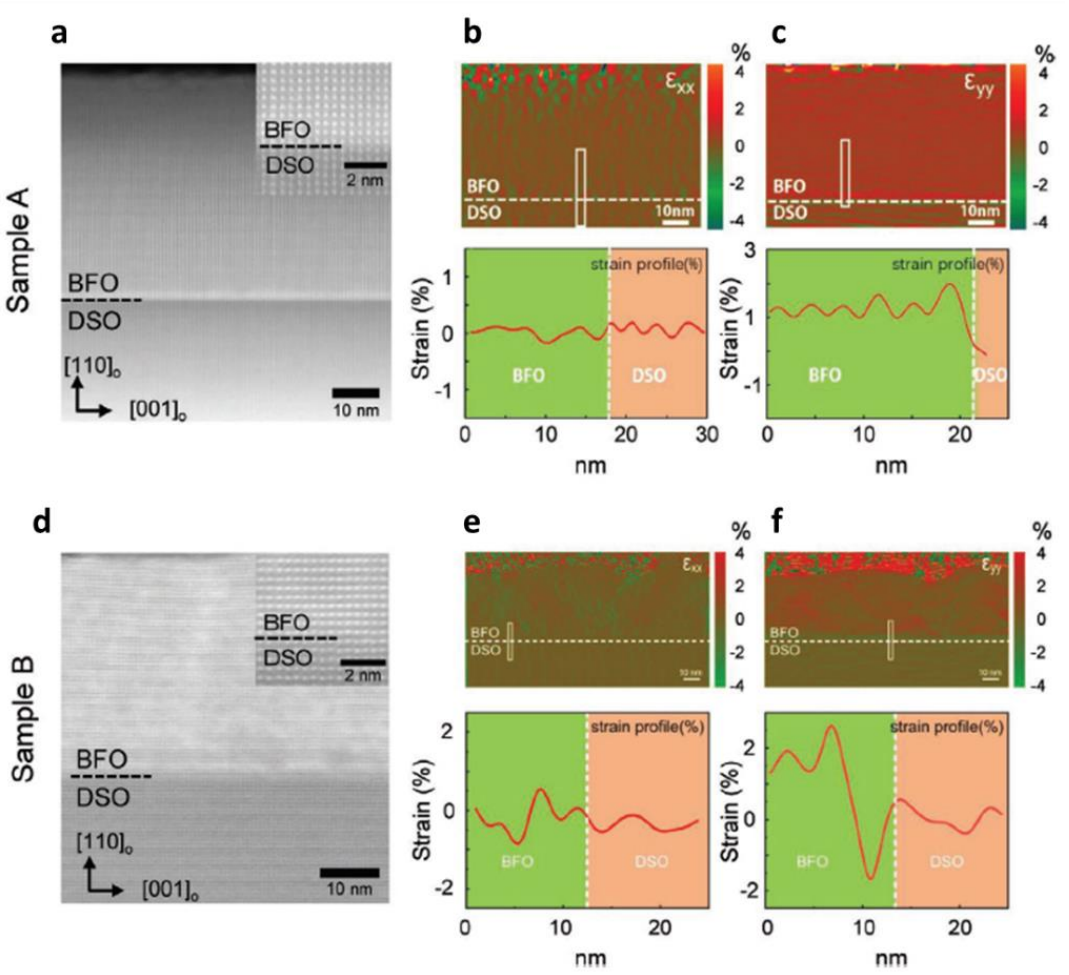

Figure 49 : Determination of strain profiles by HAADF-STEM imaging. ***a–c*** *HAADF image, in-plane strain (ε_{xx}), out-of-plane strain (ε_{yy}) and corresponding line profiles of marked areas for sample A (excimer).* ***d–f*** *HAADF image, in-plane strain (ε_{xx}), out-of-plane strain (ε_{yy}) and corresponding line profiles of marked areas for sample B (Nd:YAG). Adapted from [128].*

3.1.1 Optimization of the growth parameters for $BiFeO_3$ thin films

I have elaborated $BiFeO_3$ thin films in four different growth chambers during my thesis. The results come from two different KrF excimer lasers (from one of them two growth chambers are connected) and one Nd:YAG laser. More details about the mosaic films are given in paragraph 3.3.3, when a transition to the striped domain pattern is presented. In the following, I want to investigate the influence of the misfit strain on magnetic properties of ferroelectric stripe domains in $BiFeO_3$ thin films. To this end, I first optimize the growth parameters with the KrF excimer laser separately, using orthorhombic $DyScO_3$ $(110)_o$ and $SmScO_3$ $(110)_o$ substrates, and then apply these parameters for the deposition on $GdScO_3$ $(110)_o$, $TbScO_3$ $(110)_o$, and $NdScO_3$ $(110)_o$ and cubic $SrTiO_3$ (001) substrates to compare the influence of different strain levels.

This work started based on growth parameters which had previously been optimized for $BiFeO_3$ on orthorhombic $DyScO_3$ $(110)_o$ substrates using two different lasers by Hélène Béa[80], Cécile Carrétéro[109] and Daniel Sando[102]. They are listed in Table 3.

Table 3 - Pulsed laser deposition parameters for the growth of $BiFeO_3$ on $DyScO_3$ using two different lasers.

Laser	**Excimer laser**	**Nd:YAG laser**
Temperature	660°C	600°C
Pressure	0.36 mbar	0.01 mbar
Laser wavelength	248 nm (KrF)	355 nm (frequency-tripled)
Energy per pulse	50 - 80 mJ	100 mJ
Laser repetition rate	2 Hz	2.5 Hz
Distance substrate/target	56 mm	44 mm

To optimize the stripe pattern, I studied the influence of the laser energy and then the growth temperature in three different deposition chambers. One of them, a newer growth chamber, is connected to a cluster, where other experiments can be conducted in situ in the future. My goal is to obtain $BiFeO_3$ thin films with atomic steps on the surface and a parallel stripe pattern of the ferroelectric domains. To analyse the quality of the thin films, the AFM topography image is presented in combination with only one PFM in-plane phase image. The out-of-plane PFM phase is always homogeneous and only two ferroelectric variants are present, forming 71° domain walls with polarization pointing downwards for the $(001)_{pc}$ $BiFeO_3$ thin films. As a non-magnetic bottom electrode, we chose $SrRuO_3$ as its cubic structure, with a lattice parameter of 0.3985 nm, is well matched to the substrates and $BiFeO_3$. A detailed table with all the lattice parameters is given in Chapter 2.1. The growth parameters for the $SrRuO_3$ electrode that I used during my thesis on all different substrates had also been optimized by my colleagues before and are listed in Table 4.

Table 4 - Pulsed laser deposition parameters for the growth of $SrRuO_3$ electrode using two different lasers.

Laser	**Excimer laser**	**Nd:YAG laser**
Temperature	650°C	700°C
Pressure	0.2 mbar	0.2 mbar
Laser wavelength	248 nm (KrF)	355 nm (frequency-tripled)
Energy per pulse	60 mJ	60 mJ
Laser repetition rate	5 Hz	2.5 Hz
Distance substrate/target	56 mm	44 mm

Influence of the laser energy vs temperature

For $BiFeO_3$ growth with a low surface roughness and the formation of a striped ferroelectric domain pattern it is crucial to optimize the laser energy. This is shown in Figure 50 by increasing the energy from 60 to 120 $\mathrm{mJ/pulse}$. As this affects the growth rate, the number of pulses was decreased at the same time in order to keep the same film thickness. Importantly, a film grown with the optimized parameters from the previous chapter (Table 3, Figure 46) cannot be reproduced easily some time later (Figure 50**a**, **f**) and re-optimization is necessary. Changes in the growth chamber, i.e. continuous adsorption of material on the chamber window in front of the pyrometer and laser maintenance, replacing components in the laser beam path and therefore

changes in the properties of the arriving pulse at the target or replacements of the calorimeter and changes in its position can be inferred as possible reasons.

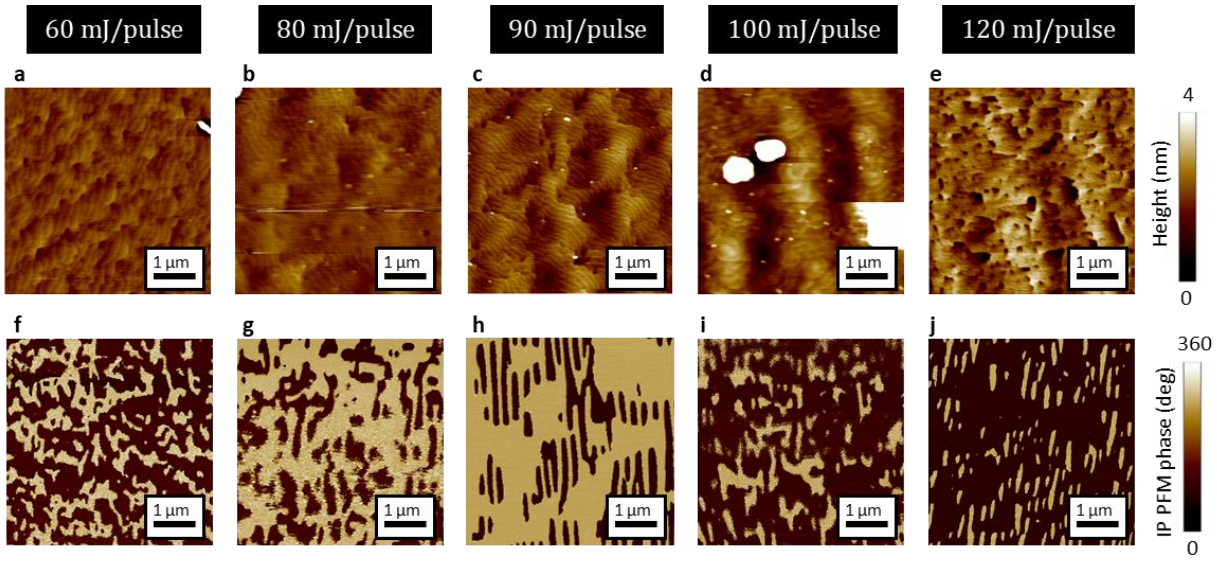

*Figure 50: $BiFeO_3/SrRuO_3$ heterostructures deposited on $DyScO_3(110)_o$ while increasing the laser energy per pulse for $BiFeO_3$. **a-e** Topography, **f-j** in-plane PFM phase.*

Figure 51 shows the influence of the growth temperature on the morphology and domain structure of the films. The stripe pattern and the surface roughness degrade abruptly at the decomposition temperature of 700°C into parasitic phases (Figure 51**c**, **f**). Furthermore, the atomic steps of the sample grown at 680°C are more regular (Figure 51**b**) than to the one at 660°C (Figure 51**a**). This shows that the optimal results are obtained just below the decomposition temperature. Unfortunately, the temperature precision is limited by the thermal transfer from the sample holder via the silver paste. On samples heated with the same power, I obtain a scattering of the temperature values by ±10°C, being in the same range as the temperature window for optimal growth. The controllability of the temperature can be a big issue in the growth optimization. Improving this point would be crucial for a more systematic study.

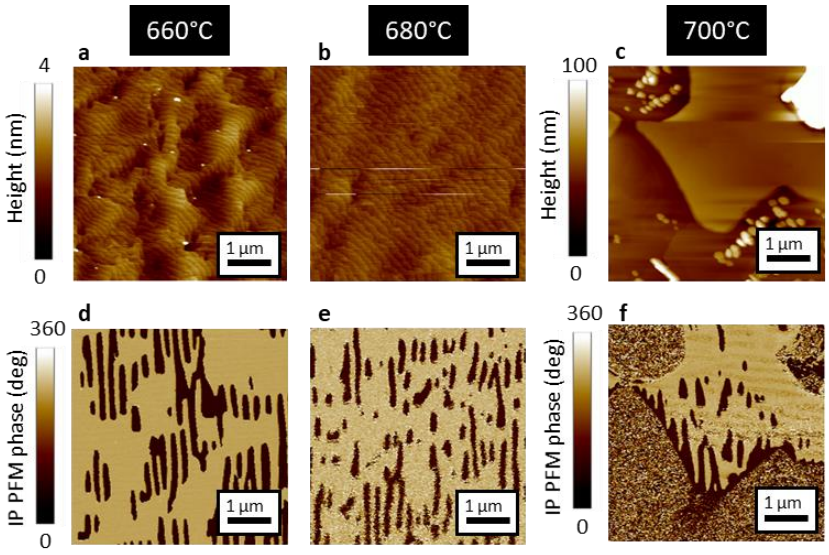

Figure 51: $BiFeO_3/SrRuO_3/DyScO_3(110)_o$ multilayers: increasing the growth temperature for the $BiFeO_3$ thin film. ***a-c*** *Topography,* ***d-f*** *in-plane PFM phase.*

Influence of the target-to-substrate distance and laser energy in another growth chamber

In our lab, a modern cluster with two PLD growth chambers connected to an excimer laser, a sputtering machine and an X-ray photoemission spectroscopy chamber became available during the second part of my thesis. I initially tested both PLD chambers to finally choose one for the growth of $BiFeO_3$. As the geometry of each growth chamber is different, the target-to-substrate distance needs to be re-examined. In one chamber, even for the highest possible energy, the domain pattern was very labyrinthine, whereas in the other one, the samples showed already promising results with the initial growth parameters. Therefore, I will only show results obtained in this second chamber.

By reducing the target-to-substrate distance, it is possible to avoid small droplets (Figure 52**a-c**) and obtain a stripy pattern in the in-plane PFM phase (Figure 52**d-f**). However, large droplets are still present at the surface (Figure 52**c**) and further optimization of the other growth parameters is required.

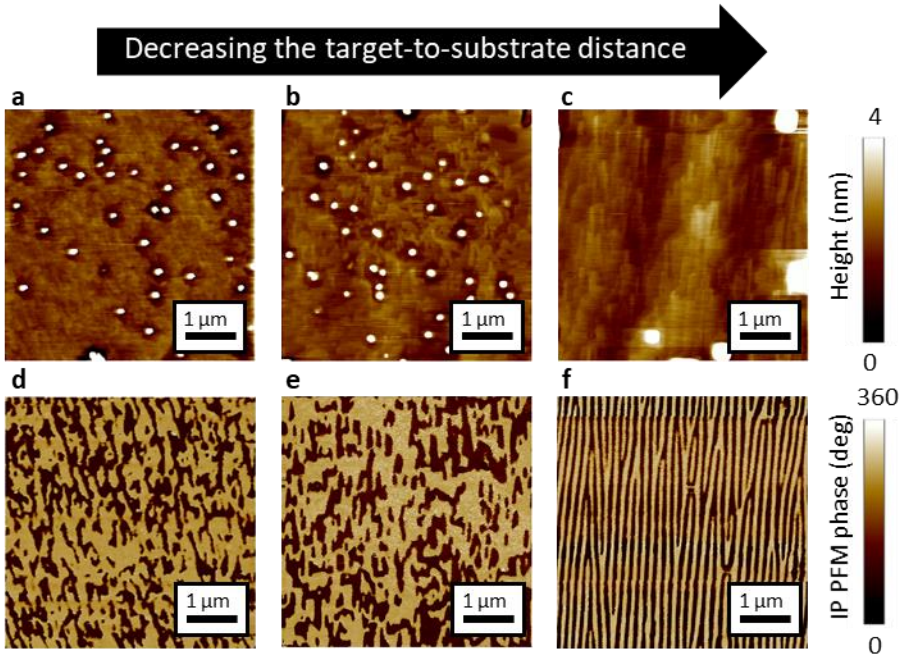

Figure 52 : $BiFeO_3/SrRuO_3$ heterostructures deposited on $DyScO_3(110)_o$ while decreasing the target-to-substrate distance. ***a-c*** *Topography,* ***d-f*** *in-plane PFM phase. The target-to-substrate distance is decreased by 1.5 cm at each step.*

As a next step, I decrease the energy per pulse (Figure 53, decrease of 5 mJ/pulse at each step) as I had started with the maximal energy of 75 mJ/pulse. Unfortunately, this is not the route to avoid droplets. In addition, the stripe domain pattern becomes less prominent.

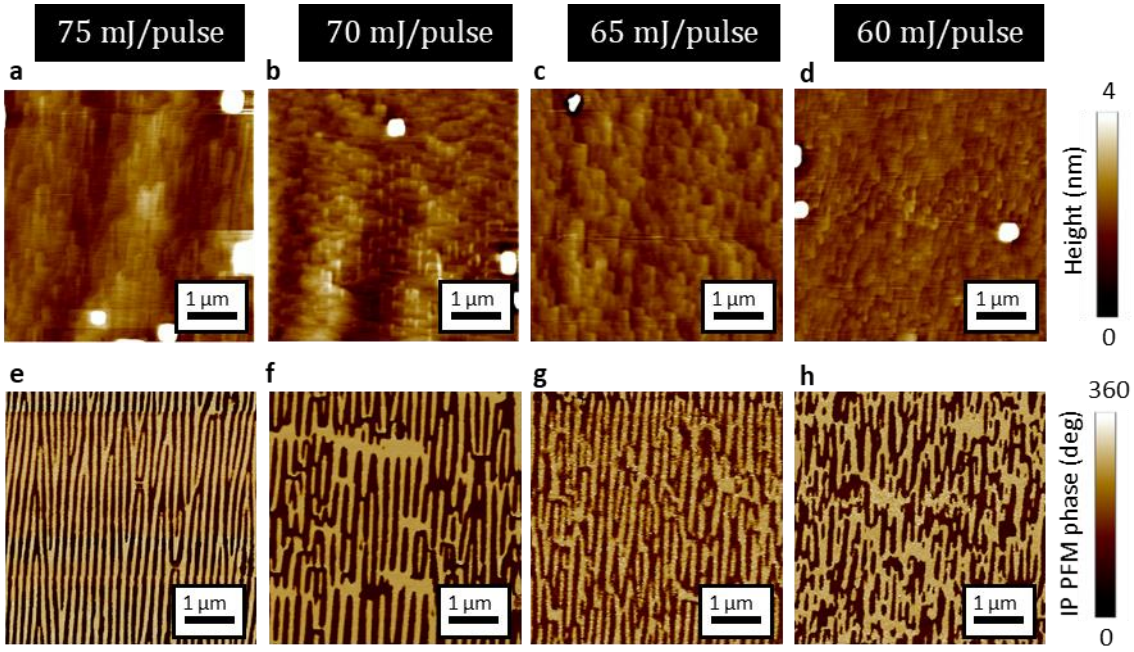

Figure 53: $BiFeO_3/SrRuO_3$ heterostructures deposited on $DyScO_3(110)_o$ while decreasing the laser energy per pulse for $BiFeO_3$. ***a-e*** *Topography,* ***f-j*** *in-plane PFM phase.*

Influence of the film thickness

By varying the thickness of $BiFeO_3$ under the same growth conditions, we found that below a critical thickness of about 15-20 nm the stripe domain pattern vanishes. This is illustrated in Figure 54, which shows this topography and in-plane PFM phase images for films thicknesses of ~11 nm (3000 pulses) (**a,d**), ~23 nm (6000 pulses) (**b,e**) and ~48 nm (12000) pulses (**c,f**).

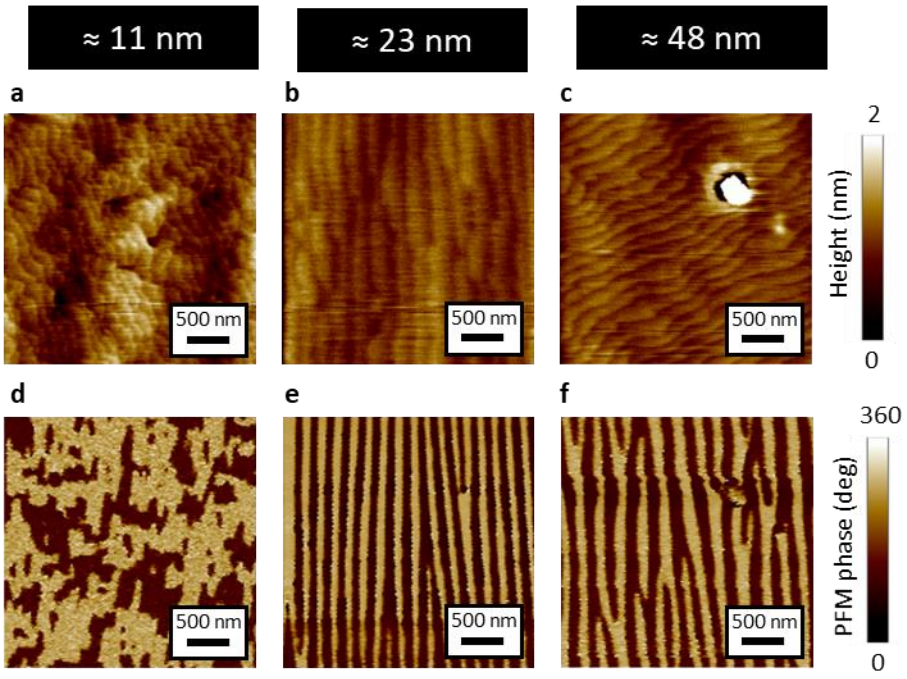

*Figure 54 : $BiFeO_3/SrRuO_3$ heterostructures deposited on $DyScO_3(110)_o$ while increasing the thickness of $BiFeO_3$. **a-e** Topography, **f-j** in-plane PFM phase.*

To summarise this chapter, the film thickness should be at least 20 nm to obtain striped $BiFeO_3$ thin films. The geometry of the growth chamber and the target-to-substrate distance can be identified as main reasons for droplet formation and should be optimized first. The oxygen pressure (in my case 0.36 mbar) was not optimized here, but growth at 0.2 mbar is also possible. I was able to optimize the striped ferroelectric domain patterns by mainly varying the laser energy and the temperature. Optimal values for the new growth chamber were around 660°C - 680°C just below the decomposition temperature and $60 - 90\ \mathrm{mJ/pulse}$, following the same idea: as high as possible, before droplets or decomposition appear.

3.1.2 Strain control of striped domains

$BiFeO_3$ films are grown on different substrates ($SrTiO_3$, $DyScO_3$, $TbScO_3$, $GdScO_3$, $SmScO_3$, $NdScO_3$) to enable a continuous variation of epitaxial strain. The results, shown in Figure 55, are obtained with the first growth chamber. Apart from $SrTiO_3$, where a higher laser energy of $80\ \mathrm{mJ/pulse}$ compared to the other substrates (here $60\ \mathrm{mJ/pulse}$) is needed to observe a stripy pattern, the samples can be grown under virtually the same growth conditions. The temperature measured with a pyrometer for the same heating power varies between the substrates ($SrTiO_3$: 645°C, $DyScO_3$: 610°C, $TbScO_3$: 633°C, $GdScO_3$: 549°C, $SmScO_3$: 628°C, $NdScO_3$: 651°C). The pressure is kept at 0.36 mbar. The growth parameters for $SrRuO_3$ (660°C, 0.2mbar, 60mJ/pulse, 5Hz) are never changed and the thickness is kept around 3-5 nm. As the lattice

mismatch between the $SrRuO_3$ electrode and $NdScO_3$ is too large, $BiFeO_3$ was grown directly on the substrate. However, as visible from the stripe pattern, the growth parameters, e.g. the growth temperature, are not optimal yet (Figure 55**l**).

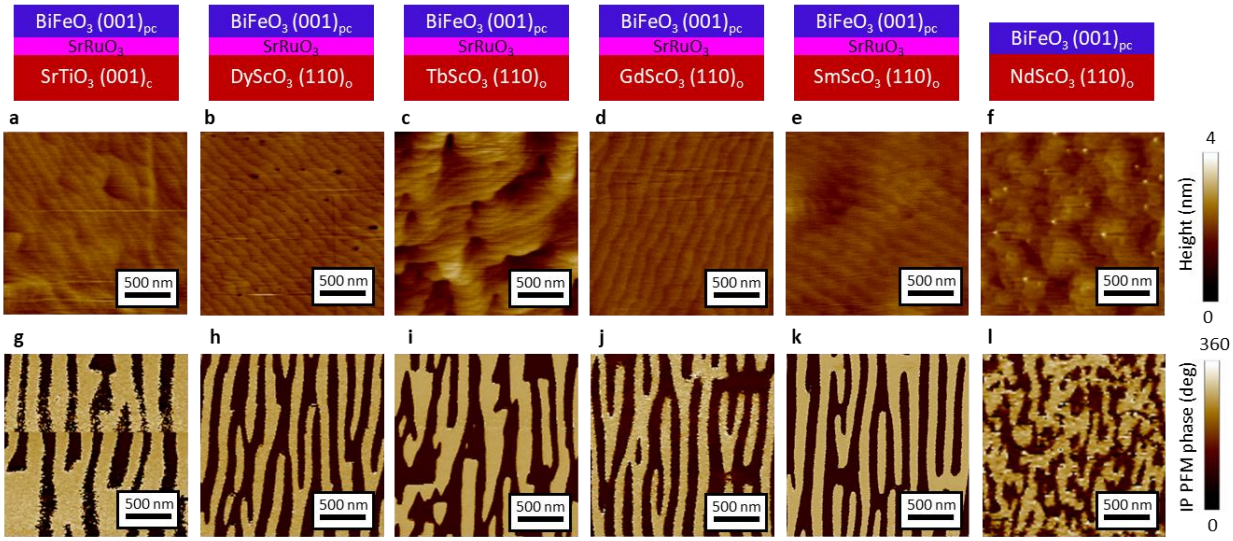

Figure 55: Topography and ferroelectric domain pattern for $BiFeO_3$ thin films grown on various substrates as sketched in the upper panel. ***a-f*** *Topography,* ***g-l*** *in-plane PFM phase.*

Figure 56 shows the same type of samples but grown in the second chamber. Remarkably, it was possible to obtain a highly-ordered stripe pattern, while droplets stayed on the surface. Therefore, depending on how sensitive an experiment is to the surface, we either choose to use the samples from Figure 55 (scanning NV magnetometry) or from Figure 56 (X-ray resonant magnetic scattering).

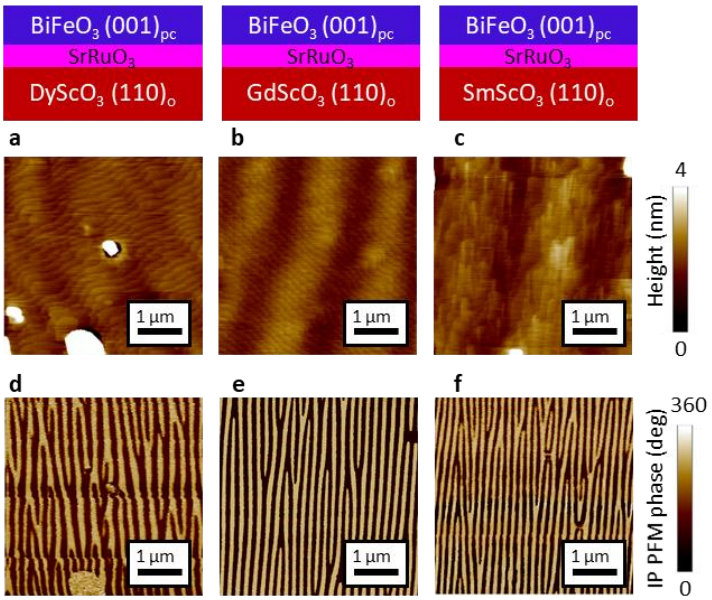

Figure 56: $BiFeO_3$ thin film growth on various substrates as sketched in the upper panel. ***a-c*** *Topography,* ***d-f*** *in-plane PFM phase.*

In the next step, we analyse the 2Θ-ω XRD scans to exclude the existence of parasitic phases and to calculate the out-of-plane lattice parameter. Furthermore, Laue fringes around the

$BiFeO_3$ peak prove the high crystalline quality of the films and permit to estimate their thickness. Figure 57 displays 2Θ-ω scans for the samples shown in the previous section (Figure 55). The Laue oscillation period indicates that the $BiFeO_3$ films on $SrTiO_3$, $TbScO_3$ and $NdScO_3$ are about 30 nm thick, whereas the ones on $DyScO_3$, $TbScO_3$, $SmScO_3$ and $GdScO_3$ are 60 nm thick. However, the results presented in this chapter do not show any thickness dependence in this range and will be treated in the same way. The relative position of the $BiFeO_3$ film peaks with respect to the substrate peaks emphasizes the out-of-plane strain engineering around almost zero strain between $BiFeO_3$ on $TbScO_3$ and $GdScO_3$ as expected from their small lattice mismatch.

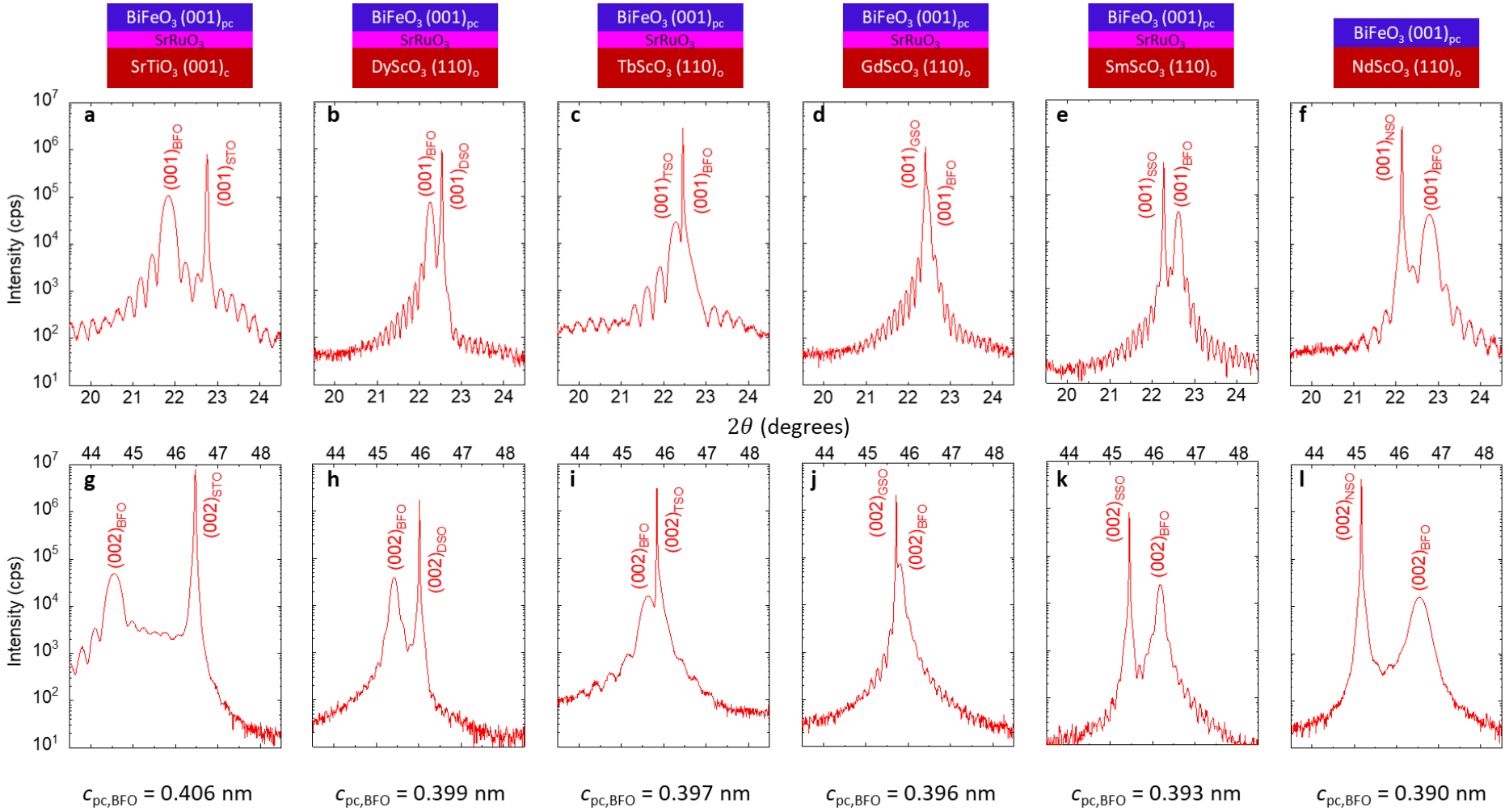

*Figure 57: 2θ-ω X-ray diffraction patterns around the (001) and (002) pseudo-cubic BFO peaks on the indicated substrates, **a-f** and **g-l**, respectively. The calculated pseudo-cubic out-of-plane lattice parameters are noted below the corresponding measurement.*

While the literature value is $c_{pc,BFO}$ = 0.3965 nm for bulk $BiFeO_3$,[112] we find that $c_{pc,BFO}$ is ranging from 0.406 nm to 0.390 nm when the films are grown on $SrTiO_3$ or $NdScO_3$, respectively. This decrease in the out-of-plane direction indicates a variation from compressive to tensile strain in the in-plane direction. In order to validate this hypothesis and take the monoclinic deformation into account, we collected asymmetric reciprocal space maps (Figure 58 and Figure 59) delivering information about the in-plane lattice constants.

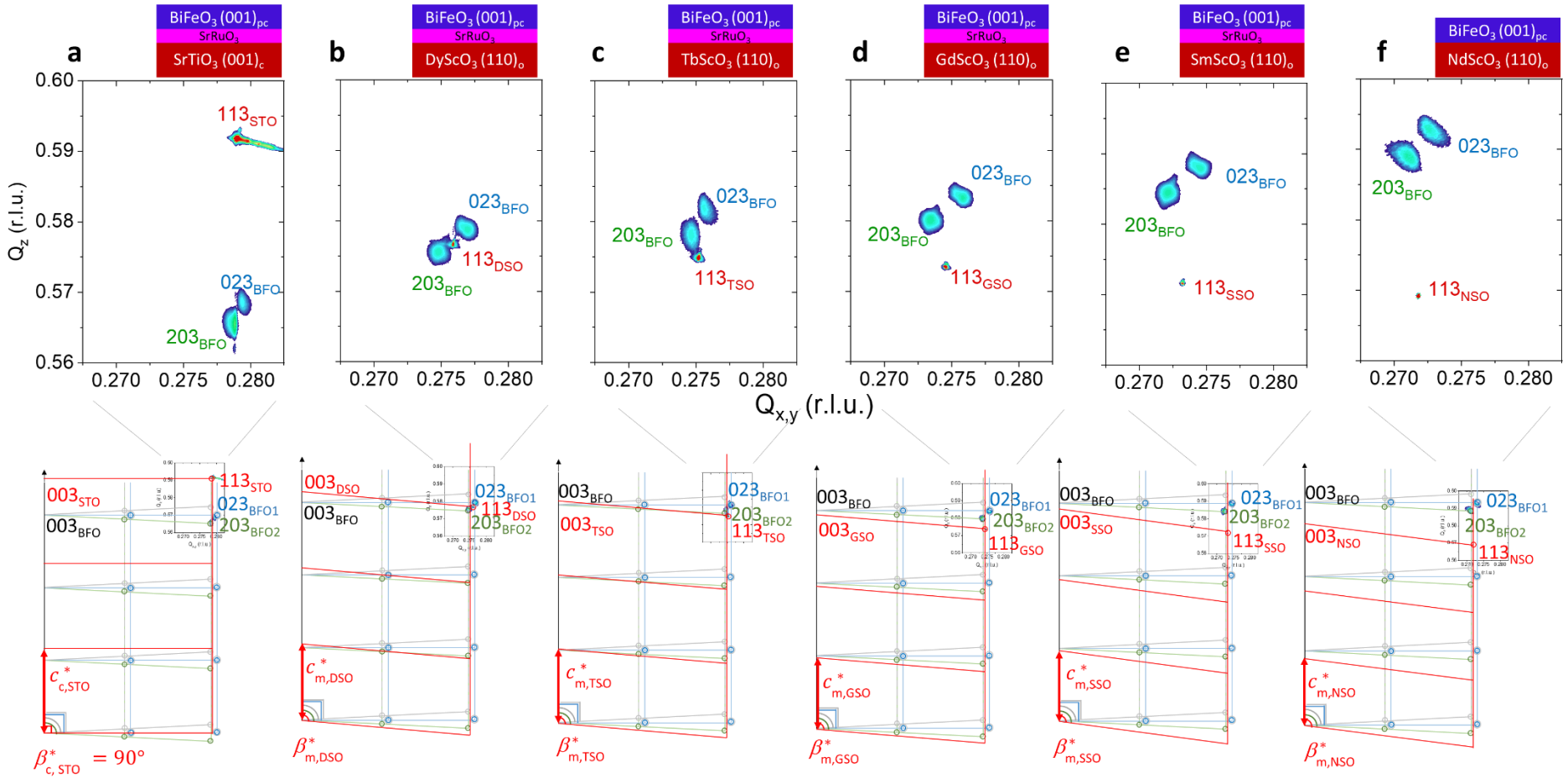

Figure 58: Reciprocal space maps for $BiFeO_3$ (BFO1 and BFO2) monoclinic domains on $SrTiO_3$, $DyScO_3$, $TbScO_3$, $GdScO_3$, $SmScO_3$ and $NdScO_3$ around the (113) monoclinic substrate peaks.

Using the equations presented in chapter 2.1.2, the calculated lattice parameter values are listed in Table 5 for each $BiFeO_3$ thin film.

Table 5: $Q_{x,y}$ and Q_z values determined from the BFO (023) and (203) diffraction peaks. Calculated monoclinic $BiFeO_3$ lattice parameters and strain values for $BiFeO_3$ films on $SrTiO_3$, $DyScO_3$, $TScO_3$, $GdScO_3$, $SmScO_3$ and $NdScO_3$.

	$BiFeO_3$ on $SrTiO_3$	$BiFeO_3$ on $DyScO_3$	$BiFeO_3$ on $TbScO_3$	$BiFeO_3$ on $GdScO_3$	$BiFeO_3$ on $SmScO_3$	$BiFeO_3$ on $NdScO_3$
$Q_{x,y}[023]$	0.279 r.l.u.	0.277 r.l.u.	0.276 r.l.u.	0.276 r.l.u.	0.275 r.l.u.	0.273 r.l.u.
$Q_z[023]$	0.569 r.l.u.	0.579 r.l.u.	0.582 r.l.u.	0.583 r.l.u.	0.588 r.l.u.	0.593 r.l.u.
$Q_{x,y}[203]$	0.279 r.l.u.	0.275 r.l.u.	0.275 r.l.u.	0.273 r.l.u.	0.272 r.l.u.	0.271 r.l.u.
$Q_z[203]$	0.566 r.l.u.	0.576 r.l.u.	0.578 r.l.u.	0.580 r.l.u.	0.584 r.l.u.	0.589 r.l.u.
a_m	0.553 nm	0.561 nm	0.561 nm	0.563 nm	0.566 nm	0.568 nm
b_m	0.551 nm	0.556 nm	0.559 nm	0.559 nm	0.561 nm	0.565 nm
c_m	0.406 nm	0.399 nm	0.397 nm	0.396 nm	0.393 nm	0.390 nm
β_m	89.42°	89.34°	89.22°	89.33°	89.27°	89.18°
V_m	0.124 nm^3	0.125 nm^3	0.124 nm^3	0.125 nm^3	0.125 nm^3	0.125 nm^3
ε	-1.33 %	-0.37 %	-0.10 %	0.05 %	0.47 %	0.93 %

In the reciprocal space maps around the (013) and (103) substrate peaks of $SrTiO_3$, $DyScO_3$, $TbScO_3$, $GdScO_3$, $SmScO_3$ and $NdScO_3$, the $BiFeO_3$ film peaks are aligned along the $Q_{x,y}$ direction (Figure 59). This demonstrates that the BFO films grow fully strained on top of those substrates. In addition, the peak positions are in accordance with the values expected from the lattice parameters calculated before.

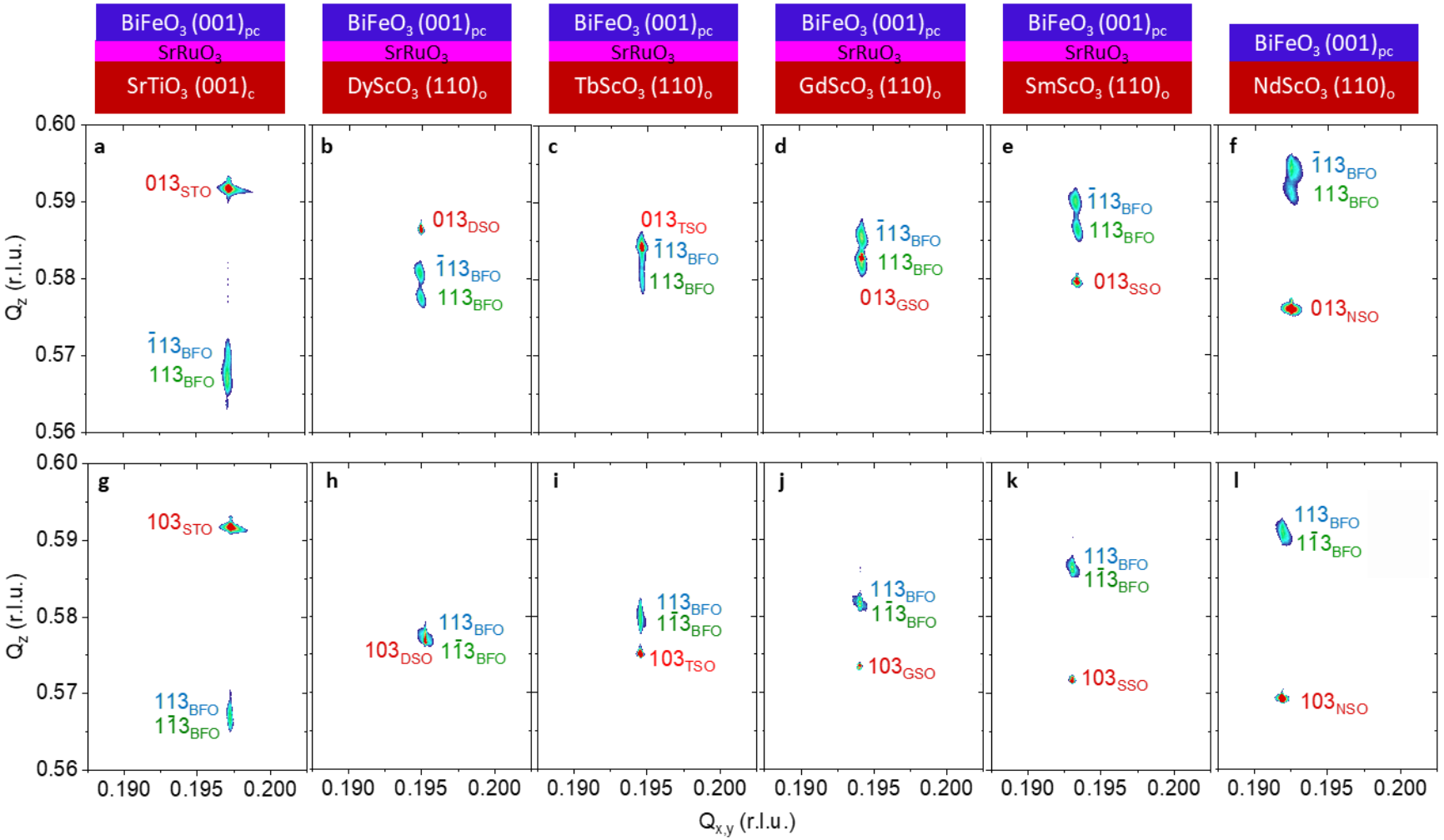

*Figure 59 : Reciprocal space maps along around **a-f** the (013) and **g-l** (103) substrate peaks of $SrTiO_3$, $DyScO_3$, $TbScO_3$, $GdScO_3$, $SmScO_3$ and $NdScO_3$.*

3.2 Single domains

Following the very recent work of Price et al. on thick films (1 μm) of $BiFeO_3$ grown by off-axis sputtering,[130] we grow pseudo-cubic $BiFeO_3$ $(111)_{pc}$ on orthorhombic $DyScO_3$ $(101)_o$, $TbScO_3$ $(101)_o$, $DyScO_3$ $(011)_o$ and $TbScO_3$ $(011)_o$ substrates (see Section 2.1.3 for more details), in order to seek for a single ferroelectric domain with a pure out-of-plane polarization direction.

In Figure 60, the topography and PFM images of four samples grown in the same PLD growth process are shown. However, as we can see in the topography images (Figure 60**a-d**), the thin film morphology tends to deviate from flat terraces and steps, as previously observed for $(110)_o$ orthorhombic substrates. Nevertheless, for $BiFeO_3$ thin films grown on $DyScO_3$ $(011)_o$, the surface morphology is flat with unit-cell steps and terraces. In addition, the out-of-plane PFM phase (Figure 60**g**), is homogeneous and bright while the in-plane phase (Figure 60**k**) is not well defined. This suggests that the polarization is along the growth direction (no in-plane components) and pointing downwards. In contrast, for the other substrates, there are multiple domains pointing in other possible {111} directions (Figure 60**e-l**),. All the four samples were grown together in one deposition process at 5 Hz, 0.36 mbar, 80 mJ/pulse and 670°C (on $DyScO_3$), 652°C (on $TbScO_3$) and have a $BiFeO_3$ film thickness of 50 nm.

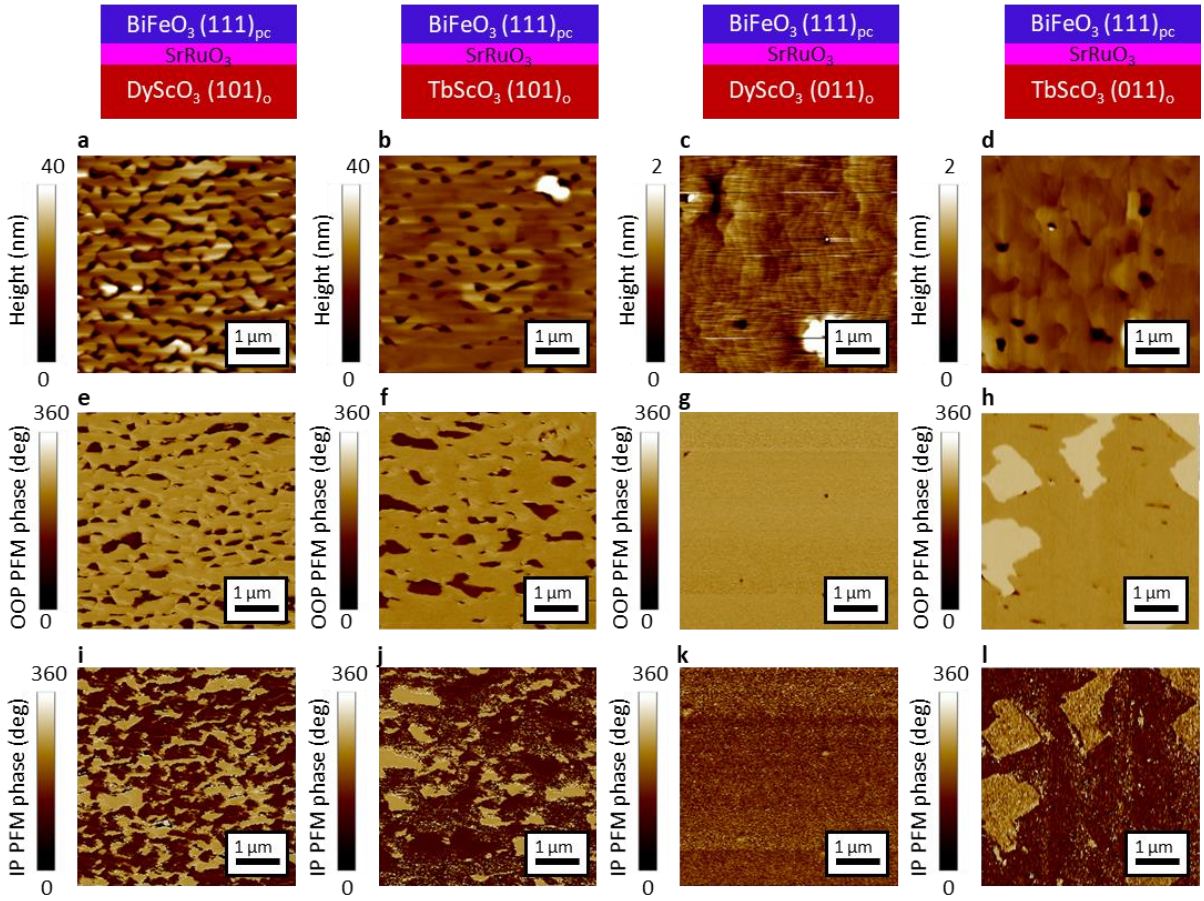

Figure 60 : $BiFeO_3$ thin film growth on various substrates indicated in the sketches above. ***a-d*** *Topography,* ***e-h*** *out-of-plane PFM phase, and* ***i-l*** *in-plane PFM phase.*

We now focus on the structural analysis of the $BiFeO_3$ sample on $DyScO_3$ $(011)_o$ in which a single electric domain seems to be detected (sample from Figure 60**c, g, k**). Considering that $BiFeO_3$ grows with the polarization axis parallel to the growth direction, it is easier to use a hexagonal unit cell to describe the in-plane lattice strain with the substrate (Figure 61, pink). If the $BiFeO_3$ film grows fully strained by the orthorhombic $DyScO_3(011)_o$ substrate, one may anticipate an anisotropic distortion of this hexagonal cell (Figure 61, purple) (for more details on the method, see Paragraph 2.3.2). Hence, we refer to the symmetry of the film as pseudo-hexagonal.

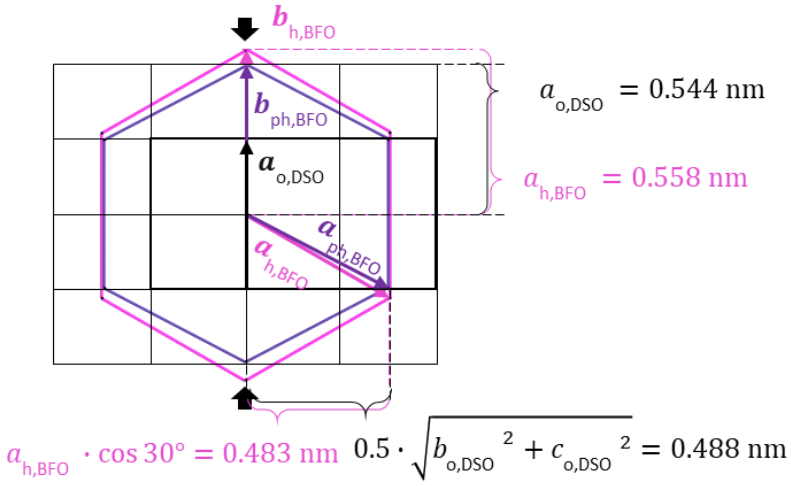

Figure 61 : In-plane lattice of the orthorhombic (011) $DyScO_3$ substrate (black), the hexagonal (001) bulk $BiFeO_3$ lattice (pink) and the pseudo-hexagonal deformation (violet) under anisotropic strain, imposed by the substrate (bold black arrows). We here consider theoretically that the film is fully strained, with large compressive and small tensile strains in the vertical and horizontal directions, respectively.

The hexagonal (00l) growth direction and the out-of-plane lattice parameter can be determined from the 2Θ-ω X-ray diffraction pattern (Figure 62) to

$$c_{\mathrm{ph,BFO}} = 1.385 \text{ nm}.$$

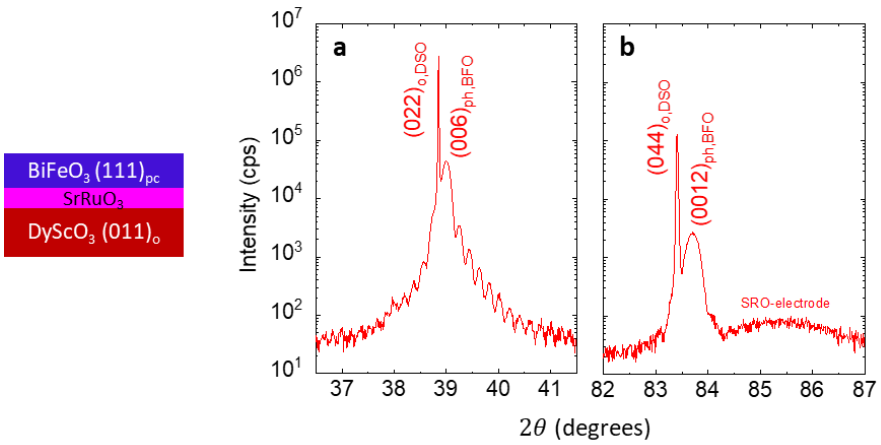

Figure 62 : 2Θ-ω X-ray diffraction patterns around the pseudo-hexagonal $(006)_{ph}$ and $(0012)_{ph}$ $BiFeO_3$ peaks on the orthorhombic $DyScO_3$ $(011)_o$ substrate.

For the determination of the whole pseudo-hexagonal $BiFeO_3$ unit cell, we recorded reciprocal space maps at different phi angles (Figure 63**a**, violet). The anisotropic strain from the $DyScO_3$ substrate induces a larger (smaller) reciprocal unit cell along (orthogonal to) the $\vec{a}^*_{\mathrm{o,DSO}}$ direction compared to the hexagonal one (pink). The influence of the anisotropic strain is visible in the $BiFeO_3$ (108), $(\bar{1}18)$ and $(0\bar{1}8)$ peaks in Figure 63**b-d**, which are not exactly at the same position, breaking a 120° rotation symmetry. The maps recorded at $\phi = 120°$ and $\phi = 240°$ (Figure 63**c,d**), as well as $\phi = 90°$ and $\phi = -90°$ (Figure 63**f,g**) are roughly identical and can be associated to the strain of the hexagonal lattice along $\vec{a}^*_{\mathrm{o,DSO}}$ in the film plane (bold black arrows in **a**). The perfect alignment of the substrate and the film peak in Figure 63**b, e** ($\phi = 0°, 180°$) shows that the film is fully strained perpendicular to $\vec{a}^*_{\mathrm{o,DSO}}$.

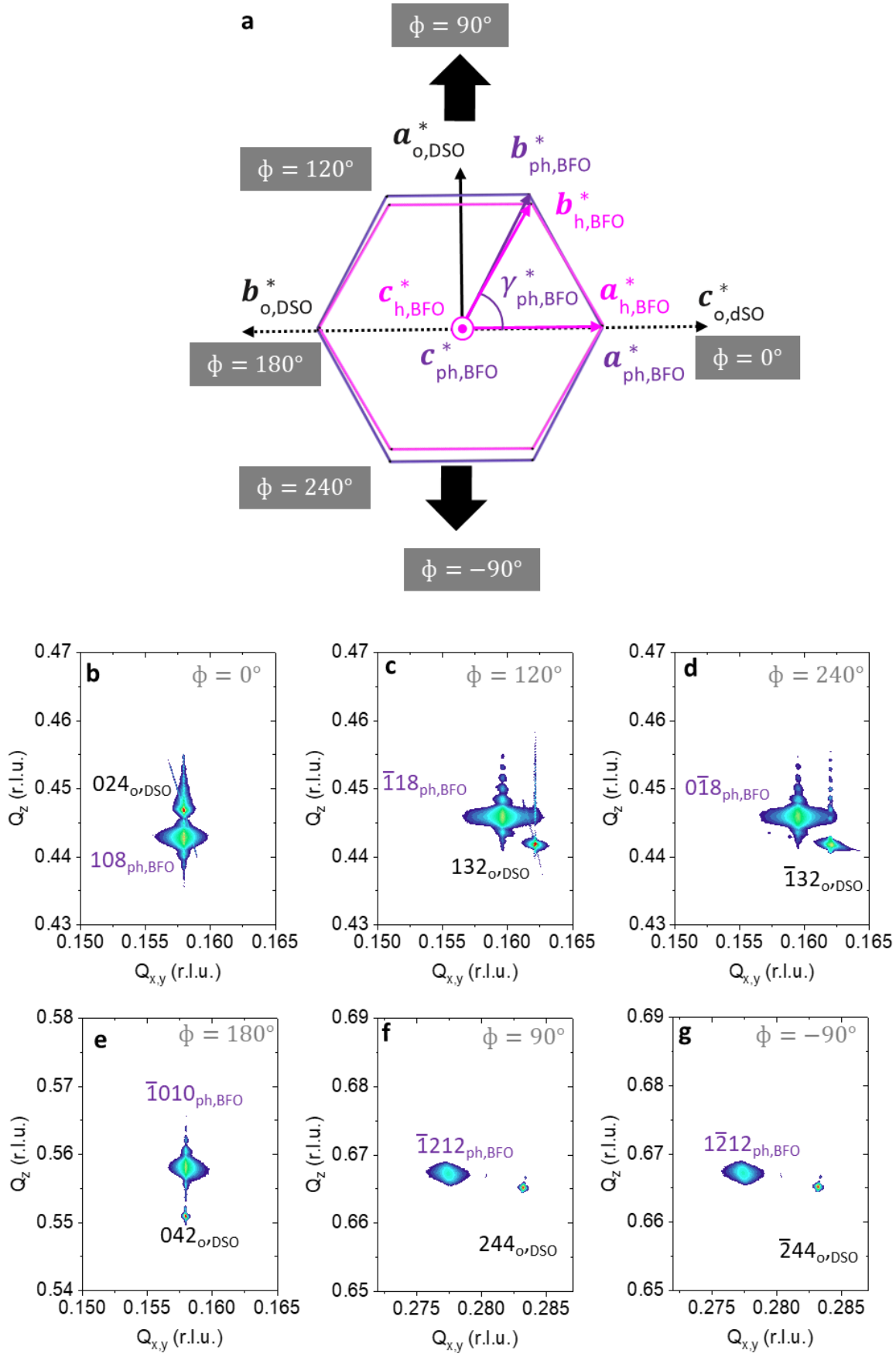

*Figure 63 : **a-c, e-f** Reciprocal space maps of the pseudo-hexagonal $BiFeO_3$ film (violet indices) on the $DyScO_3$ substrate (black indices) for different azimuthal angles.*

Using the equations presented in paragraph 2.3.2, we deduce all the lattice parameters for the pseudo-hexagonal unit cell from the positions of the $BiFeO_3$ peaks in the reciprocal space maps shown in Figure 63. The results are listed in Table 6.

Table 6 : $Q_{x,y}$ and Q_z values determined from the $BiFeO_3$ 108, $\bar{1}010$, $0\bar{1}8$ and $\bar{1}212$ spots. Calculated pseudo-hexagonal $BiFeO_3$ lattice parameters and strain values for this $BiFeO_3$ film on $DyScO_3$ $(011)_o$.

	$Q_{x,y}$	Q_z
$[108]$	0.158 r.l.u.	0.443 r.l.u.
$[\bar{1}010]$	0.158 r.l.u.	0.558 r.l.u.
$[0\bar{1}8]$	0.160 r.l.u.	0.446 r.l.u.
$[\bar{1}212]$	0.277 r.l.u.	0.667 r.l.u.

a_{ph}	0.561 nm
b_{ph}	0.555 nm
c_{ph}	1.386 nm
α_{ph}	89.63°
β_{ph}	89.26°
γ_{ph}	119.61°

V_{ph}	0.375 nm³
ε_a	0.54 %
ε_b	-0.54 %

In summary, as sketched in Figure 64, this structural analysis shows that the $BiFeO_3$ film grows on the orthorhombic $DyScO_3(011)_o$ substrates in a distorted hexagonal unit cell (violet) with tensile and compressive strains along the $\vec{a}_{ph,BFO}$ and $\vec{b}_{ph,BFO}$ directions, respectively. Along the $\vec{c}_{ph,BFO}$ direction, the film has a larger lattice constant than the bulk hexagonal cell (pink). Since this direction is associated to the $[111]_{pc}$ direction, this larger lattice may favour the out-of-plane polarization vector (red arrow). For comparison, the pseudo-cubic unit cell and the hexagonal unit cell in bulk are sketched in grey and pink, respectively. In conclusion, the distorted hexagonal plane resulting from the anisotropic strain from the orthorhombic $(011)_o$ substrate should lift the degeneracy between the three possible cycloidal propagation vectors of $BiFeO_3$ from a crystallographic point of view.

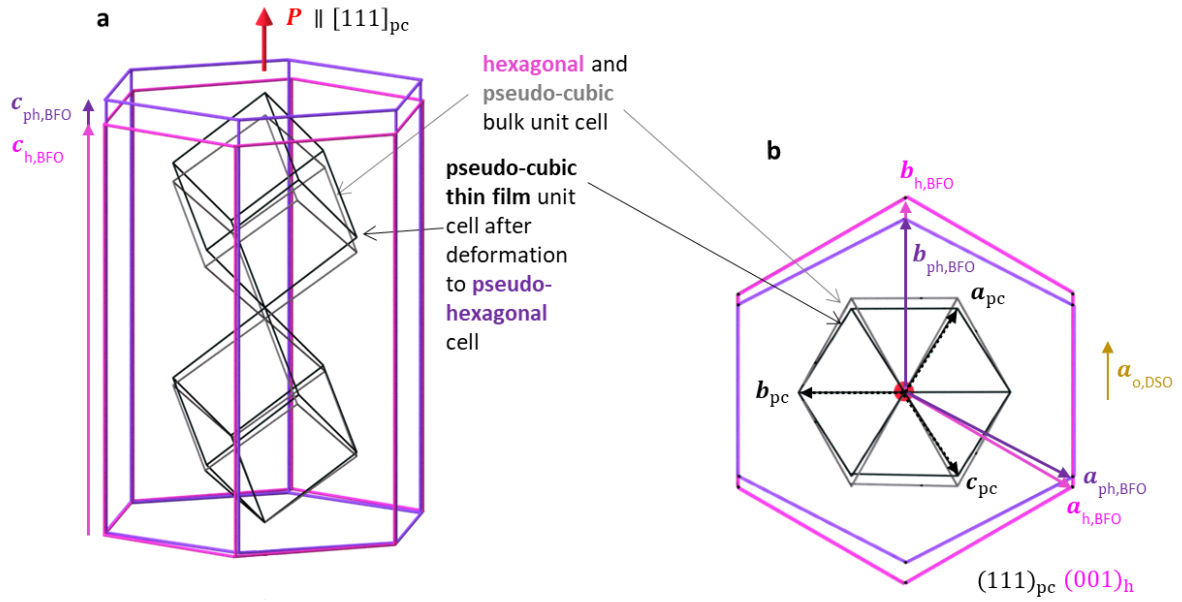

Figure 64 : Sketches summarizing the deformation of $BiFeO_3$ in the case of $(111)_{pc}$ growth on $DyScO_3(011)_o$. The grey and pink cells represent the pseudo-cubic and hexagonal unit cells in the bulk, respectively. The black and violet ones show the distorted cells in the thin film. A polarization P (red) along either the $[111]_{pc}$ or the $[\bar{1}\bar{1}\bar{1}]_{pc}$ direction is favoured by this deformation.

3.3 Inverse transition in ferroelectric thin films

At the beginning of my thesis, our colleagues from the University of Arkansas found a previously unseen, temperature dependent inverse phase transition in ferroelectric thin films. They used an ab initio-based effective Hamiltonian approach and investigated ultrathin $Pb(Zr_{0.4}Ti_{0.6})O_3$ films. Following their predictions, we conducted an experimental investigation of such an inverse dipolar transition in $BiFeO_3$ thin films. Our joint experimental and theoretical results suggest the universality of this phenomenon in ferroelectric oxides.[131] After a brief summary of the theoretical work, I will present my experimental approach to this inverse transition.

3.3.1 Summary of the theoretical work

Inverse phase transitions seem to contradict the fundamental law of thermodynamics that disorder increases with increasing temperature. First proposed in theory and later demonstrated experimentally,[132,133] some highly-degenerated frozen states may exhibit the counterintuitive inverse-symmetry-breaking phenomenon. However, up to now, none of them could be found in ferroelectric materials. Here the theoretical calculations for ultrathin $Pb(Zr_{0.4}Ti_{0.6})O_3$ films reveal that a labyrinthine configuration of dipolar moments can be transformed in a more ordered stripy pattern with lower symmetry when heated above an inverse transition temperature T_{inv} (Figure 65).

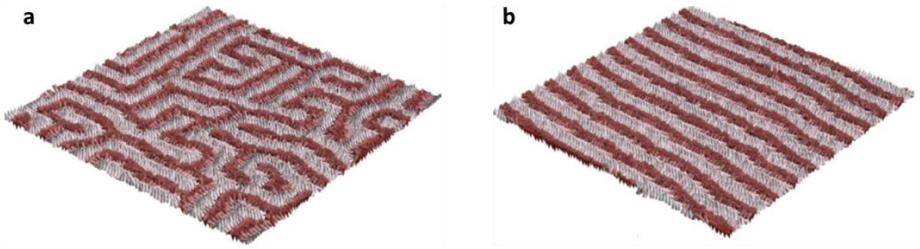

*Figure 65 : Fast quenching from the paraelectric state of an ultrathin $Pb(Zr_{0.4}Ti_{0.6})O_3$ thin film stabilizes a labyrinthine pattern (**a**), while slow temperature decrease leads to the parallel striped configuration ground state (**b**). Adapted from reference [131].*

A low compressive strain of -2.65% in the 2.0 nm thick $Pb(Zr_{0.4}Ti_{0.6})O_3$ films with a cubic quasi-Z_2 symmetry imposes an anisotropy energy leading to a favourable out-of-plane orientation of the dipoles (Figure 66**a**). However, a single domain out-of-plane polarization all over the sample would lead to a large depolarizing field (Figure 66**b**) and the incomplete screening of the surface charges favours the formation of 180° ferroelectric domains on a mesoscopic length scale.

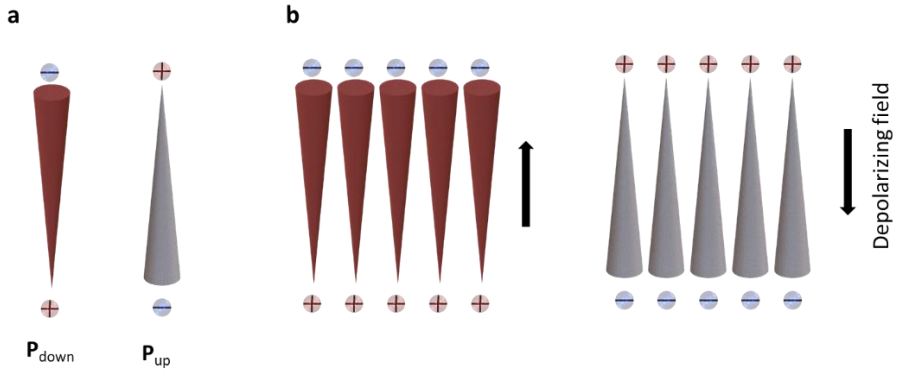

*Figure 66 : **a** Electric dipoles, pointing downwards $\boldsymbol{P}_{down}$ and upwards $\boldsymbol{P}_{up}$, respectively. **b** Out-of-plane dipole orientation, leading to uncompensated surface charges and hence a depolarizing field in the opposite direction.*

As the processes of individual dipole fluctuations and collective dipole arrangement relaxation, which determine the mesoscopic domain pattern, underlie different dynamics, the motion and relaxation of domains are influenced by the cooling rate. While under slow annealing, the system can relax into its ground state with regular parallel stripes (Figure 65**b**), a fast quenching from the paraelectric state to low temperatures leaves the system in a labyrinthine domain pattern (Figure 65**a**) (with a slightly higher internal energy of 0.6%). Furthermore, the maze pattern can transform into the stripy one, when raising the temperature above T_{inv} (Figure 67**a-f**). The evolution of the domain pattern can be quantified from its Fourier transformation (insets, Figure 67**a-f**). The resulting order parameter is plotted in Figure 67**g** as a function of temperature. Further heating of the parallel stripe state leads to the transition into the paraelectric phase above T_C.

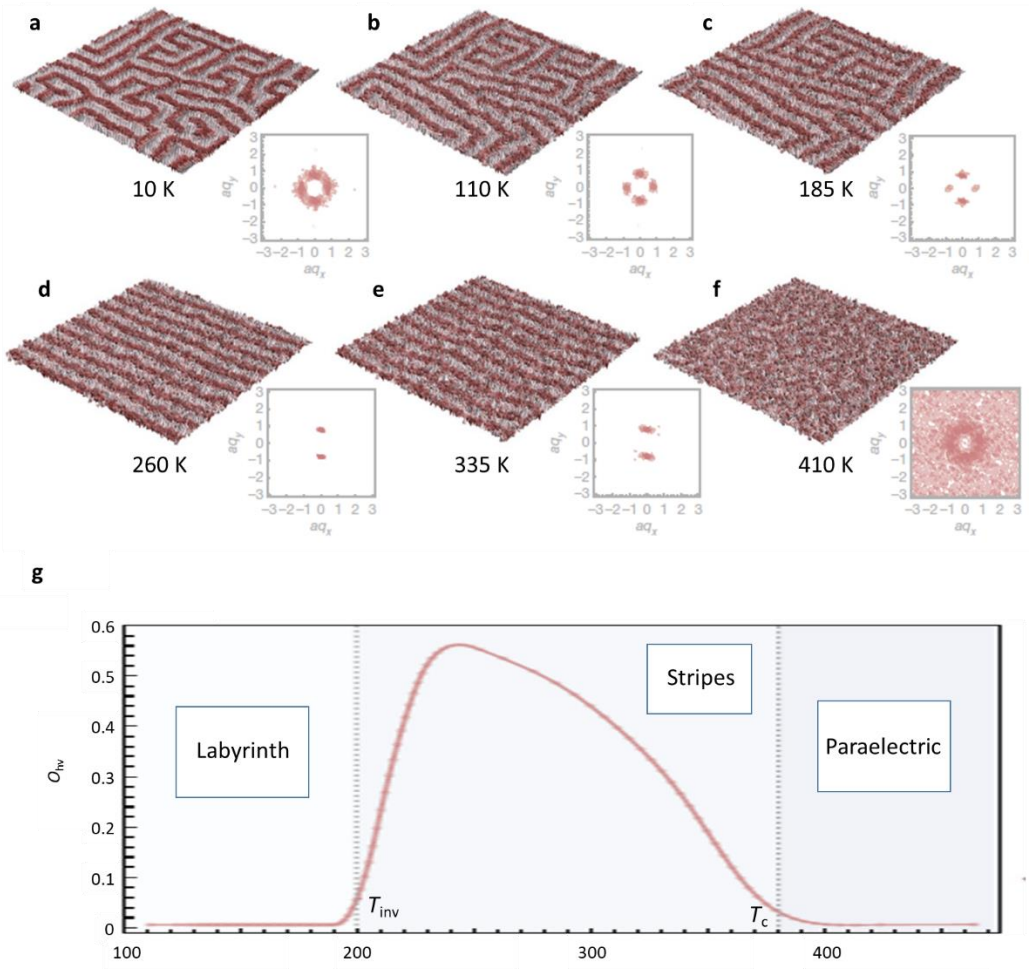

*Figure 67 : Inverse transition of a maze ferroelectric domain pattern into a perfectly striped domain pattern, before turning into the paraelectric state (**a-f**). Corresponding order parameter (**g**) evolution with temperature. Adapted from reference [131].*

Even though this inverse phase transition seems to be counterintuitive from the mesoscopic point of view, on a microscopic level, considering the transverse component of the dipoles at a domain wall, it could be calculated that thermal fluctuations of the dipoles are increasing with higher temperature. The free-energy-like potential of the system is plotted in Figure 68 for different temperatures. It displays a global minimum in the centre which corresponds to domain wall orientations along the out-of-plane direction. In addition, at 10K the potential shows two local (outer) minima representing more Néel-type domain walls with a higher transverse component. With increasing temperature, the barriers between the minima decrease and, at the inverse transition temperature T_{inv} = 110 K, the local minima disappear. Simultaneously, thermal fluctuations increase and favour reorientation flips of the dipoles from one out-of-plane direction to the antiparallel one. This is accompanied by a rearrangement of meandering stripes and an enhanced domain wall fluidity. To decrease the cost of the domain wall energy, the system aims to shorten the overall length of the domain walls, which results in the formation of parallel striped domains.

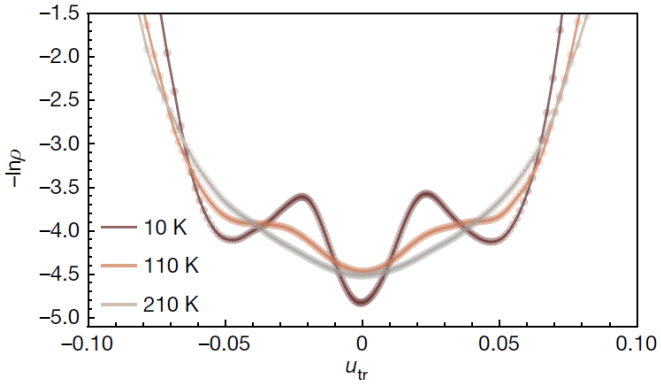

Figure 68 : Free-energy-like potentials of the labyrinthine domain pattern at increasing temperatures. Adapted from reference [131].

The transition from the maze to the stripe order represents a loss of configurational entropy of the labyrinthine stripes (greater mesoscopic order). This loss is offset by the increase of the vibrational entropy of dipoles (greater microscopic disorder). Hence, from a microscopic thermodynamics point of view, the maze-to-stripe phase transition is not contradicting any fundamental law and is only inverse on the mesoscopic scale.

The reconfiguration of the domain wall patterns with increasing temperature towards the maze-to-stripe transition is accompanied by a change in elementary point-topological defects. Those are in the current interest for domain-wall-based technologies, promising devices with gigahertz microwave tuneability and low dielectric losses in materials with a high strain-induced ferroelectric domain wall density.[134] Here, the densities of the stripe end-point defects d_I (Figure 69**a**) and threefold junctions d_{III} (Figure 69**b**) decrease with increasing temperature (Figure 69**c**), as they are recombined or annihilated as seen in the inset sketch in Figure 69**c**.

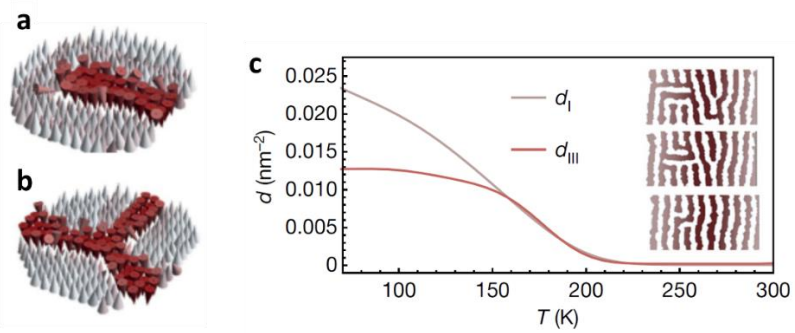

*Figure 69 : End-point (**a**) and threefold junctions (**b**) topological defects and their density evolution (**c**) with increasing temperature. Adapted from reference [131].*

Furthermore, the calculations for $Pb(Zr_{0.4}Ti_{0.6})O_3$ thin films could be expanded for $BiFeO_3$ films with different thicknesses and strain levels of -0.16% and-0.5%. Considering the ferroelectric and antiferrodistortive order parameters, $BiFeO_3$ displays a maze to stripe transition between 1000K and 1200K as well (Figure 70). It is also predicted, that the domain wall type tends towards 109° domain walls above the transition temperature, whereas below it consists of a mix of 71° and 109° domain walls.

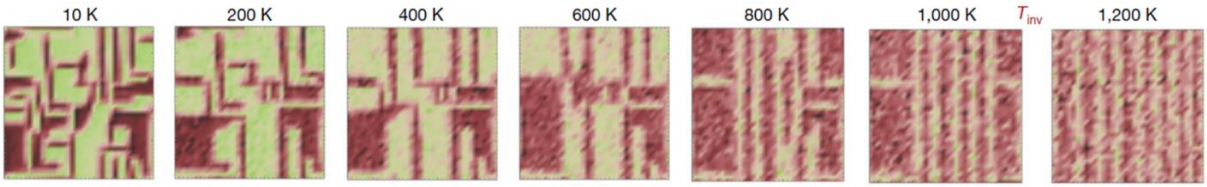

Figure 70 : Calculated inverse phase transition in a $BiFeO_3$ thin film under -0.16% compressive strain. Adapted from reference [131].

3.3.2 Annealing experiments: from maze to stripe electric domains

We conducted annealing experiments with $BiFeO_3$ thin films in order to confirm the validity of the theoretical calculations. A 95 nm thick $BiFeO_3$ thin film and a 5 nm thick $SrRuO_3$ electrode, grown by pulsed laser deposition on a $DyScO_3$ substrate, as presented in the previous chapter, is annealed ex-situ under constant oxygen flow at successively increasing temperatures at each step. From room temperature, the sample is heated up with 20 K min^{-1} and kept at the maximum temperature for an hour, before being cooled down with a very slow rate of approximately 2 K min^{-1}. The precision of the cool down process is limited by the inertia of the oven and the rate can only be estimated. We investigated possible modifications of the domain pattern after each annealing experiment by doing PFM measurements at room temperature.

Figure 71 shows the topography and PFM signal of the as grown sample as well as after three different annealing steps. Not visible in the topography images shown here (Figure 71**a-d**), is an additional surface desorption appearing at each step. However, the step terrace structure is widely preserved between those particles. After the first two annealing temperatures (500°C and 750°C), the ferroelectric domain pattern shown in the in-plane PFM phase images (Figure 71**f, g**) and corresponding amplitude (Figure 71**j, k**) do not vary from the as-grown state (Figure 71**e, i**). However, after the 800°C annealing step, a profound modification of the ferroelectric pattern occurs into a perfectly striped domain pattern (Figure 71**h, l**), thus defining T_{inv} in between 750°C and 800°C. Using X-ray diffraction 2Θ-ω scans, we confirm that the inverse phase transition does not involve any structural changes (Figure 72) such as strain relaxation or the formation of parasitic phases.

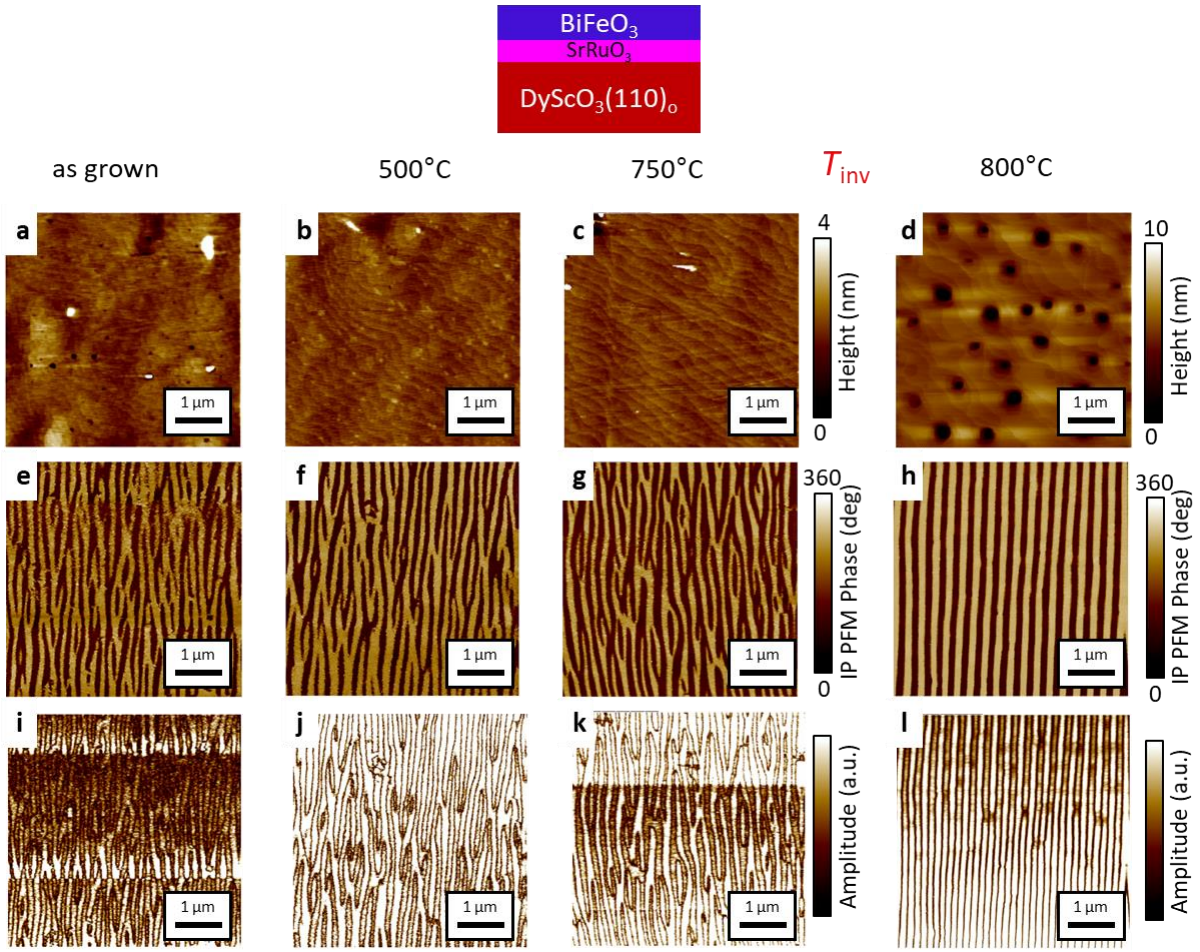

Figure 71 : Experimental observation of the inverse phase transition in the third annealing step at 800°C from the left to the right. ***a-d*** *Topography images,* ***e-h*** *in-plane PFM phase and* ***i-l*** *corresponding amplitude images.*

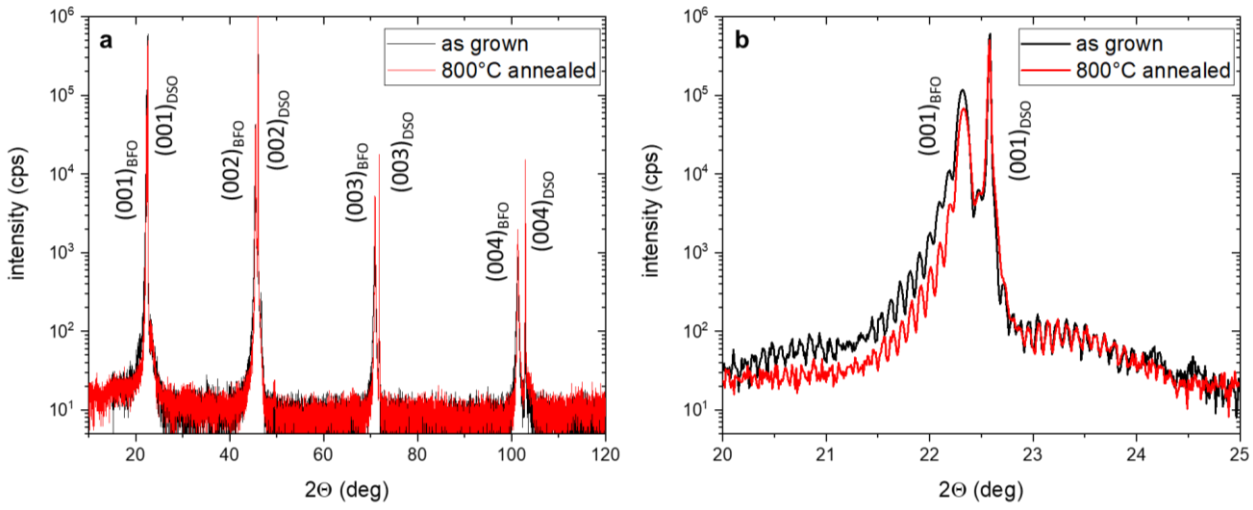

Figure 72 : ***a*** *Full-range 2θ-ω scans of the sample in the as-grown sate, as well as after the annealing step at 800°C.* ***b*** *zoom-in at the orthorhombic $DyScO_3$ $(001)_o$ and the monoclinic $BiFeO_3$ $(001)_m$ peak.*

In addition reciprocal space maps around the monoclinic $BiFeO_3$ $(002)_m$ peak show the appearance of satellite peaks after the annealing step (Figure 73**a,b**). These features disappear when rotating the sample by ϕ = 90° (Figure 73**c,d**) and are clearly related to the high order of the

stripes in the ferroelectric pattern where each polarization direction is related to an elastic deformation.[135]

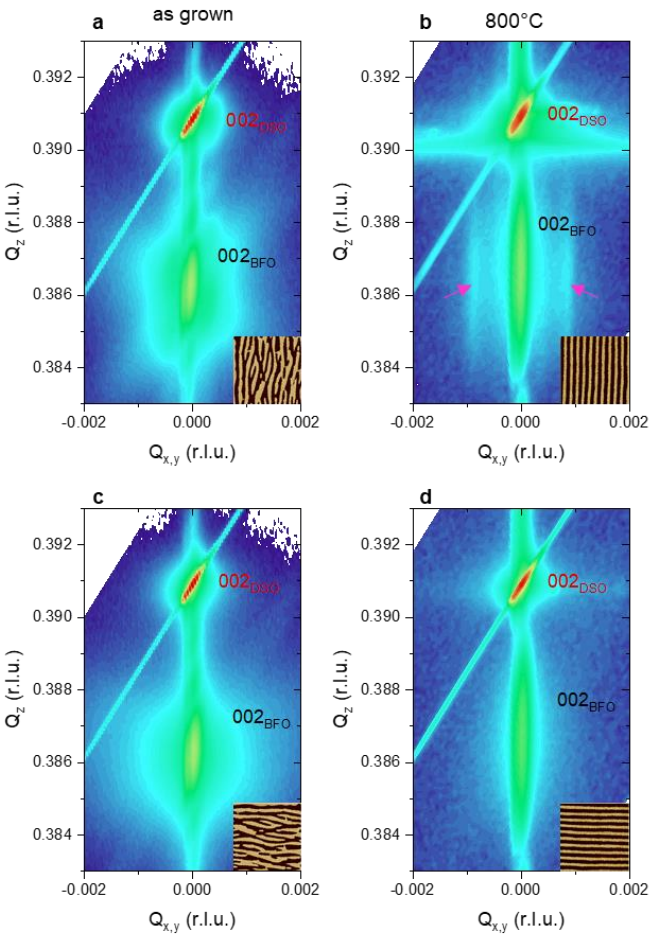

*Figure 73 : Reciprocal space maps around the orthorhombic $DyScO_3$ $(002)_o$ and the monoclinic $BiFeO_3$ $(002)_m$ peak, before (**a,c**) and after (**b,d**) the inverse phase transition for two different orientations of the sample (as shown in inset).*

The same inverse phase transition is observed in another 30 nm thick $BiFeO_3/SrRuO_3$ heterostructure on $DyScO_3$, as well as on a 60 nm thick film directly grown on $GdScO_3$ and a 66 nm on $SmScO_3$ after a single annealing process at 800°C (Figure 74). Interestingly, the as-grown pattern has a more pronounced square symmetry maze state on $GdScO_3$ but the pattern after the inverse transitions still shows a stripy state, although less perfect.

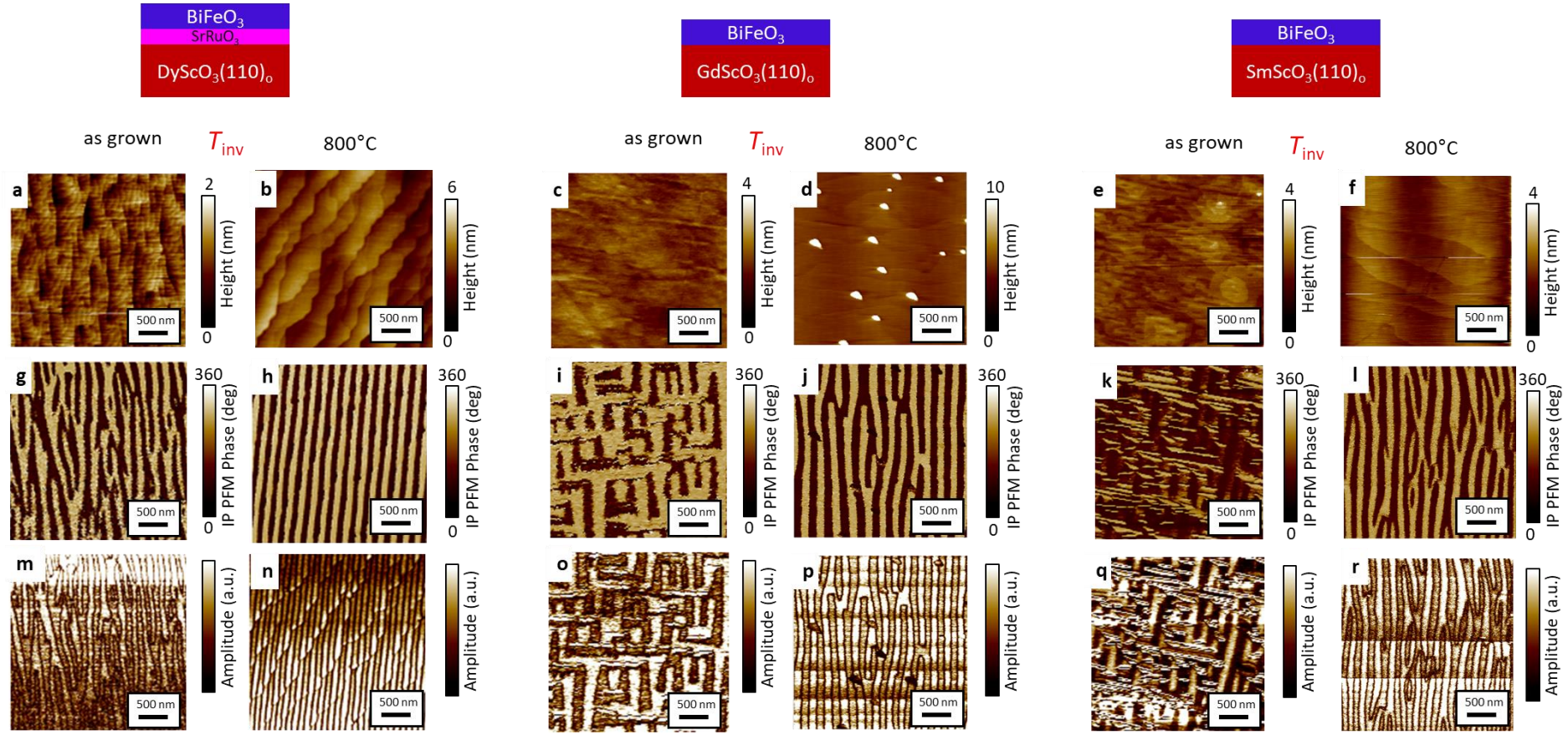

Figure 74 : Generalization of the inverse phase transition in $BiFeO_3$ thin films grown on $DyScO_3$, $GdScO_3$ and $SmScO_3$ substrates. ***a-f*** *Topography,* ***g-l*** *in-plane PFM phase, and* ***m-r*** *corresponding amplitude images.*

All these results confirm the theoretical calculations with the only difference that the present domain wall type, namely 71° domain walls, does not change with the annealing processes. All domains shown in this paragraph have a homogenous downward polarization.

We rule out the possibility of inducing this dramatic change in the ferroelectric domain pattern by crossing the critical ferroelectric-to-paraelectric transition of $BiFeO_3$ using temperature dependent X-ray diffraction. As visible from Figure 75, the out-of-plane lattice parameter of the $BiFeO_3$ film on $DyScO_3$ is measured up to 1160 K where the film decomposes. The quasi-linear variation indicates no phase transition in this regime.

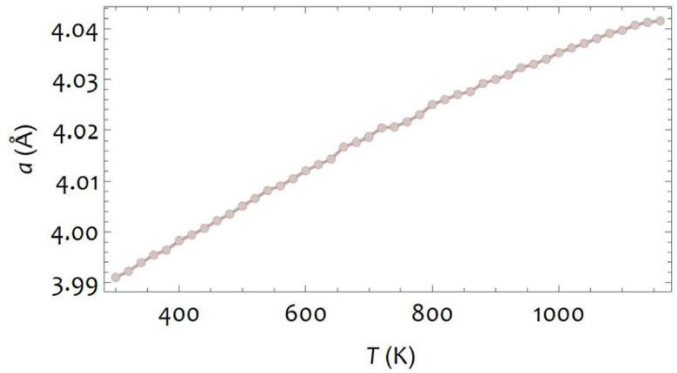

Figure 75 : Out-of-plane lattice parameter vs. temperature of the $BiFeO_3$ film on $DyScO_3$ extracted from X-ray diffraction measurements up to its decomposition at 1160 K. Adapted from reference [131].

As mentioned in the previous paragraph, elementary point-topological defects can also be found in our $BiFeO_3$ samples. They are revealed by in-plane PFM (Figure 76**a**) as well as by conductive atomic force microscopy (C-AFM) images while applying a DC-current of 1.7 V to the $SrRuO_3$ bottom electrode (Figure 76**b**-**d**). High conduction spots can be observed in Figure 76**c** and **d**, indicating threefold junctions and stripe end-point defects, respectively. Thus, this inverse transition in the thin films of $BiFeO_3$ can be accompanied by the annihilation of topological defects, which contain high current density, offering a perspective for tuneable topological resistive devices.

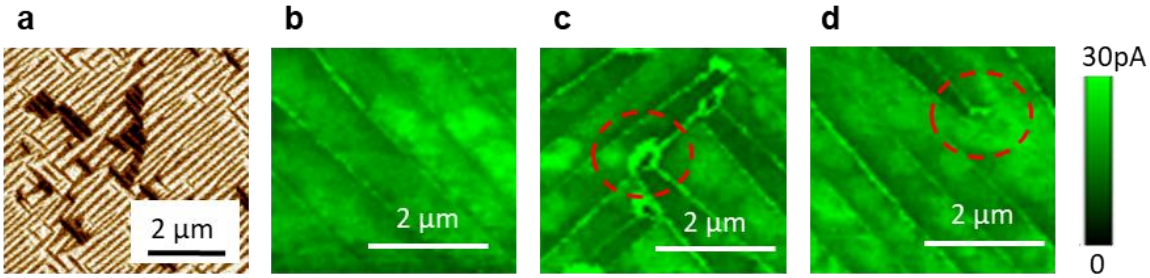

*Figure 76 : **a** In-plane PFM image. **b-d** C-AFM images in different zones of **a** to analyse different three-fold junction (**c**) and end-point (**d**) topological defects (red dotted lines) with enhanced conduction compared to the regular ferroelectric domain walls (**b**). Adapted from reference [131].*

3.3.3 Transition from mosaic to striped domains

The post-annealing ordering effect of the ferroelectric domain pattern can also be observed in the mosaic samples grown with the Nd:YAG laser. In this section, results of three $BiFeO_3$ samples grown on orthorhombic $DyScO_3$ $(110)_o$ samples are presented. The target used for their growth is a $BiFeO_3$ target enriched with iron of the isotope Fe^{57}, which was necessary for other measurements analysing their magnetic properties with Mossbauer spectroscopy (details are presented elsewhere[128]). All the samples have a thickness of 25-40 nm. The topography of those films after the growth shows a large roughness without atomic steps (Figure 77**a**). The out-of-plane polarization direction is slightly inhomogeneous with a large majority of domains pointing downwards (Figure 77**b**). In a vectorial in-plane analysis, we observe mosaic domains pointing in only two different directions (Figure 77**c, d**). When subjected to the same ex-situ annealing procedure presented in the previous paragraph, the domain morphology changes to a striped pattern with atomic steps on the surface (Figure 77**e-h**).

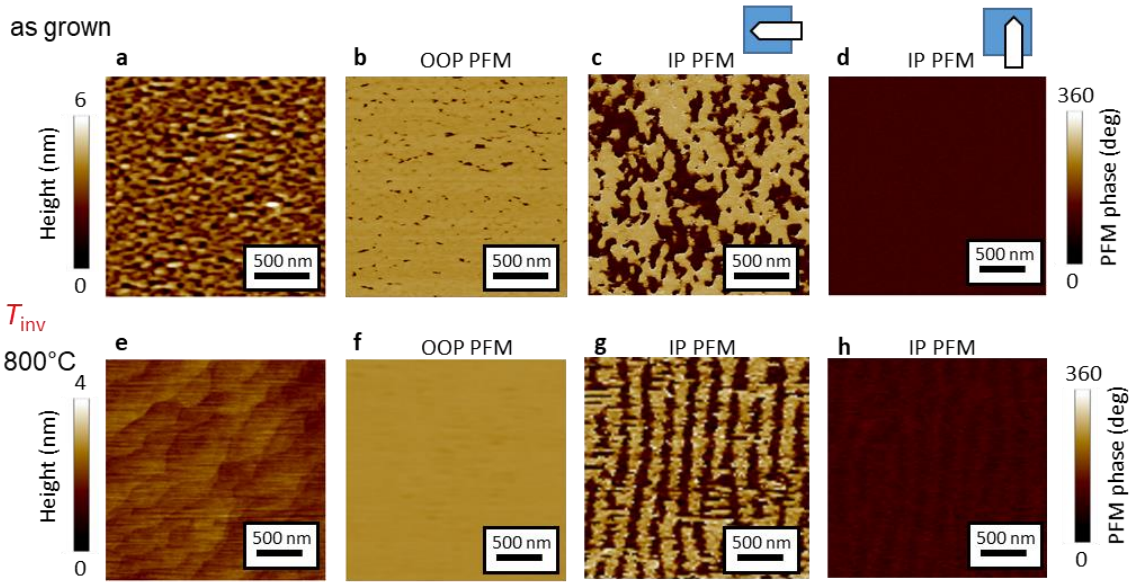

Figure 77 : Transition from a mosaic to a stripe pattern after annealing for one hour at 800°C. ***a, e*** *Topography,* ***b, f*** *out-of-plane PFM phase,* ***c, g*** *in-plane PFM phase in a first orientation, and* ***d, h*** *in-plane PFM phase in a second orientation, as sketched in the upper panel.*

Here, it is not only a rearrangement of the ferroelectric domains towards a more ordered pattern, but the removal of a strain gradient that decoupled the film from the substrate in the growth process. 2Θ-ω x-ray diffraction scans show single-phase $BiFeO_3$ before and after the annealing step (Figure 78**a**,**e**), but the crystalline quality and the out-of-plane lattice parameter change (Figure 78**b**,**f**, grey dotted lines). The ω scan (rocking curve) measurement around (002) reveals that the as-grown film has a large mosaicity (Figure 78**c**), while the FWHM decreases by about one order of magnitude after the annealing (Figure 78**g**). The Williamson-Hall plot (Figure 78**d**) yields a value of inhomogeneous strain of 0.2%, once again an order of magnitude larger than the corresponding value after annealing (Figure 78**h**).

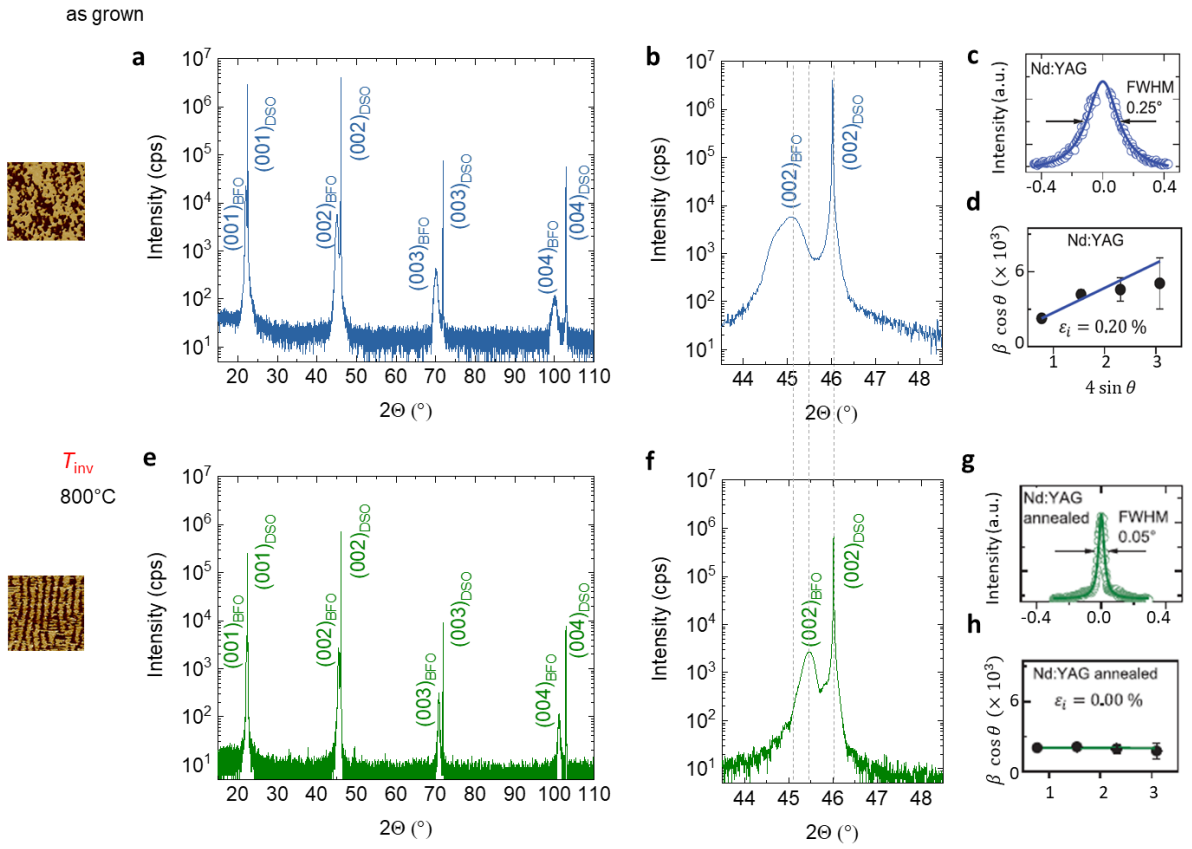

*Figure 78 : **a, b, e, f** 2θ-ω scans, **c, g** rocking curve and **d, h** out-of-plane Williamson-Hall plots of a mosaic $BiFeO_3$ film. **a-d** As-grown film and **e-h** annealed sample. The zoomed-in view (**b, f**) around the (002)-BFO-peak shows the change of the form of the film peak after the annealing step. **c, d, g, h** Adapted from reference [128].*

In contrast to the thin films presented in section 3.1.2 where the strain level in the entire film varied homogeneously, here, the shift of the out-of-plane lattice parameter has to be treated on a subtler level. It turns out that the faster growth rate prevents a direct coupling of the film at the interface. This results in the tilting of the entire unit cells and a strain gradient along the film thickness. In the reciprocal space map in Figure 79**a**, a horizontal splitting of the $BiFeO_3$ (003)-peak is visible. This is not a result of strain relaxation, but pointing out the tilting of the (00l) lattice planes.[129] However, it is remarkable that upon rotation of the sample the splitting narrows significantly, showing that the tilting is mainly of uniaxial nature (Figure 79**b-d**).

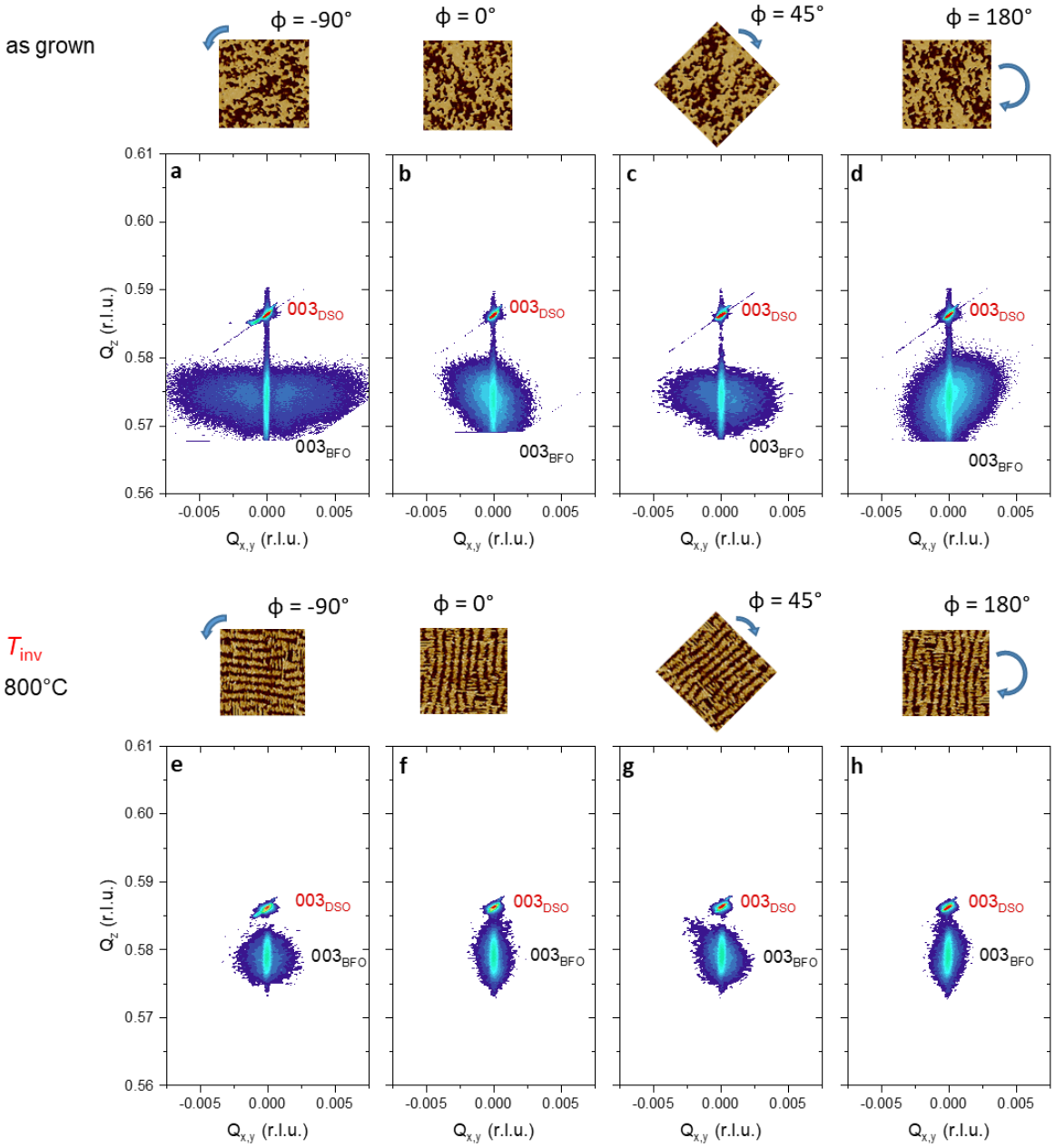

*Figure 79 : Reciprocal space maps analysing the peak-splitting of the symmetrical (003) $BiFeO_3$ peak before (**a-d**) and after the annealing (**e-h**) for different azimuthal angles φ.*

The increase of the crystalline quality and the release of the domain tilting is clearly visible in the scans around the (003) $BiFeO_3$ peaks after annealing (Figure 79**e-h**), where the peak-splitting disappears and the out-of-plane lattice parameter decreases to the value measured for the striped $BiFeO_3$ thin films grown with the excimer laser.

Regarding the in-plane lattice in the asymmetrical reciprocal space maps (Figure 80), a decrease of the Q_z value after annealing shows the release of the tilting as well. Furthermore, we observe two monoclinic domains around the $DyScO_3$ (013), $(\bar{1}\bar{1}3)$ and (113) peak before and after the annealing. In the maps around the $(\bar{1}03)$ and the (103) substrate peak they are overlapping, due to the crystal symmetry (more details on this can be found in section 2.1). Even though the position of the film peaks changes due to variations in the strain of the film, it

confirms the results from the vectorial PFM analysis of two monoclinic domain variants before and after the inverse phase transition. However, because of the tilting and inhomogeneous strain in the film, no strain value can be calculated from the reciprocal space maps in Figure 80.

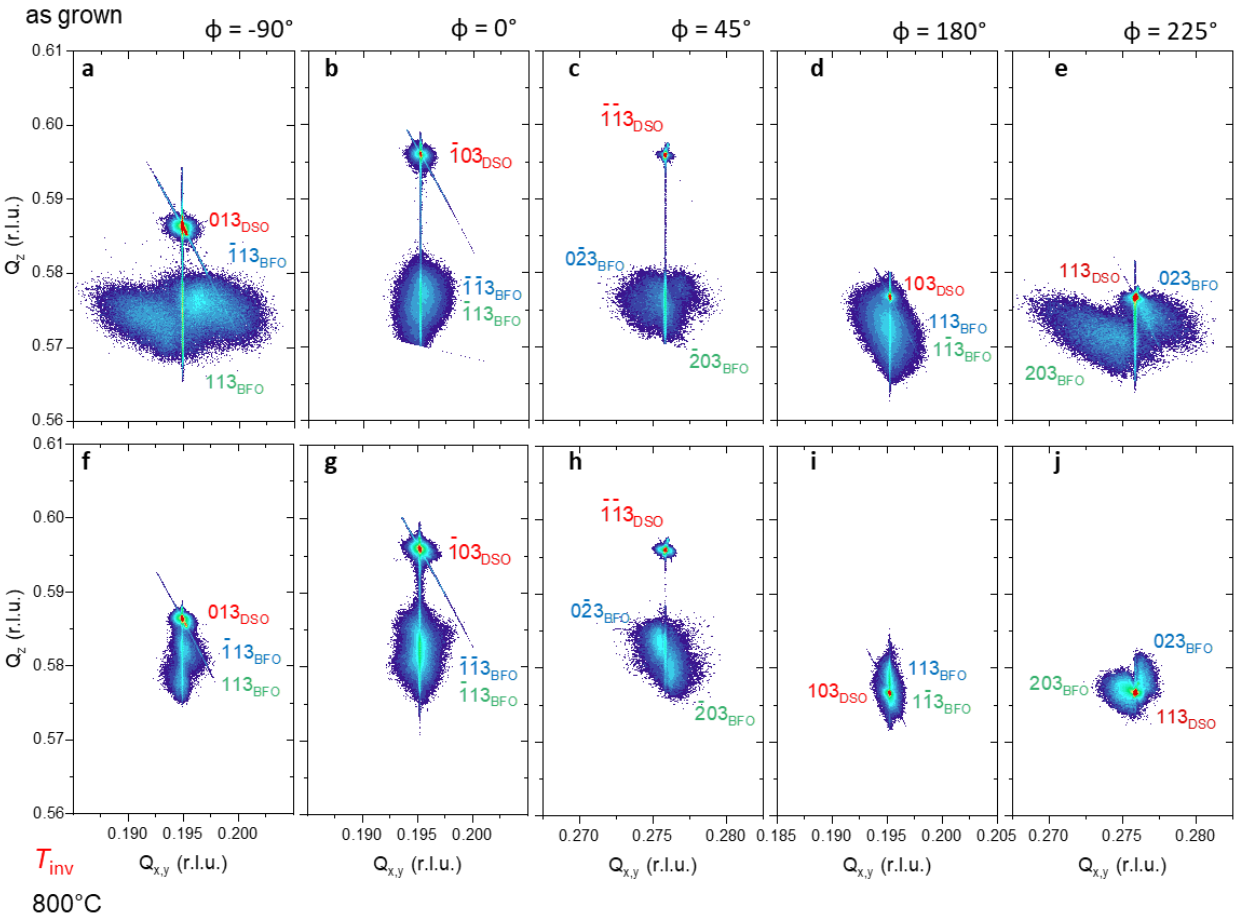

*Figure 80 : Asymmetrical reciprocal space maps of a Nd:YAG $BiFeO_3$ thin film before (**a-e**) and after annealing (**f-j**).*

To conclude this section, it is worth noting that, even though we observed a transition to a higher ordered state with better crystalline quality in all annealed samples from the Nd:YAG laser, the result is not always as stripy as the one shown in Figure 77. It sometimes tends more towards a maze pattern, and the appearance of parasitic $Bi_2Fe_4O_9$ and Fe_2O_3 phases was seen in one case. However, a release of both the tilting and the strain gradient is always observed.

In summary, we highlight an inverse phase transition in ferroelectric thin films of $BiFeO_3$, which seems to contradict a fundamental principle of thermodynamics at first sight. Under continuous heating, the labyrinthine domain pattern in a ferroelectric thin film transforms in a highly ordered striped phase with a lower symmetry, displaying a unidirectional straight arrangement. Numerical investigations, based on an effective Hamiltonian approach derived from first principle calculations, allow for the comprehension of this inverse phase transition due to an increase of the entropic contributions of the domain walls and the diffusions of topological defects they are triggering. The numerical calculations have been executed for standard ferroelectrics such as thin films of $Pb(Zr_{0.4}Ti_{0.6})O_3$ and $BiFeO_3$. The experimental reproducibility of this

phase transition in $BiFeO_3$ thin films on various substrates suggests the universality of this phenomenon in ferroelectric oxides. Conductive mapping of the sample surface with nm-resolution reveals the presence of topological defects, showing a fifty times higher conductivity than at the domain walls. Hence, the inverse transition associated with the diffusion of the topological defects is electrically detectable, opening perspectives for possible applications.

4 A journey into the antiferromagnetic textures of $BiFeO_3$ thin films

$(001)_{pc}$ $BiFeO_3$ thin films are grown on $SrTiO_3$, $DyScO_3$, $TbScO_3$, $GdScO_3$, $SmScO_3$ and $NdScO_3$ substrates using pulsed laser deposition. Details on the growth technique can be found in section 2.2 and the growth optimization is detailed in section 3.1.1. For all samples apart from the one on $NdScO_3$, a thin metallic $SrRuO_3$ electrode is inserted between the substrate and the $BiFeO_3$ thin film for electric switching experiments. The crystallographic lattice is analysed using X-ray diffraction, see section 2.3 for the method and section 3.1.2 for the results. All structurally equivalent samples display a flat surface and high crystalline quality, visible in the Laue-fringes in the 2Θ-ω scans. $BiFeO_3$ film thicknesses are between 30 and 60 nm. Two elastic domain variants are found and can be related directly to the ferroelectric domains imaged with piezoresponse force microscopy (method in section 2.4.2, results in 3.1.2).

We now focus on the magnetic textures in this set of structurally equivalent $BiFeO_3$ thin films (Chapter 3.1.2, Figure 55). Distinguishable only by their strain level (Figure 57-43), they all display a stripy ferroelectric pattern, composed of two polarization variants. We here present the evolution of the antiferromagnetic textures as a function of the epitaxial strain. Scanning NV magnetometry in combination with resonant elastic X-ray scattering is used to examine two different types of spin cycloids and the pure G-type antiferromagnetic order. In a second step, we define single ferroelectric domains with the piezoresponse force microscope. We demonstrate the possibility to change the cycloid propagation direction and eventually even to toggle between the antiferromagnetic ordering and the two types of cycloids. Finally, we investigate the spin textures of a single domain ferroelectric sample. The anisotropic strain in the $(111)_{pc}$ plane favours only one of the three possible cycloidal propagation vectors. Given the pure out-of-plane polarization direction and the single cycloid propagation direction in the sample surface and its rotation plane perpendicular to it, this last $BiFeO_3$ sample would be a fantastic playground to investigate the interplay between spin transport and non-collinear antiferromagnetic textures.

4.1 Strain control of antiferromagnetic textures

In addition to the bulk-like cycloidal order (cycloid type I), epitaxial strain is expected to favour another type of cycloid (so called type II cycloid) or pure G-type antiferromagnetic order. The epitaxial strain imposed by the substrate can be used as setscrew for the prevailing magnetic textures. The two types of cycloid, presented in more detail in Figure 81**a-c,** are distinguishable by their possible propagation directions, marked in light green $\mathbf{k_1}$-$\mathbf{k_3}$ for type I cycloid and violet $\mathbf{k'_1}$-$\mathbf{k'_3}$ for type II. All propagation vectors are contained in the (111) plane orthogonal to the polarization (red arrow). Among all propagation vectors, $\mathbf{k_1}$-$\mathbf{k_3}$ are oriented along $\langle\bar{1}10\rangle$, with $\mathbf{k_1}$, $\mathbf{k_2}$, $\mathbf{k_3}$ along $[\bar{1}10]$, $[0\bar{1}1]$, $[10\bar{1}]$, respectively, and $\mathbf{k'_1}$-$\mathbf{k'_3}$ along $\langle11\bar{2}\rangle$ with $\mathbf{k'_1}$, $\mathbf{k'_2}$, $\mathbf{k'_3}$ along $[\bar{2}11]$, $[1\bar{2}1]$, $[11\bar{2}]$, respectively. For better visibility, they are summarized in three double arrows, each. However, in the experiments we found that only one $\mathbf{k}$-vector is present per ferroelectric domain.

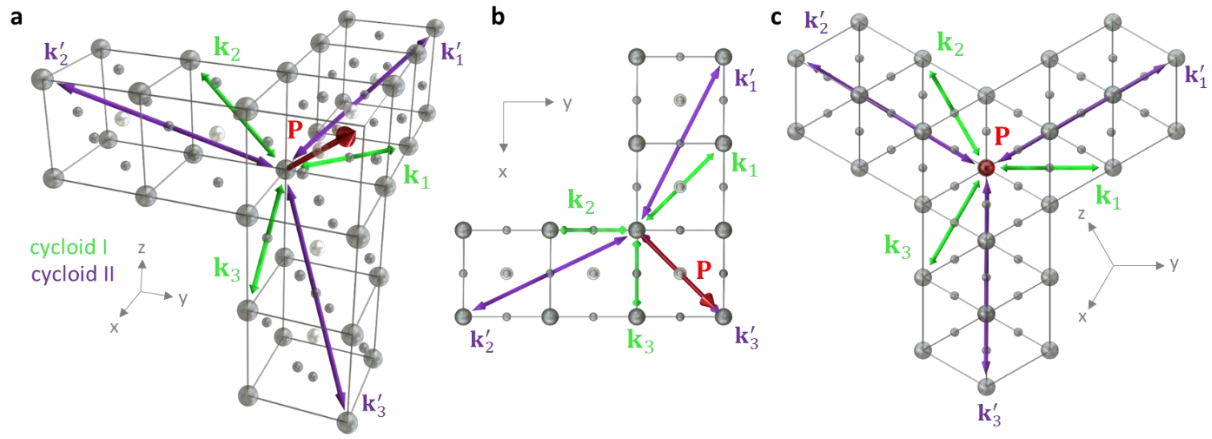

*Figure 81 : Sketches of the different types of spin cycloids in $BiFeO_3$, possible set of propagation vectors **k** for type I and type II cycloids in light green and turquoise, respectively. **a** 3D view, **b** projection on the $(001)_{pc}$ sample surface, and **c** on the $(111)_{pc}$ plane perpendicular to the polarization direction (**P**, red arrow). Figure adapted from reference [136].*

In our $BiFeO_3$ thin films, the exploration of magnetic textures and their interpretation is simplified by the ordered ferroelectric landscape. All samples can be considered as a stripy periodic array of ferroelectric domains ($\mathbf{P_3^-}$ and $\mathbf{P_4^-}$) separated by 71° domain walls (Figure 82**a-f**). For each sample, the corresponding antiferromagnetic spin textures (Figure 82**g-l**) are imaged in real space with a scanning NV-magnetometer operated in dual-iso-**B** imaging mode (methods in section 2.4.3). In the strain range of −1.33% to +0.05%, the NV images display a similar zig-zag pattern of periodic stray fields generated by cycloidal antiferromagnetic orders. More precisely, in each vertical ferroelectric domain (separated by dashed lines in Figure 82**g-j**), we observe a single propagation direction of the spin cycloid. As the in-plane component of the polarization vector rotates from one domain to another, the spin cycloid propagation direction rotates accordingly. This implies a one-to-one correspondence between the ferroelectric and antiferromagnetic domains. A closer look at the different zig-zag patterns indicates a 90-degree in-plane rotation of the cycloidal propagation direction for films grown on $DyScO_3$ (−0.37%) and $TbScO_3$ (−0.10%). This corresponds to cycloid type I with propagation vector $\mathbf{k_1}$, contained in the film plane, for both ferroelectric variants $\mathbf{P_3^-}$ and $\mathbf{P_4^-}$ (Figure 82**m**).

A subtle change of the strain towards the tensile side (+0.05%, $GdScO_3$) greatly influences the magnetic landscape. Indeed, the zig-zag features are no longer orthogonal to each other, but rather at 120° ± 5° (Figure 82**j**) and, therefore, the spin texture can no longer be explained by the bulk-like cycloid type I. The large angle of the zig-zag pattern is only compatible with alternating $\mathbf{k_1'}$, $\mathbf{k_2'}$ propagation vectors of the type II cycloid. We calculate an angle of 127°, projected on the film surface from the sketch in Figure 82**n**. Surprisingly, a similar scenario takes place for large compressive strain (−1.33%, $SrTiO_3$) where the zig-zag angle (Figure 82**g**) is almost the same as for $BiFeO_3$ grown on $GdScO_3$. In contrast, for large tensile strain (+0.47 to +0.93%) corresponding to $BiFeO_3$ films grown on $SmScO_3$ and $NdScO_3$ substrates, the periodic magnetic signal related to spin cycloids is lost (Figure 82**k,l**) and the observed magnetic order can be associated with a pure G-type antiferromagnet without cycloid. In addition, the ferroelectric periodicity formerly detected as the zig-zag pattern is no longer visible in the magnetic

landscape, cancelling the one to one imprint between ferroelectric and magnetic orders for the G-type antiferromagnetic case.

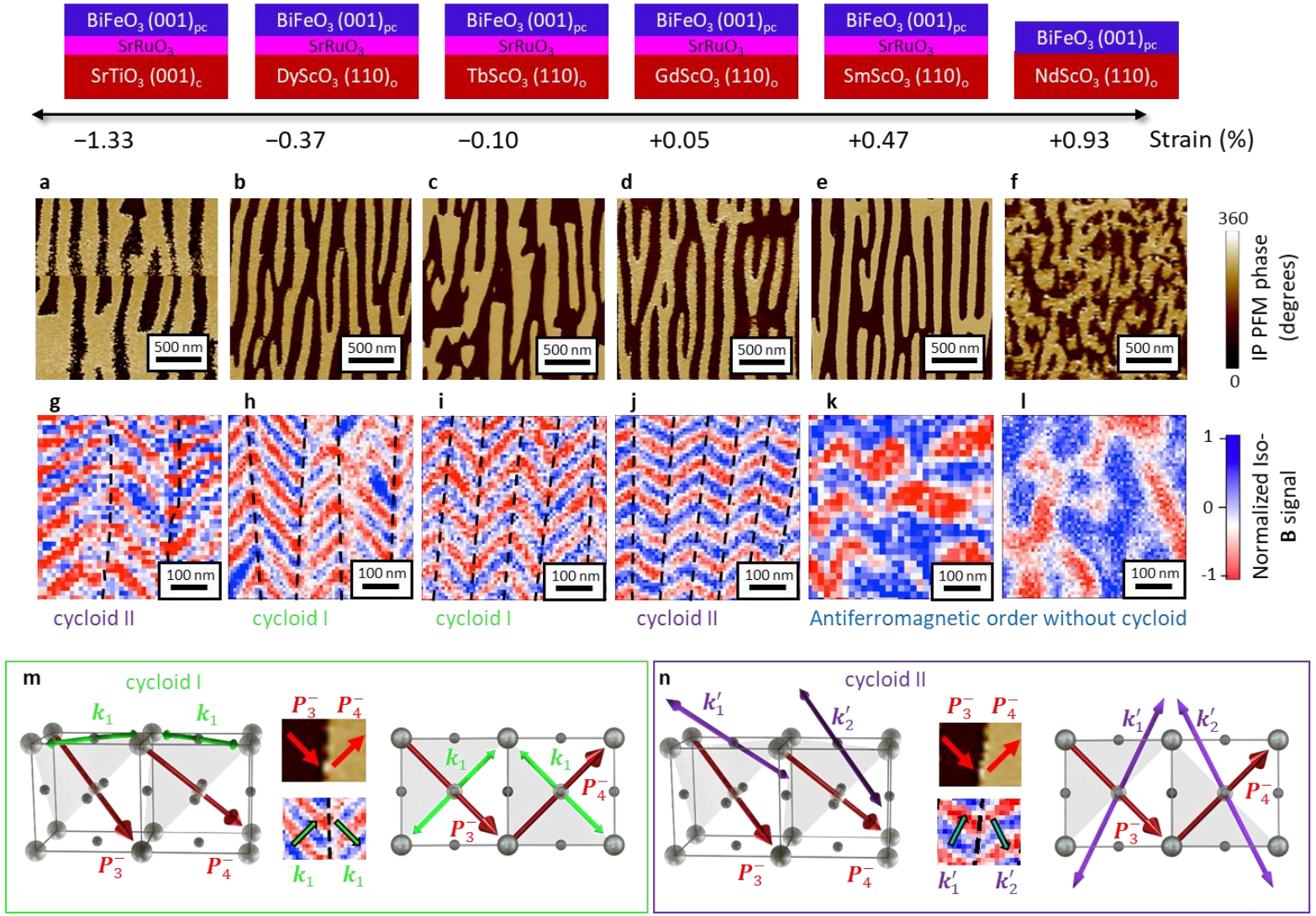

*Figure 82 : **a-f** In-plane PFM phase images of $BiFeO_3$ films grown on substrates imposing different epitaxial strain. **g-l** Corresponding NV-magnetometry images. **m,n** Sketches in side and top views to explain the relation between the ferroelectric variants $\boldsymbol{P_3^-}$ and $\boldsymbol{P_4^-}$ and the magnetic zig-zag patterns for cycloid type I and II, respectively. Figure adapted from reference [136].*

We now want to give a rough estimation of the cycloid period in these films using the Fourier transformations of scanning NV magnetometry images (Figure 83). When the magnetic structure is imaged with NV magnetometry, it is necessary to consider the projection on the $(001)_{pc}$ sample surface (Figure 81**b**). As a result, for all cases except the cycloid I $\mathbf{k_1}$, the apparent cycloid period λ_{surf} is larger than the actual cycloid period λ in the three-dimensional sample, because $\mathbf{k}$ is not contained in the $(001)_{pc}$ plane. λ_{surf} can be calculated for cycloid I, $\mathbf{k_2}$ and $\mathbf{k_3}$ as

$$\lambda_{surf} = \sqrt{2} \cdot \lambda,$$

for cycloid type II, $\mathbf{k_1'}$, $\mathbf{k_2'}$ as

$$\lambda_{surf} = \sqrt{\frac{6}{5}} \cdot \lambda \approx 1.1 \cdot \lambda$$

and $\mathbf{k_3'}$ as

$$\lambda_{surf} = \sqrt{3} \cdot \lambda.$$

Hence, by inverting these equations for the cycloid type I, we obtain close values of $\lambda \approx (69 \pm 7)$ nm for the sample grown on $DyScO_3$ (Figure 83**b**) and $\lambda \approx (68 \pm 7)$ nm for the sample on $TbScO_3$ (Figure 83**c**). For the type II cycloid, the value for $BiFeO_3$ of $\lambda \approx (69 \pm 7)$ nm on $SrTiO_3$ (Figure 83**a**) is slightly larger than the period of $\lambda \approx (64 \pm 7)$ nm for the sample grown on $GdScO_3$ (Figure 83**d**). We suppose that this difference can be assigned to the different strain level in the samples, although there is no reference period for the type II cycloid.

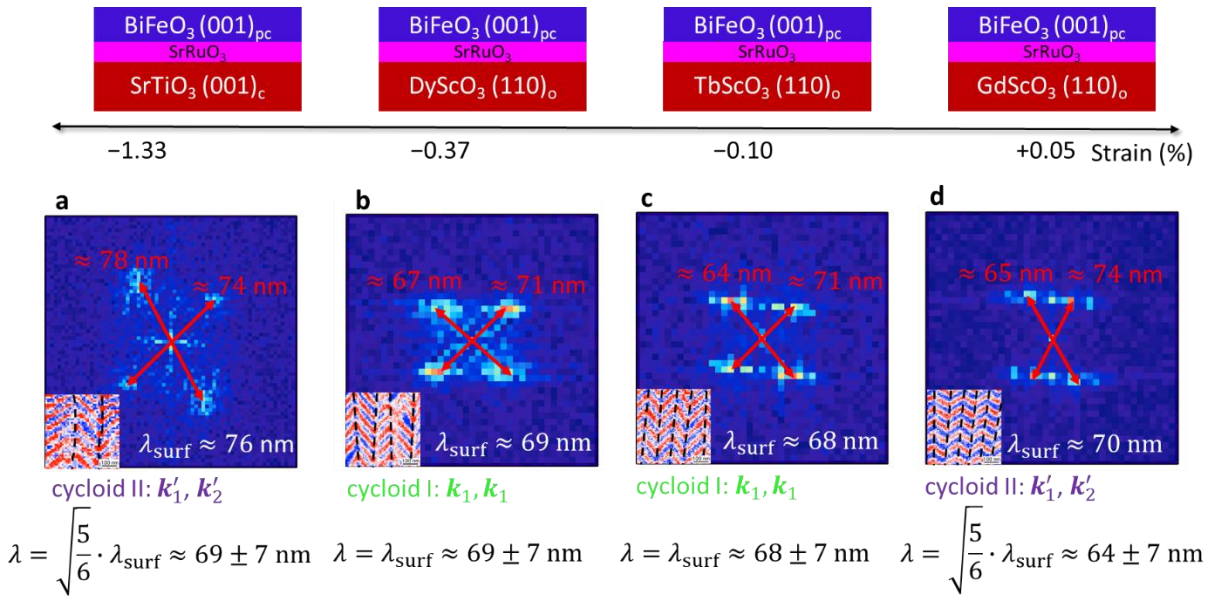

*Figure 83 : Fourier transformations of the scanning NV magnetometry images on cycloidal states in Figure 82**g-j**. Calculated cycloid wavelengths λ from the projections on the surface (λ_{surf}) for samples grown on **a** $SrTiO_3$, **b** $DyScO_3$, **c** $TbScO_3$ and **d** $GdScO_3$.*

4.2 Insights into the different cycloids using resonant X-ray scattering

A complementary macroscopic investigation to further corroborate the nanoscale real-space images of the magnetic arrangements is resonant elastic X-ray scattering (REXS). For details on this technique, see section 2.5. The spin cycloid is a periodic magnetic object, giving rise to a diffraction pattern at the Fe resonant L-edge. In order to highlight the diffracted signal of magnetic origin only, the difference between left and right polarized light is plotted as a dichroic diffracted pattern (Figure 84**a**, **c,** red and blue correspond to positive and negative dichroism, respectively). In both diagonals from the specular spot, the inverted contrast between +q and −q spots is a signature of chirality. Indeed, $BiFeO_3$ spin cycloids in which spins rotate in a plane defined by the polarization ($\mathbf{P}$) and the propagation vector ($\mathbf{k}$) are chiral objects. Data are taken on $BiFeO_3$ samples grown on $DyScO_3$ (cycloid I) and $GdScO_3$ (cycloid II) substrates (Figure 84**a** and **c,** respectively).

For $BiFeO_3$ thin films grown on $DyScO_3$, the presence of two orthogonal cycloid propagation directions (light green arrows in Figure 84**a**) with identical periods gives rise to two orthogonal lines of diffracted spots, thus defining a square diffracted pattern. The fine structure of this pattern is rendered more complex by additional spots that arise from the modulation of the magnetic periodicity by the ferroelectric domain structure. However, here our focus is on the cycloid propagation direction and periodicity. The spacing between the +q and −q spots corresponds to a cycloid period of $\lambda \approx 72 \pm 5\ \mathrm{nm}$ for both spin cycloids with $\mathbf{k_1}$ propagation vector. Consistently at the local scale, the combination of PFM and scanning NV magnetometry allows to identify the relative orientation of the ferroelectric polarizations ($\mathbf{P_3^-}$ and $\mathbf{P_4^-}$, red arrows in Figure 84**b**) and cycloid propagation direction ($\mathbf{k_1}$, light green arrows in Figure 84**b**) on both sides of a domain wall. Thus, our microscopic real-space experiments and macroscopic reciprocal-space observations both attest for a single cycloidal vector ($\mathbf{k_1}$) in $BiFeO_3$ thin films under moderate compressive strain.

In contrast, for $BiFeO_3$ films grown on $GdScO_3$ imposing slight tensile strain, the dichroic diffracted pattern is no longer square-shaped but rectangular (Figure 84**c**). Hence, we exclude the above-mentioned scenario with two bulk-like (cycloid I) orthogonal vectors. The two diagonals of the rectangular pattern (turquoise arrows in Figure 84**c**) form an angle of about 115° ± 5°, in accordance with the typical angles observed in NV magnetometry images (Figure 82**j**). The only plausible scenario, therefore, corresponds to two types of ferroelectric domains, respectively harbouring alternating $\mathbf{k_1'}$, $\mathbf{k_2'}$ propagation vectors of the cycloid type II, as observed in real space (Figure 84**d**). Consequently, these cycloidal $BiFeO_3$ films, under either compressive or tensile strain, exhibit a one-to-one imprint between ferroelectric and antiferromagnetic order. Taking into account the projection on the sample surface, we calculate a cycloid period of $\lambda \approx 69 \pm 5\ \mathrm{nm}$ for the type II cycloid. Considering the uncertainties for both NV-centre magnetometry and X-ray resonant magnetic scattering, the same tendency is observed with a slightly smaller period for the sample with type II cycloid, grown on $GdScO_3$, than for the type I cycloid grown on $DyScO_3$.

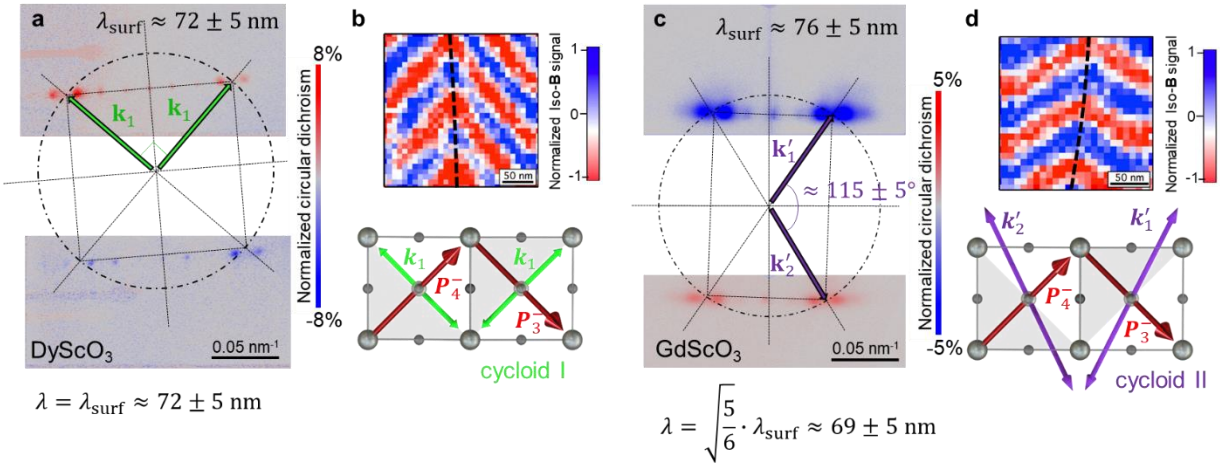

Figure 84 : The two types of spin cycloids in real and reciprocal spaces. ***a, c*** *X-ray resonant magnetic scattering at the Fe L-edge for $BiFeO_3$ grown on $DyScO_3$ and $GdScO_3$, repectively.* ***b, d*** *Corresponding NV magnetometry image zoomed in, with the propagation vectors sketched for both polarization variants. Figure adapted from reference [136].*

To conclude this study on the influence of epitaxial strain on the antiferromagnetic textures, we compare our results using NV magnetometry and resonant elastic X-ray scattering, to the ones from Daniel Sando *et al.* from Mössbauer and Raman spectroscopy. Data are taken from reference [102] and private communication. In Figure 85, the upper panel presents results from studies carried out in the past years. $BiFeO_3$ samples have been grown using an excimer laser and a Nd:YAG laser growth chamber. By the choice of the growth chamber, the epitaxial strain imposed in the $BiFeO_3$ thin film can be influenced significantly, changing the observed antiferromagnetic textures. Regarding the results, presented in this thesis (summarized in the lower panel), slight modifications in the antiferromagnetic phase diagram need to be considered. Whereas previously only the type I cycloid has been reported on the compressive strain side, we observe the type II cycloid in $BiFeO_3$ samples grown on $SrTiO_3$. For the samples grown on $DyScO_3$, $TbScO_3$ and $GdScO_3$, our results are in good agreement, but for $SmScO_3$, we again obtain a contradictory result. NV-centre magnetometry reveals more prominently pure G-type antiferromagnetic order and no type II cycloid. Additionally, we investigate a sample grown on $NdScO_3$, representing an intermediate strain level between $SmScO_3$ and $PrScO_3$ and confirm G-type order on the tensile side at higher strain levels.

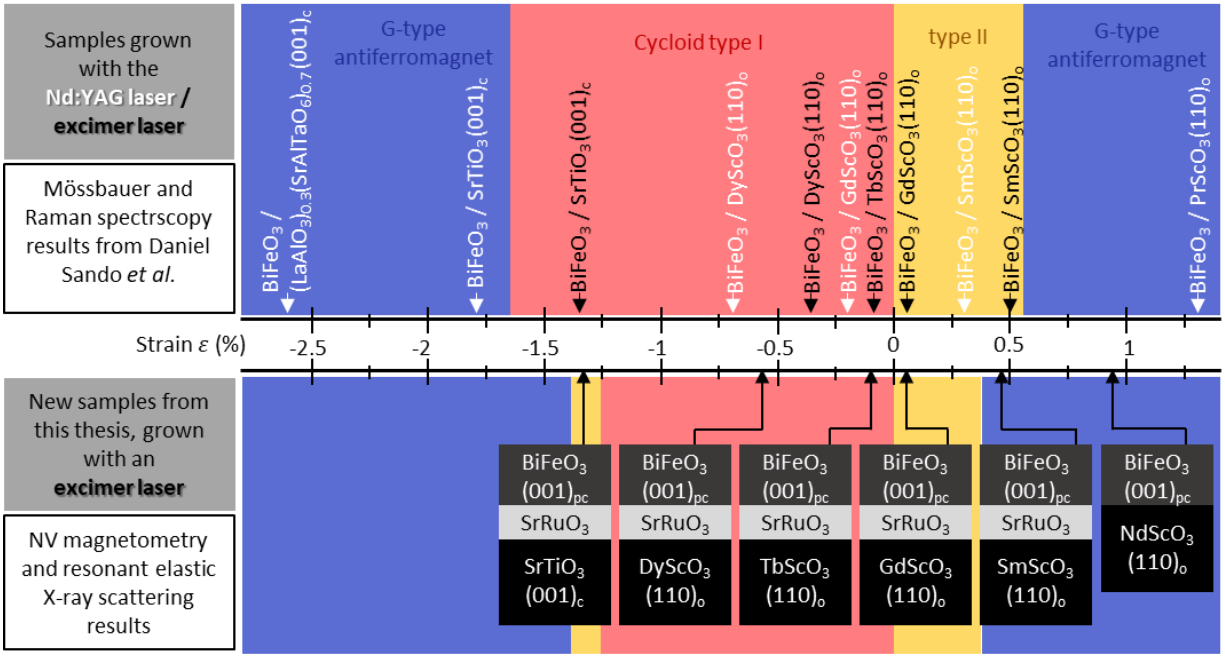

Figure 85 : Modifications in the antiferromagnetic phase diagram, comparing results from Daniel Sando et al. (reference [102]) and private communication in the upper panel) to the results presented in this thesis (lower panel).

4.3 Electric control of antiferromagnetic textures

Beyond the observations in pristine configurations of ferroelectric domains in which the cycloid propagation is locked onto the polarization, we now manipulate the ferroelectric order via electric fields, with the aim to design antiferromagnetic landscapes on demand. We first use PFM to write micron-size ferroelectric domains by virtue of the so-called trailing field (details about the method in section 2.4.2).[118,137]

An example on a $BiFeO_3/SrRuO_3//DyScO_3$ sample is shown in Figure 86. During the lithography process, markers are patterned next to the microwave antenna (Figure 86**a**) to localize the different written areas in PFM and scanning NV magnetometry. The vectorial analysis (chapter 2.4.2) of the out-of-plane and in-plane PFM images (Figure 86**b**) show a ferroelectric monodomain of 1 x 3 μm^2 with polarization **P** indicated in red. The bright out-of-plane phase contrast indicates a downwards polarization. In the first position of the in-plane PFM analysis, the PFM phase is not defined and the amplitude is close to zero, because the polarization is parallel to the cantilever. For the second in-plane position, the bright phase contrast indicates that **P** is pointing to the left of the image. When scanning NV magnetometry is subsequently performed on the same area, we can use the markers next to the microwave line for positioning. A combination of multiple images is used to correlate accurately the PFM and the NV magnetometry images (Figure 86**c**) and determine the precise location of the written ferroelectric domain. In this example, we observe that the ferroelectric single domain induces a single spin cycloid with a vertical propagation vector, as sketched in the inset of Figure 86**c**.

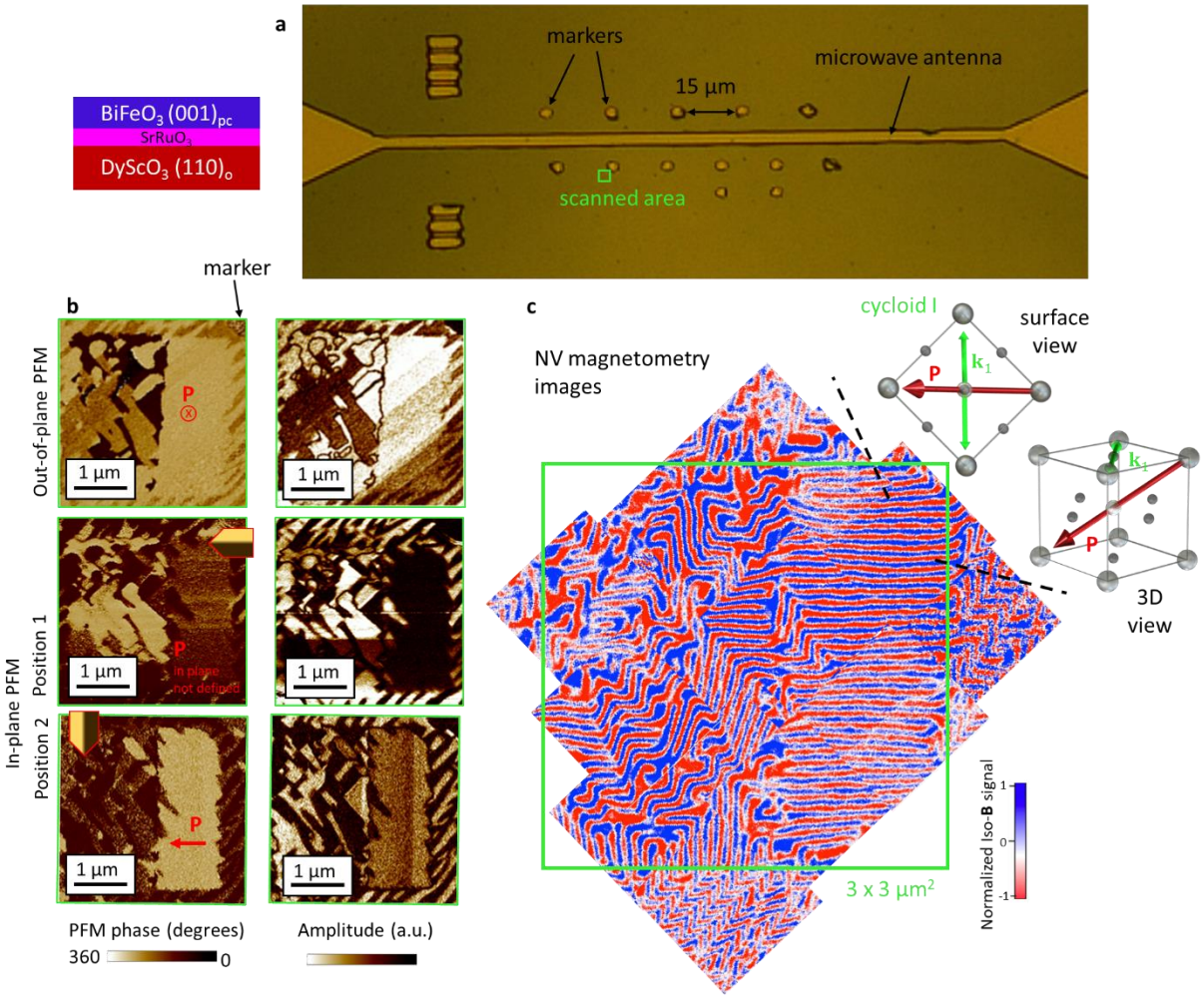

Figure 86 : Antenna and markers defined to spatially correlate PFM and NV imaging. ***a*** *Optical microscope image.* ***b*** *PFM images in the scanned area (green square in* ***a****). Out-of-plane PFM phase and amplitude (top) as well as in plane PFM phase and amplitude from two different positions (middle and bottom) indicated by the schematic PFM tip.* ***c*** *Scanning NV magnetometry images assembled in a patchwork to correlate them to the PFM. The single ferroelectric domain corresponds to a single spin cycloid with a propagation vector in the film plane.*

Following the same procedure, monodomains are written on samples grown on $TbScO_3$, $GdScO_3$ and $SmScO_3$ (Figure 87**a-c**). Again, a vectorial analysis combining out-of-plane and in-plane data is carried out to assign the indicated polarization direction. The two in-plane PFM measurement positions are at an angle of 45° with respect to the polarization direction. Hence, a bright in-plane PFM amplitude is generally observed, and the combination of the in-plane PFM phase signal for both positions is necessary to unambiguously determine the direction of **P**.

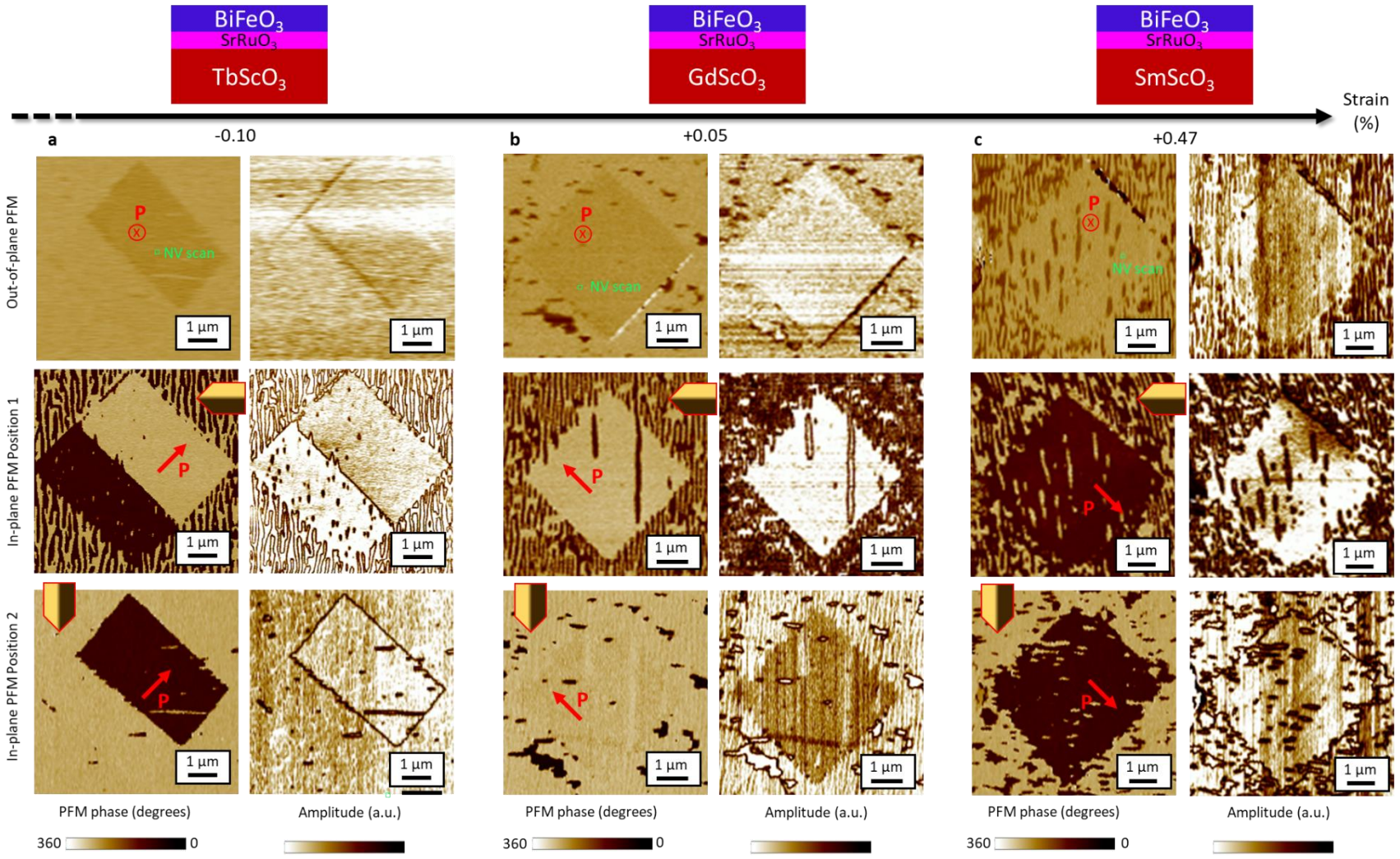

Figure 87: *PFM images of artificially written ferroelectric single domains. Out-of-plane PFM phase and amplitude as well as in plane PFM phase and amplitude from two different positions indicated by the schematic PFM tip for $BiFeO_3$ films grown on* ***a*** *$TbScO_3$,* ***b*** *$GdScO_3$ and* ***c*** *$SmScO_3$. The out-of-plane and in-plane components of the polarization direction* ***P*** *are indicated in red.*

Scanning NV magnetometry is then performed on these artificial domains to reveal the corresponding magnetic textures (Figure 88**a-d**). For the sake of easy comparability, these images are all represented with **P** pointing in the same direction and hence rotated with respect to their corresponding PFM images in Figure 86 and Figure 87.

For strain states ranging from −0.37% to +0.47%, single ferroelectric domains always correspond to a spin cycloid with a single propagation vector. For $BiFeO_3$ films grown on $DyScO_3$ (−0.37%, Figure 88**a**) or $TbScO_3$ (−0.10%, Figure 88**b**), the spin cycloid propagates in a direction perpendicular to the ferroelectric polarization. This implies that the in-plane $\mathbf{k_1}$ propagation is still favoured, switching from two pristine type I cycloids to a single written type I cycloid. Interestingly, the spin cycloid period λ decreases from about (78 ± 5) nm in the pristine (two domain) state to (65 ± 2) nm for the switched (single domain) state.

In single domains, the spin cycloid period thus appears closer to that observed in bulk $BiFeO_3$ (λ_{bulk}= 64 nm[60]) and one may conclude that the writing process modifies the strain state of the $BiFeO_3$ films. Using microdiffraction experiments (Figure 89), we looked at the influence of the writing processes on the strain state of the films. Microdiffraction experiments were carried out by our collaborator Y. A. Birkhölzer from the University of Twente on a $BiFeO_3$ sample grown on $DyScO_3$.[136] For precise alignment and orientation on the sample, a lithographically defined hard mask of 90 nm thick Au with 30 x 30 μm^2 wide square openings is deposited by sputtering and lift-off prior to the microdiffraction experiments. Selected written (Figure 89**c, d**) and pristine (Figure 89**b**) areas, with different domain wall densities, are first analysed by PFM (insets in Figure 89**b-d**) and subsequently by microdiffraction to obtain local structural information. All three areas show identical structural properties (Figure 89**a**-**d**) despite the large variations in domain configurations, ruling out different strain states between artificially written and as-grown domains in $BiFeO_3$ thin films. Consequently, the reduced cycloidal period in written domains compared to pristine striped domains suggests that periodic electric/elastic boundary conditions influence the cycloid period.

For $BiFeO_3$ films grown on $GdScO_3$ (+0.05%, Figure 88**c**), the spin cycloid propagates horizontally, i.e. at 45° from the in-plane polarization variant of the single ferroelectric domain. This implies that the cycloid type I out-of-plane propagation vector ($\mathbf{k_2}$) is selected, corresponding to a switching from two type II cycloids ($\mathbf{k_1'}$, $\mathbf{k_2'}$) to a single type I cycloid ($\mathbf{k_2}$). In addtion, the apparent cycloid period of (92 ± 3) nm in the single domain is compatible with its projection onto the sample surface ($\lambda_{\mathrm{surf}} = \sqrt{2} \cdot \lambda$), giving rise to an intrinsic period of λ = (65 ± 2) nm, close to the bulk value. These experiments on single domains suggest that strain primarily has an influence on the direction of the bulk-like cycloid propagation (in-plane for compressive and out-of-plane for tensile strains).

In the case of $BiFeO_3$ films grown on $SmScO_3$ (+0.47%, Figure 88**d**), the cycloid is observed to propagate in a direction almost parallel to the in-plane variant of the polarization. Considering the three vectors of each cycloidal type (Figure 81), this is only compatible with the $\mathbf{k_3'}$ propagation vector of a cycloid II. In this case, we find an apparent cycloid period of (146 ± 5) nm leading to an intrinsic period of (84 ± 3) nm ($\lambda_{\mathrm{surf}} = \sqrt{3} \cdot \lambda$). The enhanced period compared to

the bulk value is here attributed to the significant tensile strain of $BiFeO_3$ films grown on $SmScO_3$.[111] In this latter example, we have demonstrated electric-field switching from a pseudo-collinear G-type antiferromagnetic order to a non-collinear cycloidal state.

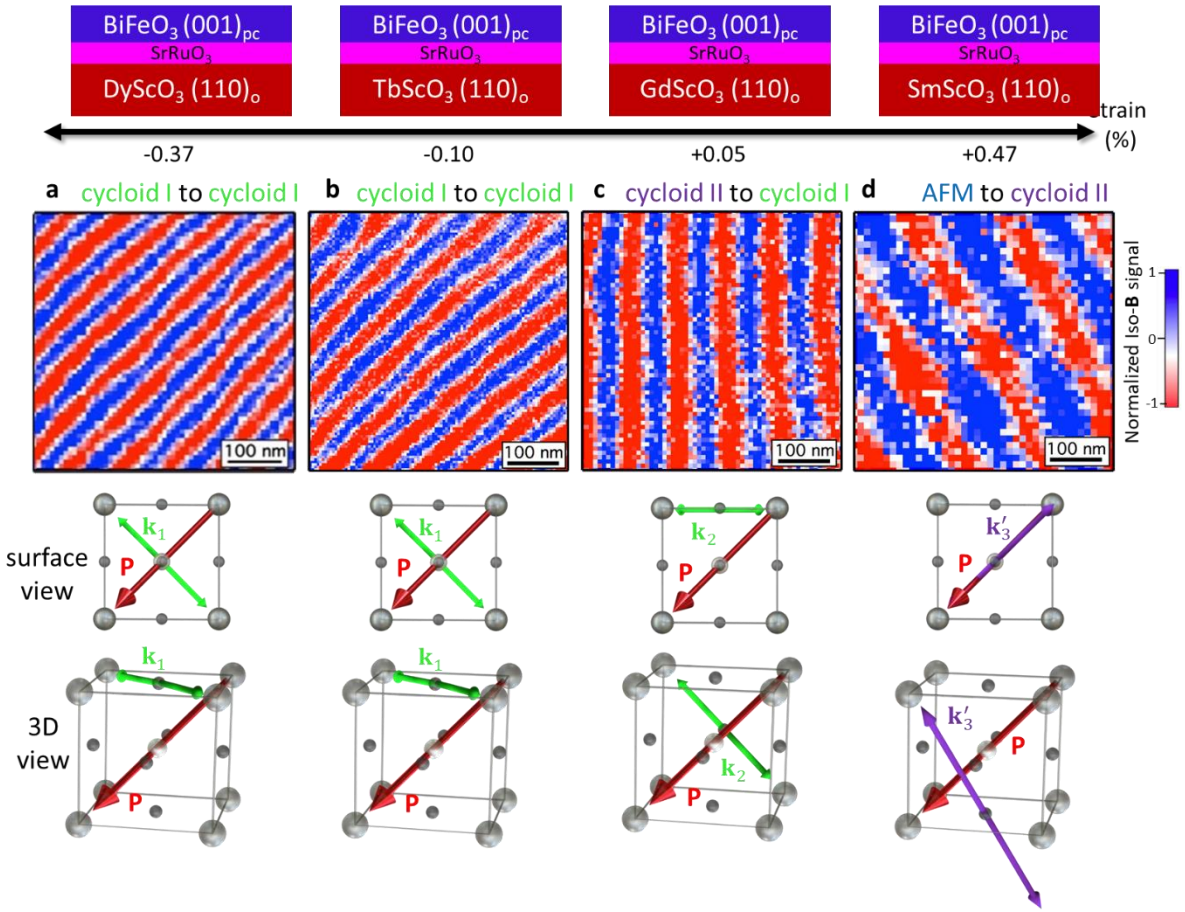

Figure 88 : Magnetic textures in electrically written single ferroelectric domains. ***a-d*** *Corresponding NV magnetometry images and sketches of the propagation vectors in the written zones of the $BiFeO_3$ thin films grown on $DyScO_3$, $TbScO_3$, $GdScO_3$ and $SmScO_3$, shown in Figure 86 and Figure 87, respectively. Figure adapted from reference [136].*

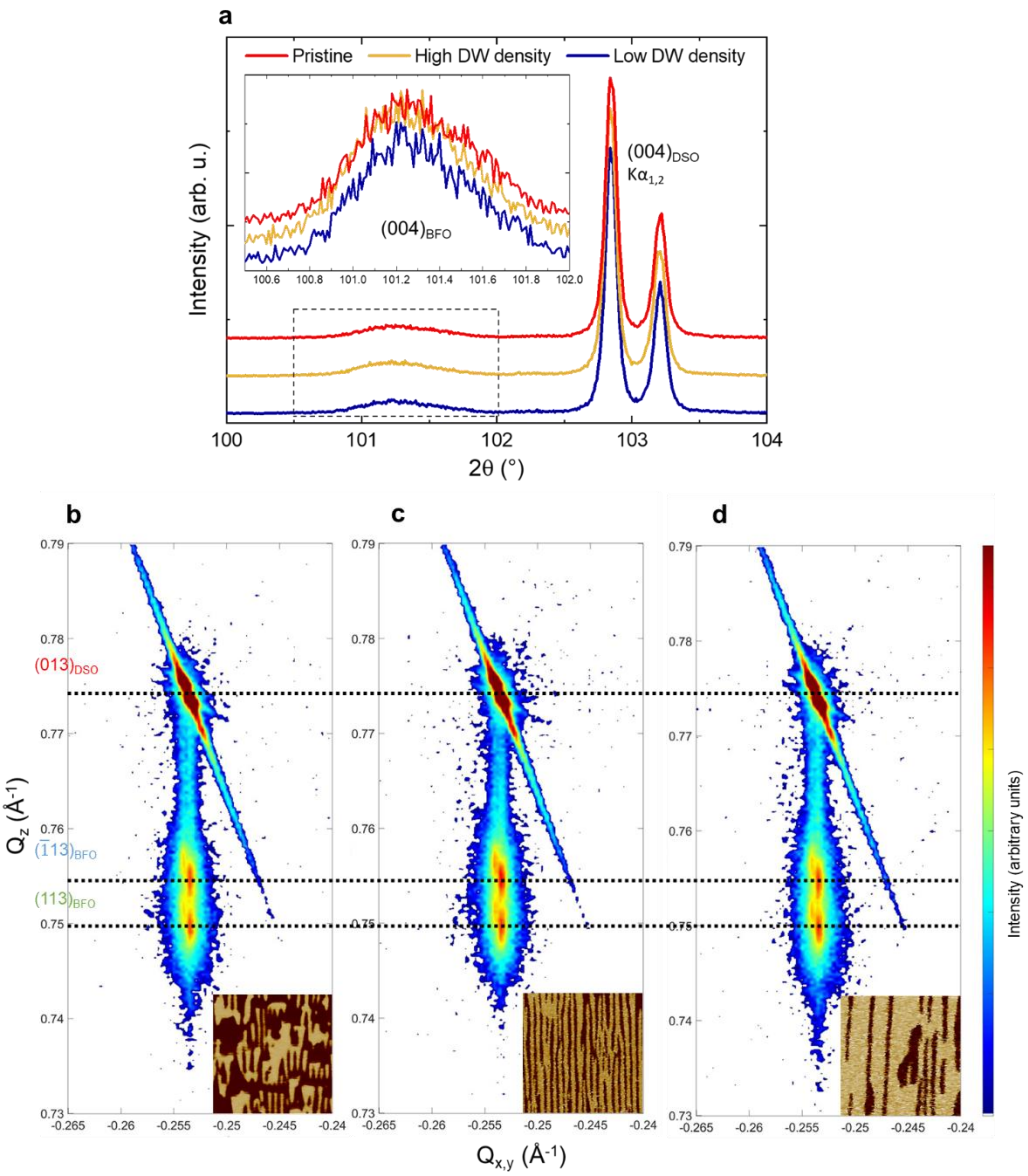

*Figure 89 : Microdiffraction on pristine and written areas of a $BiFeO_3$ thin film grown on $DyScO_3$. **a** 2θ−ω XRD scans of the (004) peaks and **b-d** RSMs around the (013) substrate peak collected from a pristine area (**b**), a written area with high domain wall (DW) density (**c**), and a written area with low domain wall density (**d**). The dotted horizontal lines are guides to the eye to aid comparison. The insets in panels (**b-d**) show 4 x 4 μm^2 in-plane PFM phase images of the areas measured by microdiffraction. Figure adapted from reference [136].*

From these experiments, we observe that the electric-field modification of striped domains to artificially-written single domains either influences the period of the spin cycloid or leads to more dramatic changes, such as a change of the cycloidal type or a collinear to non-collinear transition. Overall, these results suggest that combining strain and electric field results in a complex zoology of antiferromagnetic textures in $(001)_{pc}$-oriented films of $BiFeO_3$.

4.4 As grown single antiferromagnetic domains

We now apply the same experimental techniques to investigate the antiferromagnetic textures in the single ferroelectric domain sample, presented in chapter 3.2. In the crystallographic analysis on this $BiFeO_3$ $(111)_{pc}$ sample grown on $DyScO_3$ $(011)_o$, we demonstrate there, that the degeneracy between the three possible propagation directions in the $(111)_{pc}$ sample plane (Figure 90**a**) is lifted by a small anisotropic strain imposed by the substrate. Here, we reveal that this anisotropic strain has a strong impact on the magnetic textures of $BiFeO_3$ and favours one cycloidal propagation vector over the two others. This is illustrated in Figure 90**b** with an exaggerated sketch to make the distortion visible. As a result, the geometrical relations in this sample can be considered as a perfect reference frame to analyse the properties of the spin cycloid. With the polarization perpendicular to the sample surface, the rotation plane of the cycloid is expected to be vertical (Figure 90**c**).

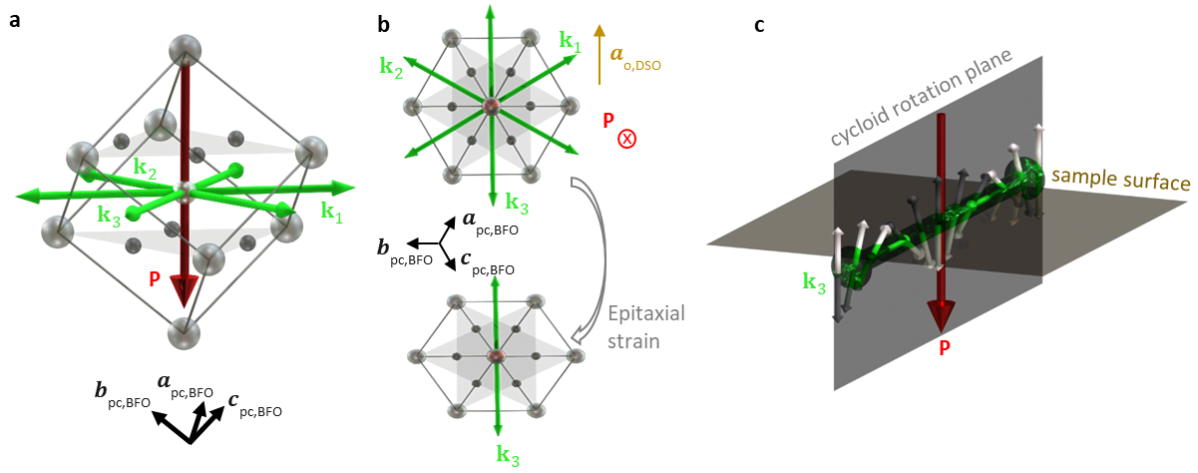

*Figure 90 : Relation between the polarization direction **P** and the possible cycloid propagation directions for a $BiFeO_3$ $(111)_{pc}$ sample grown on $DyScO_3$ $(011)_o$. **a** 3D-view, **b** Surface view: bulk-like and when grown under anisotropic epitaxial strain on the orthorhombic substrate (the deformation is exaggerated to be visible). **c** Rotation plane of the cycloid, spanned by the propagation direction and the polarization vector, perpendicular to the sample surface.*

In Figure 91**a**, we show a vectorial PFM analysis in which the pure out-of-plane ferroelectric polarization direction is coherent with the undefined in-plane PFM phase and vanishing amplitude, measured from two different positions. The scanning NV magnetometry image (Figure 91**b**) supports the crystallographic analysis and indicates that only one of the three in-plane propagation vectors of the type I cycloid is present in our films, with $\mathbf{k_2}$ propagation vector parallel to the a_o axis of the $DyScO_3$ substrate. These observations are confirmed in multiple locations of the $BiFeO_3$ sample and the Fourier transformation analysis of the NV images leads to a calculated wavelength of $\lambda \approx (71 \pm 7)\ \mathrm{nm}$. It appears that the small compressive strain along $\mathbf{k_3}$ in these (111) films favours this propagation vector over the other two. This is somehow similar to the $\mathbf{k_1}$ propagation vector for (001) films that is favoured by biaxial compressive strain on $DyScO_3$ while out-of-plane $\mathbf{k_{2,3}}$ propagation vectors tend to be stabilized for small tensile strain, as in $GdScO_3$.

In order to characterize macroscopically the antiferromagnetic order in these films, we performed REXS experiments at the SEXTANTS beamline of SOLEIL synchrotron. Measurements at

the Fe L edge indicate a single pair of diffraction spots around the specular (Figure 91**c**). The inverted dichroic signal between the +q and -q spots with a contrast of more than 50% indicates that this pair of diffraction spots is the signature of a single spin cycloid present all over the sample. The propagation direction is confirmed to be along the a_o axis of the $DyScO_3$ substrate, hence corresponding to the $\mathbf{k_3}$ propagation vector. From the distance between the +q and -q spots, a cycloid period of $\lambda \approx (76 \pm 5)\ \mathrm{nm}$ is estimated in close agreement with scanning NV magnetometry experiments. The azimuthal dependence of the REXS signal has been performed and we observe that the dichroic signal changes its sign with the angle for both the +q and -q spots. We are currently investigating carefully this angular dependence with theoretician colleagues in order to obtain more insights in this unique spin cycloid.

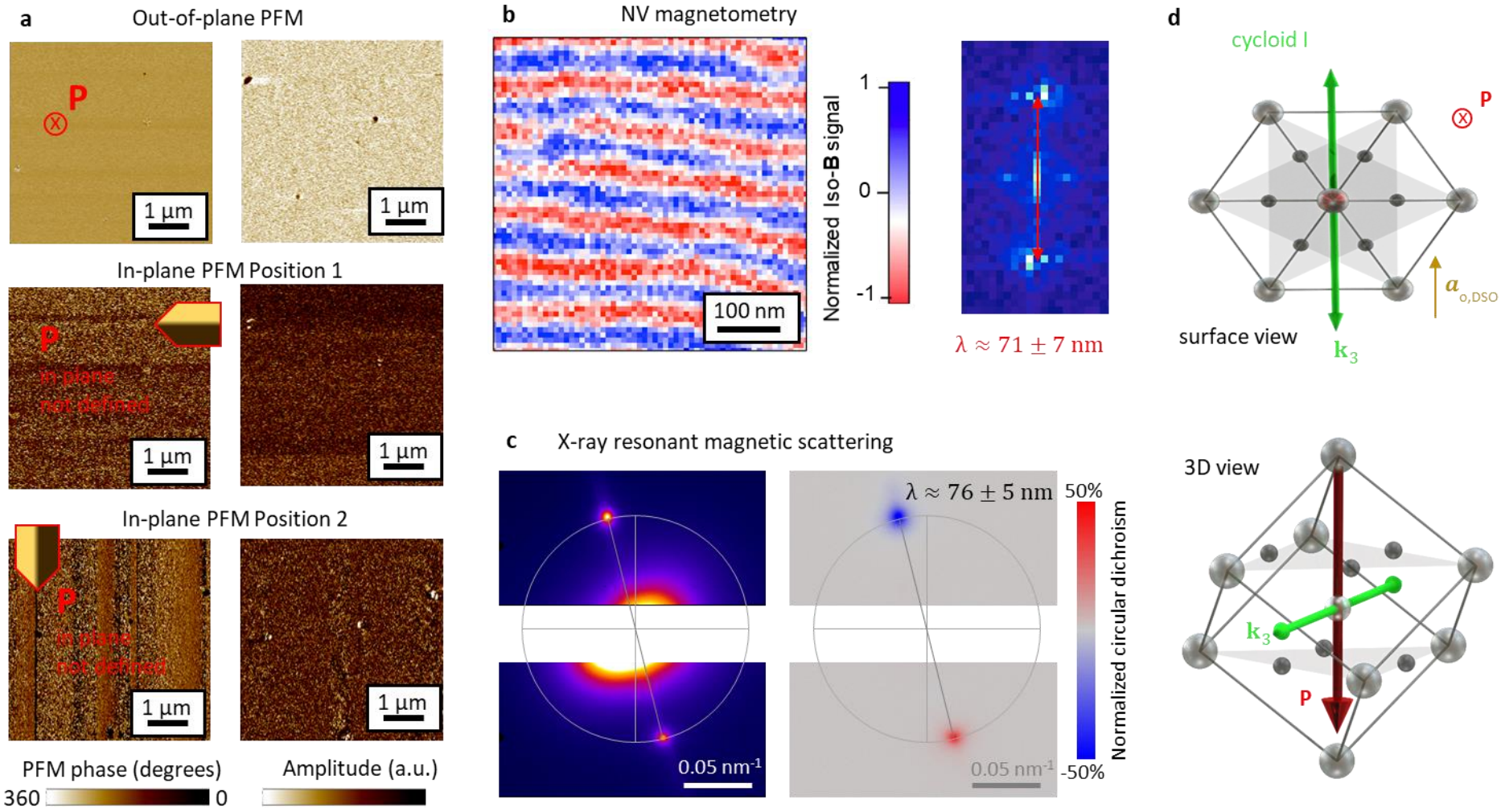

*Figure 91 : Analysis of the electric and magnetic landscapes in a $BiFeO_3$ $(111)_{pc}$ sample grown on $DyScO_3$ $(011)_o$. **a** Vectorial PFM analysis, showing a vertical polarization, pointing downwards. **b** Scanning NV magnetometry image with its Fourier transformation, **c** resonant elastic X-ray scattering pattern at the Fe L edge and the corresponding circular dichroism pattern and **d** sketches for the corresponding configuration of the polarization **P** and cycloid propagation direction **k**.*

Finally, we investigate the switching behaviour in this $BiFeO_3$ thin film using the electric field from a scanning AFM tip. The PFM images in the written zone indicate that the polarization is switched by 180°, pointing upwards without any in-plane components (Figure 92**a**). The associated antiferromagnetic texture remains unchanged (Figure 92**a**) with the same cycloidal periodicity. However, given the fact that the polarization is reversed, as depicted in the sketch in Figure 92**c**, this indicates a reversal of the cycloidal chirality which should be examined more in detail.

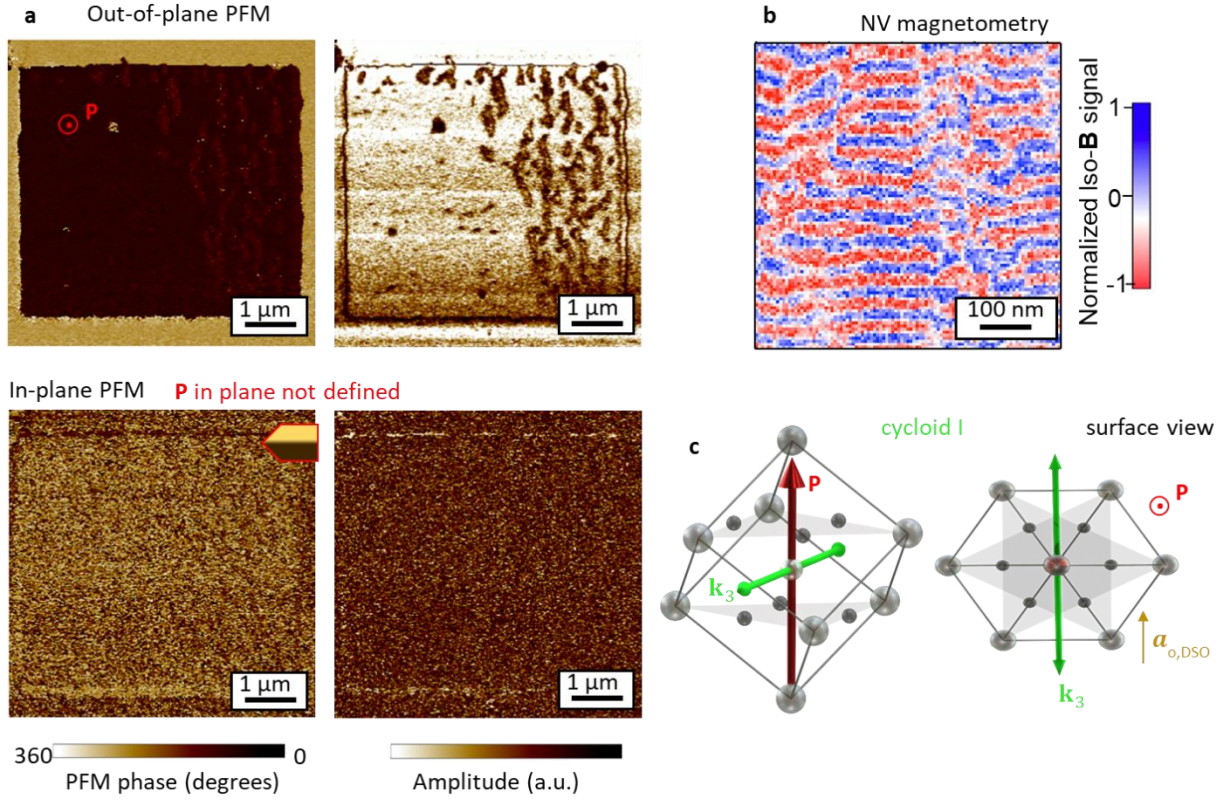

*Figure 92 : **a** Written ferroelectric domain, pointing upwards. The absence of the in-plane PFM signal is in line with a vertical polarization. **b** Scanning NV-magnetometry image of a scan inside the written zone and **c** sketches for the corresponding configuration of the polarization **P** and cycloid propagation direction **k**.*

Conclusions and perspectives

The work presented in this thesis is devoted to the investigation of the ferroelectric and antiferromagnetic domain patterns in the room-temperature multiferroic oxide, $BiFeO_3$, and their interrelations. On the material side, a main achievement is the elaboration by pulsed laser deposition of strain-engineered $BiFeO_3$ thin films over a wide range of strain, using appropriate substrates. We conducted a detailed structural X-ray diffraction analysis to precisely determine the monoclinic lattice parameters, as well as the exact strain level. The atomically flat films are of high epitaxial quality. In perfect agreement with the elastic domains observed in the X-ray diffraction analysis, we map ordered ferroelectric landscapes such as a periodic array of two domain variants or a single ferroelectric domain, imaged with piezoresponse force microscopy.

In two-domain $BiFeO_3$ samples, we observe evidence for an unusual phase transition where the labyrinthine arrangement of ferroelectric domains transforms to a higher, striped order with increasing temperature. We experimentally demonstrate this effect via an a posteriori annealing step in our $BiFeO_3$ films, while this effect was so far only predicted from ferroelectric $Pb(Zr_{0.4}Ti_{0.6})O_3$. Our observations support the inverse phase transition theory proposed by our collaborators from the University of Arkansas. From a microscopic thermodynamics point of view, this maze-to-stripe phase transition is counterintuitive as the global electrical order increases with increasing temperature. Nevertheless, it is not contradicting any fundamental law and is only inverse on the mesoscopic scale.

Using a non-invasive scanning magnetometer based on a single nitrogen-vacancy defect in diamond, we present the first real-space visualization of a room-temperature magnetic phase diagram as a function of epitaxial strain in antiferromagnetic $BiFeO_3$ thin films. We demonstrate that a fine tuning of the epitaxial strain stabilizes different types of non-collinear antiferromagnetic states (bulk-like and exotic spin cycloids), as well as collinear antiferromagnetic textures, in as-grown $BiFeO_3$ thin films. In addition, we macroscopically confirm the existence of both types of cycloids using resonant elastic X-ray scattering. In contrast to previous studies, we are able to reveal the exotic type II cycloid in both tensile and compressive strained films, suggesting a symmetry of the antiferromagnetic phase diagram around zero epitaxial strain.

We furthermore take advantage of the magnetoelectric coupling in $BiFeO_3$, to deterministically control the antiferromagnetic textures using an electric field. The modification of the ferroelectric landscape via local electric fields allows us (i) to deterministically control the spin cycloid propagation, (ii) to switch from one type of antiferromagnetic spin cycloid to another or (iii) to convert a collinear antiferromagnetic texture to a spin cycloid. Our results highlight the unique potential of the combination of piezoresponse force microscopy with scanning NV magnetometry for imaging complex ferroelectric/antiferromagnetic orders at the nanoscale.

In $BiFeO_3$ films on (011)-oriented $DyScO_3$ substrates, a single ferroelectric domain state is stabilized. Resorting on the anisotropic strain imposed by the substrate, the film grows in the (111)-crystallographic direction and contains one bulk-like spin cycloid with a single propagation direction. In such films, the polarization is perpendicular to the sample surface and the cycloid is propagating in the film plane. We combine real-space scanning NV magnetometry images and X-ray elastic resonant scattering data to demonstrate that

$BiFeO_3$(111)/$DyScO_3$(011) represents an archetypical model system for further investigations of the interplay between non-collinear antiferromagnetic order and spin transport.

My publications during this thesis:

1. *Antiferromagnetic textures in $BiFeO_3$ controlled by strain and electric field*
A. Haykal*, J. Fischer*, W. Akhtar, J.-Y. Chauleau, D. Sando, A. Finco, F. Godel, Y.A. Birkhölzer, C. Carrétéro, N. Jaouen, M. Bibes, M. Viret, S. Fusil, V. Jacques, V. Garcia
NATURE COMMUNICATIONS 11, 1704 (2020)
Personal contribution: I prepared the samples, carried out X-ray diffraction experiments and analyzed the structural properties of the samples. I performed the piezoresponse force microscopy experiments and worked closely together with the colleagues in Montpellier who performed the NV experiments. All together we discussed and commented on the data from the different experiments and I contributed with input to the sections concerning my work to the writing of the paper.

2. *Inverse transition of labyrinthine domain patterns in ferroelectric thin films*
Y. Nahas, S. Prokhorenko, J. Fischer, B. Xu, C. Carrétéro, S. Prosandeev, S. Fusil, M. Bibes, B. Dkhil, V. Garcia, L. Bellaiche
NATURE 577, 47-51 (2020)
Personal contribution: I carried out the annealing experiments to confirm the theoretical predictions from our collaborators.

3. *Interfacial Strain Gradients Control Nanoscale Domain Morphology in Epitaxial $BiFeO_3$ Multiferroic Films*
D. Sando, M. Han, V. Govinden, O. Paull, F. Appert, C. Carrétéro, J. Fischer, A. Barthélémy, M. Bibes, V. Garcia, S. Fusil, B. Dkhil, J. Juraszek, Y. Zhu, X. Ma, V. Nagarajan
ADVANCED FUNCTIONAL MATERIALS Volume 30, Issue 22, 2000343 (2020)
Personal contribution: Together with D. Sando we came up with the idea for the annealing experiments. I then carried out the annealing, including PFM and XRD diffraction experiments and the related structural analysis.

The perspectives from this thesis are multiple. We demonstrate that the antiferromagnetic textures in $BiFeO_3$ can be tuned with epitaxial strain. So far this is demonstrated in a static way by using various substrates for different strain levels. A novel method for strain-tuning would be to use of a piezoelectric substrate such as (1-x)[$Pb(Mg_{1/3}Nb_{2/3})O_3$]-x[$PbTiO_3$] (PMN-PT). Indeed, PMN-PT has a perovskite structure (a = 4.02 Å) compatible with $BiFeO_3$ epitaxial growth on the tensile side and its record piezoelectric properties (d_{33} ~ 2000 pC/N) qualifies this compound as a functional substrate for electric tuning of the antiferromagnetic order via tuneable strain. The epitaxial strain could be varied continuously and all possible antiferromagnetic textures would become accessible in the same $BiFeO_3$ thin film.

Another strategy via the magnetoelectric coupling reported here, is to design capacitors or in-plane electrodes so that the in-situ control of the antiferromagnetic textures of the film could be achieved. This way, depending on the relative crystallographic properties and electrode geometry, the cycloidal propagation direction, chirality or propagating plane could be switched back and forth.

Even though scanning NV magnetometry is a very powerful tool to determine the antiferromagnetic textures at the nanoscale, on the road to antiferromagnetic spintronics, one would desire a device-realistic method for read-out of the magnetisation state. When combined with our knowledge about the precise spin texture, the spin Hall magnetoresistance effect could provide a path to determine the antiferromagnetic texture via a simple resistivity measurement in prototypical $BiFeO_3$ single domain films. Furthermore, this allows investigating the spin-dependent transport properties as a function of an external magnetic field in the simplest non-collinear configuration.

We have only been looking at static phenomena so far. Magnon transport was recently reported in non-ferroelectric antiferromagnets like Fe_2O_3.[5] These results pave the way to magnonics in multiferroics, and especially for $BiFeO_3$, with particular emphasis on the propagation of magnons in reconfigurable antiferromagnetic textures. Beyond non-collinear antiferromagnetic textures, strategies to deterministically control collinear antiferromagnetic textures in $BiFeO_3$ thin films would be highly desirable to investigate magnon propagation.

Ferroic domain walls are currently moving into the focus of research due to their intriguing properties, such as enhanced conductivity and anomalous magnetic order. In this context, the $BiFeO_3$ antiferromagnetic textures call for a detailed investigation of the domain walls. In our $BiFeO_3$ samples, we initiated an analysis of the correlated antiferromagnetic domain walls at different types of ferroelectric domain walls. Preliminary results on written domain walls reveal complex stitching of the antiferromagnetic cycloid. Indeed, when several propagation vectors encounter, typically at ferroelectric domain walls, embryos of antiferromagnetic skyrmions may be formed. The pristine high-density network of ferroelectric stripe domains as observed in this thesis is imprinted onto the antiferromagnetic order, forcing cycloids with different propagations to stitch in a chiral knot.[127] Beyond this magnetic chirality, the ferroelectric domain walls in such thin films have also been demonstrated to be chiral, which is in contrast to the long-standing common belief that ferroelectric walls are Ising type. This directly opens the question about the interplay between magnetic and ferroelectric chiralities in multiferroic $BiFeO_3$.

Finally, a particularly active field of research deals with skyrmions. Magnetic skyrmions were discovered in MnSi chiral magnets[138] and are nowadays generated in metallic multilayers with broken inversion symmetry.[139] These chiral objects are envisioned as the most stable and smallest magnetic objects achievable thanks to their topological protection. $BiFeO_3$ could be a promising template to electrically-design antiferromagnetic skyrmions. Polarisation flux closure-windings have up to now been artificially patterned in $BiFeO_3$ thin films by scanning probe techniques[140,141] and recently demonstrated to be stabilised by edge effects in nano-sized pillars.[142,143] Preliminary atomistic simulations point towards the stabilisation of antiferromagnetic skyrmions for suitable ferroelectric winding. Peculiar conduction mechanisms associated to each topological winding are experimentally reported, allowing full electrical writing and reading, en route towards electrically-reconfigurable topological antiferromagnetic objects.

Résumé étendu

La spintronique, fondée sur l'utilisation du spin de l'électron à la place de sa charge électronique, se base traditionnellement sur des matériaux ferromagnétiques. Les matériaux antiferromagnétiques utilisés dans le passé seulement comme éléments passifs pour bloquer l'aimantation des couches minces ferromagnétiques, suscitent un intérêt croissant pour la spintronique. En effet, leur insensibilité aux champs magnétiques parasites, leur dynamique magnétique ultrarapide (THz), et la possibilité d'intégration plus dense permise par l'absence de champ de fuite, constituent des atouts spécifiques des matériaux antiferromagnétiques.[1–3] Cependant, la lecture et le contrôle de l'ordre antiferromagnétique restent des verrous pour le développement des dispositifs. Plusieurs approches ont été proposées dans la littérature pour la lecture par des effets magnétorésistifs, à la fois dans les systèmes métalliques (AMR, TAMR) et dans les isolants (SMR)[11,15,18] . D'autre part, dans les matériaux non centrosymétriques comme le CuMnAs,[33] l'écriture de l'ordre antiferromagnétique devient possible grâce à des effets relativistes induisant un mécanisme de transfert de spin. L'approche de cette thèse repose sur les multiferroïques où plusieurs ordres ferroïques coexistent (tels que ferroélectricité, (anti)ferromagnétisme, ferroélasticité): le couplage magnétoélectrique pourrait permettre de contrôler l'antiferromagnétisme avec un champ électrique. $BiFeO_3$ est l'archétype des matériaux multiferroïques. Cet oxyde est à la fois ferroélectrique et antiferromagnétique à température ambiante, et donc un candidat idéal pour contrôler électriquement des textures de spin antiferromagnétiques.

Dans $BiFeO_3$, l'activité stéréochimique du doublet non liant des électrons des atomes de Bi produit une asymétrie des charges et induit une forte polarisation.[50] La déformation cristallographique associée induit un lien direct entre les domaines ferroélectriques et la structure cristalline. L'interaction magnétique dominante est le super-échange, créant un ordre antiferromagnétique de type G avec un arrangement antiparallèle des spins des premiers voisins. Une interaction antisymétrique de type Dzyaloshinskii-Moriya induit une cycloïde de spin à longue portée.[59] Une deuxième interaction Dzyaloshinskii-Moriya génère quant à elle un moment faible perpendiculairement au plan de la cycloïde, ou « onde de densité des spins ».[62] Contrairement au cas des cristaux massif, il est possible d'exercer des contraintes d'épitaxie dans les couches minces de $BiFeO_3$ et ainsi d'influencer l'ordre antiferromagnétique. Différentes mesures spectroscopiques ont en effet indiqué qu'il était possible d'accéder à différents types de cycloïdes ainsi qu'à un ordre antiferromagnétique colinéaire de type G selon l'état de contrainte.[102] Cependant, ces résultats n'ont pas été confirmés par des mesures des textures antiferromagnétiques dans l'espace réel, car peu de techniques expérimentales permettent d'imager l'ordre antiferromagnétique avec la résolution nanométrique pertinente.

Dans cette thèse, nous imageons une grande variété de textures antiferromagnétiques que nous contrôlons par l'ingénierie des contraintes et le champ électrique. Nous élaborons des films minces de $BiFeO_3$ sous différentes contraintes d'épitaxie, maîtrisant ainsi la texture de domaines ferroélectriques, telle qu'imagée par microscopie à force piézoélectrique. De plus, nous montrons qu'une transition de phase inverse peut être utilisée pour accroître l'ordre électrique global, d'une configuration labyrinthique de domaines vers un réseau périodique en bandes rectilignes (Figure 93). La magnétométrie à centre NV nous permet de corréler les textures antiferromagnétiques et ferroélectriques. Nous démontrons que les contraintes stabilisent différents types de cycloïdes ainsi qu'un ordre antiferromagnétique colinéaire

(Figure 94). La diffraction X élastique résonante permet de confirmer macroscopiquement l'existence de deux types de cycloïdes (Figure 95). Enfin, nous contrôlons électriquement ces textures antiferromagnétiques, passant d'une cycloïde à une autre ou transformant un ordre colinéaire en cycloïde (Figure 96). Sur la base d'un substrat imposant une contrainte anisotrope, nous stabilisons également des films ne présentant qu'un seul domaine ferroélectrique associé à un unique domaine antiferromagnétique (Figure 97). Ceci ouvre de larges perspectives pour explorer le couplage entre l'antiferromagnétisme non-colinéaire et le transport de spin.

Le travail expérimental présenté dans cette thèse est dédié à la croissance, la caractérisation et l'imagerie des domaines ferroélectriques et antiferromagnétiques dans des films minces de $BiFeO_3$. Ces films sont élaborés par ablation laser pulsé sur différents substrats. Selon la symétrie et l'orientation cristalline du substrat, le film mince adopte différentes configurations en domaines ferroélectriques. Les structures cristallines des films sont caractérisées par des modes avancés de diffraction de rayons X qui permettent de déterminer le nombre de variantes élastiques, les paramètres de maille, et la contrainte pour chaque configuration. Les variantes élastiques imposées par la symétrie du système gouvernent la sélection des variantes ferroélectriques, imagées par microscopie à force piézoélectrique. Cette approche permet de minimiser le nombre de variantes ferroélectriques présentes afin de mieux corréler par la suite les images de domaines ferroélectriques et magnétiques. Après optimisation des paramètres de dépôt (température, pression, longueur d'onde du laser, énergie par pulse laser, fréquence des pulses et distance cible substrat), nous obtenons des textures ferroélectriques modèles telles qu'un réseau ordonné de domaines pour les échantillons à deux variantes, ou un état monodomaine selon l'orientation du substrat. De plus, nous montrons qu'une transition de phase inverse peut être utilisée pour accroître l'ordre électrique global, d'une configuration labyrinthique de domaines vers un réseau périodique en bandes parfaitement rectilignes. Cette transition est initiée par recuit ex-situ après croissance (Figure 93**a**). Ces résultats expérimentaux sont en accord avec les prédictions théoriques de transitions de phases élaborées par nos collaborateurs de l'Université d'Arkansas (Figure 93**b**).[131] Cette transition est associée à l'annihilation de défauts topologiques présentant des propriétés de conduction spécifiques, laissant envisager des applications dans les domaines de la nanoélectronique et le neuromorphisme.

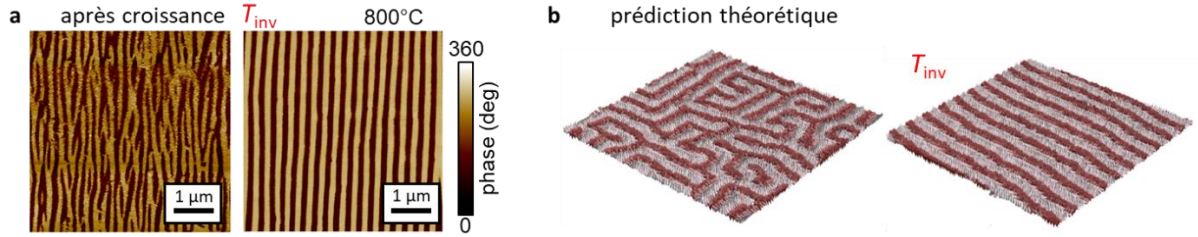

Figure 93 : Transitions de phase inverses dans les films minces ferroélectriques. ***a*** *Images par microscopie à force piézoélectrique d'un film mince de $BiFeO_3$ sur $DyScO_3$ avant et après un recuit à 800°C (phase dans le plan). Le recuit induit une transition d'un état labyrinthique à une structure en bandes rectilignes.* ***b*** *Prédictions de transitions de phases inverses dans les films ultraminces de $Pb(Zr_{0.4}Ti_{0.6})O_3$. Figure adaptée de la référence [131].*

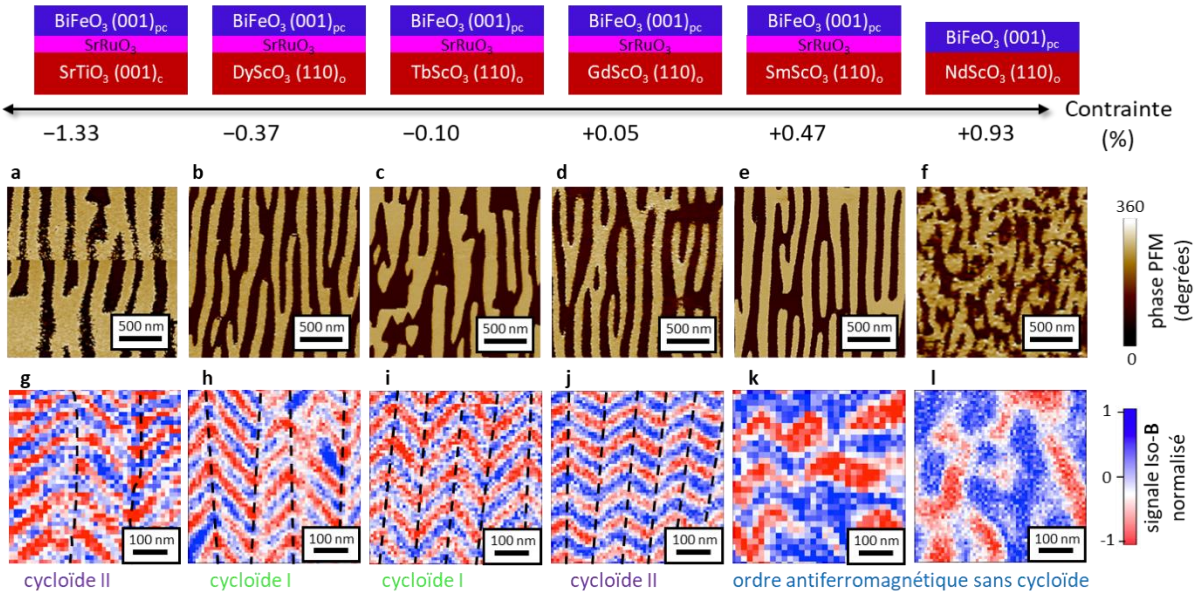

Figure 94 : Corrélation entre les textures électriques et magnétiques dans les films minces de $BiFeO_3$ soumis à différentes contraintes épitaxiales. Les différents substrats utilisés sont représentés schématiquement. ***a-f*** *Images en microscopie à force piézoélectrique de la structure des domaines ferroélectriques (phase dans le plan). Hormis le cas sur $NdScO_3$, les films de $BiFeO_3$ présentent une structure sous formes de bandes de deux variantes de polarisation.* ***g-l*** *Textures antiferromagnétiques associées, imagées par la magnétométrie à centre NV. Figure adaptée de la référence [136].*

Des films minces correspondant à différentes contraintes d'épitaxie sont élaborés, tout en maîtrisant la texture ferroélectrique arrangée sous formes de domaines en bandes, telle qu'imagée par microscopie à force piézoélectrique (Figure 94**a-f**). L'analyse structurale en diffraction de rayons X d'un ensemble d'échantillons épitaxiés sur les substrats $SrTiO_3$, $DyScO_3$, $TbScO_3$, $GdScO_3$, $SmScO_3$ and $NdScO_3$ démontre une variation de contrainte de -1.33% de compression à +0.93% de tension. La magnétométrie à centre NV nous permet de corréler les textures antiferromagnétiques et ferroélectriques. Nous démontrons que les contraintes stabilisent différents types de cycloïdes ainsi qu'un ordre antiferromagnétique colinéaire (Figure 94**g-l**). Pour les échantillons $BiFeO_3$ sur $DyScO_3$ et $TbScO_3$, la cycloïde I identique à celle de l'état massif est observée (Figure 94**h-i**). Ceci démontre qu'un ordre cycloïdal peut être stabilisé dans des films minces de $BiFeO_3$. A forte compression ($BiFeO_3$ sur $SrTiO_3$, Figure 94**g**) et à faible contrainte en tension ($BiFeO_3$ sur $GdScO_3$, Figure 94**j**), une cycloïde plus exotique caractérisée par une autre direction de propagation par rapport à la polarisation (**P**) dans chaque domaine (cycloïdes II) est stabilisée. La diffraction résonante élastique de rayons X permet de confirmer macroscopiquement l'existence de deux types de cycloïdes (Figure 95). Cette technique, basée sur le dichroïsme au seuil du fer permet de caractériser les structures magnétiques chirales et leur direction de propagation (**k**). Pour les échantillons soumis à de fortes contraintes en tension (sur $SmScO_3$ et $NdScO_3$), la cycloïde disparait et l'ordre antiferromagnétique colinéaire de type G est stabilisé (Figure 94**k-l**). Ces résultats nous conduisent à établir un nouveau diagramme de phase des textures antiferromagnétiques dans $BiFeO_3$, contrôlées par la contrainte d'épitaxie.

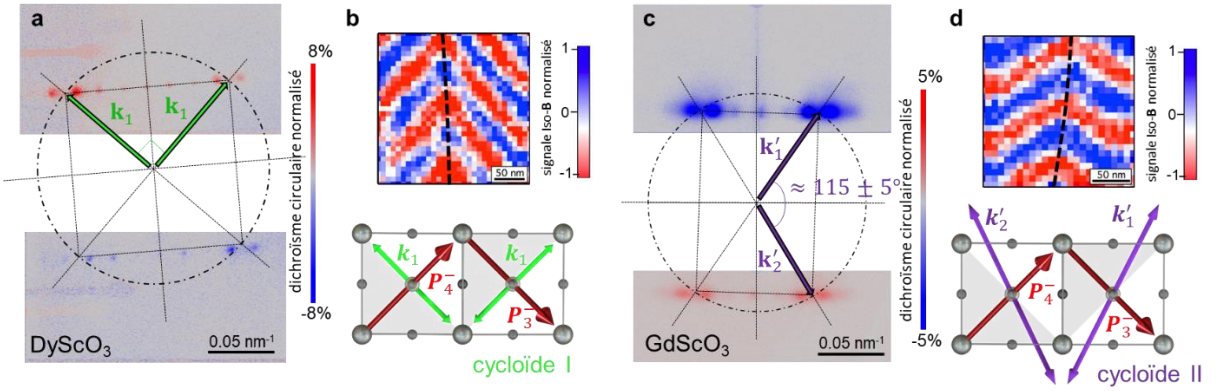

*Figure 95 : La diffraction résonante élastique de rayons X au seuil du Fe (**a, c**) permet de confirmer macroscopiquement l'existence de deux types de cycloïdes, mesurées avec la magnétométrie à centre NV (**b, d**). Figure adaptée de la référence [136].*

Grâce à la microscopie à force piézoélectrique, nous pouvons définir des domaines artificiels de taille micronique, dans lesquels nous imageons les textures antiferromagnétiques associées (Figure 96). Nos travaux montrent que nous pouvons (i) sélectionner la direction de propagation de la cycloïde I (Figure 96**a, b** : $BiFeO_3$ sur $DyScO_3$ et $TbScO_3$), (ii) transiter d'une cycloïde II à la cycloïde I (Figure 96**c** : $BiFeO_3$ sur $GdScO_3$) ou (iii) transformer un ordre colinéaire en cycloïde II (Figure 96**d** : $BiFeO_3$ sur $SmScO_3$). Le contrôle des domaines antiferromagnétiques par champ électrique externe constitue une étape décisive pour l'applicabilité de $BiFeO_3$ dans des dispositifs de spintronique.

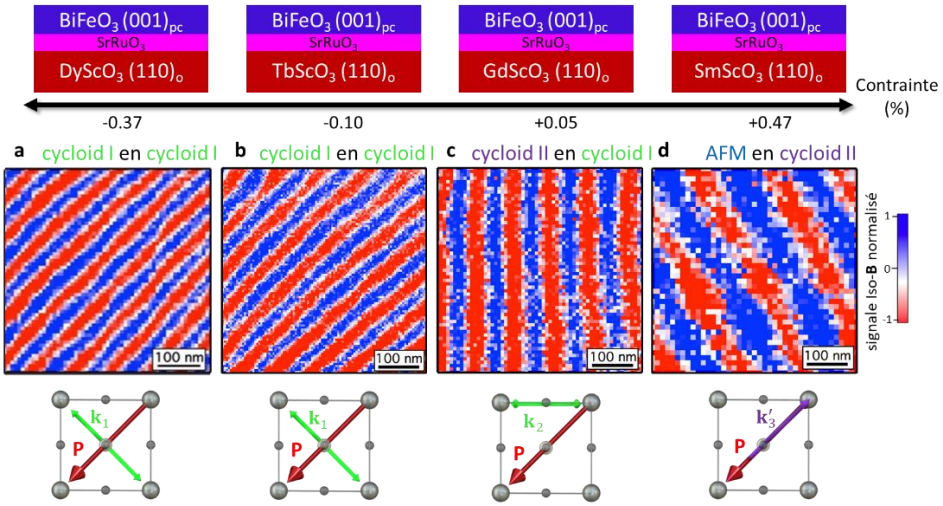

*Figure 96 : Contrôle des textures antiferromagnétiques avec un champ électrique externe. Images par magnétométrie à centre NV dans des domaines électriques écrits avec le microscope à force piézoélectrique. **a, b** Contrôle de la direction de propagation de la cycloïde I dans $BiFeO_3$ sur $DyScO_3$ et $TbScO_3$. **c** Transformation de la cycloïde II en cycloïde I dans $BiFeO_3$ sur $GdScO_3$. **d** Transition d'un ordre antiferromagnétique colinéaire de type G en ordre cycloïdal de type II dans $BiFeO_3$ sur $SmcO_3$. Figure adaptée de la référence [136].*

En privilégiant une autre orientation de croissance, sur la base d'un substrat de $DyScO_3(011)$ imposant une contrainte anisotrope, nous stabilisons des films ne présentant qu'un seul domaine ferroélectrique (Figure 97**a**). La direction de la polarisation électrique est alors purement verticale. La magnétométrie à centre NV révèle un unique domaine antiferromagnétique (Figure 97**b**) constitué d'une cycloïde de spin de type I se propageant dans le plan de l'échantillon. La diffraction résonante élastique de rayons X montre également l'existence d'une cycloïde unique sur l'ensemble de l'échantillon en accord avec les mesures

dans l'espace réel (Figure 97**c**). Dans cette orientation, la polarisation est perpendiculaire à la surface de l'échantillon et la cycloïde se propage dans le plan du film mince (Figure 97**d**). Cette configuration modèle permettra d'investiguer le couplage entre l'antiferromagnétisme non colinéaire et le transport de spin.

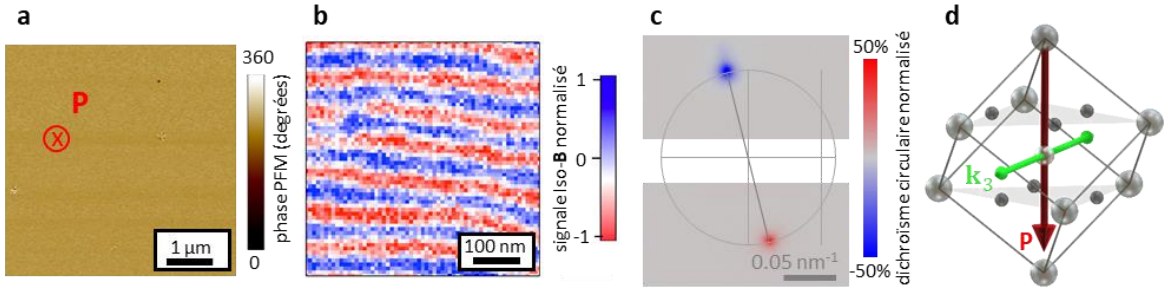

*Figure 97 : Domaine unique ferroélectrique et antiferromagnétique dans les films minces de $BiFeO_3$ sur $DyScO_3$(011). **a** Image du domaine ferroélectrique par la microscopie à force piézoélectrique (phase hors plan). **b** Image de la texture de spin associée par la magnétométrie à centre NV. Une cycloïde unique est stabilisée par les contraintes anisotropes dans le plan du film. **c** Confirmation de l'existence d'une cycloïde unique par la diffraction résonante élastique de rayons X. **d** Illustration de la direction de la polarisation (**P**) et la direction de propagation de la cycloïde (**k**) dans ce système archétypal.*

Les travaux de cette thèse ouvrent des perspectives sur la manipulation dynamique de textures antiferromagnétiques non colinéaires. Un substrat piézoélectrique permettrait d'ajuster la contrainte épitaxie, et donc de contrôler électriquement la texture antiferromagnétique associée. Une approche alternative consisterait à intégrer des électrodes métalliques permettant l'application d'un champ électrique local et réversible. En outre, une lecture purement électrique de l'information pourrait être réalisée en utilisant la magnétorésistance induite par effet Hall de spin, par l'intermédiaire d'un métal à fort couplage spin-orbite. Enfin, une voie émergente consisterait à explorer les textures de spin non colinéaires associées à des systèmes confinés tels que les parois ferroélectriques, ou les vortex ferroélectriques, en quête de nouvelles textures antiferromagnétiques bénéficiant potentiellement de protection topologique.

Bibliography

(1) Marti, X.; Fina, I.; Jungwirth, T. Prospect for Antiferromagnetic Spintronics. *IEEE Trans. Magn.* **2015**, *51* (4), 1–4. https://doi.org/10.1109/TMAG.2014.2358939.

(2) Olejník, K.; Seifert, T.; Kašpar, Z.; Novák, V.; Wadley, P.; Campion, R. P.; Baumgartner, M.; Gambardella, P.; Němec, P.; Wunderlich, J.; Sinova, J.; Kužel, P.; Müller, M.; Kampfrath, T.; Jungwirth, T. Terahertz Electrical Writing Speed in an Antiferromagnetic Memory. *Sci. Adv.* **2018**, *4* (3), eaar3566. https://doi.org/10.1126/sciadv.aar3566.

(3) Wienholdt, S.; Hinzke, D.; Nowak, U. THz Switching of Antiferromagnets and Ferrimagnets. *Phys. Rev. Lett.* **2012**, *108* (24), 247207. https://doi.org/10.1103/PhysRevLett.108.247207.

(4) Kampfrath, T.; Sell, A.; Klatt, G.; Pashkin, A.; Mährlein, S.; Dekorsy, T.; Wolf, M.; Fiebig, M.; Leitenstorfer, A.; Huber, R. Coherent Terahertz Control of Antiferromagnetic Spin Waves. *Nature Photon* **2011**, *5* (1), 31–34. https://doi.org/10.1038/nphoton.2010.259.

(5) Lebrun, R.; Ross, A.; Bender, S. A.; Qaiumzadeh, A.; Baldrati, L.; Cramer, J.; Brataas, A.; Duine, R. A.; Kläui, M. Tunable Long-Distance Spin Transport in a Crystalline Antiferromagnetic Iron Oxide. *Nature* **2018**, *561* (7722), 222–225. https://doi.org/10.1038/s41586-018-0490-7.

(6) Chappert, C.; Fert, A.; Van Dau, F. N. The Emergence of Spin Electronics in Data Storage. *Nature Mater* **2007**, *6* (11), 813–823. https://doi.org/10.1038/nmat2024.

(7) Núñez, A. S.; Duine, R. A.; Haney, P.; MacDonald, A. H. Theory of Spin Torques and Giant Magnetoresistance in Antiferromagnetic Metals. *Phys. Rev. B* **2006**, *73* (21), 214426. https://doi.org/10.1103/PhysRevB.73.214426.

(8) Duine, R. A.; Haney, P. M.; Núñez, A. S.; MacDonald, A. H. Inelastic Scattering in Ferromagnetic and Antiferromagnetic Spin Valves. *Phys. Rev. B* **2007**, *75* (1), 014433. https://doi.org/10.1103/PhysRevB.75.014433.

(9) Saidaoui, H. B. M.; Waintal, X.; Manchon, A. Robust Spin Transfer Torque in Antiferromagnetic Tunnel Junctions. *Phys. Rev. B* **2017**, *95* (13), 134424. https://doi.org/10.1103/PhysRevB.95.134424.

(10) Wang, Y.; Song, C.; Wang, G.; Miao, J.; Zeng, F.; Pan, F. Anti-Ferromagnet Controlled Tunneling Magnetoresistance. *Adv. Funct. Mater.* **2014**, *24* (43), 6806–6810. https://doi.org/10.1002/adfm.201401659.

(11) Marti, X.; Fina, I.; Frontera, C.; Liu, J.; Wadley, P.; He, Q.; Paull, R. J.; Clarkson, J. D.; Kudrnovský, J.; Turek, I.; Kuneš, J.; Yi, D.; Chu, J.-H.; Nelson, C. T.; You, L.; Arenholz, E.; Salahuddin, S.; Fontcuberta, J.; Jungwirth, T.; Ramesh, R. Room-Temperature Antiferromagnetic Memory Resistor. *Nature Mater* **2014**, *13* (4), 367–374. https://doi.org/10.1038/nmat3861.

(12) Moriyama, T.; Matsuzaki, N.; Kim, K.-J.; Suzuki, I.; Taniyama, T.; Ono, T. Sequential Write-Read Operations in FeRh Antiferromagnetic Memory. *Appl. Phys. Lett.* **2015**, *107* (12), 122403. https://doi.org/10.1063/1.4931567.

(13) Kriegner, D.; Výborný, K.; Olejník, K.; Reichlová, H.; Novák, V.; Marti, X.; Gazquez, J.; Saidl, V.; Němec, P.; Volobuev, V. V.; Springholz, G.; Holý, V.; Jungwirth, T. Multiple-Stable Anisotropic Magnetoresistance Memory in Antiferromagnetic MnTe. *Nat Commun* **2016**, *7* (1), 11623. https://doi.org/10.1038/ncomms11623.

(14) Shick, A. B.; Khmelevskyi, S.; Mryasov, O. N.; Wunderlich, J.; Jungwirth, T. Spin-Orbit Coupling Induced Anisotropy Effects in Bimetallic Antiferromagnets: A Route towards Antiferromagnetic Spintronics. *Phys. Rev. B* **2010**, *81* (21), 212409. https://doi.org/10.1103/PhysRevB.81.212409.

(15) Park, B. G.; Wunderlich, J.; Martí, X.; Holý, V.; Kurosaki, Y.; Yamada, M.; Yamamoto, H.; Nishide, A.; Hayakawa, J.; Takahashi, H.; Shick, A. B.; Jungwirth, T. A Spin-Valve-like Magnetoresistance of an Antiferromagnet-Based Tunnel Junction. *Nature Mater* **2011**, *10* (5), 347–351. https://doi.org/10.1038/nmat2983.

(16) Scholl, A.; Liberati, M.; Arenholz, E.; Ohldag, H.; Stöhr, J. Creation of an Antiferromagnetic Exchange Spring. *Phys. Rev. Lett.* **2004**, *92* (24), 247201. https://doi.org/10.1103/PhysRevLett.92.247201.

(17) Geprägs, S.; Opel, M.; Fischer, J.; Gomonay, O.; Schwenke, P.; Althammer, M.; Huebl, H.; Gross, R. Spin Hall Magnetoresistance in Antiferromagnetic Insulators. *Journal of Applied Physics* **2020**, *127* (24), 243902. https://doi.org/10.1063/5.0009529.
(18) Fischer, J.; Gomonay, O.; Schlitz, R.; Ganzhorn, K.; Vlietstra, N.; Althammer, M.; Huebl, H.; Opel, M.; Gross, R.; Goennenwein, S. T. B.; Geprägs, S. Spin Hall Magnetoresistance in Antiferromagnet/Heavy-Metal Heterostructures. *Phys. Rev. B* **2018**, *97* (1), 014417. https://doi.org/10.1103/PhysRevB.97.014417.
(19) Fischer, J.; Althammer, M.; Vlietstra, N.; Huebl, H.; Goennenwein, S. T. B.; Gross, R.; Geprägs, S.; Opel, M. Large Spin Hall Magnetoresistance in Antiferromagnetic α − Fe 2 O 3 / Pt Heterostructures. *Phys. Rev. Applied* **2020**, *13* (1), 014019. https://doi.org/10.1103/PhysRevApplied.13.014019.
(20) Gomonay, H. V.; Loktev, V. M. Spin Transfer and Current-Induced Switching in Antiferromagnets. *Phys. Rev. B* **2010**, *81* (14), 144427. https://doi.org/10.1103/PhysRevB.81.144427.
(21) Tang, X.; Su, H.; Zhang, H.-W.; Jing, Y.-L.; Zhong, Z.-Y. Tuning the Direction of Exchange Bias in Ferromagnetic/Antiferromagnetic Bilayer by Angular-Dependent Spin-Polarized Current. *Journal of Applied Physics* **2012**, *112* (7), 073916. https://doi.org/10.1063/1.4757906.
(22) Gomonay, O.; Baltz, V.; Brataas, A.; Tserkovnyak, Y. Antiferromagnetic Spin Textures and Dynamics. *Nature Phys* **2018**, *14* (3), 213–216. https://doi.org/10.1038/s41567-018-0049-4.
(23) Nogués, J.; Sort, J.; Langlais, V.; Skumryev, V.; Suriñach, S.; Muñoz, J. S.; Baró, M. D. Exchange Bias in Nanostructures. *Physics Reports* **2005**, *422* (3), 65–117. https://doi.org/10.1016/j.physrep.2005.08.004.
(24) Wei, Z.; Sharma, A.; Nunez, A. S.; Haney, P. M.; Duine, R. A.; Bass, J.; MacDonald, A. H.; Tsoi, M. Changing Exchange Bias in Spin Valves with an Electric Current. *Phys. Rev. Lett.* **2007**, *98* (11), 116603. https://doi.org/10.1103/PhysRevLett.98.116603.
(25) Wei, Z.; Basset, J.; Sharma, A.; Bass, J.; Tsoi, M. Spin-Transfer Interactions in Exchange-Biased Spin Valves. *Journal of Applied Physics* **2009**, *105* (7), 07D108. https://doi.org/10.1063/1.3057951.
(26) Urazhdin, S.; Anthony, N. Effect of Polarized Current on the Magnetic State of an Antiferromagnet. *Phys. Rev. Lett.* **2007**, *99* (4), 046602. https://doi.org/10.1103/PhysRevLett.99.046602.
(27) Tang, X.-L.; Zhang, H.-W.; Su, H.; Zhong, Z.-Y.; Jing, Y.-L. Changing and Reversing the Exchange Bias in a Current-in-Plane Spin Valve by Means of an Electric Current. *Appl. Phys. Lett.* **2007**, *91* (12), 122504. https://doi.org/10.1063/1.2786592.
(28) Dai, N. V.; Thuan, N. C.; Hong, L. V.; Phuc, N. X.; Lee, Y. P.; Wolf, S. A.; Nam, D. N. H. Impact of In-Plane Currents on Magnetoresistance Properties of an Exchange-Biased Spin Valve with an Insulating Antiferromagnetic Layer. *Phys. Rev. B* **2008**, *77* (13), 132406. https://doi.org/10.1103/PhysRevB.77.132406.
(29) Chernyshov, A.; Overby, M.; Liu, X.; Furdyna, J. K.; Lyanda-Geller, Y.; Rokhinson, L. P. Evidence for Reversible Control of Magnetization in a Ferromagnetic Material by Means of Spin–Orbit Magnetic Field. *Nature Phys* **2009**, *5* (9), 656–659. https://doi.org/10.1038/nphys1362.
(30) Fang, D.; Kurebayashi, H.; Wunderlich, J.; Výborný, K.; Zârbo, L. P.; Campion, R. P.; Casiraghi, A.; Gallagher, B. L.; Jungwirth, T.; Ferguson, A. J. Spin–Orbit-Driven Ferromagnetic Resonance. *Nature Nanotech* **2011**, *6* (7), 413–417. https://doi.org/10.1038/nnano.2011.68.
(31) Ciccarelli, C.; Anderson, L.; Tshitoyan, V.; Ferguson, A. J.; Gerhard, F.; Gould, C.; Molenkamp, L. W.; Gayles, J.; Železný, J.; Šmejkal, L.; Yuan, Z.; Sinova, J.; Freimuth, F.; Jungwirth, T. Room-Temperature Spin–Orbit Torque in NiMnSb. *Nature Phys* **2016**, *12* (9), 855–860. https://doi.org/10.1038/nphys3772.
(32) Železný, J.; Gao, H.; Výborný, K.; Zemen, J.; Mašek, J.; Manchon, A.; Wunderlich, J.; Sinova, J.; Jungwirth, T. Relativistic Néel-Order Fields Induced by Electrical Current in Antiferromagnets. *Phys. Rev. Lett.* **2014**, *113* (15), 157201. https://doi.org/10.1103/PhysRevLett.113.157201.

(33) Wadley, P.; Howells, B.; elezny, J.; Andrews, C.; Hills, V.; Campion, R. P.; Novak, V.; Olejnik, K.; Maccherozzi, F.; Dhesi, S. S.; Martin, S. Y.; Wagner, T.; Wunderlich, J.; Freimuth, F.; Mokrousov, Y.; Kune, J.; Chauhan, J. S.; Grzybowski, M. J.; Rushforth, A. W.; Edmonds, K. W.; Gallagher, B. L.; Jungwirth, T. Electrical Switching of an Antiferromagnet. *Science* **2016**, *351* (6273), 587–590. https://doi.org/10.1126/science.aab1031.

(34) Olejník, K.; Schuler, V.; Marti, X.; Novák, V.; Kašpar, Z.; Wadley, P.; Campion, R. P.; Edmonds, K. W.; Gallagher, B. L.; Garces, J.; Baumgartner, M.; Gambardella, P.; Jungwirth, T. Antiferromagnetic CuMnAs Multi-Level Memory Cell with Microelectronic Compatibility. *Nat Commun* **2017**, *8* (1), 15434. https://doi.org/10.1038/ncomms15434.

(35) Grzybowski, M. J.; Wadley, P.; Edmonds, K. W.; Beardsley, R.; Hills, V.; Campion, R. P.; Gallagher, B. L.; Chauhan, J. S.; Novak, V.; Jungwirth, T.; Maccherozzi, F.; Dhesi, S. S. Imaging Current-Induced Switching of Antiferromagnetic Domains in CuMnAs. *Phys. Rev. Lett.* **2017**, *118* (5), 057701. https://doi.org/10.1103/PhysRevLett.118.057701.

(36) Wadley, P.; Reimers, S.; Grzybowski, M. J.; Andrews, C.; Wang, M.; Chauhan, J. S.; Gallagher, B. L.; Campion, R. P.; Edmonds, K. W.; Dhesi, S. S.; Maccherozzi, F.; Novak, V.; Wunderlich, J.; Jungwirth, T. Current Polarity-Dependent Manipulation of Antiferromagnetic Domains. *Nature Nanotech* **2018**, *13* (5), 362–365. https://doi.org/10.1038/s41565-018-0079-1.

(37) Jungwirth, T.; Marti, X.; Wadley, P.; Wunderlich, J. Antiferromagnetic Spintronics. *Nature Nanotech* **2016**, *11* (3), 231–241. https://doi.org/10.1038/nnano.2016.18.

(38) Baltz, V.; Manchon, A.; Tsoi, M.; Moriyama, T.; Ono, T.; Tserkovnyak, Y. Antiferromagnetic Spintronics. *Rev. Mod. Phys.* **2018**, *90* (1), 015005. https://doi.org/10.1103/RevModPhys.90.015005.

(39) Železný, J.; Wadley, P.; Olejník, K.; Hoffmann, A.; Ohno, H. Spin Transport and Spin Torque in Antiferromagnetic Devices. *Nature Phys* **2018**, *14* (3), 220–228. https://doi.org/10.1038/s41567-018-0062-7.

(40) Garcés, J.; Fina, I.; Marti, X. IGSresearch: From Science to Business in the Markets of Security, Smartcity Management, and Geological Monitoring. In *Supporting University Ventures in Nanotechnology, Biomaterials and Magnetic Sensing Applications*; Peña Dopazo, J., Zivic, F., Eds.; Springer International Publishing: Cham, 2018; pp 159–163. https://doi.org/10.1007/978-3-319-61237-9_8.

(41) Yan, H.; Feng, Z.; Shang, S.; Wang, X.; Hu, Z.; Wang, J.; Zhu, Z.; Wang, H.; Chen, Z.; Hua, H.; Lu, W.; Wang, J.; Qin, P.; Guo, H.; Zhou, X.; Leng, Z.; Liu, Z.; Jiang, C.; Coey, M.; Liu, Z. A Piezoelectric, Strain-Controlled Antiferromagnetic Memory Insensitive to Magnetic Fields. *Nature Nanotech* **2019**, *14* (2), 131–136. https://doi.org/10.1038/s41565-018-0339-0.

(42) Fina, I.; Dix, N.; Menéndez, E.; Crespi, A.; Foerster, M.; Aballe, L.; Sánchez, F.; Fontcuberta, J. Flexible Antiferromagnetic FeRh Tapes as Memory Elements. *ACS Appl. Mater. Interfaces* **2020**, *12* (13), 15389–15395. https://doi.org/10.1021/acsami.0c00704.

(43) Ross, A.; Lebrun, R.; Gomonay, O.; Grave, D. A.; Kay, A.; Baldrati, L.; Becker, S.; Qaiumzadeh, A.; Ulloa, C.; Jakob, G.; Kronast, F.; Sinova, J.; Duine, R.; Brataas, A.; Rothschild, A.; Kläui, M. Propagation Length of Antiferromagnetic Magnons Governed by Domain Configurations. *Nano Lett.* **2020**, *20* (1), 306–313. https://doi.org/10.1021/acs.nanolett.9b03837.

(44) Baldrati, L.; Schneider, C.; Niizeki, T.; Ramos, R.; Cramer, J.; Ross, A.; Saitoh, E.; Kläui, M. Spin Transport in Multilayer Systems with Fully Epitaxial NiO Thin Films. *Phys. Rev. B* **2018**, *98* (1), 014409. https://doi.org/10.1103/PhysRevB.98.014409.

(45) Fiebig, M.; Lottermoser, Th.; Fröhlich, D.; Goltsev, A. V.; Pisarev, R. V. Observation of Coupled Magnetic and Electric Domains. *Nature* **2002**, *419* (6909), 818–820. https://doi.org/10.1038/nature01077.

(46) Zhao, T.; Scholl, A.; Zavaliche, F.; Lee, K.; Barry, M.; Doran, A.; Cruz, M. P.; Chu, Y. H.; Ederer, C.; Spaldin, N. A.; Das, R. R.; Kim, D. M.; Baek, S. H.; Eom, C. B.; Ramesh, R. Electrical Control of Antiferromagnetic Domains in Multiferroic BiFeO3 Films at Room Temperature. *Nature Mater* **2006**, *5* (10), 823–829. https://doi.org/10.1038/nmat1731.

(47) Spaldin, N. A.; Fiebig, M. The Renaissance of Magnetoelectric Multiferroics. *Science* **2005**, *309* (5733), 391–392. https://doi.org/10.1126/science.1113357.
(48) Moreau, J. M.; Michel, C.; Gerson, R.; James, W. J. Ferroelectric BiFeO3 X-Ray and Neutron Diffraction Study. *Journal of Physics and Chemistry of Solids* **1971**, *32* (6), 1315–1320. https://doi.org/10.1016/S0022-3697(71)80189-0.
(49) Kiselev S V, Ozerov R P, Zhdanov G. Detection of Magnetic Order in Ferroelectric BiFeO3 by Neutron Diffraction.
(50) Lebeugle, D.; Colson, D.; Forget, A.; Viret, M. Very Large Spontaneous Electric Polarization in BiFeO3 Single Crystals at Room Temperature and Its Evolution under Cycling Fields. *Appl. Phys. Lett.* **2007**, *91* (2), 022907. https://doi.org/10.1063/1.2753390.
(51) Catalan, G.; Scott, J. F. Physics and Applications of Bismuth Ferrite. *Adv. Mater.* **2009**, *21* (24), 2463–2485. https://doi.org/10.1002/adma.200802849.
(52) Seshadri, R.; Hill, N. A. Visualizing the Role of Bi 6s "Lone Pairs" in the Off-Center Distortion in Ferromagnetic BiMnO $_3$. *Chem. Mater.* **2001**, *13* (9), 2892–2899. https://doi.org/10.1021/cm010090m.
(53) Neaton, J. B.; Ederer, C.; Waghmare, U. V.; Spaldin, N. A.; Rabe, K. M. First-Principles Study of Spontaneous Polarization in Multiferroic Bi Fe O 3. *Phys. Rev. B* **2005**, *71* (1), 014113. https://doi.org/10.1103/PhysRevB.71.014113.
(54) Ravindran, P.; Vidya, R.; Kjekshus, A.; Fjellvåg, H.; Eriksson, O. Theoretical Investigation of Magnetoelectric Behavior in Bi Fe O 3. *Phys. Rev. B* **2006**, *74* (22), 224412. https://doi.org/10.1103/PhysRevB.74.224412.
(55) Goldschmidt, V. M. Die Gesetze der Krystallochemie. *Naturwissenschaften* **1926**, *14* (21), 477–485. https://doi.org/10.1007/BF01507527.
(56) Shannon, R. D.; Prewitt, C. T. Effective Ionic Radii in Oxides and Fluorides. *Acta Crystallogr B Struct Sci* **1969**, *25* (5), 925–946. https://doi.org/10.1107/S0567740869003220.
(57) Megaw, H. D.; Darlington, C. N. W. Geometrical and Structural Relations in the Rhombohedral Perovskites. *Acta Cryst A* **1975**, *31* (2), 161–173. https://doi.org/10.1107/S0567739475000332.
(58) Anderson, P. W. Antiferromagnetism. Theory of Superexchange Interaction. *Phys. Rev.* **1950**, *79* (2), 350–356. https://doi.org/10.1103/PhysRev.79.350.
(59) Sosnowska, I.; Peterlinneumaier, T.; Steichele, E. Spiral Magnetic-Ordering in Bismuth Ferrite. *Journal of Physics C-Solid State Physics* **1982**, *15* (23), 4835–4846. https://doi.org/10.1088/0022-3719/15/23/020.
(60) Lebeugle, D.; Colson, D.; Forget, A.; Viret, M.; Bataille, A. M.; Gukasov, A. Electric-Field-Induced Spin Flop in BiFeO 3 Single Crystals at Room Temperature. *Phys. Rev. Lett.* **2008**, *100* (22), 227602. https://doi.org/10.1103/PhysRevLett.100.227602.
(61) Johnson, R. D.; Barone, P.; Bombardi, A.; Bean, R. J.; Picozzi, S.; Radaelli, P. G.; Oh, Y. S.; Cheong, S.-W.; Chapon, L. C. X-Ray Imaging and Multiferroic Coupling of Cycloidal Magnetic Domains in Ferroelectric Monodomain BiFeO 3. *Phys. Rev. Lett.* **2013**, *110* (21), 217206. https://doi.org/10.1103/PhysRevLett.110.217206.
(62) Ramazanoglu, M.; Ratcliff, W.; Choi, Y. J.; Lee, S.; Cheong, S.-W.; Kiryukhin, V. Temperature-Dependent Properties of the Magnetic Order in Single-Crystal BiFeO 3. *Phys. Rev. B* **2011**, *83* (17), 174434. https://doi.org/10.1103/PhysRevB.83.174434.
(63) Ederer, C.; Spaldin, N. A. Weak Ferromagnetism and Magnetoelectric Coupling in Bismuth Ferrite. *Phys. Rev. B* **2005**, *71* (6), 060401. https://doi.org/10.1103/PhysRevB.71.060401.
(64) Dzyaloshinsky, I. A Thermodynamic Theory of "Weak" Ferromagnetism of Antiferromagnetics. *Journal of Physics and Chemistry of Solids* **1958**, *4* (4), 241–255. https://doi.org/10.1016/0022-3697(58)90076-3.
(65) Moriya, T. Anisotropic Superexchange Interaction and Weak Ferromagnetism. *Phys. Rev.* **1960**, *120* (1), 91–98. https://doi.org/10.1103/PhysRev.120.91.

(66) Katsura, H.; Nagaosa, N.; Balatsky, A. V. Spin Current and Magnetoelectric Effect in Noncollinear Magnets. *Phys. Rev. Lett.* **2005**, *95* (5), 057205. https://doi.org/10.1103/PhysRevLett.95.057205.

(67) Rahmedov, D.; Wang, D.; Íñiguez, J.; Bellaiche, L. Magnetic Cycloid of BiFeO 3 from Atomistic Simulations. *Phys. Rev. Lett.* **2012**, *109* (3), 037207. https://doi.org/10.1103/PhysRevLett.109.037207.

(68) Raeliarijaona, A.; Singh, S.; Fu, H.; Bellaiche, L. Predicted Coupling of the Electromagnetic Angular Momentum Density with Magnetic Moments. *Phys. Rev. Lett.* **2013**, *110* (13), 137205. https://doi.org/10.1103/PhysRevLett.110.137205.

(69) Albrecht, D.; Lisenkov, S.; Ren, W.; Rahmedov, D.; Kornev, I. A.; Bellaiche, L. Ferromagnetism in Multiferroic BiFeO 3 Films: A First-Principles-Based Study. *Phys. Rev. B* **2010**, *81* (14), 140401. https://doi.org/10.1103/PhysRevB.81.140401.

(70) Kornev, I. A.; Bellaiche, L.; Janolin, P.-E.; Dkhil, B.; Suard, E. Phase Diagram of Pb (Zr , Ti) O 3 Solid Solutions from First Principles. *Phys. Rev. Lett.* **2006**, *97* (15), 157601. https://doi.org/10.1103/PhysRevLett.97.157601.

(71) Lisenkov, S.; Kornev, I. A.; Bellaiche, L. Properties of Multiferroic BiFeO 3 under High Magnetic Fields from First Principles. *Phys. Rev. B* **2009**, *79* (1), 012101. https://doi.org/10.1103/PhysRevB.79.012101.

(72) Ratcliff, W.; Kan, D.; Chen, W.; Watson, S.; Chi, S.; Erwin, R.; McIntyre, G. J.; Capelli, S. C.; Takeuchi, I. Neutron Diffraction Investigations of Magnetism in BiFeO3 Epitaxial Films. *Adv. Funct. Mater.* **2011**, *21* (9), 1567–1574. https://doi.org/10.1002/adfm.201002125.

(73) Bhattacharjee, S.; Rahmedov, D.; Bellaiche, L.; Wang, D. Novel Magnetic Arrangement and Structural Phase Transition Induced by Spin–Lattice Coupling in Multiferroics. *MRS commun.* **2013**, *3* (4), 213–218. https://doi.org/10.1557/mrc.2013.45.

(74) Xu, B.; Dupé, B.; Xu, C.; Xiang, H.; Bellaiche, L. Revisiting Spin Cycloids in Multiferroic BiFeO 3. *Phys. Rev. B* **2018**, *98* (18), 184420. https://doi.org/10.1103/PhysRevB.98.184420.

(75) Park, J.-G.; Le, M. D.; Jeong, J.; Lee, S. Structure and Spin Dynamics of Multiferroic $BiFeO_3$. *J. Phys.: Condens. Matter* **2014**, *26* (43), 433202. https://doi.org/10.1088/0953-8984/26/43/433202.

(76) Heron, J. T.; Schlom, D. G.; Ramesh, R. Electric Field Control of Magnetism Using $BiFeO_3$ - Based Heterostructures. *Applied Physics Reviews* **2014**, *1* (2), 021303. https://doi.org/10.1063/1.4870957.

(77) Streiffer, S. K.; Parker, C. B.; Romanov, A. E.; Lefevre, M. J.; Zhao, L.; Speck, J. S.; Pompe, W.; Foster, C. M.; Bai, G. R. Domain Patterns in Epitaxial Rhombohedral Ferroelectric Films. I. Geometry and Experiments. *Journal of Applied Physics* **1998**, *83* (5), 2742–2753. https://doi.org/10.1063/1.366632.

(78) Chu, Y.-H.; He, Q.; Yang, C.-H.; Yu, P.; Martin, L. W.; Shafer, P.; Ramesh, R. Nanoscale Control of Domain Architectures in $BiFeO_3$ Thin Films. *Nano Lett.* **2009**, *9* (4), 1726–1730. https://doi.org/10.1021/nl900723j.

(79) Béa, H.; Bibes, M.; Barthélémy, A.; Bouzehouane, K.; Jacquet, E.; Khodan, A.; Contour, J.-P.; Fusil, S.; Wyczisk, F.; Forget, A.; Lebeugle, D.; Colson, D.; Viret, M. Influence of Parasitic Phases on the Properties of BiFeO3 Epitaxial Thin Films. *Appl. Phys. Lett.* **2005**, *87* (7), 072508. https://doi.org/10.1063/1.2009808.

(80) Béa, H. Croissance, Caractérisation et Intégration Dans Des Hétérostructures de Films Minces Du Multiferroïque BiFeO3, 2007.

(81) Jang, Y. H.; Kim, C. H.; Seo, S. J.; Cho, J. H. Relaxation of Ferroelectric Domains in Epitaxial BiFeO3 Thin Films on Vicinal SrTiO3 Substrate. *Thin Solid Films* **2013**, *548*, 52–57. https://doi.org/10.1016/j.tsf.2013.08.088.

(82) Chu, Y.-H.; Zhan, Q.; Martin, L. W.; Cruz, M. P.; Yang, P.-L.; Pabst, G. W.; Zavaliche, F.; Yang, S.-Y.; Zhang, J.-X.; Chen, L.-Q.; Schlom, D. G.; Lin, I.-N.; Wu, T.-B.; Ramesh, R. Nanoscale Domain Control in Multiferroic BiFeO3 Thin Films. *Advanced Materials* **2006**, *18* (17), 2307–2311. https://doi.org/10.1002/adma.200601098.

(83) Dedon, L. R.; Saremi, S.; Chen, Z.; Damodaran, A. R.; Apgar, B. A.; Gao, R.; Martin, L. W. Non-stoichiometry, Structure, and Properties of $BiFeO_3$ Films. *Chem. Mater.* **2016**, *28* (16), 5952–5961. https://doi.org/10.1021/acs.chemmater.6b02542.

(84) Chen, Z.; Liu, J.; Qi, Y.; Chen, D.; Hsu, S.-L.; Damodaran, A. R.; He, X.; N'Diaye, A. T.; Rockett, A.; Martin, L. W. 180° Ferroelectric Stripe Nanodomains in $BiFeO_3$ Thin Films. *Nano Lett.* **2015**, *15* (10), 6506–6513. https://doi.org/10.1021/acs.nanolett.5b02031.

(85) Bea, Hé.; Bibes, M.; Herranz, G.; Zhu, X.-H.; Fusil, S.; Bouzehouane, K.; Jacquet, E.; Deranlot, C.; Barthelemy, A. Integration of Multiferroic $BiFeO_3$ Thin Films into Heterostructures for Spintronics. *IEEE Transactions on Magnetics* **2008**, *44* (7), 1941–1945. https://doi.org/10.1109/TMAG.2008.924540.

(86) Li, J.; Wang, J.; Wuttig, M.; Ramesh, R.; Wang, N.; Ruette, B.; Pyatakov, A. P.; Zvezdin, A. K.; Viehland, D. Dramatically Enhanced Polarization in (001), (101), and (111) BiFeO3 Thin Films Due to Epitiaxial-Induced Transitions. *Appl. Phys. Lett.* **2004**, *84* (25), 5261–5263. https://doi.org/10.1063/1.1764944.

(87) Bai, F.; Wang, J.; Wuttig, M.; Li, J.; Wang, N.; Pyatakov, A. P.; Zvezdin, A. K.; Cross, L. E.; Viehland, D. Destruction of Spin Cycloid in (111)c-Oriented BiFeO3 Thin Films by Epitiaxial Constraint: Enhanced Polarization and Release of Latent Magnetization. *Appl. Phys. Lett.* **2005**, *86* (3), 032511. https://doi.org/10.1063/1.1851612.

(88) Singh, M. K.; Jang, H. M.; Ryu, S.; Jo, M.-H. Polarized Raman Scattering of Multiferroic BiFeO3 Epitaxial Films with Rhombohedral R3c Symmetry. *Appl. Phys. Lett.* **2006**, *88* (4), 042907. https://doi.org/10.1063/1.2168038.

(89) Ihlefeld, J. F.; Kumar, A.; Gopalan, V.; Schlom, D. G.; Chen, Y. B.; Pan, X. Q.; Heeg, T.; Schubert, J.; Ke, X.; Schiffer, P.; Orenstein, J.; Martin, L. W.; Chu, Y. H.; Ramesh, R. Adsorption-Controlled Molecular-Beam Epitaxial Growth of BiFeO3. *Appl. Phys. Lett.* **2007**, *91* (7), 071922. https://doi.org/10.1063/1.2767771.

(90) Rana, D. S.; Takahashi, K.; Mavani, K. R.; Kawayama, I.; Murakami, H.; Tonouchi, M.; Yanagida, T.; Tanaka, H.; Kawai, T. Thickness Dependence of the Structure and Magnetization of Bi Fe O 3 Thin Films on (La Al O 3) 0.3 (Sr 2 Al Ta O 6) 0.7 (001) Substrate. *Phys. Rev. B* **2007**, *75* (6), 060405. https://doi.org/10.1103/PhysRevB.75.060405.

(91) Christen, H. M.; Nam, J. H.; Kim, H. S.; Hatt, A. J.; Spaldin, N. A. Stress-Induced R − M A − M C − T Symmetry Changes in BiFeO 3 Films. *Phys. Rev. B* **2011**, *83* (14), 144107. https://doi.org/10.1103/PhysRevB.83.144107.

(92) Xu, G.; Hiraka, H.; Shirane, G.; Li, J.; Wang, J.; Viehland, D. Low Symmetry Phase in (001) BiFeO3 Epitaxial Constrained Thin Films. *Appl. Phys. Lett.* **2005**, *86* (18), 182905. https://doi.org/10.1063/1.1924891.

(93) Toupet, H.; Le Marrec, F.; Lichtensteiger, C.; Dkhil, B.; Karkut, M. G. Evidence for a First-Order Transition from Monoclinic α to Monoclinic β Phase in BiFeO 3 Thin Films. *Phys. Rev. B* **2010**, *81* (14), 140101. https://doi.org/10.1103/PhysRevB.81.140101.

(94) Liu, H.; Yao, K.; Yang, P.; Du, Y.; He, Q.; Gu, Y.; Li, X.; Wang, S.; Zhou, X.; Wang, J. Thickness-Dependent Twinning Evolution and Ferroelectric Behavior of Epitaxial BiFeO 3 (001) Thin Films. *Phys. Rev. B* **2010**, *82* (6), 064108. https://doi.org/10.1103/PhysRevB.82.064108.

(95) Chen, Z.; Qi, Y.; You, L.; Yang, P.; Huang, C. W.; Wang, J.; Sritharan, T.; Chen, L. Large Tensile-Strain-Induced Monoclinic M B Phase in BiFeO 3 Epitaxial Thin Films on a PrScO 3 Substrate. *Phys. Rev. B* **2013**, *88* (5), 054114. https://doi.org/10.1103/PhysRevB.88.054114.

(96) Xu, G.; Li, J.; Viehland, D. Ground State Monoclinic (Mb) Phase in (110)c BiFeO3 Epitaxial Thin Films. *Appl. Phys. Lett.* **2006**, *89* (22), 222901. https://doi.org/10.1063/1.2392818.

(97) Sando, D.; Barthélémy, A.; Bibes, M. $BiFeO_3$ Epitaxial Thin Films and Devices: Past, Present and Future. *J. Phys.: Condens. Matter* **2014**, *26* (47), 473201. https://doi.org/10.1088/0953-8984/26/47/473201.

(98) Sando, D.; Young, T.; Bulanadi, R.; Cheng, X.; Zhou, Y.; Weyland, M.; Munroe, P.; Nagarajan, V. Designer Defect Stabilization of the Super Tetragonal Phase in >70-Nm-Thick $BiFeO_3$ Films

on LaAlO $_3$ Substrates. *Jpn. J. Appl. Phys.* **2018**, *57* (9), 0902B2. https://doi.org/10.7567/JJAP.57.0902B2.

(99) Wang, J.; Neaton, J. B.; Zheng, H.; Nagarajan, V.; Ogale, S. B.; Liu, B.; Viehland, D.; Vaithyanathan, V.; Schlom, D. G.; Waghmare, U. V.; Spaldin, N. A.; Rabe, K. M.; Wuttig, M.; Ramesh, R. Epitaxial BiFeO3 Multiferroic Thin Film Heterostructures. **2003**, *299*, 5.

(100) Béa, H.; Bibes, M.; Petit, S.; Kreisel, J.; Barthélémy, A. Structural Distortion and Magnetism of BiFeO $_3$ Epitaxial Thin Films: A Raman Spectroscopy and Neutron Diffraction Study. *Philosophical Magazine Letters* **2007**, *87* (3–4), 165–174. https://doi.org/10.1080/09500830701235802.

(101) Ke, X.; Zhang, P. P.; Baek, S. H.; Zarestky, J.; Tian, W.; Eom, C. B. Magnetic Structure of Epitaxial Multiferroic BiFeO 3 Films with Engineered Ferroelectric Domains. *Phys. Rev. B* **2010**, *82* (13), 134448. https://doi.org/10.1103/PhysRevB.82.134448.

(102) Sando, D.; Agbelele, A.; Rahmedov, D.; Liu, J.; Rovillain, P.; Toulouse, C.; Infante, I. C.; Pyatakov, A. P.; Fusil, S.; Jacquet, E.; Carrétéro, C.; Deranlot, C.; Lisenkov, S.; Wang, D.; Le Breton, J.-M.; Cazayous, M.; Sacuto, A.; Juraszek, J.; Zvezdin, A. K.; Bellaiche, L.; Dkhil, B.; Barthélémy, A.; Bibes, M. Crafting the Magnonic and Spintronic Response of BiFeO3 Films by Epitaxial Strain. *Nature Mater* **2013**, *12* (7), 641–646. https://doi.org/10.1038/nmat3629.

(103) Burns, S. R.; Sando, D.; Xu, B.; Dupé, B.; Russell, L.; Deng, G.; Clements, R.; Paull, O. H. C.; Seidel, J.; Bellaiche, L.; Valanoor, N.; Ulrich, C. Expansion of the Spin Cycloid in Multiferroic BiFeO3 Thin Films. *npj Quantum Mater.* **2019**, *4* (1), 18. https://doi.org/10.1038/s41535-019-0155-2.

(104) Sharma, P.; Zhang, Q.; Sando, D.; Lei, C. H.; Liu, Y.; Li, J.; Nagarajan, V.; Seidel, J. Nonvolatile Ferroelectric Domain Wall Memory. *Sci. Adv.* **2017**, *3* (6), e1700512. https://doi.org/10.1126/sciadv.1700512.

(105) Sando, D.; Appert, F.; Xu, B.; Paull, O.; Burns, S. R.; Carrétéro, C.; Dupé, B.; Garcia, V.; Gallais, Y.; Sacuto, A.; Cazayous, M.; Dkhil, B.; Le Breton, J. M.; Barthélémy, A.; Bibes, M.; Bellaiche, L.; Nagarajan, V.; Juraszek, J. A Magnetic Phase Diagram for Nanoscale Epitaxial BiFeO $_3$ Films. *Applied Physics Reviews* **2019**, *6* (4), 041404. https://doi.org/10.1063/1.5113530.

(106) Bertinshaw, J.; Maran, R.; Callori, S. J.; Ramesh, V.; Cheung, J.; Danilkin, S. A.; Lee, W. T.; Hu, S.; Seidel, J.; Valanoor, N.; Ulrich, C. Direct Evidence for the Spin Cycloid in Strained Nanoscale Bismuth Ferrite Thin Films. *Nat Commun* **2016**, *7* (1), 12664. https://doi.org/10.1038/ncomms12664.

(107) Sando, D.; Appert, F.; Burns, S. R.; Zhang, Q.; Gallais, Y.; Sacuto, A.; Cazayous, M.; Garcia, V.; Fusil, S.; Carrétéro, C.; Le Breton, J. M.; Barthélémy, A.; Bibes, M.; Juraszek, J.; Nagarajan, V. Influence of Flexoelectricity on the Spin Cycloid in (110)-Oriented BiFe O 3 Films. *Phys. Rev. Materials* **2019**, *3* (10), 104404. https://doi.org/10.1103/PhysRevMaterials.3.104404.

(108) Bibes, M.; Barthélémy, A. Towards a Magnetoelectric Memory. *Nature Mater* **2008**, *7* (6), 425–426. https://doi.org/10.1038/nmat2189.

(109) Gross, I.; Akhtar, W.; Garcia, V.; Martínez, L. J.; Chouaieb, S.; Garcia, K.; Carrétéro, C.; Barthélémy, A.; Appel, P.; Maletinsky, P.; Kim, J.-V.; Chauleau, J. Y.; Jaouen, N.; Viret, M.; Bibes, M.; Fusil, S.; Jacques, V. Real-Space Imaging of Non-Collinear Antiferromagnetic Order with a Single-Spin Magnetometer. *Nature* **2017**, *549* (7671), 252–256. https://doi.org/10.1038/nature23656.

(110) Chauleau, J.-Y.; Haltz, E.; Carrétéro, C.; Fusil, S.; Viret, M. Multi-Stimuli Manipulation of Antiferromagnetic Domains Assessed by Second-Harmonic Imaging. *Nature Mater* **2017**, *16* (8), 803–807. https://doi.org/10.1038/nmat4899.

(111) Agbelele, A.; Sando, D.; Toulouse, C.; Paillard, C.; Johnson, R. D.; Rüffer, R.; Popkov, A. F.; Carrétéro, C.; Rovillain, P.; Le Breton, J.-M.; Dkhil, B.; Cazayous, M.; Gallais, Y.; Méasson, M.-A.; Sacuto, A.; Manuel, P.; Zvezdin, A. K.; Barthélémy, A.; Juraszek, J.; Bibes, M. Strain and Magnetic Field Induced Spin-Structure Transitions in Multiferroic BiFeO $_3$. *Adv. Mater.* **2017**, *29* (9), 1602327. https://doi.org/10.1002/adma.201602327.

(112) Kubel, F.; Schmid, H. Structure of a Ferroelectric and Ferroelastic Monodomain Crystal of the Perovskite BiFeO3. *Acta Crystallogr B Struct Sci* **1990**, *46* (6), 698–702. https://doi.org/10.1107/S0108768190006887.
(113) Johann, F.; Morelli, A.; Biggemann, D.; Arredondo, M.; Vrejoiu, I. Epitaxial Strain and Electric Boundary Condition Effects on the Structural and Ferroelectric Properties of BiFeO 3 Films. *Phys. Rev. B* **2011**, *84* (9), 094105. https://doi.org/10.1103/PhysRevB.84.094105.
(114) Opel, M.; Geprägs, S.; Althammer, M.; Brenninger, T.; Gross, R. Laser Molecular Beam Epitaxy of ZnO Thin Films and Heterostructures. *J. Phys. D: Appl. Phys.* **2013**, *47* (3), 034002. https://doi.org/10.1088/0022-3727/47/3/034002.
(115) Williamson, G. K.; Hall, W. H. X-Ray Line Broadening from Filed Aluminium and Wolfram. *Acta Metallurgica* **1953**, *1* (1), 22–31. https://doi.org/10.1016/0001-6160(53)90006-6.
(116) Jeon, B. C.; Lee, D.; Lee, M. H.; Yang, S. M.; Chae, S. C.; Song, T. K.; Bu, S. D.; Chung, J.-S.; Yoon, J.-G.; Noh, T. W. Flexoelectric Effect in the Reversal of Self-Polarization and Associated Changes in the Electronic Functional Properties of $BiFeO_3$ Thin Films. *Adv. Mater.* **2013**, *25* (39), 5643–5649. https://doi.org/10.1002/adma.201301601.
(117) Meyer, E.; Hug, H. J.; Bennewitz, R. *Scanning Probe Microscopy*; Advanced Texts in Physics; Springer Berlin Heidelberg: Berlin, Heidelberg, 2004. https://doi.org/10.1007/978-3-662-09801-1.
(118) Crassous, A.; Sluka, T.; Tagantsev, A. K.; Setter, N. Polarization Charge as a Reconfigurable Quasi-Dopant in Ferroelectric Thin Films. *Nature Nanotech* **2015**, *10* (7), 614–618. https://doi.org/10.1038/nnano.2015.114.
(119) Mara Batzer. Optimization of Single Crystalline All Diamond Scanning Probes for Quantum Sensing Applications, 2019.
(120) Patrick Appel. Scanning Nanomagnetometry: Probing Magnetism with Single Spins in Diamond, 2017.
(121) Barfuss, A. Hybrid Spin-Nanomechanics with Single Spins in Diamond Mechanical Oscillators, 2017.
(122) Isabell Gross. Exploring Non-Collinear Spin Structures in Thin Magnetic Films with Nitrogen-Vacancy Scanning Magnetometry, 2017.
(123) Maletinsky, P.; Hong, S.; Grinolds, M. S.; Hausmann, B.; Lukin, M. D.; Walsworth, R. L.; Loncar, M.; Yacoby, A. A Robust Scanning Diamond Sensor for Nanoscale Imaging with Single Nitrogen-Vacancy Centres. *Nature Nanotech* **2012**, *7* (5), 320–324. https://doi.org/10.1038/nnano.2012.50.
(124) Sacchi, M.; Jaouen, N.; Popescu, H.; Gaudemer, R.; Tonnerre, J. M.; Chiuzbaian, S. G.; Hague, C. F.; Delmotte, A.; Dubuisson, J. M.; Cauchon, G.; Lagarde, B.; Polack, F. The SEXTANTS Beamline at SOLEIL: A New Facility for Elastic, Inelastic and Coherent Scattering of Soft X-Rays. *J. Phys.: Conf. Ser.* **2013**, *425* (7), 072018. https://doi.org/10.1088/1742-6596/425/7/072018.
(125) Jaouen, N.; Tonnerre, J.-M.; Kapoujian, G.; Taunier, P.; Roux, J.-P.; Raoux, D.; Sirotti, F. An Apparatus for Temperature-Dependent Soft X-Ray Resonant Magnetic Scattering. *J Synchrotron Rad* **2004**, *11* (4), 353–357. https://doi.org/10.1107/S0909049504013767.
(126) Lovesey, S. W.; van der Laan, G. Resonant X-Ray Diffraction from Chiral Electric-Polarization Structures. *Phys. Rev. B* **2018**, *98* (15), 155410. https://doi.org/10.1103/PhysRevB.98.155410.
(127) Chauleau, J.-Y.; Chirac, T.; Fusil, S.; Garcia, V.; Akhtar, W.; Tranchida, J.; Thibaudeau, P.; Gross, I.; Blouzon, C.; Finco, A.; Bibes, M.; Dkhil, B.; Khalyavin, D. D.; Manuel, P.; Jacques, V.; Jaouen, N.; Viret, M. Electric and Antiferromagnetic Chiral Textures at Multiferroic Domain Walls. *Nat. Mater.* **2020**, *19* (4), 386–390. https://doi.org/10.1038/s41563-019-0516-z.
(128) Sando, D.; Han, M.; Govinden, V.; Paull, O.; Appert, F.; Carrétéro, C.; Fischer, J.; Barthélémy, A.; Bibes, M.; Garcia, V.; Fusil, S.; Dkhil, B.; Juraszek, J.; Zhu, Y.; Ma, X.; Nagarajan, V. Interfacial Strain Gradients Control Nanoscale Domain Morphology in Epitaxial $BiFeO_3$ Multiferroic Films. *Adv. Funct. Mater.* **2020**, 2000343. https://doi.org/10.1002/adfm.202000343.

(129) Kan, D.; Takeuchi, I. Effect of Substrate Orientation on Lattice Relaxation of Epitaxial BiFeO3 Thin Films. *Journal of Applied Physics* **2010**, *108* (1), 014104. https://doi.org/10.1063/1.3452360.
(130) Waterfield Price, N.; Vibhakar, A. M.; Johnson, R. D.; Schad, J.; Saenrang, W.; Bombardi, A.; Chmiel, F. P.; Eom, C. B.; Radaelli, P. G. Strain Engineering a Multiferroic Monodomain in Thin-Film BiFeO3. *Phys. Rev. Applied* **2019**, *11* (2), 024035. https://doi.org/10.1103/PhysRevApplied.11.024035.
(131) Nahas, Y.; Prokhorenko, S.; Fischer, J.; Xu, B.; Carrétéro, C.; Prosandeev, S.; Bibes, M.; Fusil, S.; Dkhil, B.; Garcia, V.; Bellaiche, L. Inverse Transition of Labyrinthine Domain Patterns in Ferroelectric Thin Films. *Nature* **2020**, *577* (7788), 47–51. https://doi.org/10.1038/s41586-019-1845-4.
(132) Greer, A. L. Too Hot to Melt. *Nature* **2000**, *404* (6774), 134–135.
(133) Portmann, O.; Vaterlaus, A.; Pescia, D. An Inverse Transition of Magnetic Domain Patterns in Ultrathin Films. *Nature* **2003**, *422* (6933), 701–704. https://doi.org/10.1038/nature01538.
(134) Gu, Z.; Pandya, S.; Samanta, A.; Liu, S.; Xiao, G.; Meyers, C. J. G.; Damodaran, A. R.; Barak, H.; Dasgupta, A.; Saremi, S.; Polemi, A.; Wu, L.; Podpirka, A. A.; Will-Cole, A.; Hawley, C. J.; Davies, P. K.; York, R. A.; Grinberg, I.; Martin, L. W.; Spanier, J. E. Resonant Domain-Wall-Enhanced Tunable Microwave Ferroelectrics. *Nature* **2018**, *560* (7720), 622–627. https://doi.org/10.1038/s41586-018-0434-2.
(135) Yang, S. Y.; Seidel, J.; Byrnes, S. J.; Shafer, P.; Yang, C.-H.; Rossell, M. D.; Yu, P.; Chu, Y.-H.; Scott, J. F.; Ager, J. W.; Martin, L. W.; Ramesh, R. Above-Bandgap Voltages from Ferroelectric Photovoltaic Devices. *Nature Nanotech* **2010**, *5* (2), 143–147. https://doi.org/10.1038/nnano.2009.451.
(136) Haykal, A.; Fischer, J.; Akhtar, W.; Chauleau, J.-Y.; Sando, D.; Finco, A.; Godel, F.; Birkhölzer, Y. A.; Carrétéro, C.; Jaouen, N.; Bibes, M.; Viret, M.; Fusil, S.; Jacques, V.; Garcia, V. Antiferromagnetic Textures in BiFeO3 Controlled by Strain and Electric Field. *Nat Commun* **2020**, *11* (1), 1704. https://doi.org/10.1038/s41467-020-15501-8.
(137) Balke, N.; Choudhury, S.; Jesse, S.; Huijben, M.; Chu, Y. H.; Baddorf, A. P.; Chen, L. Q.; Ramesh, R.; Kalinin, S. V. Deterministic Control of Ferroelastic Switching in Multiferroic Materials. *Nature Nanotech* **2009**, *4* (12), 868–875. https://doi.org/10.1038/nnano.2009.293.
(138) Muhlbauer, S.; Binz, B.; Jonietz, F.; Pfleiderer, C.; Rosch, A.; Neubauer, A.; Georgii, R.; Boni, P. Skyrmion Lattice in a Chiral Magnet. *Science* **2009**, *323* (5916), 915–919. https://doi.org/10.1126/science.1166767.
(139) Moreau-Luchaire, C.; Moutafis, C.; Reyren, N.; Sampaio, J.; Vaz, C. A. F.; Van Horne, N.; Bouzehouane, K.; Garcia, K.; Deranlot, C.; Warnicke, P.; Wohlhüter, P.; George, J.-M.; Weigand, M.; Raabe, J.; Cros, V.; Fert, A. Additive Interfacial Chiral Interaction in Multilayers for Stabilization of Small Individual Skyrmions at Room Temperature. *Nature Nanotech* **2016**, *11* (5), 444–448. https://doi.org/10.1038/nnano.2015.313.
(140) Balke, N.; Winchester, B.; Ren, W.; Chu, Y. H.; Morozovska, A. N.; Eliseev, E. A.; Huijben, M.; Vasudevan, R. K.; Maksymovych, P.; Britson, J.; Jesse, S.; Kornev, I.; Ramesh, R.; Bellaiche, L.; Chen, L. Q.; Kalinin, S. V. Enhanced Electric Conductivity at Ferroelectric Vortex Cores in BiFeO3. *Nature Phys* **2012**, *8* (1), 81–88. https://doi.org/10.1038/nphys2132.
(141) Li, Y.; Jin, Y.; Lu, X.; Yang, J.-C.; Chu, Y.-H.; Huang, F.; Zhu, J.; Cheong, S.-W. Rewritable Ferroelectric Vortex Pairs in BiFeO3. *npj Quant Mater* **2017**, *2* (1), 43. https://doi.org/10.1038/s41535-017-0047-2.
(142) Ma, J.; Ma, J.; Zhang, Q.; Peng, R.; Wang, J.; Liu, C.; Wang, M.; Li, N.; Chen, M.; Cheng, X.; Gao, P.; Gu, L.; Chen, L.-Q.; Yu, P.; Zhang, J.; Nan, C.-W. Controllable Conductive Readout in Self-Assembled, Topologically Confined Ferroelectric Domain Walls. *Nature Nanotech* **2018**, *13* (10), 947–952. https://doi.org/10.1038/s41565-018-0204-1.
(143) Yang, W.; Tian, G.; Zhang, Y.; Xue, F.; Zheng, D.; Zhang, L.; Wang, Y.; Chen, C.; Fan, Z.; Hou, Z.; Chen, D.; Gao, J.; Zeng, M.; Qin, M.; Chen, L.-Q.; Gao, X.; Liu, J.-M. Quasi-One-Dimensional

Metallic Conduction Channels in Exotic Ferroelectric Topological Defects. *arXiv:2006.02011 [cond-mat]* **2020**.

université PARIS-SACLAY | ÉCOLE DOCTORALE Physique en l'Île-de-France (PIF)

Titre : Contrôle et imagerie de textures électriques et antiferromagnétiques dans les couches minces multiferroïques de $BiFeO_3$

Mots clés : spintronique, multiferroïque, ferroélectrique, antiferromagnétique, oxydes, couches minces

Résumé : Les matériaux antiferromagnétiques suscitent un intérêt croissant pour la spintronique de par leur insensibilité aux champs magnétiques parasites et leur dynamique magnétique ultrarapide. Cependant, la lecture et le contrôle de l'ordre antiferromagnétique restent des verrous pour le développement des dispositifs. Dans les matériaux multiferroïques, le couplage magnétoélectrique entre les ordres électrique et magnétique pourrait permettre de contrôler l'antiferromagnétisme avec un champ électrique. Dans cette thèse, nous imageons une grande variété de textures antiferromagnétiques que nous contrôlons par l'ingénierie des contraintes et le champ électrique pour l'archétype des matériaux multiferroïques, $BiFeO_3$. Nous élaborons des films minces sous différentes contraintes d'épitaxie, maîtrisant ainsi la texture de domaines ferroélectriques, telle qu'imagée par microscopie à force piézoélectrique. De plus, nous montrons qu'une transition de phase inverse peut être utilisée pour accroître l'ordre électrique global, d'une configuration labyrinthique de domaines vers un réseau périodique en bandes rectilignes. La magnétométrie à centre NV nous permet de corréler les textures antiferromagnétiques et ferroélectriques. Nous démontrons que les contraintes stabilisent différents types de cycloïdes ainsi qu'un ordre antiferromagnétique colinéaire. La diffraction X élastique résonante permet de confirmer macroscopiquement l'existence de deux types de cycloïdes. Enfin, nous contrôlons électriquement ces textures antiferromagnétiques, passant d'une cycloïde à une autre ou transformant un ordre colinéaire en cycloïde. Sur la base d'un substrat imposant une contrainte anisotrope, nous stabilisons des films ne présentant qu'un seul domaine ferroélectrique associé à un unique domaine antiferromagnétique. Ceci ouvre de larges perspectives pour explorer le couplage entre l'antiferromagnétisme non-colinéaire et le transport de spin.

Title: Imaging and tailoring electric and antiferromagnetic textures in multiferroic thin films of $BiFeO_3$

Keywords: spintronic, multiferroic, ferroelectric, antiferromagnetic, oxides, thin films

Abstract: Antiferromagnetic materials are generating a growing interest for spintronics due to important assets such as their insensitivity to spurious magnetic fields and fast magnetization dynamics. A major bottleneck for functional devices is the readout and electric control of the antiferromagnetic order. In multiferroics, the magnetoelectric coupling between ferroelectric and antiferromagnetic orders may represent an efficient way to control antiferromagnetism with an electric field. In this thesis, we observe a wide variety of antiferromagnetic textures that we control by strain engineering and electric field in the archetypical multiferroic, $BiFeO_3$. We elaborate epitaxial $BiFeO_3$ thin films, harbouring various ferroelectric domain landscapes, as imaged by piezoresponse force microscopy. Furthermore, we resort on an inverse phase transition to improve the global electrical order from maze to perfect array of striped ferroelectric domains. Using scanning NV magnetometry, we correlate the antiferromagnetic landscapes to the ferroelectric ones. We demonstrate that strain stabilizes bulk or exotic spin cycloids, as well as collinear antiferromagnetic order. With resonant X-ray elastic scattering, we macroscopically confirm the existence of two types of cycloid. Furthermore, we electrically design antiferromagnetic landscapes on demand, changing one type of cycloid to another or turning collinear states into non-collinear ones. Finally, resorting on anisotropic strain, we stabilize a single domain ferroelectric state, in which a single spin cycloid propagates. This opens a fantastic avenue to investigate the coupling between non-collinear antiferromagnetism and spin transport.

Université Paris-Saclay
Espace Technologique / Immeuble Discovery
Route de l'Orme aux Merisiers RD 128 / 91190 Saint-Aubin, France